Development of a Tethered Biomembrane Biosensing Platform for the Incorporation of Ion Channels

James Kenneth Roger Kendall

Submitted in accordance with the requirements for the degree of
Doctor of Philosophy

The University of Leeds
School of Physics & Astronomy

September 2011

The candidate confirms that the work submitted is his own, except where work which has formed part of jointly-authored publications has been included. The contribution of the candidate and the other authors to this work has been explicitly indicated below. The candidate confirms that appropriate credit has been given within the thesis where reference has been made to the work of others.

James K. R. Kendall, Benjamin R. G. Johnson, Philip H. Symonds, Guiseppi Imperato, Richard J. Bushby, James D. Gwyer, Cees van Berkel, Stephen D. Evans, and Lars J. C. Jeuken. Effect of the Structure of Cholesterol-Based Tethered Bilayer Lipid Membranes on Ionophore Activity. *ChemPhysChem* 11:2191-2198, 2010.

Kendall et al. [2010] formed the basis of Chapter 4. All work was conducted or supervised by the candidate (James K. R. Kendall), with the exception of surface plasmon resonance experiments conducted by Benjamin R. G. Johnson. Philip H. Symonds and Guiseppi Imperato assisted with electrochemical impedance spectroscopy measurements of gramicidin incorporation into tethered bilayer lipid membranes. Richard J. Bushby provided the EO_3-cholesterol tether that the lipid bilayers were formed on, while James D. Gwyer and Cees van Berkel of Philips Research aided design of the patterned gold electrodes used in the chapter. Stephen D. Evans and Lars J. C. Jeuken provided guidance with experimental design and analysis.

Acknowledgments

I would like to thank my supervisors Dr Lars Jeuken, Professor Stephen Evans, and Dr Cees van Berkel for their advice during my PhD. Thank you also to members of the Molecular and Nanoscale Physics group - especially Dr Sophie Weiss and Dr Duncan McMillan for their technical expertise and support, as well as soon-to-be Drs Matthew Cheetham and Jono McKendry (we made it guys!). Thanks to Professor Peter Henderson, Dr Vincent Postis and others in the Astbury Centre for Structural Biology, and Professor David Beech, Dr Jacqueline Naylor and Dr Sarka Tumova of the Multidisciplinary Cardiovascular Research Centre for help and advice with the work on TRPC5, use of the IonGate system, expression in bacterial systems and protein purification in general.

Further thanks goes to Professor Andrew Nelson, Dr Zachary Coldrick and others in the Centre for Molecular Nanoscience at the School of Chemistry, University of Leeds for discussions on gramicidin and electrochemistry in general; as well as Dr James Gwyer, Dr David Pettigrew, Mr Carl Glasse and other collaborators at Philips Research in Cambridge and MiPlaza at the Philips Research High Tech Campus in Eindhoven, The Netherlands for production and development of the electrodes used.

This work was supported by a CASE studentship from the Biotechnology and Biological Sciences Research Council (BB/E527939/1) in conjunction with Philips Research (UK).

To my family - thank you for putting up with me and this life-eating thesis for the past 4 years! Without your help and support these pages would still be blank.
To my friends - thank you for much needed distractions, plentiful pints and making the last few years some of the best of my life.
Finally, a special mention to my closest of friends, the Wolfbaggers.

lupus saccus in fabula

Abstract

Solid-supported membranes present a biomimetic platform that can be adapted for biophysical, biochemical and electrophysiological studies. In addition to this they offer an environment to host membrane proteins for the purposes of biosensing. This thesis examines the use of such a system and the possibilities it presents for the studies of ion channels and their potential applications in biosensing. Electrochemical impedance spectroscopy (EIS) is a powerful technique in the study of solid-supported membranes giving access to capacitance and resistance data, and as such was employed as the main method of characterisation.

Electrodes were designed for this purpose in conjunction with Philips Research, and the suitability of the surface for the formation of insulating tethered bilayer lipid membranes (tBLMs). The development of these electrodes led to the incorporation of a SiO_2 insulating layer, however its addition resulted in difficulties with the formation of self-assembled monolayers (SAMs). However, further refinement of the manufacturing process should resolve these issues. Despite these difficulties, studies were performed using first generation electrodes (P1). Two ionophores, valinomycin and gramicidin, were employed in the characterisation of the ion transport properties of the tBLM system. These studies yielded important information about the structure of the tBLM system under investigation, as well as the ways ion transport can be presented in EIS.

Using the work on ionophores as a foundation, an investigation into the incorporation and characterisation of ion channels in tBLM was conducted. Three channels were studied - a ligand-gated eukaryotic Ca^{2+}-permeant channel (TRPC5), a voltage-gated prokaryotic Na^+-permeant channel (Na_vCbt), and a pH-gated K^+-permeant channel (KcsA). The success of these studies varied, but provided strong evidence that ion channel incorporation is possible. Further investigation of channel function in the tBLM is required as measured activity is lower than that suggested by literature.

Contents

Abbreviations and Constants xii

1 Background to Work **1**

1.1 Fundamentals of Biosensors 1

1.2 A History of Biosensors 1

1.2.1 Amperometric Biosensors 2

1.2.2 Affinity Biosensors 3

1.2.3 Whole Cell Biosensors 3

1.3 Membrane-Based Biosensors 5

1.3.1 Cell Membranes 5

1.3.2 Bilayer Lipid Membranes 9

1.3.3 Solid-Supported Bilayer Lipid Membranes 11

1.3.4 Tethered Bilayer Lipid Membranes 13

1.4 Ion Transport 18

1.4.1 Nernst Equation 19

1.4.2 Ionophores as Model Systems 19

1.4.3 Ion Channels 23

2 Theory of Experimental Techniques **30**

2.1 Electrochemical Impedance Spectroscopy (EIS) 30

2.1.1 Electric Double Layer 30

2.1.2 Basic Theory 32

2.1.3 Experimental Setup 35

2.1.4 Impedance Plots 36

2.1.5 Equivalent Circuits 37

2.1.6 Fitting 42

2.1.7 Case Study: Impedance of a EO_3C SAM 42

2.2 Cyclic Voltammetry 45

2.2.1 Use of Redox Probes for Determination of Electrode Surface Area . 46

2.2.2 Microelectrode Behaviour 48

2.2.3 Electrode Array Behaviour 51

2.3 IonGate SURFE2R/Solid Supported Membrane Electrophysiology 53

2.3.1 Ion Pumps in IonGate 55

2.3.2 Ion Channels in IonGate 56
2.4 Atomic Force Microscopy (AFM) 57
2.5 Surface Plasmon Resonance (SPR) 59
2.6 Electron Spectroscopy 62
2.6.1 Electron Notation 62
2.6.2 X-Ray Photoemission Spectroscopy (XPS) 65
2.6.3 Auger Emission Spectroscopy (AES) 66
2.7 Scanning Electron Microscopy (SEM) 69

3 Characterisation and Development of Electrodes 72
3.1 Introduction 72
3.1.1 Self-Assembled Monolayers and Factors That Affect Their Formation 73
3.1.2 Manufacture of Patterned Electrodes by MiPlaza 79
3.2 Experimental Section 81
3.2.1 Materials 81
3.2.2 Production of Electrodes 81
3.2.3 Cleaning of Electrodes 82
3.2.4 Formation of Self Assembled Monolayers 82
3.2.5 Vesicle Formation 82
3.2.6 Tethered Bilayer Lipid Membrane (tBLM) Formation 82
3.2.7 Electrochemical Impedance Spectroscopy (EIS) 82
3.2.8 Cyclic Voltammetry 85
3.2.9 Scanning Electron Microscopy 87
3.2.10 X-Ray Photoemission Spectroscopy 87
3.2.11 Scanning Auger Emission Spectroscopy 87
3.2.12 Atomic Force Microscopy 87
3.2.13 Light Microscopy 88
3.3 Initial Studies on the Cleaning of Gold Surfaces 89
3.3.1 X-Ray Photoelectron Spectroscopy (XPS) 89
3.3.2 Atomic Force Microscopy (AFM) 90
3.3.3 Electrochemical Impedance Spectroscopy (EIS) 91
3.3.4 Conclusions 95
3.4 Philips Research Electrodes: Series 1 96
3.4.1 Atomic Force Microscopy (AFM) 97
3.4.2 Cyclic Voltammetry 100
3.4.3 EIS of EO_3C and 6MH SAMs 104
3.4.4 Formation of Tethered Bilayer Lipid Membranes 106
3.4.5 Conclusions and alterations to be made 111
3.5 Philips Research Electrodes: Series 2 - MKI 112
3.5.1 Electrochemical Impedance Spectroscopy of 6MH and EO_3C SAMs . 112
3.5.2 Light microscopy 113

3.5.3 Scanning Electron Microscopy and Scanning Auger Electron Spectroscopy . . . 114
3.5.4 Conclusions and alterations to be made . . . 114
3.6 Philips Research Electrodes: Series 2 - mkII . . . 117
3.6.1 Initial study by CV . . . 117
3.6.2 Initial study by EIS . . . 118
3.6.3 Initial study by Light Microscope . . . 119
3.6.4 Initial study by XPS . . . 121
3.6.5 Effect of HF Cleaning on Removal of TiO_2 Layer . . . 123
3.6.6 Conclusion . . . 123
3.7 Philips Research Electrodes: Series 2 - mkIII . . . 125
3.7.1 EIS of ODT SAM . . . 125
3.7.2 XPS . . . 126
3.7.3 AFM . . . 128
3.7.4 Conclusions . . . 131
3.8 Conclusions & Discussions . . . 132

4 Ionophores as Model Ion Transporters 134
4.1 Introduction . . . 134
4.2 Experimental Section . . . 137
4.2.1 Materials . . . 137
4.2.2 Preparation of Electrodes . . . 137
4.2.3 Vesicle Formation . . . 137
4.2.4 Formation of Self-Assembled Monolayers (SAMs) . . . 137
4.2.5 Tethered Bilayer Lipid Membrane Formation . . . 138
4.2.6 Ionophore Reconstitution and Measurement . . . 138
4.2.7 Electrochemical Impedance Spectroscopy (EIS) . . . 138
4.2.8 Surface Plasmon Resonance (SPR) . . . 139
4.3 Results . . . 141
4.3.1 Formation of Tethered Bilayer Lipid Membranes . . . 141
4.3.2 Valinomycin . . . 141
4.3.3 Gramicidin . . . 142
4.4 Discussion . . . 148
4.5 Conclusions . . . 153

5 TRPC5 154
5.1 Introduction . . . 154
5.2 Experimental Section . . . 156
5.2.1 Materials . . . 156
5.2.2 Cell Culture . . . 156
5.2.3 Expression of TRPC5 . . . 156

5.2.4 Protein Preparation . . . 157
5.2.5 BCA Assay . . . 157
5.2.6 SDS-PAGE . . . 158
5.2.7 Western Blot . . . 158
5.2.8 IonGate . . . 158
5.2.9 Electrochemical Impedance Spectroscopy . . . 159
5.2.10 Formation of Mixed Proteoliposomes . . . 160
5.3 Results . . . 162
5.3.1 Protein Expression . . . 162
5.3.2 IonGate Solid-Supported Membrane Electrophysiology . . . 164
5.3.3 Electrochemical Impedance Spectroscopy . . . 172
5.4 Discussion . . . 175
5.4.1 Membrane Preparation . . . 175
5.4.2 IonGate - Solid-Supported Membrane Electrophysiology . . . 176
5.4.3 Electrochemical Impedance Spectroscopy . . . 177
5.5 Conclusion . . . 180
5.5.1 Future Ion Channel Candidates . . . 180

6 Incorporation of Prokaryotic Ion Channels 182
6.1 Introduction . . . 182
6.1.1 KcsA . . . 182
6.1.2 Na$_v$Cbt . . . 187
6.2 Experimental Section . . . 189
6.2.1 Materials . . . 189
6.2.2 Ion Channel Production . . . 189
6.2.3 Protein Determination . . . 191
6.2.4 Formation of Tethered Bilayer Lipid Membranes . . . 191
6.2.5 EIS Measurements . . . 191
6.3 Results . . . 193
6.3.1 KcsA . . . 193
6.3.2 NavCbt . . . 196
6.4 Discussion . . . 202
6.4.1 KcsA . . . 202
6.4.2 Na$_v$Cbt . . . 202
6.5 Conclusion . . . 204

7 General Discussion and Conclusion 206

References 213

Appendices 239

A Philips Research Electrode Designs 239
A.1 Series 1 electrodes (P1) 239
A.2 Series 2 electrodes (P2) 241

B Effect of HF on Removal of Ti Layer Present on P2 MKII Electrodes 243
B.1 EIS following Ti Etch 243
B.2 Post-Etch study by XPS and SAES 244

List of Tables

1.1 TRP channels and their ligands 27

2.1 Impedance equations for equivalent circuit components. 41
2.2 Membrane protein preparations studied with the IonGate system 54
2.3 The relationship between quantum numbers, spectroscopist's notation and X-ray notation 64

3.1 Roughness of various Au electrodes 75
3.2 XPS data expressed as percentages relative to the Au $4f_{7/2}$ peak 90
3.3 Roughness as root mean square (RMS) values for the various cleaning protocols trialled on evaporated gold as measured with AFM. 92
3.4 The effect of ethanolic reduction of gold on SAM formation 94
3.5 Dimensions of P1 electrodes 96
3.6 Table of electrode dimensions for various electrode designs 98
3.7 CV parameters for P1 electrodes 100
3.8 Results of ferrocyanide probing of P1E electrodes 102
3.9 EIS parameters for 100% EO_3C and 100% 6MH SAMs formed on P1 electrodes 104
3.10 EISFit parameters for tBLMs formed on either 100%, 80% or 40% EO_3C SAMs with P1 electrodes 106
3.11 Dimensions of P2 electrodes 112
3.12 Comparison of cleaning methods and their effects on capacitance of 6MH and EO_3C SAMs 113
3.13 XPS ratios of P2 MKII electrodes before and after cleaning with acetone . . 123
3.14 EIS of ODT SAMs on P2 MKIII electrodes following acetone cleaning steps of varying lengths 125
3.15 XPS ratios of P2 MKIII electrodes displayed as % of total counts 128

4.1 EIS parameters for ionophore-doped tBLMs formed on pure EO_3C SAMs . 145
4.2 EIS parameters for ionophore-doped tBLMs formed on mixed EO_3C/6MH SAMs 146

5.1 EISFit parameters for the addition of La^{3+} to tBLM-containing TRPC5 . . 173

5.2 EISFit parameters for the addition of La^{3+} to control tBLM containing no TRPC5 . . . 174

6.1 EISFit parameters for tBLM containing KcsA . . . 195
6.2 EISFit parameters for tBLM containing Na$_v$Cbt . . . 199
6.3 EISFit parameters for control tBLM containing no Na$_v$Cbt . . . 201

B.1 XPS ratios for P2 MKII electrodes following Ti etch . . . 245

List of Figures

1.1 An outline of a biosensor 1

1.2 Clark and Lyons' proposed glucose biosensor 2

1.3 The system of arsenic resistance in *E. coli* 4

1.4 The Fluid Mosaic Model 6

1.5 The structure of a phospholipid 6

1.6 Various phospholipid structures 7

1.7 Structure of cholesterol 8

1.8 Membrane proteins 9

1.9 Lipid raft 10

1.10 BLM varieties 12

1.11 Chemical structure of triethyleneoxy cholesterol (EO_3C) 14

1.12 Schematic representation of a tBLM formed from EO_3 cholesterol and 6-mercaptohexanol 14

1.13 Diphytanoyl lipids inspired by archaeal lipids 15

1.14 Ion Channel Switch biosensor 16

1.15 Mixed hBLM 17

1.16 Structure of valinomycin 20

1.17 Structure of gramicidin 21

1.18 Structures of the pore-forming peptides, alamethicin and hemolysin. 22

1.19 Structure of KcsA 24

1.20 Ion channel architectures 24

1.21 The use of helix dipoles in ion channels 25

1.22 Models of voltage-gating in channels 26

1.23 Structure of the nicotinic acetylcholine receptor (nAChR) 27

1.24 Features of the nicotinic acetylcholine receptor (nAChR) 28

1.25 TRP channel architecture 29

2.1 Models of the electric double layer 33

2.2 Phase shift 34

2.3 An electrochemical cell used in EIS 36

2.4 Polarising effect of an electric field on molecules 39

2.5 Examples of impedance data 44

2.6 Example cyclic voltammogram and its waveform 45
2.7 Electron transfer schemes 46
2.8 CV before and after ohmic drop correction 47
2.9 Different type of microelectrode 48
2.10 CV of electron transfer at a microelectrode. 49
2.11 CV of electron transfer at a hybrid electrode 50
2.12 Diffusion schemes of various electrodes 51
2.13 Differences in diffusion schemes shown as $\sqrt{\text{scan rate}}$ vs current. 52
2.14 Diffusion layer for a micro electrode array 52
2.15 IonGate workstation 53
2.16 IonGate principle 55
2.17 IonGate current response 56
2.18 IonGate measurements with gramicidin 57
2.19 IonGate measurements with nAChR 58
2.20 An AFM cantilever tip 58
2.21 The workings of an atomic force microscope (AFM) 59
2.22 Surface plasmon resonance 60
2.23 Surface plasmon resonance 61
2.24 Diagram of electron orbitals 63
2.25 Diagram of electron sub-orbitals 64
2.26 The principle of X-ray photoemission spectroscopy. 65
2.27 X-ray photoemission spectra and peak fitting 67
2.28 The principle of Auger emission spectroscopy. 68
2.29 Auger Contrast Mapping 68
2.30 The interaction volume of beam electrons 71
2.31 Comparison of a sample imaged with electron and light microscopy 71

3.1 AFM images showing the roughness of various Au surfaces 76
3.2 Equivalent circuits used in analysis of impedance data. 84
3.3 Complex equivalent circuit 86
3.4 XPS spectra for cleaning protocols 91
3.5 EIS showing the effect of ethanolic reduction of gold on SAM formation . . 93
3.6 AFM data for evaporated and sputtered gold 99
3.7 CVs of ferrocyanide probing on P1 electrodes 101
3.8 CVs of ferrocyanide probing on P1E electrodes 103
3.9 EIS of 100% EO_3C and 100% 6MH SAMs 105
3.10 EIS plots for hBLM and tBLM 109
3.11 Membrane resistance for tBLM formed on various P1 electrode designs . . . 110
3.12 EIS of P2 MKI electrodes 113
3.13 Light microscope images of first iteration P2 MKI F electrodes 114
3.14 SEM and SAES images of P2 MKI F electrodes 116

3.15 CV of P2 MKII electrodes 117
3.16 EIS of ODT SAMs formed on P2 MKII electrodes 118
3.17 Light microscopy of P2 MKII electrodes in initial state 119
3.18 P2 MKII electrodes following exposure to 4 M NaOH 120
3.19 P2 MKII electrodes following harsh cleaning methods 120
3.20 XPS scans of P2 MKII F electrodes 121
3.21 EIS of ODT SAMs on P2 MKIII electrodes following acetone cleaning steps of varying lengths 125
3.22 XPS spectra of P2MKIII electrodes following acetone cleaning steps of varying lengths 127
3.23 AFM of P2 MKIII electrodes 130

4.1 Chemical structure of EO_3C cholesterol, and a schematic representation of a tBLM formed on a mixed EO_3C/6MH SAM 135
4.2 Equivalent circuits used in analysis of impedance data. 139
4.3 EIS data showing effect of valinomycin on tBLMs formed on pure EO_3C or mixed EO_3C/6MH SAMs. 142
4.4 EIS data showing effect of gramicidin on tBLMs formed on pure EO_3C or mixed EO_3C/6MH SAMs. 143
4.5 EIS data showing titration of gramicidin on tBLMs formed on mixed EO_3C/6MH SAMs. 144
4.6 SPR data for addition of gramicidin to tBLMs formed on pure EO_3C or mixed EO_3C/6MH SAMs 147
4.7 Schematic of ionophore transport in different regions of a tBLM formed on a mixed EO_3 cholesterol/6-mercaptohexanol SAM 153

5.1 Equivalent circuit used in analysis of impedance data. 161
5.2 SDS-PAGE gel of fractionated TRPC5-containing membranes 163
5.3 Western Blot of fractionated TRPC5-containing membranes 163
5.4 Schematic representation of the flux of ions at each phase of IonGate experiments 164
5.5 TRPC5 IonGate data showing titration with La^{3+} 167
5.6 TRPC5 IonGate Analysis of Peak Height and Integrals vs La^{3+} concentration 168
5.7 TRPC5 IonGate data for the effect of 2-APB 169
5.8 TRPC5 IonGate Analysis of Effect of 2-APB on Peak Height and Integrals vs La^{3+} concentration 170
5.9 TRPC5 IonGate data showing titration with TCEP 171
5.10 EIS data for TRPC5-containing tBLM with addition of La^{3+} 172
5.11 EIS data for the effect of La^{3+} on mixed SAM tBLMs containing no TRPC5. 173

6.1 Sequence alignment of KcsA with various K^+ channels 183
6.2 Schematic representations of various K^+ channels 183

6.3 Structure of KcsA as determined by X-ray crystallography. 184
6.4 Diagram of the KcsA channel lumen 184
6.5 Schematic representation of the use of helix dipoles to stabilise ions in the channel lumen 185
6.6 SOSUI plot of $\mathrm{Na_v}$Cbt 187
6.7 Equivalent circuit used in analysis of impedance data of KcsA and $\mathrm{Na_v}$Cbt. 192
6.8 SDS-PAGE gel of KcsA purification products 193
6.9 EIS of tBLM containing KcsA where activity was detected 194
6.10 EIS of tBLM containing KcsA where activity was poor 195
6.11 SDS-PAGE gel of $\mathrm{Na_v}$Cbt purification products 196
6.12 EIS of tBLM containing $\mathrm{Na_v}$Cbt 198
6.13 EIS of control tBLM containing no $\mathrm{Na_v}$Cbt 200

A.1 Schematic of layers in series 1 (P1) electrodes 239
A.2 Schematic layout of P1A electrodes 239
A.3 Schematic layout of P1B electrodes 240
A.4 Schematic layout of P1C electrodes 240
A.5 Schematic layout of P1D electrodes 240
A.6 Schematic layout of P1E electrodes 240
A.7 Schematic of layers in first iteration of series 2 (P2) electrodes 241
A.8 Schematic of layers in second iteration of series 2 (P2) electrodes 241
A.9 Schematic of layers in third iteration of series 2 (P2) electrodes 241
A.10 Schematic layout of P2C electrodes 242
A.11 Schematic layout of P2E electrodes 242
A.12 Schematic layout of P2F electrodes 242

B.1 EIS of ODT SAMs formed on P2 MKII electrodes following Ti etching . . . 243
B.2 XPS spectra of P2 MKII electrodes following Ti etch 245
B.3 SAES contrast maps of P2 MKII electrodes following Ti etch protocol. . . . 246
B.4 SEM and SAES contrast maps of P2 MKII electrodes following Ti etch protocol. 248

Abbreviations and Contstants

Abbreviations

2-APB - 2-aminoethoxydiphenyl borate
6MH - 6-mercaptohexanol
AES - Auger emission spectoscopy
AFM - atomic force microscopy
BLM - bilayer lipid membrane
CV - cyclic voltammetry
CPE - constant phase element
DCM - dichloromethane
DOPC - 1,2-dioleoyl-*sn*-glycero-3-phosphocholine
DOPE - 1,2-dioleoyl-sn-glycero-3-phosphoethanolamine
DOPG - 1,2-dioleoyl-sn-glycero-3-phospho-(1'-rac-glycerol)
DOPI - 1,2-dioleoyl-sn-glycero-3-phospho-(1'-myo-inositol)
DOPS - 1,2-dioleoyl-sn-glycero-3-phospho-L-serine
DPhyHDL - di-phytanylglycerol-hexaethyleneglycol-di-lipoic acid
DPhyPC - 1,2-diphytanoyl-*sn*-glycerol-3-phosphocholine
DPhyPE - 1,2-diphytanoyl-*sn*-glycerol-3-phosphoethanolamine
DPhyTL - 2,3-di-*O*-phytanyl-*sn*-glycerol-1-tetraethylene glycol-D,L,-α-lipoic acid ester lipid
DTT - dithiothreitol
EDTA - ethylenediaminetetraacetic acid
EIS - electrochemical impedance spectroscopy
EO_3C - triethyleneoxythiol cholesterol
GFP - green fluorescent protein
GPCR - G-protein coupled receptor
hBLM - hybrid Bilayer Lipid Membrane
hCG - human chorionic gonadotrophin
ITO - indium-tin oxide
MOPS - 3-(*N*-morpholino)propanesulfonic acid
ODT - octadecanethiol
P1[A–E] - Philips first generation electrodes [designs A–E]
P2[C/E/F] - Philips second generation electrodes [designs C, E and F]
PC - phosphatidylcholine
PE - phosphatidylethanolamine
PG - phosphatidylglycerol
PI - phosphatidylinositol
PS - phosphatidylserine
pac - point of zero charge
QCM - quartz crystal microbalance

sBLM - supported Bilayer Lipid Membrane
SAES - scanning Auger emission spectroscopy
SAM - self assembled monolayer
SEM - scanning electron microscope
SPR - surface plasmon resonance
SUV - Small unilamellar vesicle
tBLM - tethered bilayer lipid membrane
TCEP - Tris (2-carboxyethyl) phosphine
TEGL - tetraethylene glycol-D,L-α-lipoic acid
TMA - tetramethylammonium
TRP - transient receptor potential
TRPC5 - canonical transient receptor potential channel 5
TSG - template stripped gold
WC14 - 20-tetradecyloxy-3,6,9,12,15,18,22-heptaoxahexatricontane-1-thiol
XPS - X-ray photoemission spectroscopy

Constants

F - Faraday's constant (96485.339924 C.mol^{-1})
R - Universal gas law constant (8.3145 m^3.Pa/(mol.K))
T - Room temperature (taken to be 293 K)

Chapter 1

Background to Work

1.1 Fundamentals of Biosensors

> ***biosensor* n.** *a biologically active substance (as an enzyme or antibody) or a living organism which is used as the basis of a device for detecting the presence of a particular chemical; a device of this kind.*
>
> - Oxford English Dictionary

Advancements in biotechnology and surface sciences have allowed us to isolate biological components. Many of these have a high degree of specificity for certain molecules; a property that can be exploited in the creation of biosensors. A biosensor like any other sensor has three main parts to it (Figure 1.1) - **a sensing component**, such as mercury in a thermometer or biosensor's enzyme or antibody, that will have a specific reaction to a change in conditions; **a transducer**, that will detect the sensing component's reaction and produce a secondary signal that is more readily detectable, such as an increase in electrical current; and **an interface** that makes the signal received easily understood, this could be as simple as the temperature scale on a mercury thermometer, or a microelectronic device with a liquid crystal display.

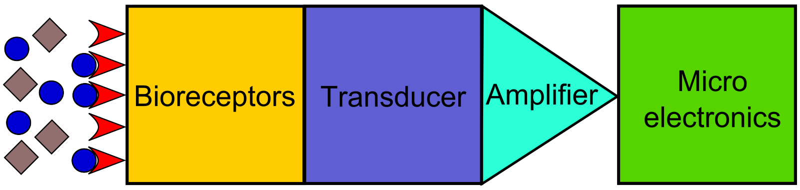

Figure 1.1: An outline of a biosensor

1.2 A History of Biosensors

There are a great variety of biosensors that can grouped by their sensing component (such as DNA, enzymes, antibodies, and so on), or the method used to measure the response (amperometry, impedance, quartz crystal microbalance, fluorescence, etc). Biosensors such as these have been under development in various forms for several decades now. This section provides an overview of developments in biosensor technology.

1.2.1 Amperometric Biosensors

Amperometric biosensors are among the oldest biosensors. They work by detecting current to, or from, the biosensor electrode. This current is used or produced in electrochemical reactions such as changes in oxidation state of metal sites in enzymes, or the hydrolysis of H_2O_2. One of the first commercial applications for biosensors was the measurement of blood glucose levels in diabetics. This remains the largest biosensor market to date.

The Clark Oxygen Electrode/Leland Clark Jr. The idea of a glucose biosensor was first conceived by Clark and Lyons [1962], who suggested that the enzyme glucose oxidase (GOx) could be used for the catalysis of glucose to gluconic acid. Their proposed sensor (Figure 1.2) was comprised of a layer of concentrated glucose oxidase sandwiched between two Cuprophane membranes, that would be fitted over the interface of a pH electrode. The conversion of glucose to gluconic acid would result in a drop in pH, which could then be measured by the pH electrode.

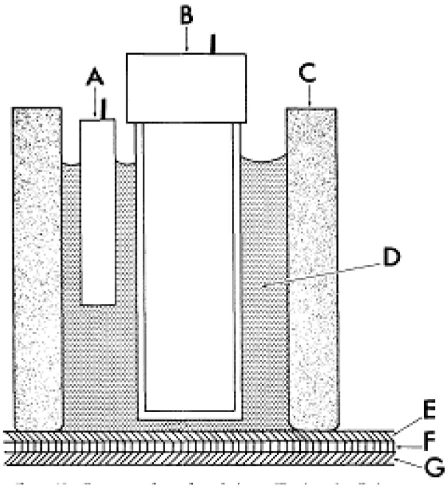

Figure 1.2: Clark and Lyons' proposed glucose biosensor[Clark and Lyons, 1962]. (A) reference electrode, (B) pH sensing electrode, (C) glass wall of electrode, (D) electrolyte, (E) & (G) Cuprophane or dialysis membranes, (F) layer of concentrated enzyme.

This original idea was refined and submitted by Clark in a patent outlining the use of one or more enzymes for the catalysis of electrochemically inert analytes into electroactive products[Clark, 1970]. The patent also covered the use of two electrodes to reduce noise - one containing a GOx membrane to for detection, and a second without to form a stable baseline. Clark's work continued with the Yellow Spring Instrument Company, Ohio, USA, where the GOx biosensor was eventually commercialised into the Model 23 Glucose Analyzer in 1975.

Since then, a significant amount of biosensor evolution has been driven by the advancement of blood glucose sensors. The development of amperometric biosensors, that measure electrical current at an applied potential allowed mercury, required as an electrode in the previously used polarometric methods, to be phased out. Removing mercury electrodes from these systems paved the way for *in vivo* biosensors, by removing the toxicity associated with mercury in the event of sensor damage, as well as personal/handheld devices given the fragility of the hanging drop mercury electrode.

In addition to the advances made in moving away from mercury-based systems, there have also been considerable improvements in noise-to-signal ratios and detection limits with the development of polymers to entrap the system's enzymes and the inclusion of electroactive mediators to aid electron transport to and from the enzymes.

1.2.2 Affinity Biosensors

Amperometric biosensors, such as the GOx biosensor, detect electron flow in the form of electrical current. While this is very useful for enzymes that liberate or commit electrons during their reactions (oxidoreductases, EC1), there are a large number of proteins that do not act in this manner nor have substrates or products that are electroactive. Protein-substrate interactions can be utilised as a detection mechanism instead. Over the past 40 years, biosensors that utilise the most basic of protein-substrate interactions have been developed. These biosensors utilise a variety of analytical techniques to detect the specific binding of a substrate to the protein being used. This simple idea can be applied to any specific binding event, such that affinity biosensors now incorporate a wide range of biomolecules including antibodies, proteins, RNA aptamers and DNA probes. The interactions can also be detected in a great many ways, including surface plasmon resonance (SPR), quartz crystal microbalance (QCM), electrochemical impedance spectroscopy (EIS) and visual markers such as nanoparticles or fluorescent tags.

One biosensor that can be commonly found in shops around the world is the pregnancy test. This uses human chorionic gonadotropin (hCG) as its analyte, which is found in the urine of a pregnant female. The biosensor itself is made up of a number of nanoparticles that are connected to antibodies specific for hCG. Normally these nanoparticles are dispersed and too small to see with the naked eye. However, when a hCG-containing sample is supplied the antibodies bind to the analyte. This brings the nanoparticles closer together, where they are able to diffract light waves producing the coloured band which indicates to the user that they are probably pregnant.

1.2.3 Whole Cell Biosensors

Using interactions with specific biomolecules can give a very precise sensor read out, but sometimes a more general effect is required. Whole cell biosensors incorporate living cells that will respond to a range of environmental conditions or analytes. This is analogous to the canary that miners historically took with them for early warning of noxious gases, such as methane and carbon monoxide. They can also be engineered to include reporter genes, such as green fluorescent protein (GFP), to give a clear indicator. A range of techniques are being investigated for the development of these biosensors including electrochemical and optical methods[Bentley et al., 2001], with major applications being testing in defence and ecotoxicity.

Arsenic contamination of groundwater is an application of particular interest due to its high level of toxicity and widespread use in industrial processes (such as mining, chemical manufacturing and wood preservation among others)[Strosnider, 2003]. While levels of contamination can be high, only certain forms of arsenic, As(III) and As(V), are readily taken up by biological systems[Cullen and Reimer, 1989; Daunert et al., 2000]. For this reason, the use of a biological system as a sensor is ideal. Some gram-negative bacteria have developed resistance genes for As(III) (Figure 1.3a). These specifically detect the presence of As(III) by its binding to the *ars* operon repressor protein. This event leads to the transcription and expression of several resistance genes - *ars*A, *ars*B, *ars*C, *ars*D, and *ars*R[Daunert et al., 2000; Roberto et al., 2002]. These express an As(III)-specific ATPase, an As(III)-specific efflux channel, a reductase to convert As(V) to As(III) for efflux, a regulatory protein, and a transcriptional repressor, respectively (Figure 1.3b). Gram-positive have a very similar operon that lacks *ars*A and *ars*D.

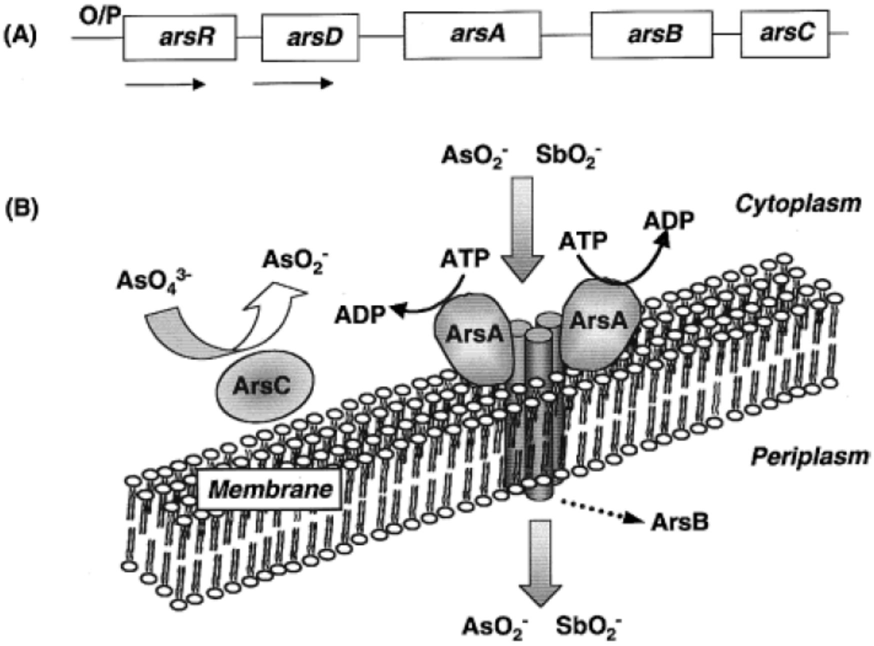

Figure 1.3: The system of arsenic resistance in *E. coli.* (a) The *ars* operon, (b) The arrangement of the *ars* operon's expression products[Daunert et al., 2000].

The expression of these genes can be linked to a reporter gene, such as green fluorescent protein (GFP) from the jellyfish *Aequorea victoria*[Roberto et al., 2002]. Roberto et al. [2002] excised the regulatory components of the *ars* operon and ligated them into pGFPuv - a plasmid that expresses UV-excitable GFP. Addition of 1 ppm As(III) resulted in the expression of GFP with a lag time of 6 hours before fluorescence was first observed and 10 hours before maximal fluorescence was obtained. Detection occurred at concentrations as low at 1 ppb, however a linear relationship was not observed until 100 ppb.

Several other systems have been used making use of the bacterial luminescence gene *lux*[Cai and DuBow, 1997; Ramanathan et al., 1997; Tauriainen et al., 1997]. These systems have shown promise due to faster response times, and in the case of Ramanathan et al. [1997] (non-linear) sub-attomolar detection ranges. Similar approaches have also been adopted for other heavy metals including cadmium, mercury and lead.

1.3 Membrane-Based Biosensors

While all the afore-mentioned biosensor types have strong potential in a variety of applications, the work that has been carried out during the course of this thesis has focused on the development of biosensors based on lipid membranes. These offer the advantage of accommodating the huge variety of membrane proteins used by the cell to interact with its environment. Their wide range of specificities allow numerous compounds to be detected through their use.

Although the range of membrane proteins is incredibly vast, and in the majority of organisms account for approximately 30% of the genome, this thesis will look exclusively at ion channels. In addition to these, it should be noted that there are many other membrane proteins which may find use in biosensor development, especially, G-protein coupled receptors (GPCRs). Ion channels and GPCRs are the top two classes of proteins currently targeted by the pharmaceutical industry for drug development[Grigoriadis et al., 2009; Hubner and Jentsch, 2002; Overington et al., 2006].

1.3.1 Cell Membranes

Prokaryotic cells are essentially made up of two main components - an aqueous region known as the cytosol where most of the cell's biochemistry occurs, and a lipid membrane that separates the cytosol from the exterior. Eukaryotic cells are more complex having internal compartments called organelles, which are also have lipid membranes. These lipid membranes (collectively referred to as plasma membranes) are incredibly important not just for the afore mentioned role, but also for signalling. Their importance is two-fold - firstly, compartmentalisation of biochemical processes allows for varying conditions, such as pH, as well as segregating moieties which may otherwise interfere with the normal functioning of the cell. Secondly, the membrane plays an important role in signalling. While the lipid bilayer's barrier properties isolate cellular environments this renders the biochemical pathways unable to interact with each other or export their products. To facilitate these interactions the plasma membrane is studded with a huge variety of membrane proteins, glycolipids and other components, which allow information, nutrients, waste and cell products to be passed across the membrane in a number of ways.

The ‘fluid mosaic model’ was presented by Singer and Nicolson [1972] as a hypothesis for the general structure and composition of cell membranes. As shown in Figure 1.4, the model is comprised of two monolayers of phospholipids, embedded with integral membrane proteins, peripheral membrane proteins, glycolipids, and non-phospholipids (such as cholesterol).

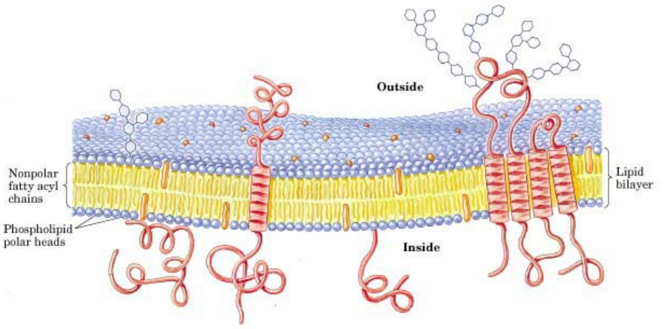

Figure 1.4: The Fluid Mosaic Model[Singer and Nicolson, 1972]

Lipids are amphiphilic in nature and are comprised of a hydrophilic headgroup and a hydrophobic hydrocarbon tail. Figure 1.5 shows a phospholipid with its hydrophilic and hydrophobic regions indicated. Due to this structure lipids will group together tail-to-tail in a polar environment, this produces micelles, tubules or vesicles depending on the type of lipids available and their concentration.

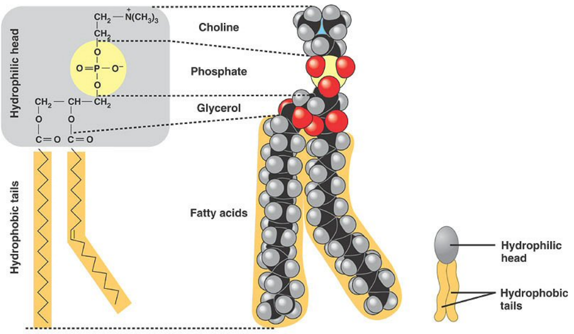

Figure 1.5: The structure of a phospholipid. Phosphatidylcholine used as a demonstration of the amphiphilic nature of lipids[Gallant, 2008]. This phospholipid is comprised of two fatty acid tails that are hydrophobic in nature, which are connected to a glycerol group that has a choline group bound to it via a phosphate group to form a hydrophilic headgroup.

Phospholipids are the most common form of lipid and are typically comprised of 2 hydrophobic fatty acid tails, linked to a glycerol (or sphingosine) which is phosphorylated.

The fatty acid tails can be the same or different, and are optimised to present different properties like certain transition temperatures (T_m). Figure 1.6 shows the most prevalent phospholipids in many membranes - phosphatidylcholine (PC), phosphatidylethanolamine (PE), phosphatidylglycerol (PG), phosphatidylinositol (PI), and phosphatidylserine (PS). PC and PE are both neutral at pH 7, with PC having a pKa of 1.0 and PE having pKas of 1.7 and 9.8 for its phosphate headgroup and amine groups, respectively. PG and PI are negatively charged (pKa's of 3.5 and 2.5, respectively). PI plays an important role as a secondary messenger on the cytosolic side of the membrane where it can be phosphorylated. PS is negatively charged at pH 7, but has pKa's of 2.6, 5.5 and 11.55 for its phosphate, carboxylate and amine groups, respectively. In addition to their chemistry, their structures vary resulting in different packing formations.

While these are all important lipids, their distribution varies amongst different organisms, and different membranes within those organisms. PC accounts for approximately 55% of the lipid membranes in rat liver, yet is barely found at all in many prokaryotes. Conversely, PG is highly important in prokaryotes but rarely found in eukaryotes.

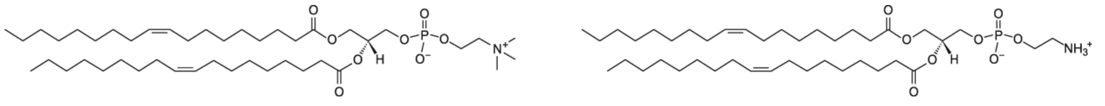

(a) DOPC (b) DOPE

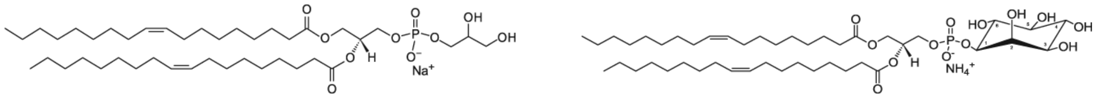

(c) DOPG (d) DOPI

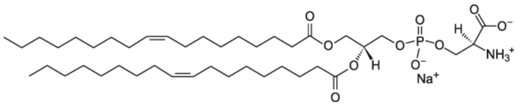

(e) DOPS

Figure 1.6: Various phospholipid structures. 18:1 (Δ9-cis) forms of (a) phosphatidylcholine (DOPC), (b) phosphatidylethanolamine (DOPE), (c) phosphatidylglycerol (DOPG), (d) phosphatidylinositol (DOPI), (e) phosphatidylserine (DOPS).

Glycolipids are lipids that have been modified with sugar groups. These sugars vary from short simple chains, to complex branching ones. They are primarily used for cell recognition by other cells to form tissues. In addition to phospho- and glycolipids, there are many other types of lipid such as cholesterol.

Cholesterol is a sterol, a class of lipids that are comprised of a hydrocarbon ring structure as seen in Figure 1.7. Like phospholipids, it is amphipathic, having both hydrophobic hydrocarbon rings and a hydrophilic 3β-hydroxyl group. While it is of vital importance for proper membrane function in mammalian cells, it is rarely found in bacteria. In mammalian cells it has two main roles - reducing membrane permeability (especially to H^+, Na^+ and K^+[Deng et al., 2008; Haines, 2001]), and modulating membrane fluidity[Dhal and Dhal, 1988; Yeagle, 1990]. Changing these properties of the lipid bilayer can affect the activity of membrane proteins[Beech et al., 2009; Dhal and Dhal, 1988; Gennis, 1989; Yeagle, 1991], and some proteins even interact with cholesterol directly[Murata et al., 1995; Porter et al., 1996; Yeagle, 1991] via sterol-sensing domains[Lange and Steck, 1998; Osborne and Rosenfeld, 1998]. Additionally it also has important roles in clathrin-mediated endocytosis and lipid raft formation[Papanikolaou et al., 2005; Petrie et al., 2000]. The EO_3C tether used in this thesis and discussed in Section 1.3.4 contains a cholesterol moiety. As such it can be expected to affect the properties of tBLMs along similar lines to those mentioned above. For example, reduced membrane permeability can be observed as an increase in membrane resistance between 80% EO_3C tBLM and 100% EO_3C tBLM in Table 3.10.

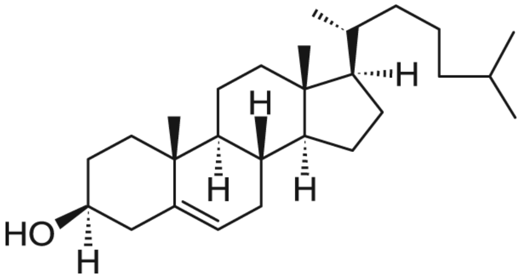

Figure 1.7: Structure of cholesterol

In addition to the wide variety of lipids that has already been discussed, the cell membrane is studded with membrane proteins. These come in two main varieties - integral membrane proteins (including transmembrane proteins), and peripheral membrane proteins (Figure 1.8). Integral membrane proteins are those which are permanentally embedded in the cell membrane. They have annular lipids associated with them, which are in direct contact with the protein and often remain attached when proteins are purified. A subset of integral proteins are transmembrane proteins. These are proteins that span the entire breadth of cell membrane, whereas non-transmembrane integral proteins only span part of the membrane. Transmembrane proteins commonly have roles in transport or signal transduction. Peripheral membrane proteins are only attached to the membrane. Quite often this attachment is via a single hydrophobic α-helix. These proteins have a range of roles, but are also often linked to signal transduction, such as G-proteins that interact with G-protein coupled receptors.

While most proteins are adapted to exist in the aqueous environment of the cytosol, the membrane interior is highly hydrophobic. As such, membrane proteins have adapted to make their presence in this environment energetically favourable. This is done by presenting apolar sidechains, such as alanine, glycine, phenylalanine, leucine, valine, etc. to the regions of the protein in contact with the hydrophobic membrane core. In the case of an integral membrane protein this may be in form of a single α helix composed of apolar residues. Transmembrane proteins are more complex than peripheral membrane proteins and their function often requires the presence of polar and even charged residues in the protein interior. As such, the protein will often present a wall of apolar resides which encircle the entire protein. This allows the protein's internal mechanics to continue unhindered. Peripheral membrane proteins on the other hand associate themselves with the membrane. This may be via protein-protein interactions with transmembrane or integral membrane proteins, or via interactions with membrane lipids themselves. These lipids may be permanent members of the membrane with the interaction occurring transiently between the protein and a glycosylated lipid.

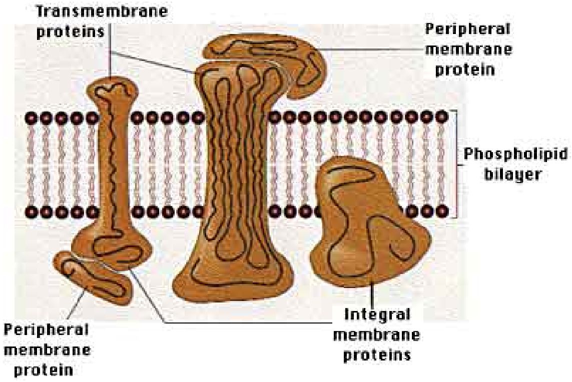

Figure 1.8: Diagram showing the difference between integral, transmembrane and peripheral membrane proteins[Lummis et al., 2005].

Since the proposition of the fluid mosaic model, additional theories on the distribution of membrane components have been put forward. Of these the most prevalent is that of lipid rafts. This theory suggests that the membrane is not a homogeneous distribution of proteins and lipids. Instead there are regions termed 'rafts', which contain higher levels of certain lipids and proteins than the rest of the membrane (Figure 1.9). These rafts are thought to be rich in sphingolipids and cholesterol. The high number of saturated bonds in their structures aids lateral adhesion, which helps hold together molecules over short distances. The saturated nature of their bonds causes these lipid rafts to be thicker than the rest of the membrane. This is energetically more favourable for some membrane proteins and as such they accumulate in these regions. This behaviour has led to suggestions that lipid rafts are instrumental in the function of some proteins where they are required to interact with other proteins (e.g. protein supercomplexes in the electron transport chain in mitochondria). Another function of lipid rafts is thought to be the concentrating of membrane proteins prior to packaging in small vesicles such as endosomes.

1.3.2 Bilayer Lipid Membranes

Bilayer lipid membranes (BLM) were the first artificial membranes to be experimented with. They are formed from reconstituted lipid mixtures and are used as model membranes, primarily for electrophysiology experiments. Many different lipid compositions

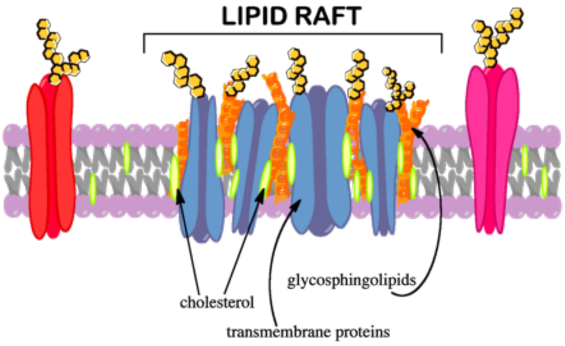

Figure 1.9: Lipid raft[Anon., 2010]

have been used in the past and each has its own properties that can be exploited for different experimental setups.

The lipid extract that is primarily used in this project is *Escherichia coli* polar extract (Avanti Polar Lipids Inc.) which is comprised of approximately 67.0% phosphatidylethanolamine, 23.2% phosphatidylglycerol and 9.8% cardiolipin[Ava]. As mentioned in the previous section, these lipids each have their own properties which shape the properties of bilayers formed with them. PE has pKas of 1.7 and 9.8 for the phosphate and amine groups in its headgroup. As such it is zwitterionic between pH 4.0 and 7.0, with the phosphate being deprotonated, and the amine being protonated. PG has a pKa of 3.5, giving it a negative charge above this pH due to the deprotonation of the phosphate group. Cardiolipin is a diphosphatidylglycerol lipid and has pKas of 3.0 and 7.5 for its two phosphates. These give the molecule a single negative charge at pH 7, as one of them is protonated, and the other deprotonated. As such a bilayer formed from *E. coli* polar lipid extract can be expected to have a slight negative charge at pH 7. This remains the case until a pH of less than 4 is reached, at which point the negative charge lessens and the bilayer approaches neutrality.

Other commonly used lipids in model membranes include egg phosphatidylcholine (eggPC) and archael lipid analogues such as 1,2-di-*O*-phytanoyl-*sn*-glycero-3-phosphocholine (DPhyPC)[Koper, 2007; Vockenroth et al., 2008b, c]. The phosphocholine headgroup in each case has an pKa of approximately 1.0 as discussed previously. EggPC is a natural mixture of phosphatidylcholines from chicken eggs. It is comprised of a variety of saturated and unsaturated fatty acid tails, with the major constituents having fatty acid tails of 16:0, 18:0, 18:1 and 18:2. It is generally considered to be a good generic lipid to use in many situations. DPhyPC is a lipid from archaea. Its structure is somewhat different because of this, having isoprenoid tails rather than fatty acids. These are bulkier and give the lipid a comparatively low phase transition temperature making the resultant lipid bilayer very fluid. This has the benefit of producing a highly insulating lipid bilayer[Mathai et al., 2001; Schiller et al., 2003; Yamauchi et al., 1993]. It also has no double bonds, which are prone to oxidation in ambient conditions. For these reasons diphytanoyl lipids are often used in BLMs and their variants which will be discussed shortly.

BLM protocols involve the formation of a bilayer over small apertures (<1 mm) in a division between two aqueous compartments[Montal and Mueller, 1972; Mueller et al., 1962], as can be seen in Figure 1.10a. By placing an electrode in the aqueous compartment on either side of the BLM, electrochemical measurements of the BLM can be taken. Very high resistances (> 100 MΩ) are common, but the system suffers from poor stability and short lifetimes (< 8 hours) [Ottova-Leitmannova and Tien, 1992; Steinem et al., 1996; Tien and Ottova-Leitmannova, 2000]. More recently, agarose gel-matrices have been introduced to provide extra stability to the BLM allowing lifetimes of over 3 weeks[Costello et al., 1999; Jeon et al., 2005; Vockenroth et al., 2008c]. While the BLM continues to play an important role, especially in the field of electrophysiology (where is can be used with purified samples to verify patch-clamp data), its poor stability precludes its use in biosensing applications. Furthermore, its incompatibility with surface analysis techniques limits its use as a model membrane for the purpose of biophysical studies.

1.3.3 Solid-Supported Bilayer Lipid Membranes

In the mid-1980s Brian and McConnell [1984] published the first example of a solid supported BLM. These have been proven to be far more robust than normal BLMs. By adsorbing vesicles on a certain substrates, such as glass and mica, supported BLMs (sBLMs) will form via the rupture and subsequent spreading of the lipid. The sBLM is supported on top of a thin layer of aqueous solvent typically 10–20 Å thick (Figure 1.10b). While these are useful for studying membrane properties via surface analysis techniques, such as atomic force microscopy and quartz crystal microbalance, the bilayer is inaccessible to electrochemical techniques due to the isolating nature of the supporting substrate. The use of the indium-tin oxide (ITO) has proven useful in this area as it is both optically transparent and electrically conductive. It has been particularly well utilised in work investigating the photoelectric properties of lipid bilayers for the study of photosynthetic systems[Gao et al., 2001]. Attempts to form sBLMs directly onto metals did not prove terribly successful and often resulted in denaturing of any proteins that came into contact with the surface. The discovery of gold-thiol chemistry and self-assembled monolayers (SAMs) by Nuzzo and Allara [1983] allowed the creation of a new platform for the study of BLMs. SAMs can be formed from a wide variety of molecules to form a well ordered monolayer, including thiols, silanes[Ulman, 1996] and alkanoic acids[Tao, 1993; Ulman, 1996]. In this thesis the term ‘SAM’ will primarily be used to refer to self-assembled monolayers formed from compounds with a thiol group. The thiol group forms a strong bond to gold, and other metals, with covalent-like behaviour producing a monolayer and presenting a well ordered hydrophobic surface. Rupture of lipid vesicles on these functionalised surfaces allows the production of sBLMs on metal surfaces. When the SAM is formed form alkanethiols, it is hydrophobic in nature and the resultant sBLM is generally referred to as a hybrid BLM (hBLM) with a lower leaflet of alkanethiols and an upper leaflet of lipids (Figure 1.10c). This new system, first described by Plant [1993], allowed the use of both electrochemical and surface analysis techniques of solid supported BLMs.

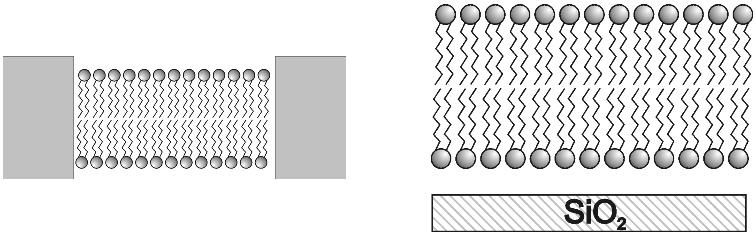

(a) A BLM formed over a small aperture.

(b) A sBLM formed on glass.

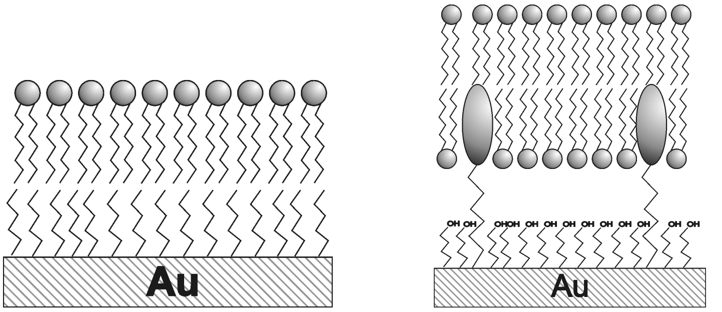

(c) A hBLM formed of a SAM and a lipid monolayer.

(d) A tBLM formed on a mixed SAM with regions of lipid monolayers and bilayers.

Figure 1.10: The four main types of bilayer that are formed.

1.3.4 Tethered Bilayer Lipid Membranes

As work with SAMs and hBLMs continued, problems were encountered in some cases with the incorporation of membrane proteins that spanned a bilayer (transmembrane proteins) and compounds that diffused across it such as ion transporters. It was realised that by creating a SAM from thiolated molecules of differing lengths with different head-group functionalities (i.e. lipophilic and hydrophilic) aqueous compartments could be formed beneath the BLM. Lipophilic compounds, such as cholesterol or other lipids, can insert into the bilayer while a tether allow them to be attached to the surface producing a tethered BLM (tBLM, Figure 1.10d). These thiols may phase separate on the surface into different domains, creating islands of lipophilic tethers surrounded by a sea of hydrophilic spacers[Jeuken et al., 2006, 2007b]. Thiolipids and other alkanethiols with lipid moieties can be used as tether molecules to anchor the bilayer to the gold surface (Figure 1.10d). Silane chemistry provides an alternative linkage that allows tethering to oxides, such as SiO_2[Atanasov et al., 2005] and ITOHillebrandt$_{99}$, by covalently linking to a SiH_3-terminated molecule.

EO_3 Cholesterol

This thesis has primarily used tBLMs based on the triethyleneoxythiol cholesterol (EO_3C) compound developed by Boden et al. [1997]. EO_3C is comprised of a cholesteryl moiety with a thiol-terminated triethyleneoxy linker (Figure 1.11). It is approximately 30 Å long. To produce aqueous domains within the SAM, EO_3C is often mixed with short chain hydroxy-terminated thiols such as 2-mercaptoethanol or 6-mercaptohexanol. This allows us to fine tune the SAM to give desired properties such as a large sub-membrane aqueous regions (Figure 1.12). These mixed SAMs undergo phase separation at around 20–60% surface coverage[Jeuken et al., 2007b]. The dimensions of the resultant sub-membrane aqueous regions are thought to be on the nanoscale based on AFM studies[Jeuken et al., 2007b] and, while not measured, are predicted to be less than 20 Å deep[Jeuken et al., 2007a]. Surface coverage of EO_3C affects the quality of the bilayer, with a large increase in the quality of the bilayer being observed when EO_3C surface coverage exceeds 60% EO_3C. 'Quality' is here defined as a highly insulating bilayer as identified by a large bilayer resistance, coupled with a double layer capacitance with a phase angle of -90°[Jeuken et al., 2007a]. Thus we find that tBLMs are advantageous for the study of ion transporters, membrane proteins and bilayers with a range of surface analytical and electrochemical techniques [Castellena and Cremer, 2006; Janshoff and Steinem, 2006; Jenkins et al., 1998; Jeuken et al., 2005, 2006; Keizer et al., 2007; Koper, 2007; Rose and Jenkins, 2007; Sinner and Knoll, 2001; Steinem et al., 1996; Vockenroth et al., 2008a, b, c].

Archaeal Thiolipids

A popular alternative to EO_3C is a synthetic thiolipid inspired by a novel archaeal lipid analog, 2,3-di-*O*-phytanyl-*sn*-glycerol-1-tetraethylene glycol-D,L-α-lipoic acid ester

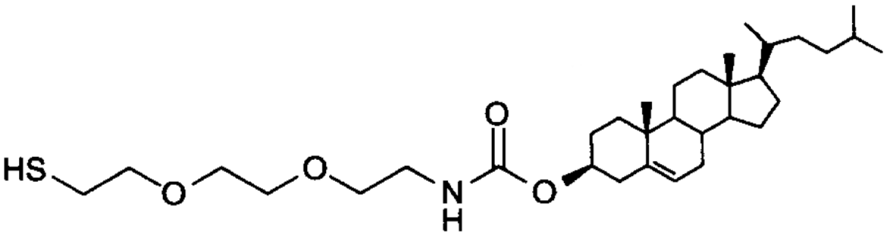

Figure 1.11: Chemical structure of triethyleneoxy cholesterol (EO_3C)

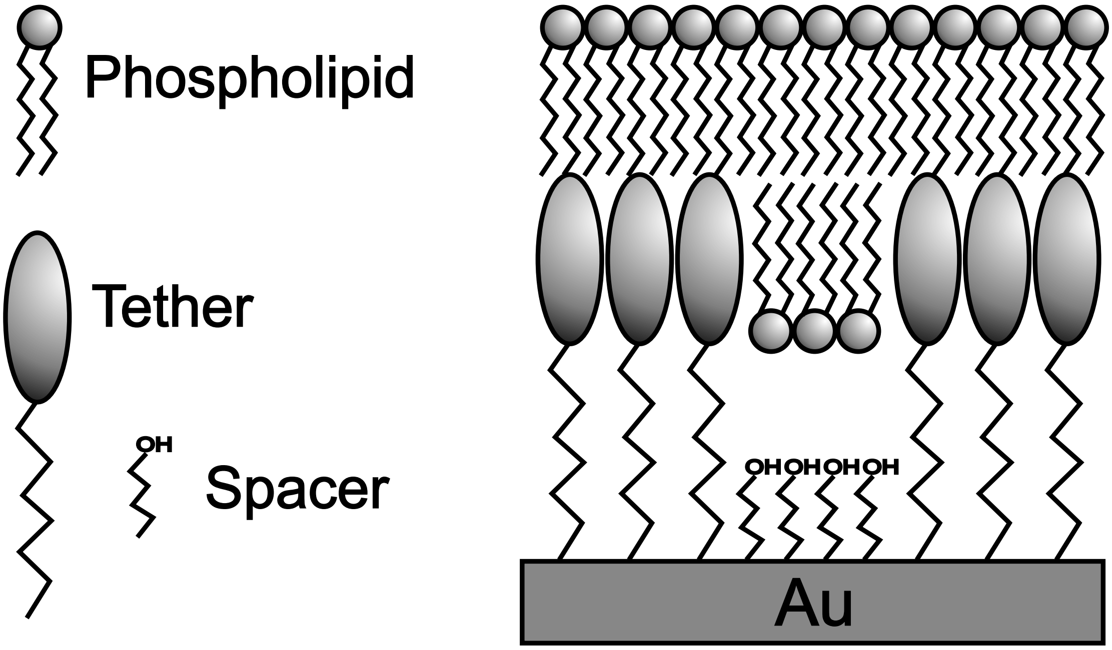

Figure 1.12: Schematic representation of a tBLM formed from EO_3 cholesterol and 6-mercaptohexanol

lipid (DPhyTL, Figure 1.13a)[Schiller et al., 2003]. When used in conjunction with 1,2-diphytanoyl-*sn*-glycerol-3-phosphocholine (DPhyPC, Figure 1.13b) and/or 1,2-diphytanoyl-*sn*-glycerol-3-phosphoethanolamine (DPhyPE), the resultant bilayers possess very high resistances in excess of 10 $M\Omega.cm^2$[Junghans and Koper, 2010; Knoll et al., 2007; Naumann et al., 2003a]. These tBLMs generally do not include spacer thiols as found in previously mentioned systems, however, a study by He et al. [2005] investigated the use of tetraethylene glycol-D,L-α-lipoic acid (TEGL) as such a spacer. Additionally, the incorporation of functional proteins has also been reported[Andersson et al., 2008; Koper, 2007].

Other Tethers

In addition to EO_3C and archaeal thiolipids, two other synthetic thiolipids that have been studied are 1,2-dimyristyl- 3-[ω-mercaptohexa(ethylene oxide)] glycerol (WC14) and 1,2-dipalmityl-3- [ω-mercaptonona(ethylene oxide)] glycerol (FC16)[Heinrich et al., 2009; McGillivray et al., 2007]. These thiolipids have been used with 2-mercaptoethanol as

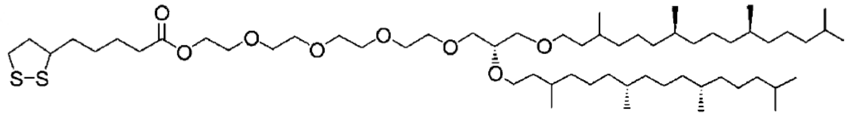

(a) DPhyTL

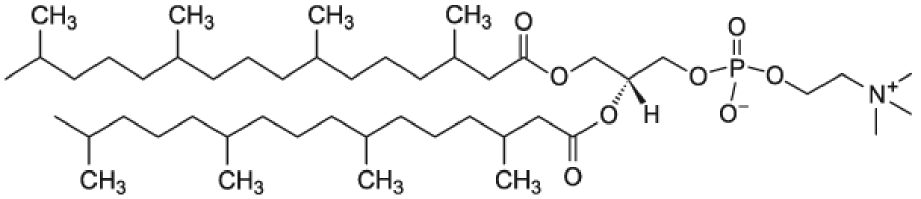

(b) DPhyPC

Figure 1.13: Diphytanoyl lipids inspired by archaeal lipids

a spacer to produce sparsely tethered BLMs (stBLMs) with good results. McGillivray et al. [2007] showed WC14 to produce tBLMs with capacitances of 0.6 μF.cm^{-2} and membrane resistances of 1 MΩ.cm^2. FC16 also produced good results with an additional 0.5 nm of sub-membrane space and increased tBLM resistance ($>$ 1 MΩ.cm^2), when compared to WC14[Heinrich et al., 2009]. These thiolipids have been used to produce tBLMs with incorporated membrane proteins, including α-hemolysin[McGillivray et al., 2009] and KcsA[Goh et al., 2010].

Case Study: Ion-Channel Switch Biosensor

In 1997, Nature published a paper demonstrating the potential for a so called ‘Ion Channel Switch’ biosensor [Cornell et al., 1997]. This biosensor utilised a tBLM with gramicidin channels. Gramicidin monomers (half-channels) in the lower leaflet of the bilayer were anchored to the gold surface, while half-channels in the upper leaflet were modified with antibodies via a biotin-streptavidin-biotin linkage. Membrane spanning thiolipids, similar to the archaeal thiolipids mentioned previously, were both anchored and modified with antibodies (Figure 1.14). In an analyte-free solution, the gramicidin half-channels dimerised to allow conductance across the membrane, however when analyte was added the antibodies of both the membrane spanning thiolipid and the upper gramicidin half-channel were cross-linked preventing dimerisation with the lower leaflet. As a result, analyte was detected by a loss of conductance. This idea of combining a non-specific pore-forming ionophore with a highly specific receptor component, such as antibodies, has demonstrated the capability of these systems to act as highly specific biosensors. Although this work turned out difficult to reproduce by other groups, the Nature publication resulted in a surge of research in biosensor applications of tBLMs.

Alternatively a sensor could make use of the receptors already present in nature for the

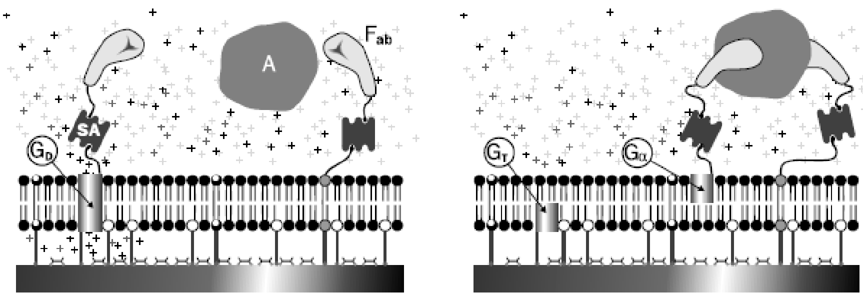

Figure 1.14: A schematic of Cornell's Ion Channel Switch biosensor [Cornell et al., 1997]. 'A' is the analyte, which is bound by two antibody fragments 'F_{ab}'. These are connected via a biotin-streptavidin-biotin complex to a mobile gramicidin monomer (G_α) and a membrane spanning thiolipid. A second static gramicidin monomer (G_T) is bound to the electrode surface via a thiol tether. When no analyte is present, the gramicidin monomers are free to form a dimer and ions are conducted through the tBLM. On addition of analyte to the system, both antibody fragments bind to the analyte causing the mobile gramicidin monomer to be pulled away from the static gramicidin monomer preventing further ion conductance across the tBLM.

detection of analytes. While a great many receptors exist in nature a vast number of these result in downstream signalling via biochemical reactions and protein modifications, such as phosphorylation. In order to be easily detectable by an electrochemical system a flux of ions is required. Ligand-gated ion channels are ideal for this purpose as they contain a gated pore and a ligand binding region that regulates the pore's activity. The archetypal ligand-gated ion channel is the nicotinic acetylcholine receptor (nAChR). This protein is a pentamer formed from 4 homologous subunits (2 α, 1 β, 1 γ, 1 δ) which come together to form a central pore region. Upon binding of the neurotransmitter acetylcholine to the two extracellular binding sites on the α subunits, the protein undergoes a conformational change resulting in the opening of the pore to allow diffusion of Na^+ and K^+ ions across the membrane. This ion flux can be measured via various electrochemical techniques. The acetylcholine receptor is, however, just one of many ion channels to be found in nature. One family of closely related ligand-gated ion channels is that of the transient receptor potential (TRP) channels.

Mixed Hybrid Bilayer Lipid Membranes

A more recent development in the field of solid supported BLMs has been the formation of tBLMs which span apertures in the order of a few hundred nanometers to a couple of micrometers in diameter. This combines the high resistances and (single channel) sensitivity obtained with BLMs, with the stability of a tBLM. While there are several ways in which the solid support can be manufactured, one of the simplest is to use track-etched polycarbonate membranes of the type used in this thesis for the extrusion of lipid vesicles. The example shown in Figure 1.15 is from work done by Favero et al. [2005]. A 1 μm pore membrane is coated with gold and a octadecanethiol (ODT) SAM formed on the surface, before the addition of 25% cholesterol:75% phosphatidylcholine vesicles. This results in a hBLMs being formed over the majority of the surface where ODT SAM is present. However, where the pores preclude the formation of hBLMs the bilayer spans the gap producing BLM like structures. Proteoliposomes containing proteins of interest can also be added to the vesicle solution, leading to their incorporation as shown below.

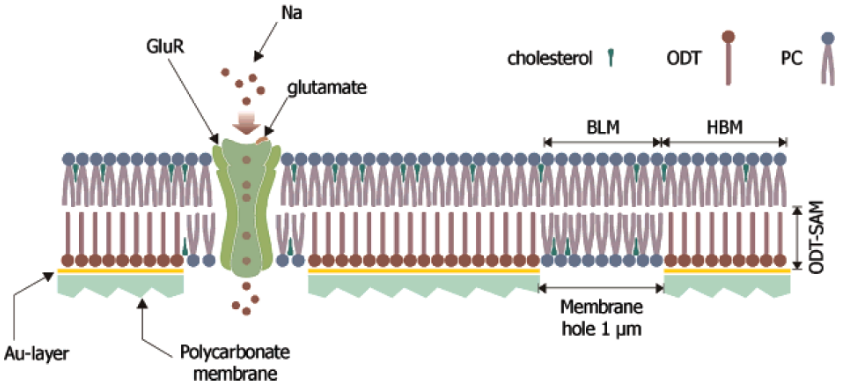

Figure 1.15: Mixed hBLM[Favero et al., 2005]

Variations on this approach have been used by a number of other groups. Of particular interest to this thesis, due to the use of EO_3C, is the work of Schmitt et al. [2008]. In this system hBLMs of EO_3C and DPhyPC are formed on the surface of porous alumina, with DPhyPC bilayers spanning pores which have, on average, diameters of 60 nm. Other systems deviate from the use of tBLMs, reverting to chip-based versions of the traditional BLM[Kresak et al., 2009; Studer et al., 2011; Zagnoni et al., 2007].

1.4 Ion Transport

Ion transport across lipid bilayers can be facilitated by a range of molecules. These include ionophores, ion channels and ion transporters. While all these molecules are capable of transporting ions across lipid bilayers, they use different mechanisms to do so. Despite these differences the theoretical treatment of ion transport is based on a shared group of principles.

The lipid bilayer presents a high resistance barrier to the diffusion of polar, charged, or large molecules. This is due to the hydrophobic core of the bilayer which makes their passage across energetically unfavourable. Furthermore, ions are, in general, hydrated under normal conditions. This makes them not only charged, but also relatively large and polar. In order to traverse this region an ion must be presented as apolar entity. There are several ways in which ions can be transported and this will be discussed in detail later, however they can be briefly summarised as one of two main methods.

The first is to produce a large pore that hydrated ions are able to diffuse across. The pore is formed by a proteinaceous framework which presents hydrophobic residues to the protein's exterior (making it energetically favourable to exist within the bilayer), while also presenting hydrophilic residues on the surface of the pore lumen (making the pore interior an energetically favourable region for the hydrated ion to exist in).

While this approach is simple in concept and used in nature by pore-forming proteins such as OmpF and aquaporins, it is not very selective in the ions it allows to transit. In order to provide this specificity the pore needs to use a combination of polar or charged residues on the pore interior, as well as a finely tuned pore diameter. Using these features, a protein is able to use weak co-ordination bonds provided by the lumen residues to both strip an ion of its hydration shell (making the ion far smaller) and stabilise it in its passage across the bilayer. Note, however, that if the co-ordination bonds are too favourable the rate of ion transport can be impeded. By positioning the residues just the right distance away from the path of the ion a high degree of specificity can be provided.

The second approach is that used by mobile ion carriers, a type of ionophore. These will be discussed in greater detail shortly, but essentially function by coordinating ions via a series of weak bonds and enveloping the ion. This makes the passage of the ion across the bilayer energetically more favourable.

The following sections will examine specific examples of ionophores and ion channels to demonstrate how they mediate ion transport, how their specificities differ, and in the case of ion channels, how they are 'gated'. It should be noted that there are a great many classes of ion channels, and other membrane proteins capable of ion transport, including mechanosensitive channels (respond to membrane pressure), channelrhodopsins (light-gated) and ion pumps. However, the discussion presented here has been limited to those relevant to the channels examined in the course of this thesis.

1.4.1 Nernst Equation

The Nernst equation describes the equilibrium potential formed across a membrane by an imbalance in the concentrations of a particular ion on either side of the membrane. This is given in Equation 1.1, where E_S is the equilibrium potential for ion S, RT is room temperature and pressure, F is Faraday's constant, $[S]_o$ is the concentration of ion S on the outside of the membrane, and $[S]_i$ is the concentration of S on the inside of the membrane.

$$E_S = \frac{RT}{F} ln \frac{[S]_o}{[S]_i} \tag{1.1}$$

This equilibrium potential exists when the membrane is at rest and net ion transport is 0. These potentials vary for different ions in different cells. In mammalian skeletal muscle at a temperature of 37°C, the extracellular concentration of Na^+ is 145 mM and the intracellular concentration 12 mM leading to an equilibrium potential of +67 mV. In the same tissue the K^+ extracellular concentration is 4 mM, while the intracellular concentration is 155 mM giving an equilibrium potential of -98 mV. In an ion transport system, moving the membrane potential from this equilibrium causes a net flow of ions than can be recorded as current.

1.4.2 Ionophores as Model Systems

Ionophores are molecules that allow the transport of ions across a lipid bilayer. They are found in nature where they are used as antibiotics, which work by disrupting the electrochemical gradients across lipid bilayers that are essential for active transport of nutrients and oxidative phosphorylation via ATP-synthase. Two major classes of ionophores exist-mobile ion carriers and pore formers.

Mobile Ion Carriers

Mobile ion carriers are generally small cyclic peptides with a number of polar residues, each separated by at least one hydrophobic residue. This alternating structure provides both the polar residues required to complex an ion, as well as the hydrophobic residues required to be lipid soluble. While there are many examples of ion carriers, some of the most frequently used include valinomycin (*Streptomyces fulvissimus*, K^+-specific), enniatin B (*Fusarium orthoceras*, Ca^{2+}), monensin (Na^+), nystatin (*Streptomyces noursei*, Na^+), A23187 (*Streptomyces chartreusensis*, $Ca^{2+}/Mg^{2+}/Mn^{2+}$), CCCP (H^+) and ionomycin (*Streptomyces conglobatus*, $Ca^{2+}/Mg^{2+}/Mn^{2+}$). Due to their mechanism of capturing a single ion, diffusing across the lipid bilayer, and releasing the captured ion, they present comparatively slow transport rates in the region of 10^{2-3} ions/molecule/sec. However, the way in which they complex ions makes them highly specific - valinomycin, for example, exhibits a binding affinity for K^+ 10^5 times greater than that for Na^+.

An excellent example of a mobile ion carrier is valinomycin. Its 12 amino acid cyclic structure is comprised of 3 repeats of 4 amino acids (-Ala-Val-Val-Val-) in a flexible ring formation. Its selectivity for K^+ comes from the co-ordination geometry of the hydrogen bonds provided by peptide linkages. When in an aqueous solution the carbonyl groups of these peptide linkages face outwards allowing solvation of the ionophore via hydrogen bonding. When the ionophore enters hydrophobic regions like the lipid membrane, the molecule undergoes a conformational change with isopropyl (valine) and methyl (alanine) groups facing the molecule's exterior, allowing it to diffuse across the membrane. Meanwhile 6 of the carbonyl groups provided by the peptide linkage coordinate the K^+ ion on the interior of the structure (Figure 1.16)[Pullman, 1991].

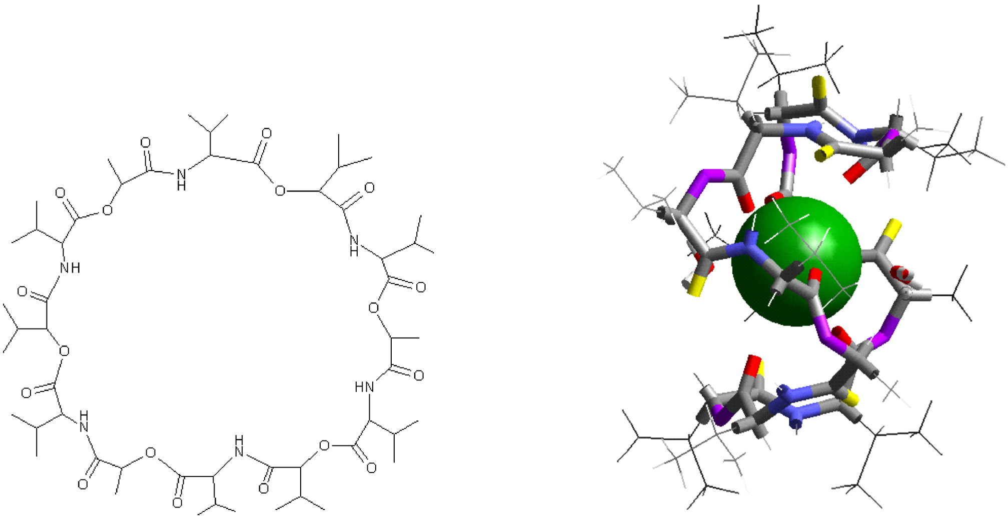

(a) Valinomycin

(b) Valinomycin with K^+ ion

Figure 1.16: Valinomycin - (a) Flattened 2D representation of the primary chemical structure of valinomycin; (b) A 3D representation of valinomycin complexed with a K^+ ion (green). 6 of the double bonded oxygens facing outwards in (a), and shown as red rods in (b) co-ordinate the K^+ ion. The valinomycin backbone wraps around the K^+ ion like a tennis ball seam as seen in (b)[Reisberg, 1999].

Pore-Forming Channel

Pore-forming channels are another major class of ionophore. They provide a continuous channel allowing ions to diffuse from one side of the bilayer to the other, with no diffusion or conformation change required by the channel. This results in them having far higher transport rates, in the order of 10^{7-8} ions/molecule/sec. However, they often exhibit less selectivity with regards to the ions they allow passage to.

A few of key pore-forming channels include gramicidin (*Bacillus brevis*), alamethicin (*Trichoderma viride*), α-hemolysin (*Staphylococcus aureus*) and amphotericin B (*Streptomyces nodosus*). While all these compounds produce pores in the lipid bilayer, the manner in which they do so differs greatly.

Gramicidin is a linear peptide made up of 15 amino acids that has a β-helical structure. Each monomer forms a half-channel in one leaflet of the bilayer and associates with a monomer in the opposite leaflet to dimerise and span the membrane (Figure 1.17). This dimer has a head-to-head alignment. It is selective for monovalent cations ($H^+ > K^+ > Na^+$), and divalent cations have a blocking effect. Ions travel single file through the pore, displacing up to 6 water molecules that inhabit it. Two binding sites within the pore promote cation transport while preventing anion transport. Gramicidin has been the basis of much biosensor research [Favero et al., 2002; Hassler et al., 2004; Jenkins et al., 1998], most notably Cornell's Ion Channel Switch [Cornell et al., 1997].

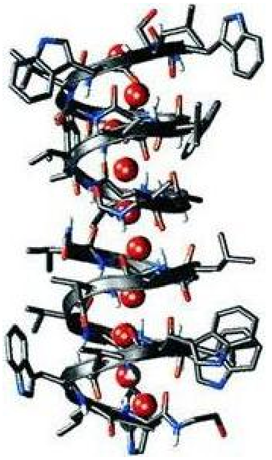

Figure 1.17: A g ramicidin dimer. Two helical peptides (black ribbons) with a proton wire (red balls) running through the middle, these protons are displaced by other ions as they pass through the pore[Pomes and Roux, 2002].

Other pore-forming channels, such as alamethicin, amphotericin B and α-hemolysin, all operate by forming a toroidal structure in the bilayer. Alamethicin contains a 14 amino acid long α-helix which inserts into the lipid bilayer (Figure 1.18a). Several of these monomers aggregate in the bilayer, with hydrophobic residues being present to the exterior of the toroid aggregate. The lumen meanwhile contains a small number of charged residues which aid the solvation of the lumen once the aggregate is formed.

α-hemolysin is another example of a pore-forming peptide. It is comprised of 293 residues which form a water-soluble monomer. When inserted into a lipid bilayer these monomers associate with one another to form a mushroom-shaped protein with a central heptameric pore (Figure 1.18b). In nature this peptide is used as a toxin to initiate cell lysis, and large molecules of up to 2 kDa in size, or long strands of nucleic acid, are able to pass through the α-hemolysin pore, in addition to smaller compounds and ions. This structure has been utilised[Vockenroth et al., 2008a] and in some cases modified (chemically[Movileanu et al., 2000] or genetically[Walker et al., 1994]) to provide selectivity to a bilayer. Braha et al. [1997] was able to genetically engineer the channel to be specific for divalent cations, while Gu et al. [1999] made used of a class of compounds called cyclodextrins (that are able to fit in the lumen of the channel) to provide selectivity to various pharmaceuticals. The range of modifications made to α-hemolysin continue to expand, with more recent developments including the detection of the explosive TNT[Guan et al., 2005], and the secondary messenger IP$_3$[Kang et al., 2007].

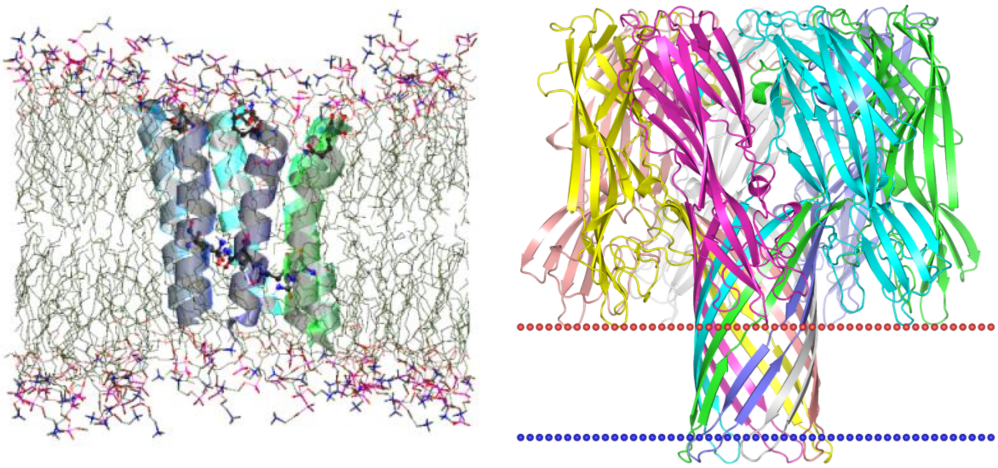

(a) Alamethicin

(b) Hemolysin

Figure 1.18: Structures of the pore-forming peptides, alamethicin and hemolysin.

Each ionophore is likely to handle differently and various strategies may be required to incorporate them into the bilayer. Valinomycin is soluble in methanol and can be added to solution in this form resulting in diffusion to the bilayer. Rose and Jenkins have reported, however, that they were unable to get valinomycin to incorporate from solution and were required to incorporate the ionophore into eggPC vesicles instead[Rose and Jenkins, 2007]. Other ionophores or channel proteins may require similar approaches and need to be reconstituted into vesicles. These can then either be added to a pre-existing lipid bilayer where they should incorporate or be used to form a bilayer from scratch.

1.4.3 Ion Channels

It is also possible to incorporate transmembrane proteins into a solid supported membrane, however these are much harder to work with than ionophores. A few examples include OmpF[Becucci et al., 2006; Stora et al., 1999], cytochrome bo_3[Jeuken et al., 2006], the nicotinic acetylcholine receptor (nAChR)[Downer et al., 1992] and its M2 pore peptide (M2δ)[Vockenroth et al., 2007], GluR0[Favero et al., 2005], and G-Protein coupled receptors (GPCR)[Fang et al., 2002; Pennetta et al., 2006].

Ion channels often combine the high degree of selectivity experienced by mobile ion carriers, along with the rapid ion translocation rates of pore-forming channels. In addition to these features, they are gated. By this it is meant that they can be opened or closed according to environmental conditions, such as pH (KcsA), membrane potential (K_v1.2), chemical messengers (nAChR) and more. This section will examine the basic pore architecture of ion channels, as well as the two main classes of gating mechanisms.

KcsA - the prototypical ion channel

Of all the gated ion channels discovered thus far, KcsA is one of the simplest. It was one of the first channels to have its structure resolved at a high resolution[Doyle et al., 1998] and has formed the basis of a great many studies on ion channel structure and function. Originally found in *Streptomyces lividans*, the channel is comparatively small, consisting of 4 subunits of 160 amino acids each[Schrempf et al., 1995]. The channel lacks any substantial intra- or extra-cellular domains, but has two transmembrane helices (TM1 and TM2) that are separated by a short loop containing a further short helix, termed the pore helix (Figure 1.19)..

The channel's pore is created by the TM1 and TM2 helices, with the TM2 helix forming the pore lumen and the TM1 helix facing the lipid environment. The TM2 helices are angled at 25°, and cross close together near the intracellular surface of the membrane blocking the channel pore. Linking these helices is a region of approximately 20 residues that form the pore's selectivity filter. The precise positioning of backbones carbonyl groups from a short amino acid sequence (TVGYG) in the TM2-pore helix loop provides this selectivity. This gives the channel the ability to select for cations over anions and even provide a high level of specificity towards K^+ over Na^+ and other cations. Additionally, these helices are directed towards the centre of the pore, with the helix's dipole helping to stabilise K^+ ions.

Many of the features of KcsA are replicated throughout biology, forming a framework for many other ion channels. Figure 1.20 shows the basic architecture of a number of ion channels. The tetrameric two helix structure of KcsA (Figure 1.20i) can be found in both prokaryotic and eukaryotic channels, such as K_v1.2 (Figure 1.20iii), K_{ir}Bac1.1 (Figure 1.20iv) and MthK (Figure 1.20v). The use of helix dipoles to stabilise ions in the channel are also common, with a similar approach being used in both KcsA and the ClC chloride channel (Figure 1.21).

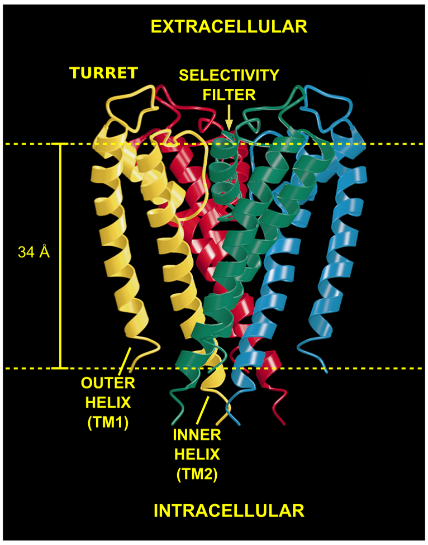

Figure 1.19: Structure of KcsA, the potassium channel of *Streptomyces lividans*[Doyle et al., 1998]

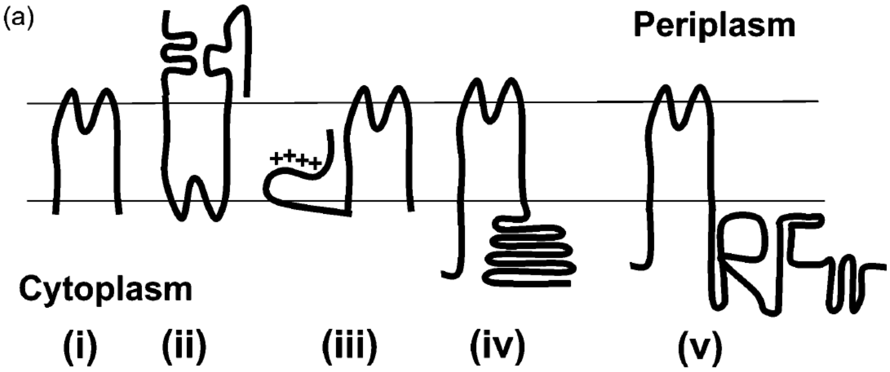

Figure 1.20: Ion channel architectures[Booth et al., 2003]. (i) KcsA, (ii) $GluR_0$, (iii) voltage-gated K^+ channel, (iv) KirBac1.1, (v) MthK.

Voltage-Gated Ion Channels

Voltage-gated channels, such as $K_v1.2$ and KvAP, have their conductivity determined by the membrane potential. $K_v1.2$ shares the basic architecture of KcsA's pore forming helices, but adds an additional four transmembrane helices termed S1-4. S4 contains several positively charged residues (lysine and arginine). While the precise mechanism of how these residues move in the membrane has not been fully elucidated, there are a few competing theories, as shown in Figure 1.22. One of the most popular of these is shown in Figure 1.22b - where the S3a, S3b and S4 helices form a voltage-sensing paddle. Under resting conditions where the channel is closed, the paddle does not adopt any discrete position but is thought to rest towards the intracellular side of the membrane. However, when the membrane potential is elevated the paddle moves to the extracellular surface of the membrane, a conformational change that is propagated to the pore forming helices S5-6 (TM2 and TM1 of KcsA, respectively)[Long et al., 2007].

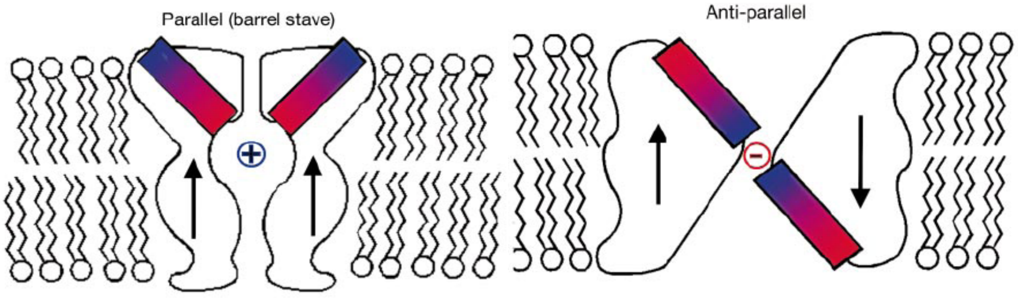

(a) KcsA (b) ClC

Figure 1.21: The use of helix dipoles in ion channels to provide electrostatic stabilisation of ions. (a) Shows the barrel-stave motif found in KcsA, while (b) shows the anti-parallel configuration adopted by ClC[Dutzler et al., 2002].

In addition to a large number of voltage-gated K^+ channels (MVP[Sesti et al., 2003], KvLm[Santos et al., 2006], *Shaker*/K_v1.2[Long et al., 2005a, b, 2007]), the voltage paddle is a domain found in many other voltage-gated proteins. These include a voltage-gated H^+ channel (Hv1)[Ramsey et al., 2006; Sasaki et al., 2006], a voltage-sensitive phosphatase (Ci-VSP)[Muller and Hartung, 1990] and a voltage-gated Na^+ channel (NavAb)[Payandeh et al., 2011].

Ligand-Gated Ion Channel

Ligand-gated ion channels are of particular interest in this thesis due to their ability to have their gating properties modulated by a variety of molecules that may be of interest in biosensing applications. The ligand binding site can be on the extracellular or cytosolic side of the membrane depending on the source of the ligand. It is thought that the binding of a ligand to one of these sites elicits a conformational change in the binding site which is translated through the body of the ion channel resulting in a small flexion of residues around the mouth of the channel. As such the binding of a ligand can lead to the opening, or closing, of the channel.

While a great many ligand-gated ion channels exist, one of the most well understood is the nicotinic acetylcholine receptor (nAChR)[Miyazawa et al., 2003; Unwin, 2005]. Comprised of 5 homologous subunits the protein is approximately 290 kDa in size, with a central 20 Å diameter channel (Figure 1.23). Its N-terminus is extracellular and constitutes the receptor domain of the channel, containing two binding sites for acetylcholine 40 Å from the membrane, positioned either side of the pore at the $\alpha - \gamma$ and $\alpha - \delta$ subunit interfaces. Each subunit also has 4 transmembrane α-helices (M1-4) and an intracellular α-helix (MA). Figure 1.24b shows the distribution of charged residues on the wall of the channel lumen. The channel is narrow enough that the charged groups that line the lumen wall can interact electrostatically, yet avoid getting too close which would slow the

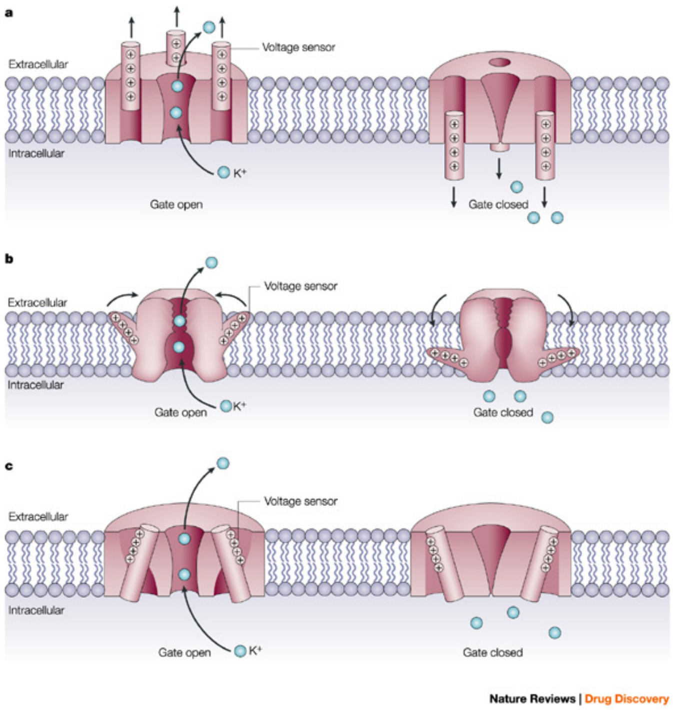

Figure 1.22: Models of the movement of the S4 helix of voltage-gated channels. (a) Helices are pulled through the membrane depending on the membrane potential, (b) Voltage-sensing paddles angle up or down, (c) The angle of S4 helical tilt alters[Ashcroft, 2004].

migration of ions along the channel. The high proportion of negatively charged residues precludes the admission of anions, and increases the local concentration of cations. The channel narrows to its smallest at the intracellular end of the M2 helix of the α subunit. These features together comprise the channel's basis for ion selectivity.

Acetylcholine interacts with the acetylcholine binding region, specifically residues Y190, Y198, C192 and W149 found in the B and C loops α subunits (Figure 1.24a). This interaction disrupts a 'distorted' conformation of the binding region, shifting it into a relaxed form. By destabilising the distorted form, acetylcholine initiates a series of conformational adjustments that run from the extracellular receptor domain along the transmembrane helices that form nAChR's channel. These adjustments allow the M2 helices to rotate by a small amount, resulting in the destabilisation of hydrophobic interactions in the channel's gating mechanism which result in its opening[Unwin, 2005].

Another family of channels that are of great interest are the transient receptor potential (TRP) channels. They respond to a wide range of ligands including menthol, eucalyptol, isothiocyanates, capsaicin and Δ^9-tetrahydrocannabinol (the active compound in cannabis), as well as some endogenous ligands produced in cells such as ATP. The ion channel is a tetramer of identical subunits, each with 6 transmembrane domains and several cytosolic and extracellular loops. Transmembrane regions 1–4 and some of the connecting loops form gating, regulatory or enzymatic domains, while transmembrane re-

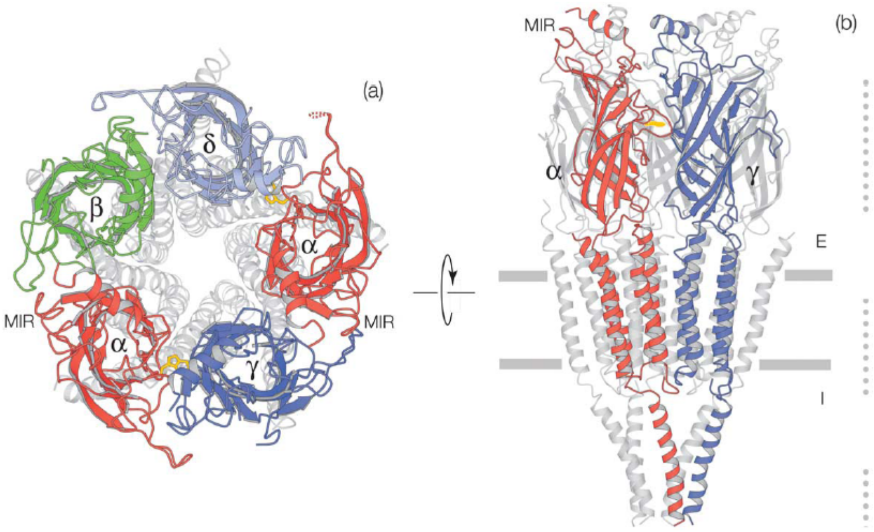

Figure 1.23: Architecture of the nicotinic acetylcholine receptor of *Torpedo marmorata*[Unwin, 2005]

gions 5 and 6, as well as the loop connecting the two, form a cation-conducting pore that allows passage of Ca^{2+}. The channels' ligand-gating behaviour allows very low concentrations of ligand to open the pore resulting in the flux of millions of cations per second. This behaviour makes ion channels very useful as signal amplifiers. These channels are only found in eukaryotes, and have so far only been overexpressed in eukaryotic expression systems such as yeast or cells naturally rich in channels.

Ligand	Source of ligand	TRP channel	Gating concentration
allicin	garlic	TRPA1	1.9 μM
allicin	garlic	TRPV1	51.2 μM
allyl isothiocyanate	mustard, wasabi	TRPA1	11–22 μM
capsaicin	chilli	TRPV1	0.02–0.7 μM
gentamycin	antibiotic	TRPA1	6.7 μM
menthol	mint	TRPM8	4–80 μM
piperine	black pepper	TRPV1	37.9 μM
Δ^9-tetrahydrocannabinol (THC)	cannabis	TRPA1	12 μM

Table 1.1: A small selection of ligands and the TRP channels they interact with

In this project we've made use of TRPC5 channels expressed in human embryonic kidney cells (HEK293 cell line). These are part of the canonical sub-family of TRP channels and respond to several activating stimuli including extracellular concentrations of Gd^{3+}, La^{3+} and Ca^{2+}, as well as muscarinic receptor activation[Zeng et al., 2004]. La^{3+} has been chosen as the gating ligand as it has been described to directly activate the channel[Jung et al., 2003], whereas some other gating factors may influence the channel via G-proteins or interactions with the lipid environment.

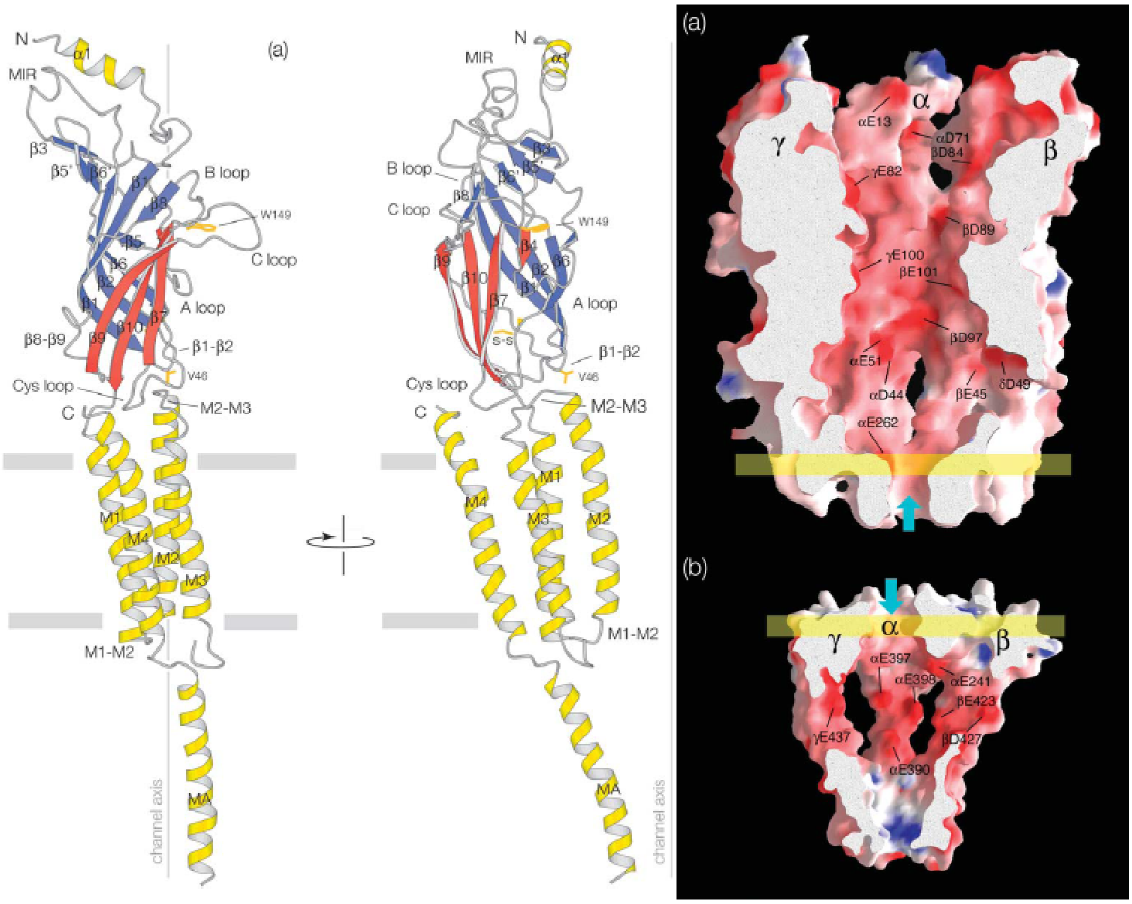

(a)

(b)

Figure 1.24: Features of the nicotinic acetylcholine receptor of *Torpedo marmorata*[Unwin, 2005]. (a) An annotated α subunit of nAChR. The B and C loops constitute the acetylcholine binding region. M2 is the pore-forming helix. (b) A cross-section of the nAChR channel lumen showing the distribution of charge, where red is negative charge and blue is postive charge.

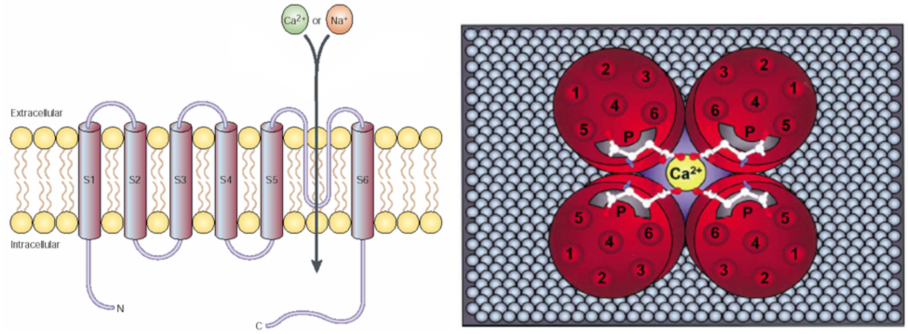

(a) Subunit architecture

(b) Tetramer architecture

Figure 1.25: TRP channel architecture. (a) Each subunit is made up of 6 transmembrane spanning helices (S1–6). The connecting loop between S5 and S6 forms part of the channel pore and provides specificity to mono- and divalent cations (e.g. Na^+, Ca^{2+}, etc., image taken from Clapham *et al*, 2001[Clapham et al., 2001]). (b) 4 subunits come together to form a tetrameric structure with the S5–S6 connecting loops forming the central pore region (image taken from den Dekker *et al*, 2003[den Dekker et al., 2003]).

Chapter 2

Theory of Experimental Techniques

2.1 Electrochemical Impedance Spectroscopy (EIS)

Electrochemical impedance spectroscopy (EIS) is a technique that makes use of alternating potentials at a range of frequencies to study an electrochemical system. The resulting current can be analysed in various ways and fitted to an equivalent circuit to characterise the system. This technique has been shown to be highly effective in the study of solid supported biomembranes and ion transport [Janshoff and Steinem, 2006; Jenkins et al., 1998; Jeuken et al., 2005, 2006; Keizer et al., 2007; Koper, 2007; Naumann et al., 2003a, b; Rose and Jenkins, 2007; Sinner and Knoll, 2001; Steinem et al., 1996; Tanaka and Sackmann, 2006; Vallejo and Gervasi, 2007; Vockenroth et al., 2008a, b, c].

Several aspects of EIS theory will be explored here, starting with a description of the electric double layer. Next, the physics of EIS will be examined as we look at the relationship between potential, current, impedance and admittance. An explanation of the equipment used for EIS studies, and how the data are presented will follow, before looking at how we interpret this via the use of computer modelling.

2.1.1 Electric Double Layer

When a potential is applied to an electrode, a charge (q_m) builds up on its surface. Due to electrostatic forces, this charge will be neutralised by an equal but opposite charge (q_s) in the form of electrolyte ions building up and water dipoles reorientating at the interface. This phenomenon is referred to as the electric double layer and will occur on any surface in a liquid.

$$q_m = -q_s \tag{2.1}$$

Several models and theories for the electric double layer have been put forward, and are shown graphically in Figure 2.1. The first and simplest of these was created by Helmholtz

[1853]. Shown in Figure 2.1a, it states that the establishment of the neutralising charge (q_s) is due to a potential difference created across the interface from the electrode surface (potential ϕ_m) to the point of zero charge (pzc) where there is no charge left in the solution - here there remains a solution potential (ϕ_s). This results in an electric field gradient being setup across the charge separation layer. Anions and cations are then redistributed across this gradient by electrostatic forces. The attracted ions build to excess at the liquid-surface interface. The precise distance from the surface is limited by the solvation shell of the ions - the distance from the nucleus of the ion to the outermost point of the van der Waals radii of water molecules adsorbed to the ion. An imaginary plane can be thought to run through the centre of these ions, referred to as the Outer Helmholtz Plane (OHP). The ions at this plane act as the counter charge to the electrode surface and as such can be thought of as the opposing plate in a capacitor, with the distance between the electrode surface and the OHP being fixed for a certain electrolyte. By changing the ions in the electrolyte, the distance between the OHP and the electrode surface will change resulting in a difference in the capacitance. This is represented by Equation 2.2, where C is the double layer capacitance, ϵ is the absolute permittivity of the electrolyte ($\epsilon = \epsilon_r.\epsilon_0$, where ϵ_r is relative permittivity and ϵ_0 is permittivity of free space), and d is the thickness of the double layer (distance from electrode surface to the OHP).

$$\begin{gathered} C_H = \frac{\epsilon}{4\pi d} \\ \epsilon = \epsilon_0 \epsilon_0 \end{gathered} \tag{2.2}$$

Helmholtz's model was improved upon by the work of Gouy [1909, 1910] and Chapman [1913]. They suggested that the counter charge needed to neutralise that of the electrode was not positioned exclusively at the OHP, but as a charge density throughout a diffuse layer close to the electrode surface. In their model, the ions that are attracted and repelled by electrostatic forces are disrupted by Brownian motion. The net charge density decreases with distance from the electrode surface, such that the majority of the counter charge exists close to the OHP with a fraction extending into the more general 'diffuse layer' until the point of zero charge is met. The thickness of this diffuse layer is referred to as the Debye length (κ^{-1}) and can be described with Equation 2.3, where ϵ_r is the permittivity of the diffuse layer, k is the Boltzman constant, T is absolute temperature, e is the charge on a proton, n_{io} is the concentration of ions in the diffuse layer, and z_i is the charge of the ions within the diffuse layer.

$$\kappa^{-1} = \sqrt{\epsilon_r k T (4\pi e^2 \Sigma n_{io} z_i^2)} \tag{2.3}$$

Further development of the model was undertaken by Stern [1924], who better described the potential drop across the interface by using two stages. An initial large drop in the potential between the electrode (ϕ_m) and the OHP (ϕ_{OHP}) is observed to account for the majority of the charge as originally described by Helmholtz. The remainder of the charge decays with a second shallower drop off extending into the diffuse layer until the point of zero charge is met (ϕ_s), in a manner similar to that presented in the Gouy-Chapman model. The major change here was the realisation that ions have a finite size and as such the charge distribution that Gouy and Chapman used can not continue all the way to the electrode surface, but must halt at the OHP. The double layer capacitance in this case is the reciprocal of the sum of the reciprocals of the Helmholtz and Gouy-Chapman models, which exist in series.

In 1947, Grahame suggested further enhancements to the models for the double layer, by allowing the specific adsorption of uncharged or desolvated species to the electrode surface. Given their smaller size these molecules can get closer to the electrode surface and exist at the Inner Helmholtz Plane (IHP). Hydrated ions remained at the Outer Helmholtz Plane as was found in Stern's model[Grahame, 1947a, b]. The ions in the IHP reduce the charge density needed in the double layer to neutralise the electrode charge and reduces the charge in a linear manner very much like the Helmholtz model. As a result of this the surface potential decays through three regions - surface (ϕ_m) to IHP (ϕ_{IHP}), IHP to OHP (ϕ_{OHP}), OHP to pzc (ϕ_s) - with the first two being treated as per Helmholtz but with marginally different permittivities and different length scales.

While these models are technically more accurate, in reality the Helmholtz portions of the double layer capacitance dominate at ionic concentrations over 0.01 M and once the surface potential is a few hundred mV away from the pzc. As such Equation 2.2 is sufficient the majority of the time. There have been other theories put forwards in more recent years, however these are largely statistical in nature and their understanding goes beyond the scope of this thesis.

2.1.2 Basic Theory

The capacitance of the double layer can be measured using EIS. It makes use of alternating current (AC) theory, which is related to more well known principles such as Ohm's law (which applies to direct currents)

$$E = iR \tag{2.4}$$

where E is potential (V), I is current (A) and R is resistance (Ω). Ohm's law can be thought of as a special case of AC theory, where frequency is zero. With AC fields the situation changes slightly as variables become functions of time.

$$\begin{aligned} E(t) &= E_0 \mathrm{sin}(\omega t) \\ i(t) &= i_0 \mathrm{sin}(\omega t + \phi) \\ \omega &= 2\pi f \end{aligned} \tag{2.5}$$

where $E(t)$ and $i(t)$ are potential and current at time t respectively, E_0 and i_0 are amplitude of potential and current respectively, ω is frequency in radians per second (rad

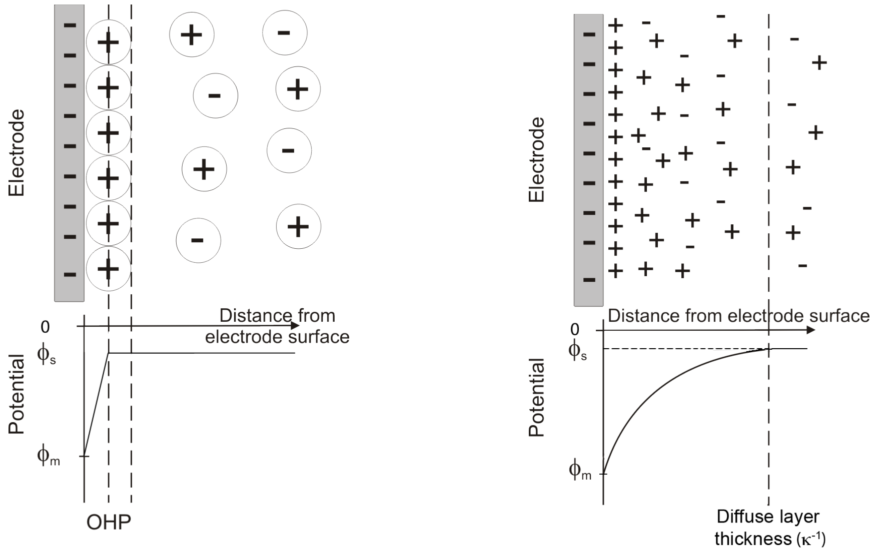

(a) Helmholtz's 1853 model (b) The Gouy-Chapman model

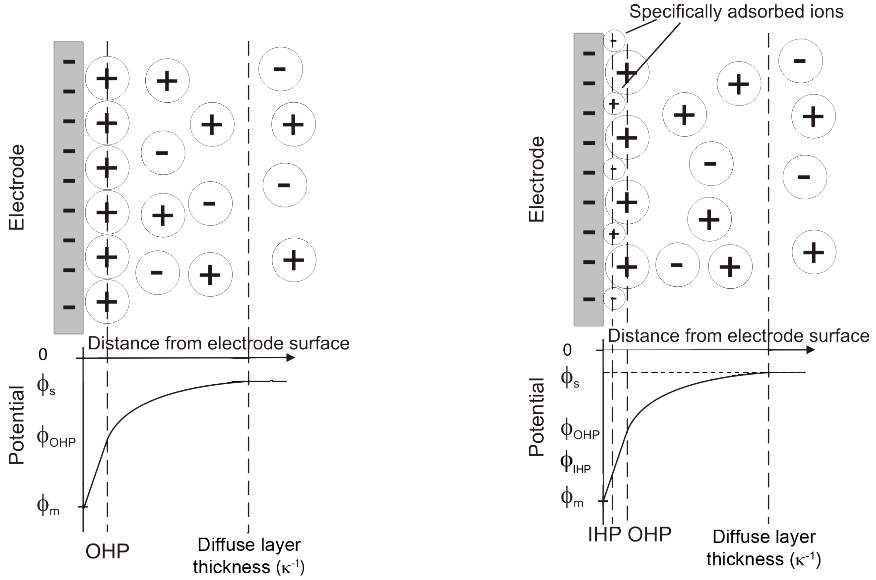

(c) Stern's 1924 model (d) Grahame's 1947 model

Figure 2.1: Models of the electric double layer. (a) The original model as proposed by Helmholtz in 1853. (b) The Gouy-Chapman model, which makes use of point charges rather than van der Waals radii. In this model there is also no Outer Helmholtz Plane as such, but drop of in potential that decreases with distance from the electrode surface. (c) Stern's 1924 model, where an Outer Helmholtz Plane from Helmholtz's model has been added to the Gouy-Chapman theory of a diffuse double layer. (d) Grahame's 1947 model in which specific adsorption of ions occurs to the electrode surface at the Inner Helmholtz Plane in addition to features seen in Stern's model.

s^{-1}), f is frequency in Hertz (Hz, cycles per second), and ϕ is phase shift between AC potential and current (see Figure 2.2).

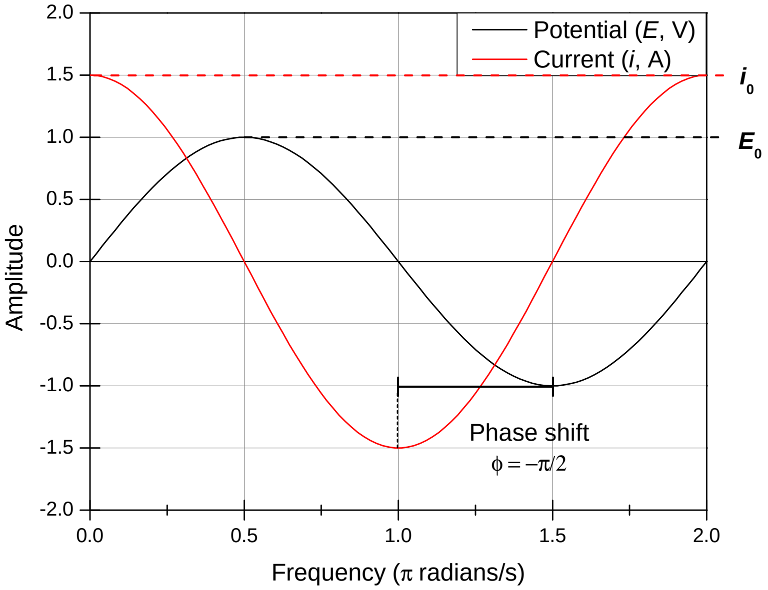

Figure 2.2: Phase shift (ϕ) between applied potential and measured current. ϕ varies depending on the frequency, and therefore the element of the electrochemical system being measured. A phase shift of $-\frac{\pi}{2}$ is shown here as would be observed for an (equivalent) circuit consisting of a capacitor only. Note that the amplitude of the potential and current can be different.

As such, Ohm's law changes to

$$E(t) = i(t)Z$$
$$Z = \frac{E(t)}{i(t)} = \frac{E_0\sin(\omega t)}{i_0\sin(\omega t + \phi)} = Z_0\frac{\sin(\omega t)}{\sin(\omega t + \phi)} \tag{2.6}$$

where Z is impedance (Ω) and is expressed as a magnitude, Z_0, and phase shift, ϕ. The magnitude of impedance, Z_0, is a ratio between the amplitudes of potential, E_0, and current, i_0, which are highlighted in Figure 2.2. Impedance, Z, can be expressed as a complex number

$$Z(\omega) = \frac{E}{i} = Z_0\exp(j\phi) = Z_0(\cos\phi + j\sin\phi) = Z_0\cos\phi + Z_0 j\sin\phi$$
$$Z_{\text{total}} = Z' + Z''j \tag{2.7}$$
$$j = \sqrt{-1}$$

and consequentially split into real and imaginary components, Z' and Z'' respectively. By splitting impedance into its real and imaginary components, both the magnitude and phase shift can be calculated by

$$
\begin{aligned}
Z_0 &= \sqrt{Z'^2 + Z''^2} \\
\tan\phi &= \frac{Z''}{Z'}
\end{aligned}
\tag{2.8}
$$

In this way impedance can be plotted as a vector with either magnitude and phase shift angle, or Z' and Z'' as x,y coordinates. Another variable referred to in EIS is admittance, Y, and is the reciprocal of impedance. It can also be expressed in real and imaginary components, Y' and Y''.

$$
\begin{aligned}
Y &= \frac{1}{Z} \\
Y = Y' + Y''j &= \frac{1}{Z' + Z''j} = \frac{1}{Z}
\end{aligned}
\tag{2.9}
$$

2.1.3 Experimental Setup

The most common EIS experimental set up is the three electrode configuration as seen in Figure 2.3. The three electrodes are connected to a potentiostat, which generates a DC potential and applies a small AC perturbation in the order of a few mV. This AC potential is applied to the working electrode, which is the electrode that is being studied. The electrode is immersed in an ionic solution, called an electrolyte, through which current passes due to the migration of ions from one electrode to another. The current flows between the working electrode and the counter electrode, which is generally made of platinum, and is recorded by the potentiostat. The third electrode, the reference electrode, has a fixed potential provided by an isolated redox system in the electrode. This redox system is made up of solutions of the reactants needed for the electrochemical reaction to occur and provides a stable reference from which the potential of the electrochemical system can be determined and, via the use of a feedback loop, maintained. Some commonly used reference potentials include those of standard hydrogen electrode (SHE), saturated calomel electrode (SCE, 244 mV vs SHE), and silver/silver chloride electrode (Ag/AgCl, 199 mV vs SHE). By analysing the potential applied and the current measured, the system can be studied. The range of frequencies that can be measured reliably is affected by the speed of the reference electrode, or more specifically the time constant of the reference electrode's RC low pass filter. This is calculated as $t = Z_{\mathrm{RE}} C_{\mathrm{RE\ input}}$, where t is time constant in seconds, Z_{RE} is the impedance of the reference electrode (Ω) and $C_{\mathrm{RE\ input}}$ is capacitance of the reference electrode input, typically 8 pF. In the course of this project, it has been necessary to measure at higher frequencies at which the time constant of the reference electrode's RC low pass filter ($t = Z \times 8 \times 10^{-12}$F) exceeds the duration of the measurement (1 MHz = 1 ns). In order to make measurements at these frequencies, a platinum wire can be coupled to the reference electrode via a 0.1–1.0 μF capacitor. This allows the AC signal to bypass the reference electrode, via the platinum wire, at higher frequencies, while the DC component still passes through the reference electrode[Ecochemie, 2003].

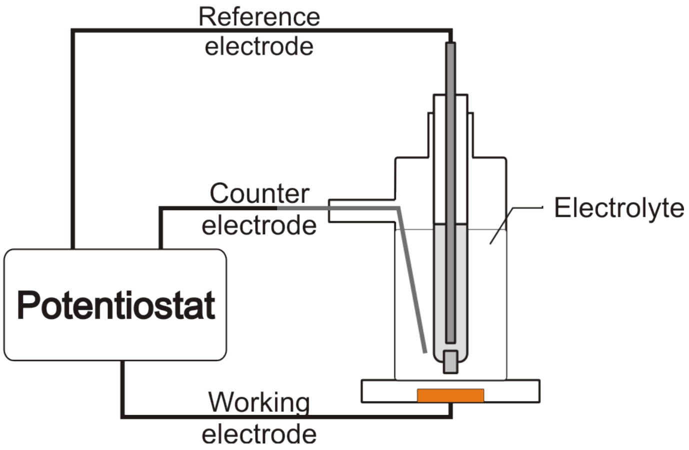

Figure 2.3: An electrochemical cell, as used in electrochemical impedance spectroscopy (EIS). A small potential is applied to the working electrode and maintained using the reference electrode. The frequency is varied to investigate different responses in the system. The current produced is measured using the counter electrode. The electrolyte allows the flow of current across the electrochemical cell. Potentials are applied and controlled by the potentiostat, which also measures the currents produced.

2.1.4 Impedance Plots

In an EIS experiment a range of frequencies are used to interrogate the system. In this thesis a range of 100 kHz – 100 mHz, distributed over 46 points on a logarithmic scale, has been used. The raw data measured by the system at each frequency is the real and imaginary components of impedance (Z', Z''). From this, the magnitude of total impedance ($|Z_0|$) and phase shift (θ), as well as real and imaginary admittance (Y', Y''), can be calculated for each frequency and displayed in numerous plots to better understand the system. There are three principle plots used in this report that require explanation.

Nyquist plots show the real impedance (Z') on the x-axis and the negative imaginary impedance ($-Z''$) on the y-axis. This plot is very useful for studying resistances in a system. The plot will generally be made up of semi-circles, or partial semi-circles appearing as arcs, the diameter of which is equal to the resistance of a component. The initial offset on the x-axis is indicative of the Ohmic resistance of the electrolyte, cables and electrochemical equipment. This can be better seen in Figure 2.5d. While changes in resistance can be observed as clear differences in the size of the semi-circles, these resistances are often only significant if interpreted on a logarithmic scale. As such, a change in resistance of a couple of orders of magnitude will result in a far smaller semi-circle being displayed. This semi-circle may be in addition to a larger semi-circle and appear to be a kink in the plot.

Bode plots show both the magnitude of impedance ($|Z_0|$) on a logarithmic scale and the phase shift (θ) against frequency (f, Hz) also on a logarithmic scale. This plot is very useful for seeing the behaviour of different components at different frequencies, particularly for identifying gross changes in resistance and assessing the quality of a surface via the phase shift associated with the capacitance of its electrical double layer. An example of a Bode plot is shown in Figure 2.5a.

Normalised Admittance plots also known as Cole-Cole plots, show the real and imaginary components of admittance normalised against frequency ($Y'.\omega^{-1}$ and $Y''.\omega^{-1}$). This plot is invaluable for calculating capacitances, which appear as semi-circles on the plot. By taking the peak value of the semi-circle on the x-axis and doubling it (see Figure 2.5b), i.e. taking the semi-circle diameter, a value for the double layer capacitance can be obtained.

2.1.5 Equivalent Circuits

The similarity between the electrical double layer of a surface and how a traditional capacitor behave allows the use of equations derived for the behaviour of components found in traditional electrical circuits. By combining these components 'equivalent circuits' can be created to simulate the behaviour of experimental systems. These equations and their formation into equivalent circuits will now be discussed.

As previously mentioned, Ohm's law links voltage, current and resistance for DC systems (Equation 2.4), similarly in AC systems a variant of Ohm's law links voltage and current to impedance (Z). When looking at a circuit, impedance is used to describe the resistance experience by current moving throughout the entire system. However, individual components within a system can be attributed with proportions of this system impedance, allowing the system impedance to be broken down into resistance (R) and reactance (X) as shown in Equation2.10.

$$\begin{gathered} Z = R + jX \\ j = \sqrt{-1} \end{gathered} \tag{2.10}$$

Resistance behaves as described by Ohm's law and applies to components that produce the same effect regardless of the frequency of the current. Reactance however, is used to describe the frequency-dependent component of impedance and applies to capacitors and inductors (the latter of which are not within the scope of this description).

Likewise, the similarity between the electric double layer and a traditional capacitor prescribes the use of capacitor theory to model a surface with an electric double layer. The equations that describes capacitance (Equation 2.11) highlights several points. First, and of great importance, is that capacitance is inversely proportional to the distance between the surface and the point of detection. In a capacitor this would refer to the distance between the two plates that charge is stored on. However, in terms of the electric double layer it refers to the distance between the surface and the ions that counter the surface's charge.

$$\begin{aligned} C &= \frac{q}{E} \\ C &= \frac{\epsilon_0 \epsilon_r A}{d} \\ X &= \frac{-1}{\omega C} \end{aligned} \tag{2.11}$$

where C is capacitance, q is charge, E is potential, ϵ_0 is the permittivity of free space (8.854×10^{-12} F.m^{-1}), ϵ_r is the relatively permittivity of the medium between the plates, A is surface area of one plate, d is the distance between the two plates, X is the reactance of the capacitor, and ω is the angular frequency being examined. The relative permittivity, or 'dielectric constant' (ϵ_r), of the medium is indicative of the extent to which it is polarisable. Polarisation of a medium occurs when an electric field is applied across it. The atoms in this medium are comprised of a positively-charged nucleus and negatively-charged electrons that are affected by the electric field. An electrostatic attraction is felt between the cathode and the nuclei, and the anode and the electrons. This results in a distortion of the electron distribution in relation to the nucleus, such that the electron distribution may become stretched in the direction of the field and the nucleus will be shifted from the centre. This produces an induced dipole, which is shown on a non-polar atom in Figures 2.4a and 2.4b. The electric field has a similar effect on polar molecules (molecules with a permanent dipole), with the additional consequence of rotating the molecule such that its dipoles align with the field (as shown in Figures 2.4c and 2.4c).

Low dielectric constants indicate poor levels of polarisation, while high values indicate that the medium is highly polarisable. By definition a vacuum has a dielectric constant of 1, as there is no matter within the vacuum to be polarised. This represents the lowest dielectric constant possible. Air at 1 atmosphere and 25°C has matter, but it is diffuse enough that it has little effect on the dielectric constant ($\epsilon_r = 1.0005$). Materials that are non-polar in nature generally have low dielectric constants due to their limited capacity for the distortion of their electron distributions - examples include glass (SiO_2, $\epsilon_r = 3.9$) and polytetrafluoroethylene (PTFE, $(C_2F_4)_n$, $\epsilon_r = 2.1$). Water (as shown in Figures 2.4c and 2.4d) is a polar molecule, and has a dielectric constant of 80 indicating that it is readily polarised. Many polar molecules also have relatively high dielectric constants. This is due to the combination of a polar molecules' pre-existing permanent dipoles and the additional distortion of the electron distribution caused by the application of an electric field.

The dielectric constants of lipid bilayers and proteins are more complex due to the heterogeneous nature of the structures. Lipid bilayers are comprised of a mix of lipids and sterols with varied properties. Saturated hydrocarbon bilayers have dielectric constants of 10-20, however by introducing unsaturated bonds this drops dramatically to 3. The addition of 30 mol% cholesterol to PC lipid bilayers has been shown to increase the polarity of the lipid bilayer head groups and portion of the hydrocarbon chain nearest the

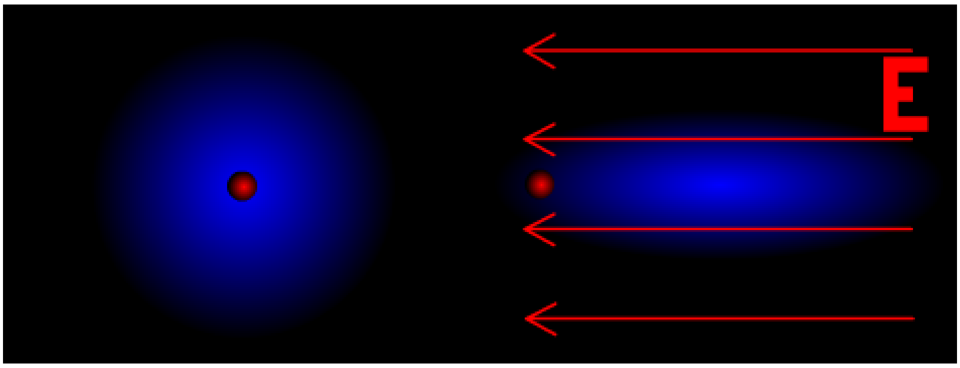

(a) Non-polar without electric field (b) Non-polar with electric field

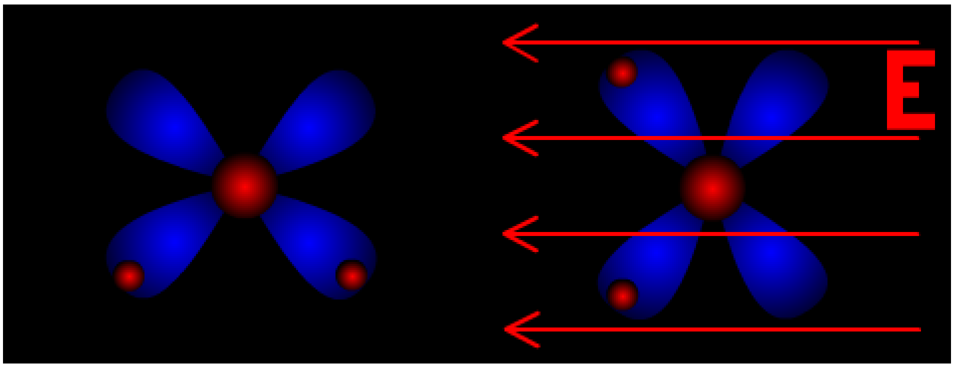

(c) Polar without electric field (d) Polar with electric field

Figure 2.4: The polarising effect of an electric field on (a/b) non-polar and (c/d) polar molecules. The red arrows marked E represent the direction of the electric field. The blue regions indicate the distribution of electrons, and the red dots indicate the position of the atomic nuclei.

surface, while the portion nearer the core ($9^{\text{th}} - 10^{\text{th}}$ C position inwards) experiences a further decrease in polarity to 2[Subczynski et al., 1994].

Proteins also have varied permittivities due to their structures - the outer surface is comprised of charged and polar side chains, while the inner core's side chains are predominantly non-polar. Modelling simulations have been used to calculate the dielectric constants of the protein interior and surface. The protein interior was found to have a dielectric in the region of 2-6 with the polar and charged solvent-facing side chains being far higher. As a result of this, the dielectric constant of the whole protein molecule is generally accepted to be between 11 and 21 depending on the composition of the protein and its environment[Simonson and Brooks III, 1996].
While the capacitor in this equation has 'perfect' surfaces, surfaces under experimental conditions rarely are generally not. This non-perfect behaviour results in a decrease in phase shift and impedance at low frequencies, compared to what would be expected for a capacitor of that size. To better simulate the surfaces encountered in an experimental system, an empirical component known as a constant phase element (CPE) is often used.

$$Z = \frac{1}{C(j\omega)^{\alpha}} \tag{2.12}$$

The impedance is calculated as above, in much the same way as the impedance of a capacitor except for an additional parameter, the exponent α, which can be used to attenuate the behaviour of the CPE. When α is 1, the CPE will behave exactly the same as a capacitor, however it can be lowered to better suit the specific system being examined. In these systems, α is often used to describe the non-ideal behaviour of surfaces, and has been attributed to surface roughness[de Levie, 1965], leakiness of the surface and non-uniform current distribution[Jorcin et al., 2006] to name a few. It should be noted that due to α the 'capacitance' calculated is not representative of the true capacitance of the surface, but is instead referred to as a 'Q value' (the nomenclature used to represent a CPE in equivalent circuit notation). While a true capacitance can be calculated from this Q value, it only holds true for a specific frequency is limited to specific equivalent circuits and as such this will not be used.

In addition to the different components used to model a system, there are different types of electrochemical systems measured with EIS that can be broadly defined as either 'Faradaic' or 'non-Faradaic'. A Faradaic system involves charge transfer, that is the transfer of electrons to or from the electrode to an electrochemically active species. These charge transfers have a resistance related to their reaction rates and as such are generally modelled as resistors. In addition to this, any limitations in the mass transfer of electrochemically active species to the electrode are modelled as 'Warburg impedances'. Given that the systems being analysed in this project generally are not Faradaic in nature, the components used will not be discussed in further detail. 'Non-Faradaic' systems are those which have no electrochemical reactions involved. Instead, charging currents are predominantly measured here. It is this type of electrochemical systems that will be studied in this project.

The circuits formed to model electrochemical systems are called equivalent circuits and can be displayed graphically as a circuit drawing using standard component symbols (Figures 2.5e and 2.5f), or displayed using nomenclature as will be now explained. The components are referred to by a letter - R for resistors, C for capacitors and Q for CPEs. In addition to this, components within a circuit may be differentiated from each other by a subscript notation. For example, solution resistance may be R_s and membrane capacitance C_m. When these components are put together to form a circuit they can be in series, in parallel or a combination of both. In series, the real and imaginary components of each electrical component's impedance are added together to give the total impedance. However, when in parallel the circuit's impedance is the sum of its components reciprocal impedances. In both these cases Z may be the sum of reactances and resistances as described in Equation 2.10.

$$\text{Series: } Z = Z_1 + Z_2 = (Z_1' + Z_2') + j(Z_1'' + Z_2'') \tag{2.13}$$

$$\text{Parallel: } \frac{1}{Z} = \frac{1}{Z_1} + \frac{1}{Z_2} = \left(\frac{Z_1'}{Z_1'^2 + Z_1''^2} + \frac{Z_2'}{Z_2'^2 + Z_2''^2}\right) - j\left(\frac{Z_1''}{Z_1'^2 + Z_1''^2} + \frac{Z_2''}{Z_2'^2 + Z_2''^2}\right) \tag{2.14}$$

To describe the layout of components in equivalent circuit nomenclature, brackets are used. Components in series are written one after another; for example, a resistor in series with a capacitor and another resistor would be RCR. Components in parallel with each other are put within brackets; for example, a resistor in parallel with a capacitor and a CPE would be (RCQ). To indicate components in series within a parallel circuit, square brackets are used; for example, a resistor in parallel with a resistor and capacitor in series would be (R[RC]).

In summary, while a DC current only experiences resistance to the flow of electrons when it encounters a resistor, an AC current responds differently. Resistors still provide resistance, or rather impedance, but so do capacitors. By examining the impedance equations for each component, we can better understand how they behave when studied at different frequencies.

Component	Impedance equation	Real	Imaginary	Phase shift (°)
Resistor (R)	$Z = R + 0j$	$Z' = R$	$Z'' = 0$	0
Capacitor (C)	$Z = 0 - \frac{j}{\omega C}$	$Z' = 0$	$Z'' = -\frac{1}{\omega C}$	-90
CPE (Q)	$Z = 0 - \frac{j}{\omega^\alpha C}$	$Z' = 0$	$Z'' = -\frac{1}{(j\omega)^\alpha C}$	< -90

Table 2.1: Impedance equations for equivalent circuit components and the phase shift they produce. CPE is a constant phase element. Impedance equations are presented in the format shown in Equation 2.10, and as such Z is used in all cases. $\omega = 2\pi f$

As we can see from Table 2.1, each component responds differently in the real and imaginary component of the impedance equation. Resistors provide a constant impedance across all frequencies and behave purely in the real component, such that the impedance of a resistor is always equal to its resistance. As we have already seen, the phase angle is calculated by dividing the imaginary component by the real component and taking the inverse tangent to get ϕ. With no imaginary component present, the phase angle is 0° (0 radians). Capacitors behave completely differently to resistors. Their impedance is obtained entirely from the imaginary component and is frequency dependent. Given that there is never any real component to the impedance of a capacitor, it always experiences $-90°$ (or $-\frac{\pi}{2}$ radians) phase shift. Frequency and capacitance are inverse to impedance. At higher frequencies, electrons begin ignore the capacitor and it acts as a short circuit resulting in impedance tending to towards zero. Conversely, at lower frequencies (approaching DC potentials) the impedance tends towards infinity.

2.1.6 Fitting

To obtain values for the various parameters associated with the components in the equivalent circuits used, modelling software can be used. Most commercial potentiostat software now comes with this facility already incorporated, however in this thesis Dr. L.J.C. Jeuken's EISFit software has been used.

Fitting an equivalent circuit to experimental data is a statistical process where a circuit is selected to approximate the physical processes occurring. While excellent fits can be obtained via the use of complex empirical equivalent circuits, it must be remembered that the circuit must be relevant to the system and with an increasing number of components the accuracy of the values obtained decreases. EISFit uses the Levenberg-Marquardt algorithm to fit the data, and a bootstrap method to estimate the errors associated with the fit.

The Levenberg-Marquardt algorithm finds a local minimum in a curve-fitting problem. In the case of fitting an equivalent circuit this means calculating the difference between the recorded data and the equivalent circuit, then changing the equivalent circuit parameters slightly and recalculating the difference. When the difference can not be made any smaller by making slight changes a local minimum is reached. This local minimum is a solution, however it is not necessarily the optimal solution. To reach this optimum the correct starting parameters are required.

The bootstrap method works by removing a portion of the recorded data and recalculating the difference between it and the equivalent circuit fit. This process is repeated many times and the deviation of the fit calculated for the full data set used to estimate an error for the equivalent circuit fit.

2.1.7 Case Study: Impedance of a EO_3C SAM

A typical measurement is shown in Figure 2.5 using both the Bode, Normalised Admittance and Nyquist representations. A P1A gold electrode (surface area = 0.03142 cm^2; described in Chapter 3) was modified with a 100% EO_3C SAM and studied in the experimental setup shown in Figure 2.3. The measured data are shown as data points, while two different equivalent circuits, R(CR) (Figure 2.5e) and R(QR) (Figure 2.5f), have been fitted to it and are shown as red and blue lines respectively. All data has been normalised vs. the surface area of the electrode. At high frequencies (point 1) we observe the electrolyte resistance as a plateau in the impedance component of a Bode plot with a 0° phase shift (left and right axes of Figure 2.5a respectively). A more accurate value of electrolyte resistance can be obtained from the Nyquist plot (Figure 2.5d, by looking at the offset of the plot from the origin. This is followed by a charging of the surface's double layer, which is seen as a slow ramping of impedance and an increase in phase shift. Peak surface capacitance as seen on the Normalised Admittance plot coincides with a $-45°$ phase shift (point 2) - this value will be used to estimate the capacitance from here on out (referred to as $\mathrm{C_{SAM}}$ or $\mathrm{C_{tBLM}}$), and in this case has been determined to be 1.27 μF.cm^{-2}. This phase shift continues to increase towards $-90°$(at point 3) when a capacitor is being measured, however under experimental conditions $-90°$is rarely reached and in the case presented here reaches approximately $-85°$. The use of a CPE here with a α value of < 1 improves the accuracy of a model in this regard. Point 3 coincides with the completion of a capacitance semi-circle, however we rarely use this value as a true indication of the double layer capacitance due to the distorting effect that additional components may have here. After this region we begin to see a decrease in phase shift dependant on the surface resistance with smaller resistances corresponding with a greater drop off (i.e. at higher frequencies) in phase shift and another impedance plateau (point 4).

Following the recording of the EIS measurement, an equivalent circuit can be fitted. Two circuits have been fitted here to demonstrate the difference between C (capacitor) and Q (constant phase element, CPE) as components for simulating the capacitance of the electrode. As can be seen the C component does not fit the data as well as Q - this is due to Q having an additional parameter α, that is able to modulate the CPE's behaviour. Due to this, Q will be used in the majority of equivalent circuits throughout this thesis.

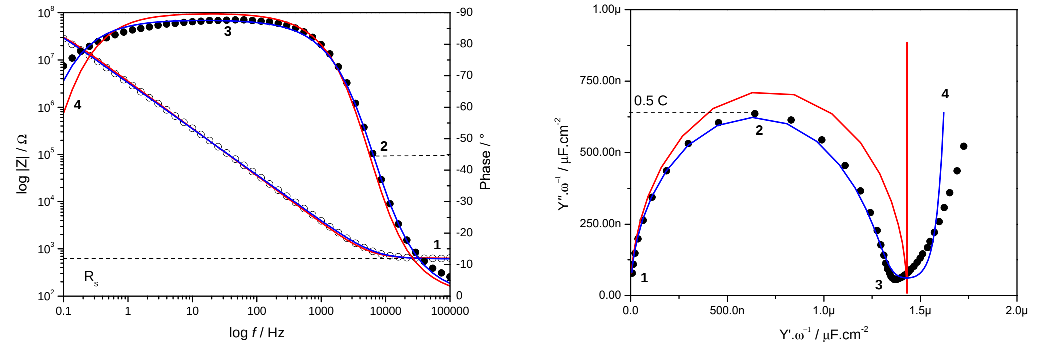

(a) Bode plot

(b) Normalised Admittance plot

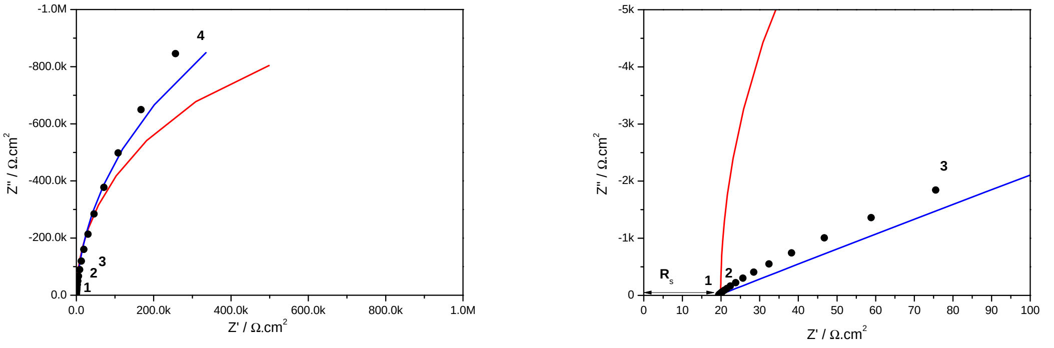

(c) Nyquist plot

(d) Nyquist plot (focused on high frequency area)

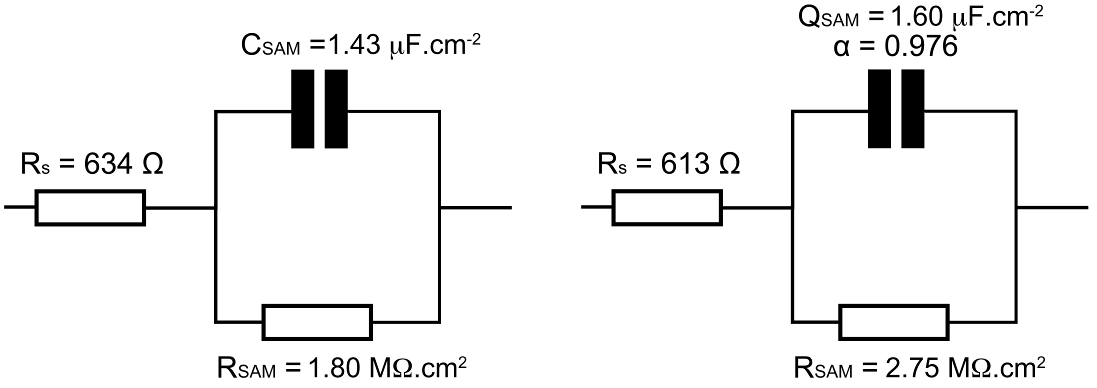

(e) R(CR) - red line

(f) R(QR) - blue line

Figure 2.5: Bode, Normalised Admittance and Nyquist plots for a gold electrode (P1A design - surface area = 0.03142 cm^2, described in Chapter 3) modified with a 100% EO$_3$C SAM. Two equivalent circuits, R(CR) and R(QR), were used to fit the data. Black = recorded data; red = R(CR) fit; blue = R(QR) fit. In the Bode plot, open symbols represent the magnitude of total impedance (left axis) and closed symbols represent the phase (right axis). Annotations: 0.5C from (b) is 0.64 μF.cm^{-2}, giving a capacitance value of 1.27 μF.cm^{-2}.

2.2 Cyclic Voltammetry

Cyclic voltammetry (CV) is an electrochemical technique that allows a changing potential to be applied to a system. The potential is cycled between two vertex potentials in a linear fashion at a speed determined by the scan rate (ν), as shown in Figure 2.6b. A current is generated, and plotted as a function of potential. This cyclic voltammogram can be interpreted to analyse the system with the maximum current being referred to as peak current (i_p).

In Figure 2.6a, we can see a typical cyclic voltammogram. Here the starting potential is -0.25 V (E_1) and the second potential is 0.25 V (E_2). The transition of potentials over time is shown as the waveform in Figure 2.6b. As the potential changes from E_1 to E_2 it reaches the oxidation potential for the transfer of electrons from an electroactive species. As the potential goes past the oxidation potential the rate of electron transfer increases. The current is also determined by surface concentration of the reduced form of the electroactive species - as the reaction progresses the surface concentration of oxidisable species decreases, leading to a drop off in current. Clearly the rate at which the electroactive species can be supplied to the surface of the electrode has a large influence on this, and as such the peak height is dependent on the diffusion rate of the species. As the potential reaches E_2 the scan direction reverses and moves back towards E_1 and we see the reduction of the oxidised form of the electroactive species.

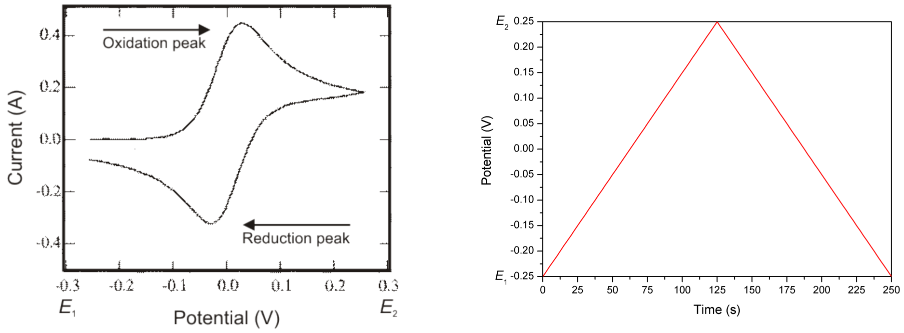

(a) Cyclic voltammogram

(b) Waveform for cyclic voltammogram

Figure 2.6: (a) An example of a cyclic voltammogram. The upper peak is the oxidation peak and the lower peak in the reduction peak. (b) The waveform for the cyclic voltammogram, showing the transition from E1 to E2 and back again over time at a scan rate of 4 mV/s.

If an electroactive substance/compound is added to the electrolyte, the electron transfer between the compound and the electrode can be followed. There are a number of electron transfer processes which can be broadly classified as reversible, quasi-reversible, or irreversible.

Reversible electron transfer (Figure 2.7a) describes conditions where the electrochemical reaction is limited by diffusion alone. It is characterised by a peak separation of 59 mV per electron involved in the transfer process, i.e. 29 mV peak separation for a 2 electron process. The reduction and oxidation peaks should be of the same amplitude.

Under irreversible electron transfer schemes, such as those depicted in Figure 2.7c, the reaction is limited by the kinetics of the electron transfer. In these cases, the electroactive compound can be readily reduced or oxidised, but the reverse electron transfer occurs so slowly despite the use of large overpotentials that the transfer is not observed and can be ignored. This accounts for the lack of a reduction peak in Figure 2.7c. The extent to which the reaction kinetics are limited affects how far the peak is displaced from the standard redox potential, this is demonstrated in Figure 2.7c by the three curves labelled a, b and c where the kinetics are slowed by an order of magnitude in each.

Quasi-reversible electron transfer (Figure 2.7b) is an intermediary scheme between reversible and irreversible electron transfer that is used to describe electron transfer processes that are controlled by a combination of diffusion and kinetics. In Figure 2.7b the diffusion component begins to dominate going from a to c, resulting in a decrease in the peak currents and an increase in the peak separation.

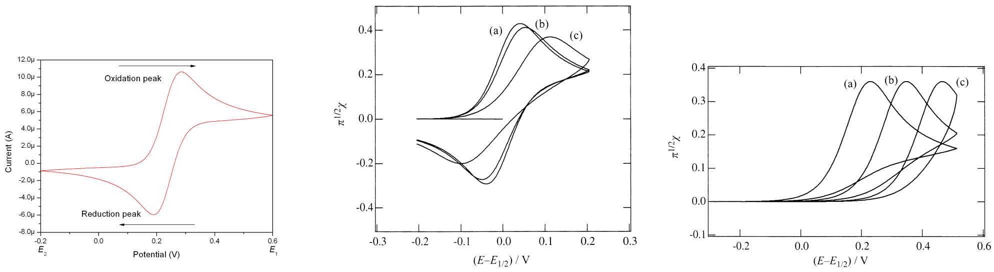

(a) Reversible (b) Quasi-Reversible (c) Irreversible

Figure 2.7: Different electron transfer schemes[Girault, 2004].

Another effect, ohmic drop (Figure 2.8), can give the appearance of slowed kinetics as seen in quasi-irreversible electron transfer. However, the effect is in fact due to an elevated electrolyte resistance and can be corrected with the use of a higher concentration electrolyte, bringing the working, counter and reference electrodes closer together or with data processing if the degree of ohmic drop is known, or by correcting the applied potential in a process known as iR compensation. By taking measurements of the system at a variety of scan rates (ν), different correlations become apparent allowing these various schemes to be assigned to the system.

2.2.1 Use of Redox Probes for Determination of Electrode Surface Area

As mentioned previous, electroactive compounds can be added to the electrolyte. These can act as probes of the system being studied, with their redox kinetics providing insight on a number of factors such as the occurrence of electron transfer, the rate of electron

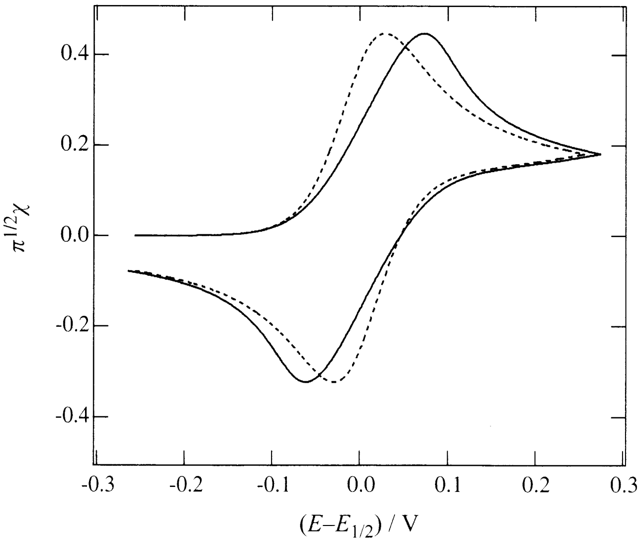

Figure 2.8: CV before and after ohmic drop correction

transfer and the electrode geometry. Additionally, they can be used to probe the integrity of a layer - for example, checking for defects in a SAM or lipid bilayer[Chailapakul and Crooks, 1995; Zhao et al., 1996]. These self-assembled layers are generally closely packed and as such prevent a barrier to the diffusion of redox probes. A signal from a probe would indicate that is able to circumvent these layers. The size of the defect can even be tested through the use of a variety of probes with a range of diameters (from 6.0 Å for $Fe(CN)_6{}^{3-/4-}$ to 11.4 Å for $Fe(bpy)_2(CN)_2{}^{0/1+}$)[Zhao et al., 1996]. The number and distribution of defects can also be alluded to by examining the diffusion schema, and can present itself as microelectrode or array-like behaviour[Chevallier et al., 2006; Finklea et al., 1993; Zhao et al., 1996]. These behaviours are discussed later.

Two redox probes used in this thesis are $Fe(CN)_6 3 - /4-$ and $Ru(NH_3)_6{}^{3-/4-}$. The $Fe(CN)_6{}^{3-/4-}$, ferricyanide/ferrocyanide, redox couple undergoes a 1 electron transfer reaction with a reduction potential of -0.358 V vs SHE[Haynes and Lide, 2011] and a diffusion constant of 7.6×10^{-6} cm^2/s for $K_3[Fe(CN)^{3-}{}_6]$[Kovach et al., 1985].$Ru(NH_3)_6{}^{3+/4+}$, the ruthenium hexaammonium redox couple also undergoes a 1 electron transfer reaction with a reduction potential of 0.100 V vs SHE[Haynes and Lide, 2011], and a diffusion constant of 6.2×10^{-6} cm^2/s for $[Ru(NH_3)^{3-}{}_6]Cl$[Kovach et al., 1985]. In this project, these probes have been used for the determination of the electrode's surface area. This is done using the Randles-Sevcik equation (Equation 2.15), where I_p is peak current, n is number of electrons transferred in the electrochemical reaction, F is Faraday's constant, A is the area of the electrode in cm^2, $[C_R]$ is the concentration of the reactant, ν is the scan rate, D_R is the diffusion constant of the reactant (given previously) and RT is the gas constant (8.3145 m^3.Pa/(mol.K)) multiplied by temperature (taken to be 293 K).

$$I_p = 0.4463nFA[C_R]\sqrt{\frac{nF\nu D_R}{RT}} \tag{2.15}$$

This equation can be rearranged to calculate surface area (A) from peak current (I_p).

$$A = \frac{I_p}{0.4463nF[C_R]\sqrt{\frac{nF\nu D_R}{RT}}} \propto \frac{I_p}{[C_R]\sqrt{\nu}} \tag{2.16}$$

2.2.2 Microelectrode Behaviour

A microelectrode is loosely defined as having dimensions "smaller than the diffusion layer found in most experiments" and according to Brett and Brett [1993], is anywhere between 50 and 0.1 μm. The values given in literature however are highly variable with different sources giving radii or band widths of under 25 μm [Bard and Faulkner, 2001], upto 20 μm [Koster et al., 2001], 10 μm [Fisher, 1996], under 10 μm [Wittkampf et al., 1997] and 'a few μm' [Girault, 2004]. Based on these definitions, the P2F electrodes described in Chapter 3 would qualify as microelectrodes with a radius of 10 μm.

While this section has thus far looked at electrochemical processes at macroelectrodes which experience planar diffusion, microelectrode behaviour is significantly different. These electrodes instead have radial diffusion schemes, and as a result gain access to a far greater volume of the bulk electrolyte thus producing higher current densities. Schematic representations of a few different types of electrodes that exhibit radial diffusion are shown in Figure 2.9 and a typical CV from one shown in Figure 2.10.

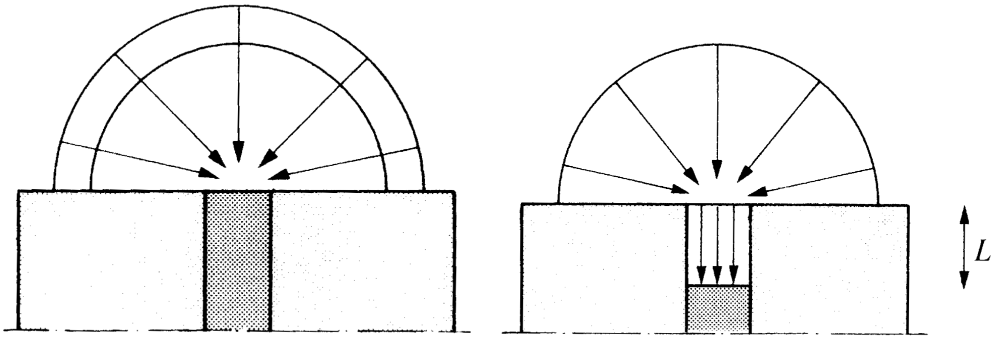

(a) Microdisc (b) Recessed microdisc

Figure 2.9: Different type of microelectrode

Each of the microelectrode geometries is subtly different and require variants on the Randles-Sevcik equation. Microdisc electrodes, as shown in Figure 2.9a, are flat circular electrodes that are seated in another, usually insulating, material such as PTFE or SiO_2 such that no side geometry is accessible. They experience radial diffusion and produce a hemispherical diffusion layer, the size of which can be calculated using Equation 2.17 as δ.

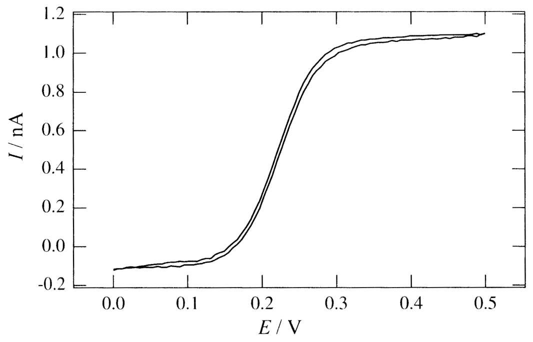

Figure 2.10: CV of electron transfer at a microelectrode.

$$\delta = \frac{\pi r D_R}{4} \tag{2.17}$$

The equation for calculating microdisc electrode areas is shown below in Equation 2.18, where A_d is the area of a microdisc, I_d is the plateau current, n is the number of electrons transferred, F is Faraday's constant, D_R is the diffusion constant for the probe being used, $[C_R]$ is the concentration of the probe, and r is the radius of the microdisc. An important point to note here is the absence of a term for scan rate (ν). This is because hemispherical diffusion is independent of scan rate.

$$\begin{aligned} I_d &= 4nFD_R[C_R]r \\ A_d &= \pi\left(\frac{I_d}{4nFD_R[C_R]}\right)^2 \propto \frac{(I_d)^2}{[C_R]} \end{aligned} \tag{2.18}$$

Recessed microdisc electrodes, have a similar geometry to that of microdisc electrodes, however they are recessed in the material that surrounds the electrode (Figure 2.9b). While the microdisc portion of the electrode produces a hemispherical diffusion layer, the channel that the electrode is recessed into confines this giving linear diffusion character. These changes to the diffusion layer require the calculation of such electrode areas to be reconsidered, and the appropriate equations are shown in Equation 2.19, where I_r is the peak current, L is the length of the channel the electrode is recessed in, and δ is the thickness of the diffusion layer for a microelectrode as given in Equation 2.17. Despite these changes, the recessed microdisc electrode still behaves as a microdisc electrode - the thickness of its diffusion layer is merely changed from δ to $L + \delta$.

$$\begin{aligned} I_r &= \frac{nFAD_R[C_R]}{L+\delta} \\ A_r &= \frac{I_r(L+\delta)}{nFD_R[C_R]} \propto \frac{I_r}{[C_R]} \end{aligned} \tag{2.19}$$

In addition to microdisc electrodes, electrode tracks if small enough may behave as microband electrodes. These electrodes will display hemicylindrical diffusion and the current measured is proportional to the area (A_{hc}). This can be calculated if one dimension

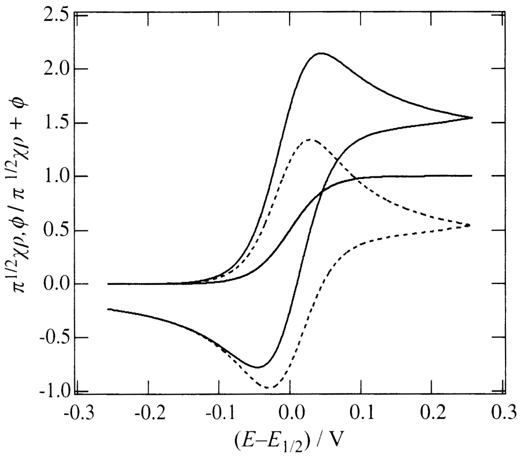

Figure 2.11: CV of electron transfer at a hybrid electrode. Broken line is the CV for an electrode exhibiting planar diffusion; the sigmoidal curve is the CV for a microelectrode exhibiting radial diffusion; and the solid line is the CV of an electrode exhibiting hybrid diffusion.

of the band measured is known, i.e. either the width (w) or length (l)[Chang and Zen, 2006].

$$\begin{aligned} I_b = A_{hc} &= \frac{i_p \ln(4\theta)}{2\pi n F D_R [C_R] w} \times w \\ \theta &= \frac{D_R R T \pi^2}{F \nu w} \end{aligned} \tag{2.20}$$

Equations 2.18 and 2.19 can also be used to assess edge effects by calculating the radial surface area, as supposed to planar surface area calculated with the Randles-Sevcik equation. It should be noted that while microelectrode behaviour has limited effect on non-faradaic EIS, when we interrogate the electrodes using cyclic voltammetry there is a far greater influence.

While microelectrodes and macroelectrodes have both been discussed, there is unlikely to be a discrete change in the diffusional properties. More likely is a transition from planar to radial diffusion as electrodes get smaller, with intermediary electrode sizes giving a hybrid diffusion layer resulting in a CV such as the one shown in Figure 2.11.

So far a macroelectrode as discussed here experiences an entirely planar diffusion layer, where as a microelectrode is entirely radial diffusion. Electrodes that fit between these two definitions experience a combination of these diffusion schemes. It is plausible that on larger electrodes planar diffusion is experienced in the centre of the electrode, while at the edges radial diffusion dominates. The degree to which the CV demonstrates either planar or radial behaviour would be proportional to the area:perimeter ratio. These diffusion patterns are demonstrated in Figure 2.12.

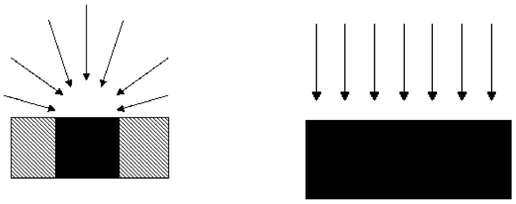

(a) Radial diffusion (b) Planar diffusion

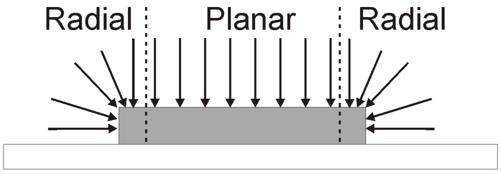

(c) Hybrid diffusion

Figure 2.12: Diffusion layers for (a) microelectrodes (radial), (b) macroelectrodes (planar) and (c) intermediate electrodes (hybrid).

To determine which diffusion scheme is in operation, cyclic voltammograms can be taken at several scan rates. Based on the Randles-Sevcik equation (Equation 2.15) discussed earlier and its variant for a microdisc electrode (Equation 2.18), it can be seen that planar diffusion is affected by scan rate while radial diffusion is not. By plotting the peak current against the square root of the scan rate, a linear correlation should be observed.

Figure 2.13 shows three such plots for electrodes of various sizes and how the currents at various scan rates would be affected by their diffusion schemes. Planar diffusion as described by Equation 2.15 has the plots passing through the origin as the currents are proportional to the square root of the scan rate (Figure 2.13a). Radial diffusion is described by Equation 2.18. The plots are parallel to the x-axis as the current is independent of scan rate. The hybrid scheme has a plot similar to that seen in Figure 2.13a but with a y-axis offset. This offset can be attributed to limited radial diffusion, a high capacitive current or an offset on the potentiostat. Assuming that the offset is due to a degree of radial diffusion, the magnitude of this offset should be proportional to the area of the electrode (Equation 2.18).

2.2.3 Electrode Array Behaviour

While microelectrodes present interesting opportunities in terms of the advantages conferred with radial diffusion, they also suffer from smaller currents due to their size. One way to counteract this is with the use of arrays of microelectrodes. By grouping a large number of individual microelectrodes together, the advantages of radial diffusion can be

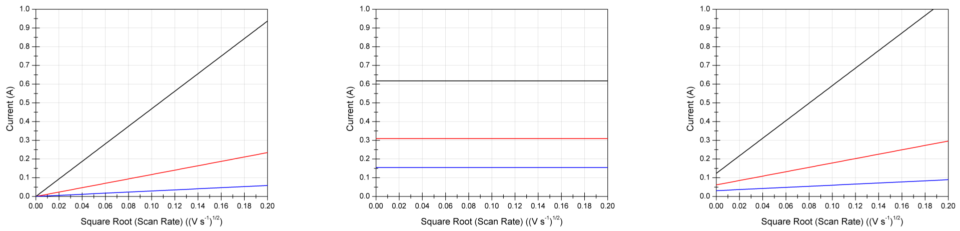

(a) Planar diffusion (b) Radial diffusion (c) Hybrid diffusion

Figure 2.13: Differences in diffusion schemes shown as $\sqrt{\text{scan rate}}$ vs current for various electrode areas. Black = 1.0 cm^2; Red = 0.5 cm^2; Blue = 0.25 cm^2.

kept, while the large number provides similar total surface areas, and consequentially similar currents, to macroelectrodes.

A different use of electrode arrays, is with the creation of multi-functionalised arrays. This type of array is of great interest in biosensing applications as multiple tests can be performed on a single biosensing chip. Additionally, differential electrode measurements can be taken in which a functionalised and a non-functionalised electrode response is recorded and subtracted leaving only the specific signal of the functionalised response. This provides a sort of on chip control which can be of great use if the system is sensitive to environmental factors or experiences problematic noise-to-signal ratios. Redundant electrodes can also be included to allow for failure of some electrodes or on-chip replicates.

An interesting consequence of forming arrays of microelectrodes is that, depending on the spacing said electrodes, their diffusion layers may overlap. If this overlap were to occur to a large enough extent the diffusion layer of the array begins to resemble that of an electrode with a planar diffusion scheme as shown in Figure 2.14[Chailapakul and Crooks, 1995].

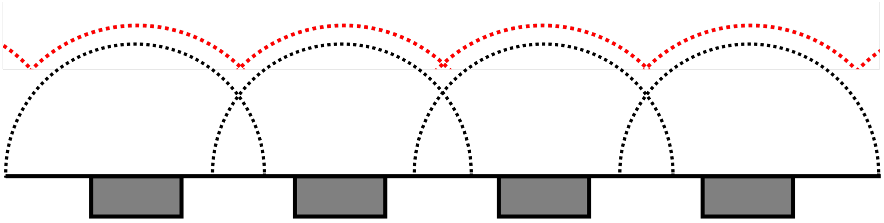

Figure 2.14: A series of microelectrodes in an array. Black dotted line indicates the radial diffusion layer of individual microdisc electrodes; red dotted line indicates the diffusion layer of the array.

2.3 IonGate SURFE2R/Solid Supported Membrane Electrophysiology

The IonGate SURFE^{2}R Workstation is a commercially available instrument developed in conjunction with Klaus Fendler's group at the Max Planck Institute for Biophysics in Main, Germany. The instrument combines the stability of solid support membranes, with the sensitivity of electrophysiological measurements. Thus far, the technology has been used by Fendler's group, and collaborators, to study a number of ion pumps and transporters from both bacterial [Burzik et al., 2003; Meyer-Lipp et al., 2004; Raunser et al., 2006; Zhou et al., 2004; Zuber et al., 2005] and eukaryotic [Pintschovius and Fendler, 1999; Tadini-Buoninsegni et al., 2006] expression systems, as well as ion channels[Schulz et al., 2009].

Figure 2.15: IonGate workstation

The system utilises a hybrid bilayer lipid membrane (hBLM) of diphytanoyl-phosphatidylcholine (DPhyPC) and octadecylamine, supported on a self-assembled monolayer (SAM) of octadecanethiol (ODT). To this a membrane protein preparation is added, usually either as proteoliposomes or membrane fragments. A number of proteins from different sources have been studied, each of which has required a certain amount of optimisation. Some of these are summarised in Table 2.2.

The technique relies on a principle called capacitative coupling, in which the DPhyPC hBLM and the membrane protein preparation form a compound membrane which can be

Protein	**Preparation**	**Orientation**	**Reference**
NaK-ATPase (pig/*Sus scrofa domesticus*)	Enriched membrane fragments from kidney	Inside-out	[Pintschovius and Fendler, 1999]
Ca-ATPase (rabbit/*Oryctolagus cuniculus*)	Sarcoplasmic reticulum vesicles	Rightside-out	[Bartolommei et al., 2004]
Nicotinic acetylcholine receptor (*Torpedo californica*)	Enriched membrane vesicles from electric organ	Rightside-out	[Schulz et al., 2009]
$P2X_2$; ATP receptor (rat/*Rattus rattus*)	Plasma membrane vesicles from HEK cells	Unknown	[Schulz et al., 2009]
MelB; melibose permease (*Escherichia coli*)	Proteoliposomes	Inside-out	[Jung et al., 1998]
PutP; Na/proline carrier (*Escherichia coli*)	Proteoliposomes	Inside-out	[Zhou et al., 2004]
NhaA; Na/H-exchanger (*Escherichia coli*)	Proteoliposomes Membrane vesicles	Rightside-out Inside-out	[Zuber et al., 2005] [Zuber et al., 2005]
Glt; aspartate transporter (*Pyrococcus horicoshii*)	Proteoliposomes	Unknown	[Raunser et al., 2006]
mEAAC1; glutamate transporter (mouse/*Mus musculus*)	Heterologous expression CHO cells	Predominantly rightside-out	
YdgR; peptide transporter (*Escherichia coli*)	Proteoliposomes	Rightside-out	[Weitz et al., 2007]
hNCX1; Ca/H exchanger (*Homo sapiens*)	Heterologous expression CHO cells	Unknown	[Geibel et al., 2006]

Table 2.2: Membrane protein preparations studied with the IonGate system. Adapted from [Schulz et al., 2008].

modelled using the equivalent circuit shown in Figure 2.16. While the figure presents a compound membrane formed with a membrane fragment, the same equivalent circuit can be applied to adsorbed proteoliposomes. The equivalent circuit presented involves two (RC) elements in series, (R_vC_v) and (R_mC_m), representing the membrane protein sample and the underlying hBLM respectively. Additionally, another component exists within the membrane protein circuit - a resistance (R_c) that represents the flow of ions through the ion channel itself.

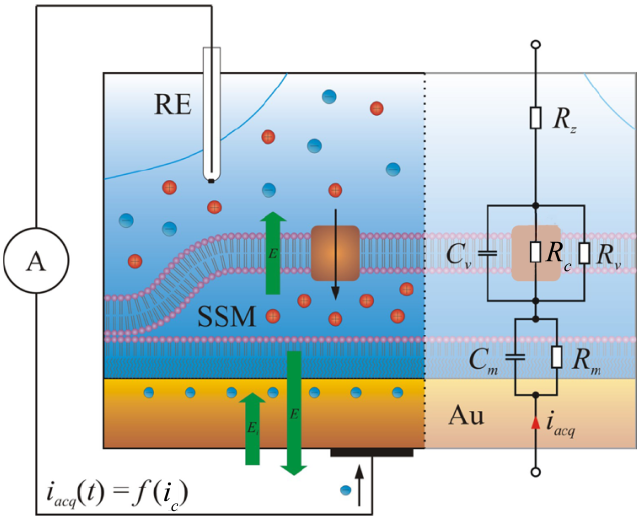

Figure 2.16: The basis of IonGate. Membrane protein preparations, either as membrane fragments or proteoliposomes, are adsorbed onto a solid supported membrane. Membrane proteins in the upper membrane allow controlled ion transport

This technique has been applied to two types of membrane protein - ion pumps and ion channels. In both cases the extracellular solution is replaced with one containing different concentrations of ions, and other chemicals, in order to illicit a response. This changing of the extracellular concentration disrupts the Nernst equilibrium (Equation 1.1) to create a transmembrane potential that can drive ion transport until the equilibrium is reestablished.

2.3.1 Ion Pumps in IonGate

The majority of work done with the IonGate apparatus, and other solid supported membrane electrophysiology setups, has focused on active transporters that are capable of transporting up a concentration gradient. The rate of transport that is exhibited can be represented by a time constant, τ_0, which can be calculated from the equivalent circuit parameters as shown in Equation 2.21.

$$\tau_0 = \frac{C_m + C_v}{G_m + G_v} \tag{2.21}$$

where τ_0 is the time constant, C_m is the capacitance of the hBLM, C_v is the capacitance of the membrane fragment or proteoliposome, G_m is the conductance of the hBLM (the reciprocal of the hBLM's resistance), and G_v is the leak conductance of the membrane fragment or proteoliposome.

Unlike with EIS where the entire circuit is considered, the IonGate system focuses largely on the capacitative charging current experienced at the hBLM. The translation of the current passing through the membrane protein to the charging current experienced at the hBLM can be seen in Figure 2.17. On the left of the figure, we see a transient pump current that has a time constant smaller than the system time constant, τ_0. In real terms this translates to the ion pump activating and pumping ions into the vesicle causing a spike in the measured current. The pump then deactivates and the ions begin to leak back out of the vesicle, resulting in a negative current being recorded. It is worth noting that the amplitude of the current measured at the hBLM is similar to that passing through the ion pump.

On the right of Figure 2.17, a pump current that is stationary and prolonged is shown. The measured current peaks initially as in the left hand figure, but decays over a longer period of time as the leaking ions are replaced giving a sustained response. To maintain the set electrode potential, a current is measured through the electrical circuit components.

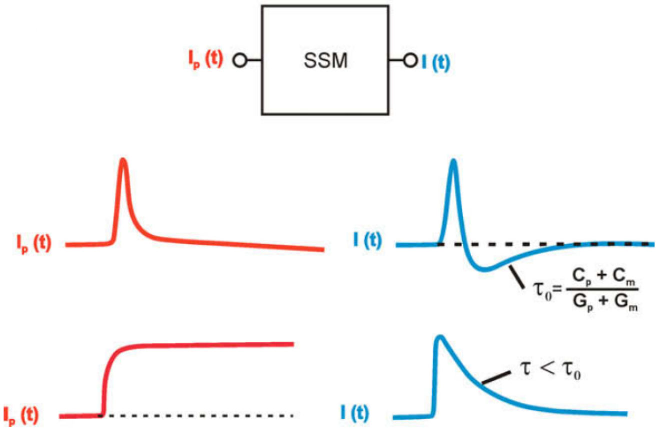

Figure 2.17: IonGate current response. How pump current, $I_p(t)$ in red, relates to the current measured on the hBLM, $I(t)$ in blue.

2.3.2 Ion Channels in IonGate

While ion transporters are capable of transporting ions against an ionic gradient, ion channels are only capable of faciliating diffusion across the lipid bilayer. Furthermore, as there is no control over a driving membrane potential as with traditional electrophysiology experiments such as patch clamp, an ionic gradient is required to generate a current. Schulz et al. [2009] studied gramicidin, the nicotinic acetylcholine receptor (nAChR), and the $P2X_2$ receptor using this approach.

The data for the gramicidin experiment are shown in Figure 2.18. Figure 2.18a shows the full time course of the experiment where the vesicles are bathed in the impermeant cation *n*-methylglucamide (NMG^+), before exchanging for K^+. As can be seen a very clear spike in current of approximately 3.5 nA is recorded. Figure 2.18b shows the response to other permeant cations, which exhibit a smaller response, but similar time constants.

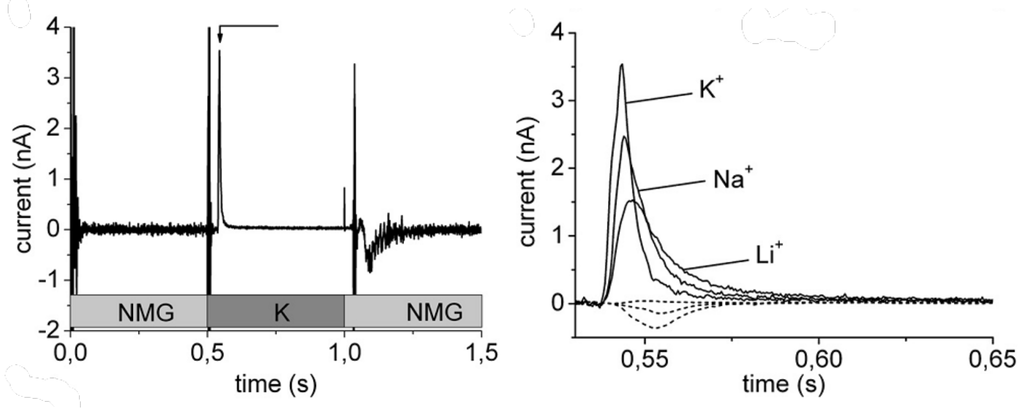

(a) (b)

Figure 2.18: IonGate measurements with gramicidin[Schulz et al., 2009].

These data indicate that the IonGate system can detect currents that are created with an ionic gradient. In the case of gramicidin, a sustained response is given which decays with the ionic gradient. No negative component is observed as there can be no excess of ions at the hBLM, only an equilibrium, and as such only an influx of electrons to the electrode is recorded.

Figure 2.19 shows data for nAChR activity. The red plot indicates Na^+ transport activated by addition of 100 μM carbamylcholine (CCh), nAChR's ligand. The orange plot shows addition of α-bungarotoxin, a nAChR inhibitor, to reduce current amplitude to near baseline. For comparison, plots for no ionic gradient (green) and no protein (blue) have also been included in Figure 2.19. As can be seen the lack of an ionic gradient results in a similar response to inhibition of the ion channel, while absence of the ion channel results in no signal at all. This shows that IonGate can also show a difference in activity with adjustment of the ionic gradient, or the addition of an inhibitor.

2.4 Atomic Force Microscopy (AFM)

The atomic force microscope (AFM) is a high resolution imaging instrument capable of measuring features as small as a fraction of a nm, greatly surpassing the limits of an optical microscope. It was developed from an earlier nanoscale imagine instrument known as a scanning tunnelling microscope (STM), both developed by Binnig and collaborators in the 1980s[Binnig et al., 1986]. The AFM utilises a microfabricated cantilever with a sharp point on a tip (Figure 2.20). This tip, or probe, is brought within extreme proximity to the

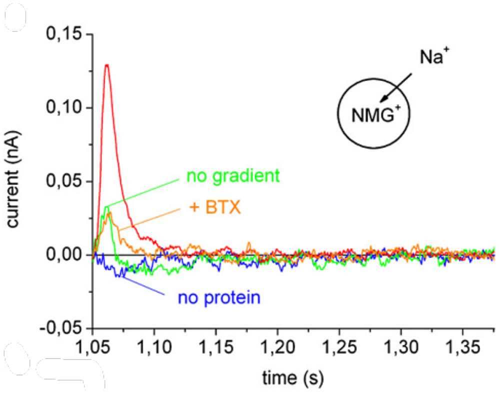

Figure 2.19: IonGate measurements with nAChR[Schulz et al., 2009]

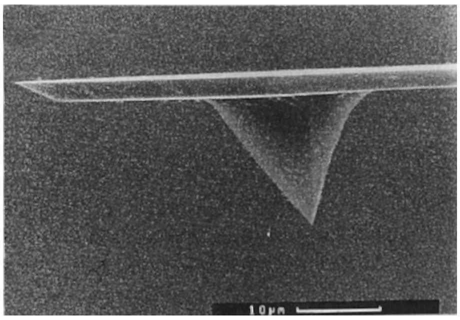

Figure 2.20: AFM cantilever tip viewed in a scanning electron microscope[Magonov and Whangbo, 1996]

sample's surface and leading to the cantilever experiencing deformation due to repulsive forces, as described by Hooke's law:

$$F = -kx \tag{2.22}$$

where F is the force exerted, k is the spring constant of the cantilever and x is the distance the cantilever has been deflected.

A number of forces are experienced here including Van der Waals forces, mechanical contact forces (Pauli exclusion) and electrostatic forces. Other forces may be intentionally studied using specific probes, such as magnetic forces. The extent to which the cantilever has been deflected is measured using a laser reflected off the top of the cantilever to a directional photodiode, Figure 2.4. These measurements are part of a feedback mechanism that adjusts the tip-sample distance, in order to prevent the tip and sample from colliding and damaging each other. The tip-sample distance is modified using a piezoelectric platform moving in the z-axis. The platform can also be moved in x and y-axes to enable scanning of the sample surface.

There are several imaging modes for the AFM, which can broadly be defined as contact or non-contact. Contact mode was used in this project for imaging of electrode surfaces (see Chapter 3). In this mode, the tip touches the sample's surface with a constant force, by maintaining a constant deflection. As such the AFM image obtained is a map

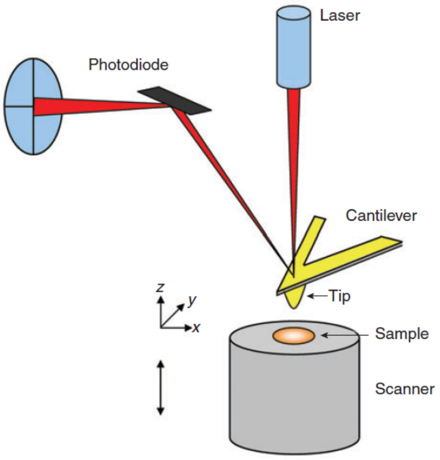

Figure 2.21: A diagram showing the workings of an atomic force microscope (AFM)[Hinterdorfer and Dufrene, 2006]

.

of the surface based on the movements of the platform in the z-axis. Non-contact, or dynamic, modes are more complex. Here the cantilever is oscillated at its resonance frequency and tip-sample interactions cause variations the oscillation amplitude, phase and frequency. Another common method is tapping mode in which the cantilever tip is oscillated with an amplitude of a couple of hundred nm. Tip-sample interactions decrease this amplitude. Tapping mode is similar to contact mode, but has the advantage that in tapping the surface rather than dragging the tip across the surface there is very little surface damage. As such this method is suitable for the imaging of softer samples such as sBLMs or polymers[Jeuken, 2008; Jeuken et al., 2007b].

2.5 Surface Plasmon Resonance (SPR)

Surface plasmons of metallic surfaces can be excited by light if the impulse of the light is matched to that of surface plasmons. This can be done by reflecting a beam of p-polarised light from the back of a crystal (see Figure 2.22). When polarised light inside a prism reflects from a side of the prism above a critical angle, total internal reflection occurs, causing all the light to be reflected back. This generates an evanescent field, which is strongest at the reflective surface. When a metal layer is present, and the energy of the evanescent field matches that of the surface plasmons, the free electrons become excited producing wave-like oscillations, referred to as surface plasmon resonance. When this occurs a drop in the intensity of the reflected light is observed. This is due to energy transfer from the light to the surface plasmon. By rotating the p-polarised light through a range of angles an intensity curve can be plotted, the minima of which correlates with the resonance angle (see Figure 2.23).

SPR is very sensitive to the surface conditions within 200 nm of the metal film,[Sigal et al., 1997] such that it can be used to detect minute alterations on the surface, such

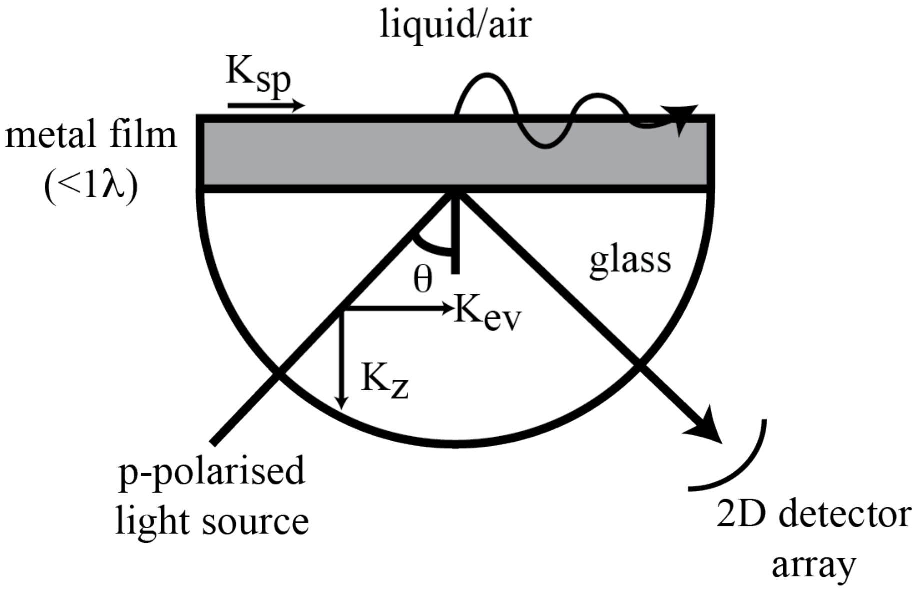

Figure 2.22: Surface plasmon resonance[Green et al., 2000].

as the adsorption of lipid vesicles or formation of a self-assembled monolayer. When this occurs the resonance angle shifts by a fraction of a degree. By tracking the resonance angle as surface conditions change the shift in resonance angle can be measured against time (see Figure 2.23a). This allows processes occurring at the surface to be monitored.

A typical experiment consists of several stages as can be seen in Figure 2.23b. The experiment starts with a baselining period, which allows the system to stabilise and changes in response to be accurately analysed later. The sample would then be added and an association phase would occur. A comparatively large change in the resonance angle would be expected here as the sample binds to the surface of the metal film. This includes both specific and non-specific binding. To remove any material that may be non-specifically bound the sample is then rinsed in a dissociation phase, resulting in a drop in the resonance angle back towards the starting angle. This dissociation usually occurs in two phases, an initial rapid dissociation of non-specifically bound material and a slower secondary dissociation as specifically bound material begins to come off the surface. The difference between the resonance angle during the baselining phase and after the rapid dissociation is termed ΔR, and can be used to calculate the amount of material on the surface.

As there is a linear relationship between the amount of deposited material and the shift of the resonance angle, details such as the thickness of deposited material and rate of deposition can be determined. This is done via the use of modelling programs based on the refractive index of the deposited material. The lipid 1,20dipalmitoyl-*sn*-glycero-3-phosphate (DPPC), for example, has a refractive index of 1.49, where as water has a refractive index of 1.33.

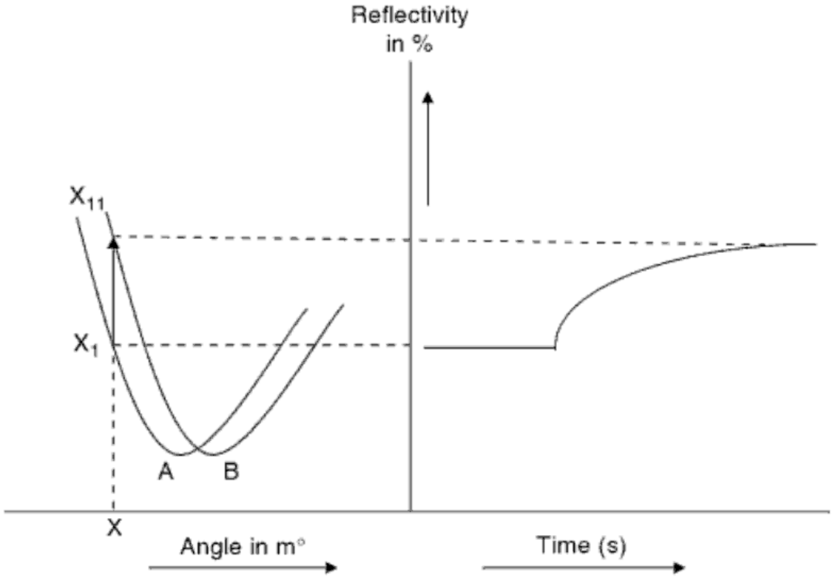

(a) Translating the shift in resonance angle into a time plot.

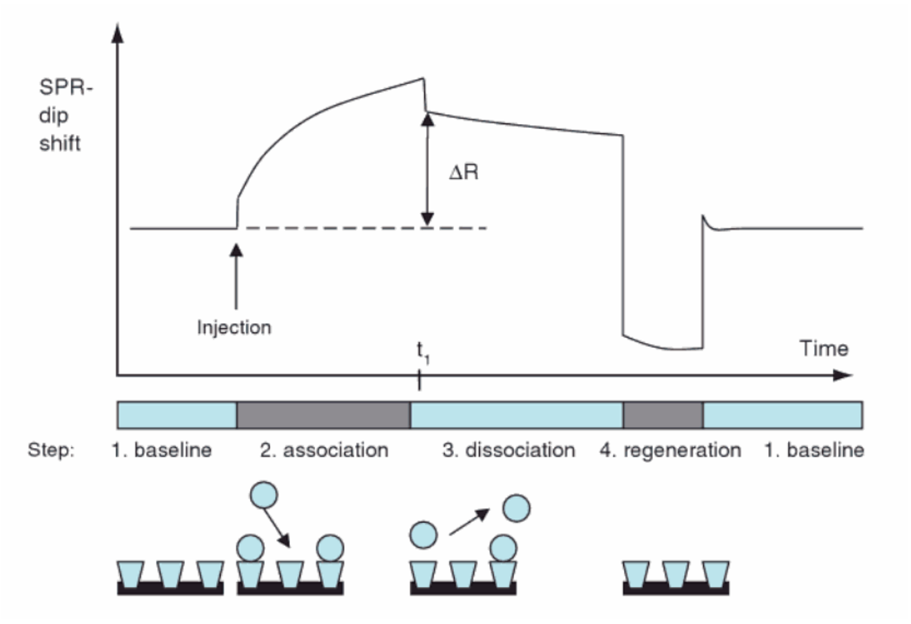

(b) An example experiment showing the change in resonance angle against the time course of the experiment. The association and dissociation of the analyte can be followed and the shift from baseline following a washing step can be used to calculate the quantity of material bound to the surface.

Figure 2.23: Surface plasmon resonance. (a) Diagram showing how the resonance angle translates into a time plot. (b) A time plot showing the changing behaviour of the surface throughout the experiment[Schasfoort and Tudos, 2008].

2.6 Electron Spectroscopy

Electron spectroscopy involves the study of low energy electrons (20–2000 eV) that have been liberated from a sample following its irradiation. The energy of the liberated electron is specific to the electron orbital and element it came from, such that an electron from the innermost orbital of an oxygen atom would have a different energy to an electron from the innermost orbital from a nitrogen atom, or the next closest orbital from the same oxygen atom. This is one of the fundamental principles of electron spectroscopy and allows a range of information to be collected depending on the specific method being used. There are several techniques that use these principles in different ways. Those used here include X-ray Photoemission Spectroscopy (XPS) and Auger Emission Spectroscopy (AES)/Scanning Auger Microscopy (SAM, here referred to as Scanning Auger Electron Spectroscopy, SAES, to avoid confusion with Self-Assembled Monolayers). However others include Ultraviolet Photoemission Spectroscopy (UPS), Electron Energy Loss Spectroscopy (EELS) and High Resolution Electron Energy Loss Spectroscopy (HREELS).

A basic electron spectroscopy set-up will include a primary radiation source, a means to focus the radiation and an electron analyser. These experiments need to be performed under vacuum, and more often than not are usually housed under Ultra-High Vacuum (UHV) conditions, with a secondary UHV chamber to load the sample into. Specialist software is usually provided as well for detailed analysis of the collected data. XPS and AES use different radiation sources - soft X-rays and electron guns respectively, but otherwise the experimental set-up is very similar such that they are often combined into a single instrument.

2.6.1 Electron Notation

Electron spectroscopy is used to determine the character of emitted electrons. In order to describe the electrons being studied, a system is required for their naming. There are two commonly used notation systems in electron spectroscopy: spectroscopist's or chemist's notation as used in XPS and X-ray notation used for the Auger electrons studied with AES.

Spectroscopist's Notation

Spectroscopic notation refers to electrons by their quantum numbers in the form of nl_j - the orbital the electron is in (n), its angular momentum quantum number within the orbital (l), and the spin of the electron ($_j$). Each of these properties is assigned a quantum number.

The orbital, or principle number, of the electron (n) relates to regions, or shells, in which there is a high probability of electrons existing. These shells can be thought of as electron clouds that surround the nucleus, much like the layers of atmosphere around a planet. As the value of n increases the electron shells are found further away from the

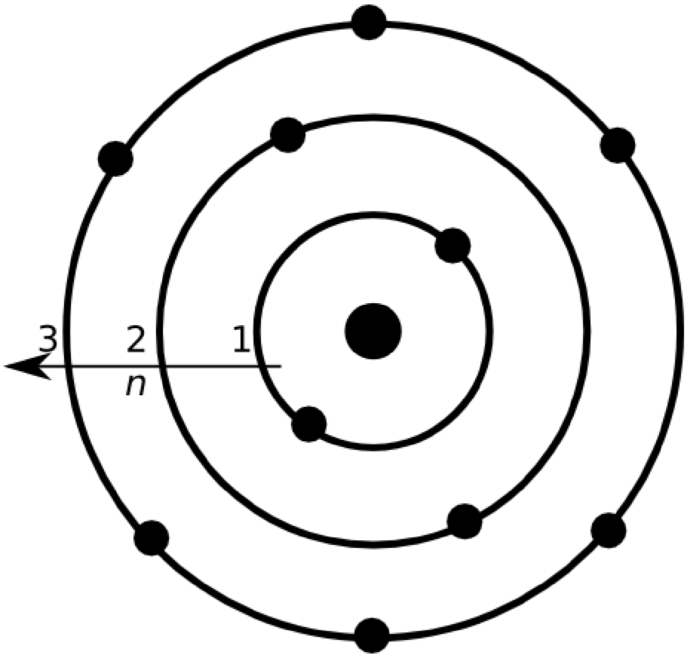

Figure 2.24: Diagram of electron orbitals. Central black dot represents the nucleus, while concentric circles represent electron orbitals and the black dots on them represent electrons. As demonstrated by the arrow, the principle number of the electron (n) increases with distance from the nucleus.

nucleus, and begin to get closer together. This is concept is demonstrated in Figure 2.24.

Within each of these orbitals, there exist sub-shells which describe the angular momentum of the electrons within the orbital. These are also assigned numbers, but are more commonly referred to by letters as can be seen in Figure 2.25 and form the l part of the spectroscopic notation. The s orbital has a quantum number of 0, while the next orbital, p, has a quantum number of 1, d orbitals are 2, etc.

Each electron has a number associated with its spin quantum number, s^2, where s can be $+1/2$ or $-1/2$. The notation for the electron's spin, $_j$, is obtained by combining the angular momenta of the electron, s, and the orbital, l, such that $_j = |l + s|$. For example, an electron in a p orbital has an orbital angular momentum (l) of 1 and can have an electron angular momentum (spin, s) of $-1/2$ or $+1/2$. Thus, $_j$ in this case takes the value of $1/2 = (1 + (-1/2))$ or $3/2 = (1 + (+1/2))$. Electrons in a d orbital have an orbital angular momentum of 2, giving a $_j$ value of 3/2 or 5/2. Putting these various components together we get descriptions of electrons including $1s_{1/2}$, $2p_{3/2}$ and $3d_{5/2}$. The construction of these descriptions can be better seen in Table 2.3.

Where the angular momentum number is greater than 0 and multiple electrons are produced for each orbital, the peaks often appear in pairs. The separation and relative intensities of these peaks doublets varies on the origin of the electrons. The expression (2_j+1) gives the relative intensity of a peak - for example, the p orbital electrons discussed previously would have intensities of 2 and 4, giving a 1:2 peak ratio whereas a d orbital doublet would have a 2:3 ratio. The spacing between these peak increases with atomic

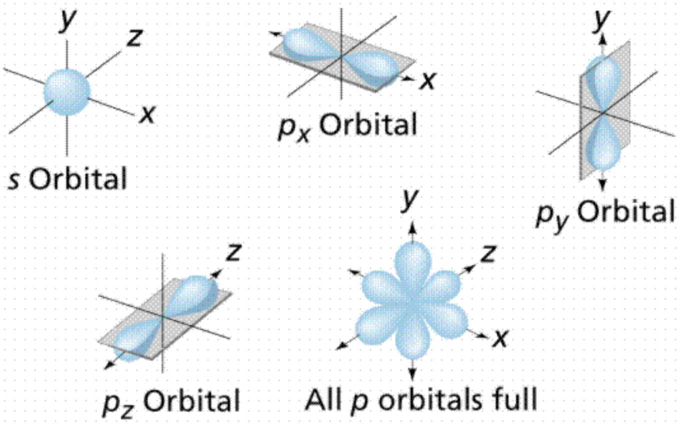

Figure 2.25: Diagram of electron sub-orbitals. Multiple 'bubbles' exist in which there is a very high probability that electrons can be found. These bubbles exist in different orientations and are referred to by the angular momentum of the electrons (l).

Quantum numbers				Spectroscopist's	X-ray
n	l	s	j	notation	notation
1	0	+1/2, −1/2	1/2	$1s_{1/2}$	K
2	0	+1/2, −1/2	1/2	$2s_{1/2}$	L_1
2	1	+1/2	1/2	$2p_{1/2}$	L_2
2	1	−1/2	3/2	$2p_{3/2}$	L_3
3	0	+1/2, −1/2	1/2	$3s_{1/2}$	M_1
3	1	+1/2	1/2	$3p_{1/2}$	M_2
3	1	−1/2	3/2	$3p_{3/2}$	M_3
3	2	+1/2	3/2	$3d_{3/2}$	M_4
3	2	−1/2	5/2	$3d_{5/2}$	M_5
					etc.

Table 2.3: The relationship between quantum numbers, spectroscopist's notation and X-ray notation. Taken from Watts and Wolstenholme [2003].

number for given values of n and l, but conversely decreases with increasing n and l numbers for a given atomic number. As such some spin coupled electrons with high n and l values appear as a singlet due to the narrow spacing.

X-ray Notation

While spectroscopic notation breaks down an electron's character into three parts (nl_j), X-ray notation utilises a two part system. Here the principle number of the electron orbital is represented by a letter instead of a number starting with K for 1, L for 2, and so on. The angular momenta of the orbital sub-shell (l) and the electron ($_j$) are numbered sequentially for each principle number, such that for where $n = 2$ possible combinations in spectroscopic notation include $2s_{1/2}$, $2p_{1/2}$ and $2p_{3/2}$, which would translate into X-ray notation as L_1, L_2 and L_3 respectively. Further examples can be seen in Table 2.3.

2.6.2 X-Ray Photoemission Spectroscopy (XPS)

X-ray photoelectron spectroscopy (XPS) provides detailed information about the chemical state of a sample surface via the study of ejected low energy (20-2000 eV) electrons. Through detailed analysis of the spectra, the electronic configurations of the sample's atoms can be determined, chemical environments and empirical formulae estimated.

To liberate these electrons, X-rays are fired at the sample surface. These X-rays are emitted from an X-ray source, usually a magnesium or aluminium anode, by bombarding it with high energy electrons, often from a thermal source such as a heated tungsten filament. These X-ray photons are focused on the sample, using a series of lenses, leading to one of three outcomes:

1. The photon passes through the sample without interaction.
2. The photon is scattered by an electron, resulting in partial loss of energy.
3. The photon interacts with an electron in an atomic orbital, completely transferring its energy to the electron and resulting in the emission of the electron from the atom.

The first case results in no electrons being emitted and is therefore undetectable by XPS, while the the second is referred to as Compton scattering and is not of interest here. It is this third outcome that we are primarily interested in. However for emission of the electron to occur, the energy of the photon must exceed that of the electron.

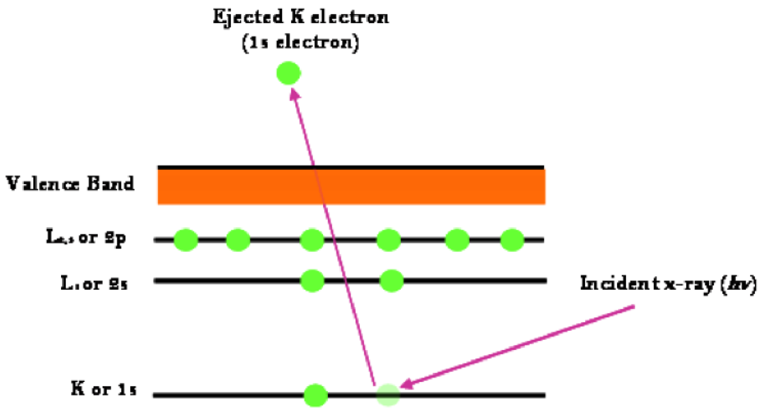

Figure 2.26: The principle of X-ray photoemission spectroscopy. An X-ray, $h\nu$, excites an electron resulting in the electron being ejected from the atom. This electron's binding energy can be determined to extract information about the chemical state of the atom it originated from.

Ejected electrons will take many different ejection trajectories with some progressing further into the sample, and some being ejected back out of the sample. These backscattered electrons are captured and their kinetic energy measured by the electron analyser.

This is then used to calculate the binding energy of the electron used instead using Equation 2.23, where E_B is the binding energy of the electron, $h \cdot \nu$ is the energy of the X-ray photon, E_K is the kinetic energy of the emitted electron and W is the work function of the spectrometer[Watts and Wolstenholme, 2003].

$$E_B = h \cdot \nu - E_K - W \tag{2.23}$$

The binding energy of the electron is used over the kinetic energy due to the difference in kinetic energy observed, for a given electron, between different X-ray sources. By referring to binding energies, the X-ray source used can be largely ignored when analysing data.

The obtained spectra are plotted as the binding energies of the measured electrons against the number measured at that particular energy. Figure 2.27 shows a high resolution scan of the C 1s peak from the XPS spectra for poly(methylmethacrylate) (PMMA) using a monochromatic AlKα X-ray source[Beamson and Briggs, 1992]. This peak does not fit the shape expected of a simple peak (a Gaussian-lorentzian mixture, where the physical lineshape is lorentzian but multiplied by a Gaussian due to broadening by the instrument), but instead hosts a ‘shoulder’ at 287 eV. By using peak fitting software, this peak can be deconvoluted into peaks 1, 2, 3 and 4. These peaks can now be analysed in their own rights and the chemical state of each determined. By comparing the binding energy of these peaks with reference values, the chemical environments can be assigned. Peak 1 has a binding energy of 285 eV, which corresponds to aliphatic carbon groups. Peak 3 has a binding energy of 286.8 eV, which corresponds to a carbon engaged in an ether bond. Peak 4 has a binding energy of 289.2 eV representing a carboxyl carbon, and peak 2 (285.8 eV) is an aliphatic carbon that has been affected by the adjacent carboxyl group. The assigned chemical environments of these peaks can be seen in the structure of PMMA in Figure 2.27.

2.6.3 Auger Emission Spectroscopy (AES)

Auger emission spectroscopy (AES) operates on similar principles to XPS - electrons are ejected and their kinetic energies are recorded to provide us with information. There are two major differences between XPS and AES however - AES uses electrons instead of X-rays as the primary radiation source, and instead of measuring the electrons that the radiation source interacts with, secondary Auger electrons are measured.

Auger electrons are emitted during the Auger process (Figure 2.28). This is when a core electron is ejected, in this case due to the interaction with an electron from the primary radiation source, leaving a vacancy. This is vacancy is energetically unfavourable and so an electron from a higher energy orbital drops down into it. This leads to the release of energy in the form of an Auger electron, although the energy can also be released as an X-ray photon.

Unlike the secondary electrons measured in XPS, the kinetic energy of Auger electrons

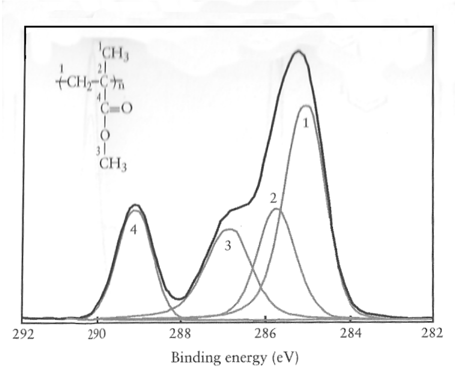

Figure 2.27: The C 1s peak from X-ray photoemission spectrum of poly(methylmethacrylate) (PMMA). The binding energies of the electrons are recorded on the x-axis with the number of electrons of that energy recorded on the y-axis. Each element has characteristic peaks that allow their identification, much like a fingerprint. Additionally, these peaks can be altered slightly dependent on the chemical environment. In this example, we find that there are two main peaks, each of which should have a Gaussian shape. The peak at 286 eV has a distinct shoulder at 287 eV. Peak fitting algorithms allow four peaks to be resolved and assigned to the structure of PMMA shown above. Taken from Beamson and Briggs [1992].

is characteristic of their orbitals regardless of the primary electron source used. As such Auger emission spectra are plotted against the kinetic, rather than binding, energy of the electrons measured.

One of the great advantages of AES is the high spatial resolution available. This is due to the ability to produce a highly focused electron beam with a cross-section of as little as 10 nm when using a field electron gun in conjunction with electromagnetic lenses[Watts and Wolstenholme, 2003]. This high spatial resolution allows detailed contrast mapped images of the sample surface to be made that are comprised of point measurements. These point measurements cover an area of the Auger spectrum that contain a peak for the element of interest, as well as an area of background counts. These measurements are then compared to produce a series of graded pixels, the brightest of which have the greatest difference between peak (P) and background (B), and the darkest have the smallest difference. These measurements are affected by the topography of the sample surface, however by normalising the data using the formula (P-B)/(P+B) the effect can be minimised.

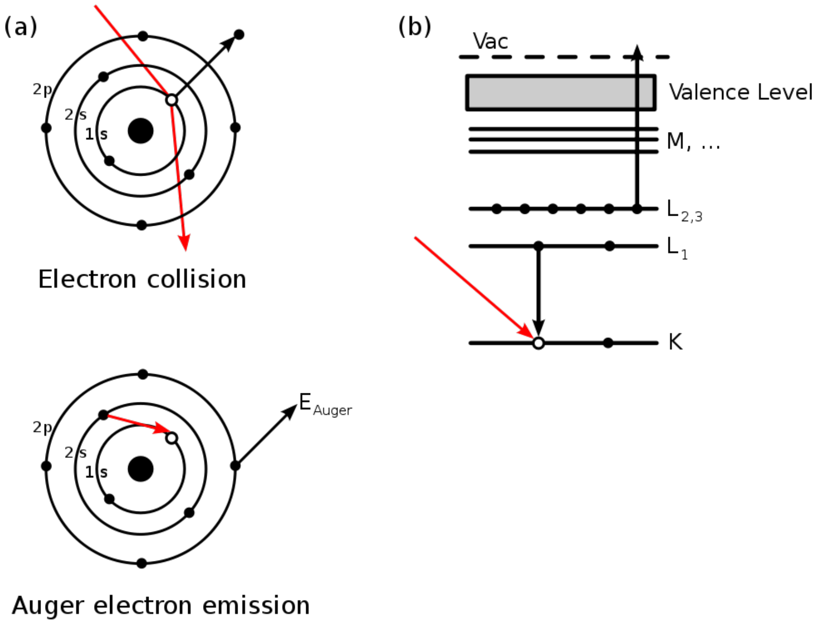

Figure 2.28: The principle of Auger emission spectroscopy. (a) An incident electron interacts with a core electron resulting in its ejection from the orbital. (b) An electron fills the vacant position by 'dropping down' from a higher level valency orbital. To balance the atom's electronic configuration another electron is ejected. This electron is referred to as an Auger electron.

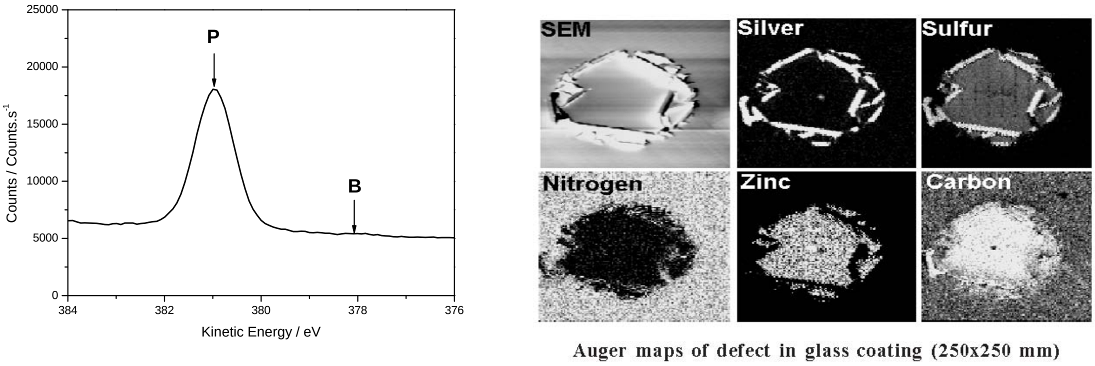

(a) Peak and Background

(b) Auger Contrast Map

Figure 2.29: Scanning Auger Electron Spectroscopy contrast maps. (a) Auger contrast maps are formed by comparing the peak (P) and background (B) regions shown. (b) Different kinetic energies can be mapped to image the atomic composition of the surface. Various contrast map modes are available, but by using the (P-B)/(P+B) algorithm topological features are eliminated.

2.7 Scanning Electron Microscopy (SEM)

The same principles that electron spectroscopy is based upon can be used to produce topographical images of a specimen's surface from backscattered electrons produced via interactions with an electron beam. An electron gun is used to produce an electron beam, which is then focused by a series of electromagnetic lenses allowing beam spot sizes as small as 1-2 nm. These same lenses can be used to deflect the beam in the x and y axes, allowing the surface to be scanned in a raster fashion (line by line). The beam electrons interact with the sample as described below, with a number of scattered and ejected electrons being collected by an electron detector. The raster scanning of the electron beam is synchronised with an image renderer (typically a cathode ray tube) that builds an image of the surface with the number of electrons detected increasing the image brightness. There are a number of electron detectors but the most common is the Everhart-Thornley detector, a scintillator-photomultipler system.

The manner in which the beam electrons interact with the sample can be broadly grouped under two headings - elastic or inelastic scattering. Elastic scattering, also known as Rutherford scattering, occurs due to the interaction of the electrostatic charges on both the electron in question and the sample's protons and electrons. The degree of deflection is influenced by the atomic number of the atom and the energy of the interacting electron, such that a larger atomic number will exert a greater effect, but a more energetic electron will be affected less. In general, it is found that smaller angles of deflection are far more likely than larger angles because of this.

Inelastic scattering is a rather general term describing any process that results in the loss of a measurable amount of energy from the electron, usually at least 0.1 eV. While there are several processes that could result in the loss of electron energy to the sample, there are three of particular importance.

- Phonon scattering - occurs when an electron transfers some of its kinetic energy into the vibrational energy of the interacting atom by exciting a phonon, the quanta of elastic waves. This results in the sample being heated. Only small amounts of energy, less than 1 eV on average, are transferred and the resultant scatter is generally around 10°.

- Plasmon scattering - by exciting a plasmon in the 'sea of electrons' of the metal conductance band (as described for surface plasmon resonance on page 59), or the bonding electrons of non-metals, the electron will lose between 5 and 30 eV of its energy. This type of scattering is common and accounts for a large proportion of the energy lost.

- Inner shell excitation - describes the rare case when a primary electron interacts with an inner (1st or 2nd) shell electron, causing that electron to be ejected from the shell. The amount of energy transferred varies depending on the atom and the shell from which the electron is ejected, but a 2nd shell electron from carbon can require approximately 283 eV, while the same electron from tungsten may require in excess of 69000 eV. For this event to occur the primary electron must have more kinetic energy than the binding energy of the inner shell electron, and as such is rarer as atomic number increases. In addition to the affect that the interaction has on the primary electron, the atom that has been excited needs to relax back to its ground state. This occurs by a valence electron filling the inner shell position, and the excess energy being liberated. This liberation of energy occurs via one of two events - the emission of an X-ray, or the ejection of an Auger electron (see Section 2.6.3).

These processes affect the kinetic energies and trajectories of the beam electrons, and can liberate additional electrons from the sample in the case of inner shell excitation. These electrons are classified into three groups - backscattered electrons, secondary electrons, and absorbed electrons.

- Absorbed electrons are those that are not picked up by the electron detector. This can be due to them having lost all their energy within the sample and thus their energy being absorbed, or alternatively by exiting the sample with a trajectory that precludes them from reaching the electron detector.
- Secondary electrons are the most abundant form of detected electrons, and are arbitrarily defined as those electrons that have an energy of less than 50 eV. They can include primary electrons that have had much of their energy transferred, or alternatively be electrons liberated following the processes that have been discussed above.
- Backscattered electrons are less abundant than secondary electrons and are of higher energy. More often than not they are primary electrons that have had their trajectories altered via scattering events such that they exit the sample before they lose the majority of their kinetic energy.

The nature of these interactions means that the volume within which electrons interact is far larger than the area of the beam spot as can be seen in Figure 2.30. The most pertinent factors in this regard include the penetrating nature of the electrons, the large number of scattering events that occur and the varying degrees to which these events can scatter the electrons. While the precise volume is highly dependent on the composition of the sample and the energy of the beam electrons, it is not unusual for a 1 nm beam spot to give an interaction volume in the order of 1 μm^3. This constitutes a huge increase over the perceived interrogation volume of a few nm^3, and as a result makes the real resolution of images captured far less than the assumed nm-scale resolution. Despite this electron microscopy offers a significant improvement over the resolution of conventional light microscopy techniques, as can be seen in Figure 2.31.

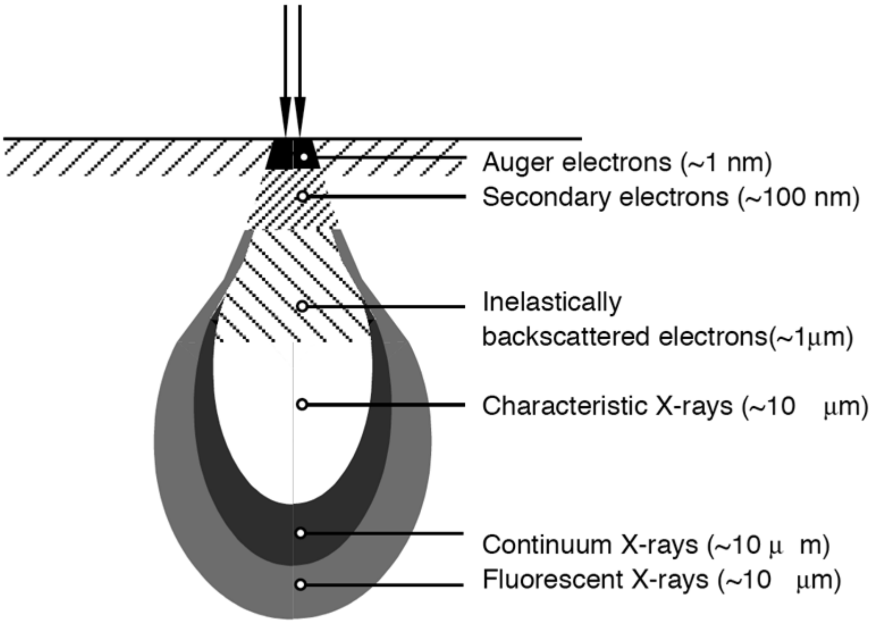

Figure 2.30: The interaction volume of beam electrons[SEM]

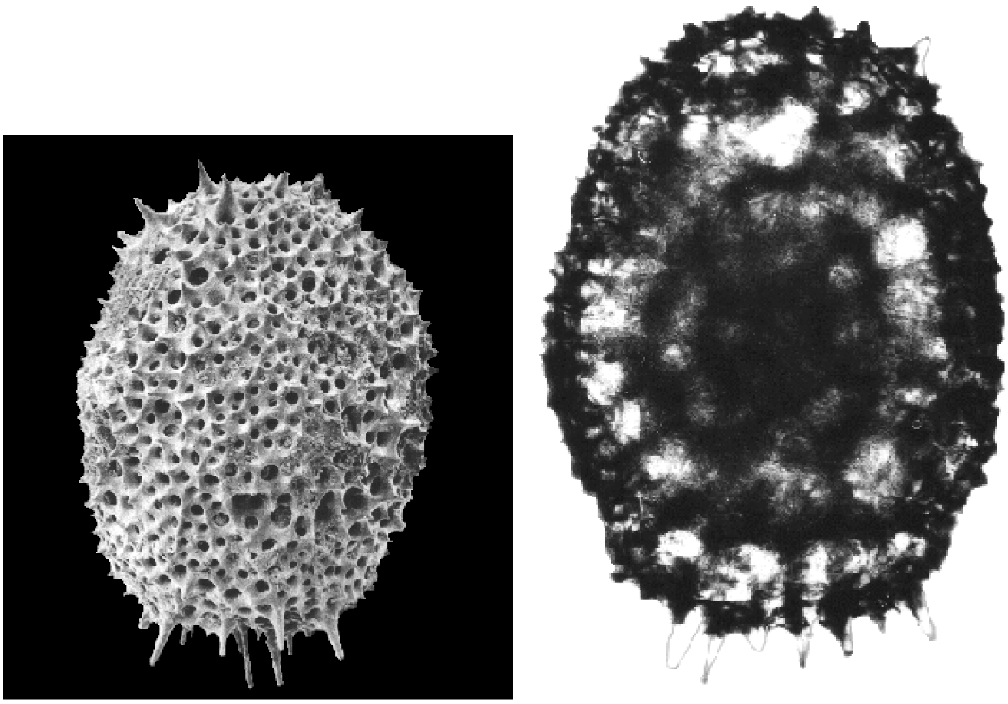

(a) (b)

Figure 2.31: A comparison of electron and light microscopy images taken of a protozoa, *Larcopyle butschlii*. SEM (left) gives a far higher resolution than light microscopy (right)[Boltovskoy, 1981; Boltovskoy et al., 1983].

Chapter 3

Characterisation and Development of Patterned Electrodes for Use in the Study of Tethered Bilayer Lipid Membranes

3.1 Introduction

To develop a platform for tBLMs containing ion channels, one requires an electrode to build them on. In order for the tBLM to be of sufficient quality to be able to detect ion transport processes several characteristics need investigating including surface roughness, surface composition, and surface cleanliness. While similar studies have been performed in the past, and found template stripped gold (TSG) to be an excellent surface, the development of a patterned electrode that could be manufactured and be used in an array format was desirable. Together with Philips Research, three series of patterned Au electrodes have been designed for the formation of tethered bilayer lipid membranes. In this chapter, cleaning protocols for Au electrodes are established and a number of electrode variants characterised. These variants include evaporated Au, TSG, and a number of Philips electrodes that vary in both their composition and geometric design.

A tBLM is comprised of a lipid layer and a tether layer. This tether layer can vary in its composition as discussed in Section 1.3.4; however, throughout this thesis thiol-based self-assembled monolayers will be used, specifically EO_3 cholesterol (EO_3C) and 6-mercaptohexanol (6MH). EO_3C is comprised of a cholesteryl headgroup joined to a polyethyleneoxy chain terminating in a thiol group. 6MH is a short alkanethiol (C_6) terminating in a hydroxyl headgroup, giving it a hydrophilic character. In addition to these, octadecanethiol (ODT) is also used, which is a longer alkanethiol (C_{18}) that terminates with a methyl group making the SAM hydrophobic. These thiols will bond to suitable metallic surfaces like gold. A high quality SAM will prevent solvent access to the electrode surface, forming a low-dielectric insulating layer on the surface and consequently lower the double layer capacitance of the surface. For most metals the capacitance of the unmodified surface is in the order of 10-100 μF.cm^{-2}; Au has a bare surface capacitance of 43 ± 15 μF.cm^{-2}[Steel et al., 1998].

3.1.1 Self-Assembled Monolayers and Factors That Affect Their Formation

The thiol SAM forms in two phases - an initial rapid phase, followed by a longer slow phase. The rapid phase generally deposits 80% of the SAM in first few minutes resulting in a rapid drop in capacitance, with the rest of the SAM forming and reorganising over hours or days in some cases[Bain et al., 1989; DeBono et al., 1996; Frubose and Doblhofer, 1995; Kim et al., 1993; Schneider and Buttry, 1993; Shimazu et al., 1992; Sun and Crooks, 1991]. This leads to an increase in the SAM resistance, as well as improving the α value of the CPE as a homogeneous surface is formed. Experiments conducted by Frubose and Doblhofer [1995] suggest that this is due to 'healing' of the SAM. Peterlinz and Georgiadis [1996] found that short chain alkanethiols (C_8 and C_{12}) formed quickly in the two-stage process already mentioned, where as longer chains (C_{16} and C_{18}) experienced a third step that occurs over a number of days. This agrees with the findings of Schneider and Buttry [1993], who described an inverse relationship between SAM quality and thiol solubility. Additionally, SAMs appear to form quicker in more concentrated solutions, however this also leads to a less well ordered SAM. While the trends appear to be consistent, the actual times required for SAM formation vary greatly between different labs, with no apparent link to any particular parameter[Schwartz, 2001].

Mixed SAMs, formed of two or more thiols, are more complicated. The final distribution of each thiol on the surface is influenced by the relative concentrations, size, solubility and diffusion coefficients of each thiol, as well as the solvent used, time allowed for SAM formation, temperature, etc. In general the thiol with the lowest solubility will be preferentially deposited[Folkers et al., 1994]. During SAM formation, the thiols will often phase separate into domains of the same thiol creating a patchwork of thiols on the surface [Bain and Whitesides, 1988].

For the study of ion transport processes a tBLM should be highly insulating, a property that is also dependent on the quality of the underlying SAM. There are several factors that require consideration to achieve this - the roughness of the surface, the composition of the surface, and the cleanliness of the surface.

Surface Roughness

The roughness of a surface plays a large role both in the quality of the SAM and how resistant the tBLM is likely to be [Creager et al., 1992; Finklea, 1996; Karpovich and Blanchard, 1994; Losic et al., 2001; Ulman, 1996]. Several studies have shown that it is microscopic roughness on the scale of the thiols themselves, rather than the visible macroscopic roughness, that is the key factor in producing a high quality SAM[Creager et al., 1992; Losic et al., 2001; Walczak et al., 1995; Widrig et al., 1991]. More specifically, it is the grain boundaries of the gold surface that appear to be linked to SAM defects. Surfaces with larger grains have more dispersed grain boundaries than those with smaller grains, resulting in higher quality SAMs[Banner et al., 2008; Creager et al., 1992; Gooding et al., 2001; Losic et al., 2001]. These surface topographies can be linked to the manner in which they are produced - sputtering has a tendency to produce larger grains than evaporation for example[Golan et al., 1992]. This is due to the relatively kinetic energies of the metallic atoms. Sputtering is a process by which a source of metal atoms is bombarded with ions, such as an argon plasma. This bombardment results in metal atoms being ejected from the source and entering a gas phase. These atoms then deposit themselves on all available surfaces in the sputtering chamber. The high kinetic energy that the metal atoms possess following ejection results in rapid deposition in a relatively uncontrolled manner, which leads to numerous nucleation sites and therefore a large number of grains. Evaporation, on the other hand, works by heating the metal source beyond its boiling point resulting in the metal atoms entering the gas phase. While the atoms are gaseous, they possess a lower kinetic energy than those found in sputtering. As such these atoms deposit at a lower rate, resulting in fewer nucleation sites producing larger grains.

Template-stripped gold (TSG) uses ultra-flat surfaces such as silicon wafers or mica as a template. A thin film of gold (approximately 200 nm thick) is deposited on the template of choice and solid supports (usually glass slides) are adhered to the surface. Peeling these solid supports off brings the gold film off with it, exposing a clean ultra-flat gold surface ready for modification with a SAM. This surface has been shown to possess a very low degree of roughness that is on average ten times lower than that of surfaces produced using the techniques mentioned previously[Losic et al., 2001; Wagner et al., 1995] (Table 3.1), with the best examples having average roughnesses in the range of 2-5 Å over a few μm^2[Hegner et al., 1993; Losic et al., 2001; Wagner et al., 1995] and grain sizes larger than those found on regular gold surfaces[Losic et al., 2001]. The roughness, and more importantly grain size, appears to vary dependent on the deposition temperature with the surface being significantly rougher at temperatures above 300° C[Hegner et al., 1993]. Post-deposition treatments, such as annealing the surface increases grain size to varying degrees depending on the substrate in question[Golan et al., 1992]. This technique also works with TSG, resulting in larger grain sizes and fewer pinhole defects leading to a higher quality SAM, as can be seen in Figure 3.1[Banner et al., 2008].

Interestingly, the process of SAM formation appears to etch the underlying gold as Edinger et al. [1993] found quantities of Au in the thiol solution following incubation for 24 hours.

Substrate	Grain size (nm^2)	Flat areas (10^3 nm^2)	RMS (nm)
Au-Ti-glass (evaporated)	2-4	1-1.5	2.1 ± 0.5
TSG (mica template)	40-80	40-80	0.12

Table 3.1: Roughness of various gold electrodes[Losic et al., 2001]

Due to the thinness of the lipid bilayer, approximately 5-7 nm, solid supported BLMs can be particularly sensitive to surface topography. While the lipid bilayer is flexible over longer length scales, on a nm-scale it is likely to be less so. As such height differences of more than a few nm, particularly those with steep gradients, are likely to disrupt the continuity of the bilayer. Additionally, terraces of the type found on the surface of flame annealed Au are also likely to disrupt bilayer[Naumann et al., 2003a]. While an atomically flat surface over both short and long length scales is clearly preferable, it is highly difficult to create on a reproducible basis. The best compromise therefore, is a surface that is flat over nm length scales, but with gentle undulations over μm length scales. This should limit the number of defects related to surface topography, while also being a producible surface.

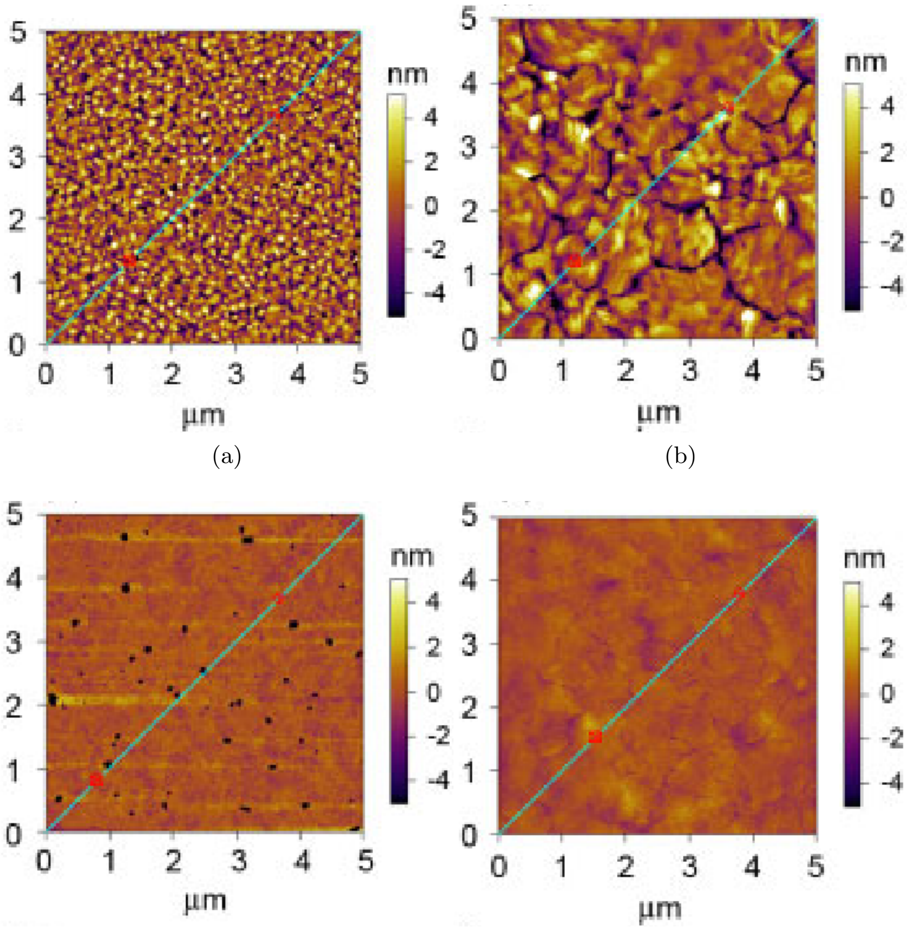

(a) (b)

(c) (d)

Figure 3.1: AFM images of Au surfaces. (a) Si wafer coated with 100 nm of electron-beam deposited Au (5 × 5 μm; Z-range = 10 nm; RMS roughness = 2.12 nm), (b) As (a) but flame-annealed (5 × 5 μm; Z-range = 10 nm; RMS roughness = 1.37 nm), (c) TSG from Si wafer (5 × 5 μm; Z-range = 10 nm; RMS roughness = 0.58 nm), (d) Annealed-TSG from Si wafer (5 × 5 μm; Z-range = 10 nm; RMS roughness = 0.36 nm)[Banner et al., 2008]

Surface Composition

Thiol SAMs can be made on a variety of metallic surfaces, including but not limited to gold[Bain et al., 1989; Banner et al., 2008; Nuzzo and Allara, 1983], silver[Abdelghani et al., 1996; Laibinis et al., 1991b; Schoenfisch and Pemberton, 1998; Walczak et al., 1991], copper[Ihs and Liedberg, 1994; Laibinis and Whitesides, 1992a, b], platinum[Shimazu et al., 1994], mercury[Demoz and Harrison, 1993; Muskal et al., 1995; Nelson, 2001], iron[Stratmann, 1990; Volmer et al., 1990], nickel and indium-tin oxide.

Gold, particularly Au(111), is the most frequently used surface[Bain et al., 1989; Banner et al., 2008; Caldwell et al., 1994; Creager et al., 1992; Diao et al., 1999; Finklea, 2006; Golan et al., 1992; Guo et al., 1994; Hegner et al., 1993; Hoogvliet et al., 2000; Jeuken et al., 2008; Jeuken, 2008; Jeuken et al., 2005, 2006, 2007a, b; Karpovich and Blanchard, 1994; Laibinis et al., 1991b; Losic et al., 2001; Nuzzo and Allara, 1983; Pan et al., 1996; Schwartz, 2001; Sellers et al., 1993; Wagner et al., 1995; Zhao et al., 1996] due to its ability to form a particularly strong covalent bond with sulphur.This bond has a high enthalpy of 418 ± 25 kJ/mol[Williams et al., 2000], which when examined with AFM was found to correspond to a bond force of 1.4 ± 0.3 nN[Grandbois et al., 1999]. Additionally, gold's low rate of oxidation under atmospheric conditions, lower price point (cf. platinum), excellent conductive properties and applicability in a number of experiment systems (such as surface plasmon resonance, quartz crystal microbalance, atomic force microscopy and electrochemical systems) all make it an attractive material for surface confined experiments.

Silver, while less popular, is also used for the formation of alkanethiol SAMs[Abdelghani et al., 1996; Gillen et al., 1994; Laibinis and Whitesides, 1992b; Laibinis et al., 1991a, b; Schoenfisch and Pemberton, 1998; Sellers et al., 1993; Walczak et al., 1991]. It is generally agreed that the silver-sulphur bond is weaker than that with gold, but is more suited to certain applications - Abdelghani et al. [1996] cite its sharper resonances as an advantage when working with surface plasmon resonance, while Hildebrandt et al. [1993] obtain superior results using it with surface-enhanced spectroscopies. The weaker Ag-S bond may be due to a change in the orientation of the SAM (a tilt of 13° *cf.* 30° for Au[Laibinis et al., 1991b; Walczak et al., 1991]) as a result of a difference in the binding of the thiolate headgroup to Ag when compared to Au[Walczak et al., 1991]. The precise chemistry of the Ag-S bond formation is not entirely clear. Work done by Laibinis et al. [1991b] suggests that there exists a combination of reactions of reducing Ag(I) to Ag(0), and Ag(I) surface oxides directly to Ag(I) thiolates. Ag readily oxidizes in air, but it appears that this oxide layer is only a few monolayers in thickness and displaced upon SAM formation[Laibinis et al., 1991b].

Copper[Laibinis and Whitesides, 1992a, b; Laibinis et al., 1991a, b] will also form a thiolate bond with the resultant SAM having a tilt of 12°[Laibinis et al., 1991b]. The surface is far more readily oxidised than gold or silver, being able to oxidize within the time course of a sample preparation protocol. Furthermore, copper oxide layers are not as easily displaced as silver oxide. A variety of methods are available for the removal of the oxide however, including etching with concentrated nitric acid[Sung et al., 2000].

While SAM formation appears to be able to displace metal oxides in some cases, there are reports that thiols can adhere to the oxide layer itself[Ron and Rubinstein, 1994]. This potentially disrupts the continuity of the monolayer, but more importantly can result in some of the surface being exposed if the oxide layer is not stable (this is particularly true of gold oxides[Ron and Rubinstein, 1994]). For these reasons it is often preferable to remove the oxide layer prior to SAM formation.

Surface Cleanliness

While the surfaces mentioned above can host thiol SAMs, there are a large number of materials that are incapable. Typically these include passivation materials such as SiO_2, Si_3N_4 and photoresists. Hard metals such as Ti and Cr are also unable to accommodate thiol SAMs. These materials all play roles in lithography processes as masks, adhesion layers or insulators. If steps are not taken to ensure that they are removed from the electrode surface they can present significant obstacles to the formation of high quality SAMs.

In addition to these SAM blocking materials, there are also other contaminants that can interfere with SAM formation - such as the aforementioned metal oxide deposits, and carbon contaminants. While small carbon compounds readily contaminate surfaces due to their prevalence in the atmosphere they are more often than not easily displaced by thiols during SAM formation. Larger organic molecules are less easily displaced however and require the employment of cleaning protocols.

Cleaning Thin Film Electrodes

Many electrodes can be reused if appropriate cleaning methods are used. While there are many ways of cleaning a surface they are not always suitable and as such appropriate methods need to be selected bearing in mind what the surface is to be used for, what effects each cleaning regime has, and if this will have a significantly adverse effect for that application. A few examples including electrochemical cleaning[Hoogvliet et al., 2000; Loglio et al., 2003], use of aqua regia[Creager et al., 1992] or oxidising agents such as piranha solution[Min et al., 2008], oxygen plasma, and ozone generated by ultraviolet light[Ishida et al., 1997; Ron and Rubinstein, 1994, 1998; Ron et al., 1998; Tsuneda et al., 1999].

Mechanical polishing of surfaces with slurry alumina can yield a fresh, relatively flat surface[Carvalhal et al., 2005]. However, it is clearly not suitable for thin film electrodes due to its abrasive nature. Applying a high potential to an electrode can oxidise or reduce the bonds that bind various contaminants to the surface. Potentials in excess of +0.85 V *vs.* SCE in 0.1 M H_2SO_4, or -1.00 V *vs.* SCE in 0.1 M NaOH on gold are sufficient to desorb the majority of contaminants one would expect to find on the electrode surface, including alkanethiols[Loglio et al., 2003]. Prolonged cycling between such potentials can also affect the structure of the surface, an effect known as electropolishing[Hoogvliet et al., 2000].

Chemical methods of cleaning the surface are also available. Piranha is a mixture of 30% hydrogen peroxide and concentrated sulphuric acid in a ratio of 1:4[Min et al., 2008]. A harsher version called super-piranha also exists which contains concentrated nitric acid, 30% hydrogen peroxide and concentrated sulphuric acid in a 1:10:6 ratio[Min et al., 2008]. *Caution*: Both piranha and super-piranha react violently with organic matter and must be handled with extreme care. On mixing the constituent parts the solution boils, and for safety reasons is it recommended that it is only used in small quantities and allowed to cool before immersing samples in it. While hazardous, they are both powerful oxidising agents and can be used for the stringent cleaning of surfaces[Creager and Clarke, 1994; Min et al., 2008]. However, it has been reported to cause roughening of thin films[Stettner and Winkler, 2010; Wang et al., 2004]. While this is acceptable for some applications, it is likely to negatively affect the quality of the tBLM for reasons discussed previously. Similarly, aqua regia is another powerful oxidising agent used in cleaning protocols. However it removes significant quantities of gold[Creager et al., 1992; Zhao et al., 1996], and is therefore unsuitable for use with thin film electrodes.

While the techniques mentioned above are all rather harsh, more gentle methods also exist. Oxygen plasma[Ron et al., 1998] and ozone[Ishida et al., 1997; Ron and Rubinstein, 1994; Ron et al., 1998; Tsuneda et al., 1999] both possess sufficient oxidative power to break down organic matter on the electrode surface, while having limited effects on the gross surface topography. It should be noted that some minor pitting of the surface is visible in studies conducted by Ron et al. [1998]. These pits were a couple of atoms deep, varied in area but were on the nanoscale, and were attributed to etching processes found upon exposure to thiol groups, air contaminants or UV/O_3 with an ethanol dip. Given that this process is common between UV/O_3 and Au-S bond formation it was deemed to not be an issue, and does not appear to adversely affect SAM properties.

3.1.2 Manufacture of Patterned Electrodes by MiPlaza

Electronics manufacturer Philips have a strong history of producing gold circuitry on glass substrates from many years of producing consumer electronics. Their partnership in the work contained within this thesis allowed me to design my electrodes based on the information in this introduction and Section 2.2, as well as results obtained through working with the various designs produced, while outsourcing the manufacturing process to MiPlaza, part of Philips Innovation Services in Eindhoven.

Patterned electrodes were manufactured by MiPlaza, Philips Research, Eindhoven. These have layers of sputtered titanium (20 nm) and gold (200 nm), which were patterned using photolithographic techniques. A layer of HPR504 photoresist was applied via spin-coating and exposed to UV light through a mask to give the desired electrode design. PLSI positive resist developer (1:1 ratio with H_2O) was then used to remove exposed regions of photoresist before being thoroughly washed with water for 5 minutes and dried in an oven for 30 minutes at 125°C. A wet gold etchant (Au-type TFA, Transene Company) was then used to remove exposed gold. The electrodes were washed in water, dried and baked for a further 30 minutes at 125°C. A wet titanium etchant ($HF{:}HNO_3{:}H_2O$ in 1:5:160 ratio) was then used before washing again for 5 minutes with water and being dried. Finally, the remaining photoresist is removed with acetone at 110°C.

3.2 Experimental Section

3.2.1 Materials

Glass slides (Menzel-Glaser), silicon wafers (Rockwood Riddings Wafer Reclaim), gold and chromium (Goodfellows), and EPOK-TEK 377 (Epoxy Technology, Inc.) were used as received for the manufacture of electrodes. Decon-90 (Decon Laboratories) was used as per manufacturer's instructions. Patterned electrodes used in Sections 3.4-3.7 were provided by MiPlaza, a subsidiary of Philips Innovation Services. EO_3 cholesterol (EO_3C) was made as described previously.[Boden et al., 1997] *Escherichia coli* (*E. coli*) polar lipid extract (Avanti Polar Lipids Inc., Alabama, Alabaster), octadecanethiol (ODT) and 6-mercaptohexanol (6MH, Sigma), dichloromethane (DCM), isopropanol, methanol, ethanol and acetone (HPLC grade, Fisher), nitrogen and argon (BOC) were used as received. NoChromix (Sigma) was mixed with concentrated H_2SO_4 (Fisher) as per manufacturer's instructions. Water was obtained from an Elga PURELAB Prima water purification system to give 18.2 MΩ.cm resistance. Electrochemical impedance spectroscopy experiments were performed in MOPS buffer (3-(*N*-morpholino)propanesulfonic acid, Sigma, 20 mM) with Na_2SO_4 (Sigma, 30 mM) adjusted to pH 7.4 with NaOH (Sigma) at 20 °C. $K_3Fe(CN)_6$ and $Ru(NH_3)_6Cl_2$ (Sigma) were used as redox probes in cyclic voltammetry experiments under buffered conditions with Na_2HPO_4/NaH_2PO_4 (Sigma, 100 mM) and KCl (Sigma, 100 mM) at pH 7.4. Ethylenediaminetetraacetic acid (EDTA, Sigma) was used as a 100 mM stock solution adjusted to pH 7.4. $CaCl_2$ (Sigma) was made up to a 1 M stock solution.

3.2.2 Production of Electrodes

Production of Evaporated Gold Electrodes

Glass slides (Menzel-Glaser) were cleaned by sonicating in 10% Decon-90 detergent for 30 minutes followed by thorough rinsing with Milli-Q water, methanol and finally sonicating in DCM for 30 minutes before drying under a stream of nitrogen. Layers of chromium (5 nm, Goodfellows) and gold (150 nm, Goodfellows) were deposited onto the slides via electrothermal evaporation (rate 0.1–0.2 $nm.s^{-1}$, pressure 8×10^{-7} mbar) with an Edwards Auto 306 evaporator. Electrodes were stored under Milli-Q water until used.

Production of Template Stripped Gold (TSG) Electrodes

Polished silicon wafers (Rockwood Riddings Wafe Reclaim) were cleaned in the same manner as the glass slides above. 150 nm of gold (Goodfellows) was evaporated on a cleaned silicon wafer using Edwards Auto 306 evaporator at $< 2 \times 10^{-6}$ mbar. The gold surfaces were then glued with EPO-TEK 377 to glass slides and cured for 120 min at 120°C. After cooling, the slides were detached from the silicon wafers to expose the TSG surface.

3.2.3 Cleaning of Electrodes

Philips electrodes (P1, P2 MKI, P2 MKII, and P2 MKIII) were rinsed with milli-Q H_2O, propanol and methanol before drying in a stream of nitrogen. They were then placed in a UV/O_3 generator (UVOCS Inc.) for at least 15 minutes to breakdown organic contaminants. The electrodes were then transferred to an ethanol Soxhlet extractor for at least twice as long.

3.2.4 Formation of Self Assembled Monolayers

Electrodes were immersed in a propanolic solution of either ODT (1 mM), 6MH (1 mM), EO_3C (0.1 mM) or EO_3C and 6MH (0.11 mM:0.89 mM) thiols overnight. These gave SAMs of pure ODT, 6MH or EO_3C, or a mixed SAM of ~80% EO_3C and ~20% 6MH by surface area respectively, as previously described in detail by Jeuken et al. [2007b]. Before use, SAM-modified electrodes were thoroughly rinsed with propanol and methanol and dried under a stream of N_2.

3.2.5 Vesicle Formation

Powdered *E. coli* polar lipid extract (100 mg) from Avanti Polar Lipids was dissolved in chloroform/methanol (5 ml, 1:1 ratio) and divided into 20 aliquots. These were then dried under a stream of nitrogen to remove the bulk of the solvent before drying further in a vacuum desiccator for at least 2 hours. Aliquots were stored under a nitrogen environment at $-20\,^{\circ}$C. 1 ml of 30 mM Na_2SO_4, 20 mM MOPS, pH 7.4 buffer was added to a single aliquot of dried lipid (5 mg) and agitated by vortex until all the lipid was resuspended in solution. The lipid solution was then tip sonicated (Banson Sonifier S-250A) at $4\,^{\circ}$C for 30 minutes to yield small unilamellar vesicles.

3.2.6 Tethered Bilayer Lipid Membrane (tBLM) Formation

The modified gold electrode was housed in an electrochemical cell made of PTFE and glass, with rubber O-rings and covered in electrolyte (20 mM MOPS, 30 mM Na_2SO_4, pH 7.4). $CaCl_2$ was added to a working concentration of 10 mM, followed by vesicles to make a 0.5 mg/ml solution. The membrane was allowed to form over 1–2 hours during which time EIS measurements were taken every 10 minutes. After membrane formation, EDTA (10 mM) was added and the cell was rinsed 5 times in buffer solution. The tBLM was then characterised using EIS.

3.2.7 Electrochemical Impedance Spectroscopy (EIS)

The electrodes were interrogated using electrochemical impedance spectroscopy (EIS). The electrochemical cell (Figure 2.3) was filled with buffered solutions at pH 7.4, and deoxygenated by bubbling argon through a capillary tube. The reference electrode was

Ag/AgCl (saturated KCl) and the counter electrode was a Pt wire. An EcoChemie PGSTAT30 with a Frequency Response Analyser (FRA2) being operated with EcoChemie's Autolab Frequency Response Analyser software (version 4.9.006) was used. Measured frequency range was 100 kHz to 100 mHz with 46 measurements being taken on a log scale at an amplitude of 10 mV with a bias potential of 0.00 V vs Ag/AgCl. Double layer capacitance ($\mathrm{C_{tBLM/PL}}$) was taken as being double the radius of a semi-circle observed in a normalised admittance plot ($\mathrm{Y}_{re}.\omega^{-1}$ vs $\mathrm{Y}_{im}.\omega^{-1}$).

Before tBLM formation, the relative coverage of 6MH:$\mathrm{EO_3C}$ in mixed SAMs was determined using Equation 3.1, described by Jeuken et al. [2007b]. Samples with less than 60% $\mathrm{EO_3C}$ surface coverage were deemed insufficient for formation of an insulating tBLM and were not used.

$$\chi_{\mathrm{EO_3C}} = \frac{C_{\mathrm{6MH}} - C_{\mathrm{SAM}}}{C_{\mathrm{6MH}} - C_{\mathrm{EO_3C}}} \tag{3.1}$$

Data were analysed with the software EISFit, written by L.J.C. Jeuken. The equivalent circuit, $\mathrm{R_s(Q_{tBLM}R_{tBLM})}$ (referred to as R(QR) for brevity, Figure 3.2), is composed of a resistor ($\mathrm{R_s}$) in series with a constant phase element (CPE, $\mathrm{Q_{tBLM}}$) and a second resistor ($\mathrm{R_{tBLM}}$) in parallel. $\mathrm{R_s}$ simulates the resistance of the electrolyte. $\mathrm{Q_{tBLM}}$ simulates the capacitance of the double layer (the SAM or the lipid bilayer) with an additional factor, α, which is taken to be a measure of surface roughness or defects in the lipid bilayer. $\mathrm{R_{tBLM}}$ models the resistance of the lipid bilayer. The equivalent circuit would theoretically terminate in a capacitor. However, the impedance spectra presented here do not extend to frequencies low enough to observe the effect of this 'final' capacitor and as such this element has been excluded during analysis (as indicated by the brackets surrounding it in Figure 3.2.

These equivalent circuits are simplifications of a far more complicated equivalent circuit that better represents the various components of the tBLM system. This circuit is presented in Figure 3.3, and is comprised of three parallel sets of two (RC) circuits in series. These the top row of (RC) circuits represent the resistances and capacitances of the lipid bilayer, while the lower row of (RC) circuits represents the SAM. Below this row there are a series of resistances connecting each column to indicate the ability of ions to migrate through the sub-membrane regions of the bilayer, and below these resistances are a number of capacitances that represent the underlying capacitance of the gold electrode at the inner Helmholtz plane. The three columns represent the three areas of the electrode - $\mathrm{EO_3C}$ SAM with a lipid monolayer, 6MH SAM with a lipid bilayer, and 6MH SAM with a lipid bilayer containing ion transporting structures (ionophores, membrane proteins, etc).

While this equivalent circuit is reasonably comprehensive, there are now so many components that the model becomes very difficult to manage and get meaningful data from. For this reason it has been condensed to produce the two equivalent circuits represented in Figure 4.2. In order to condense the model one must understand how these components appear in EIS spectra as their values change. Resistors are measured at lower frequencies

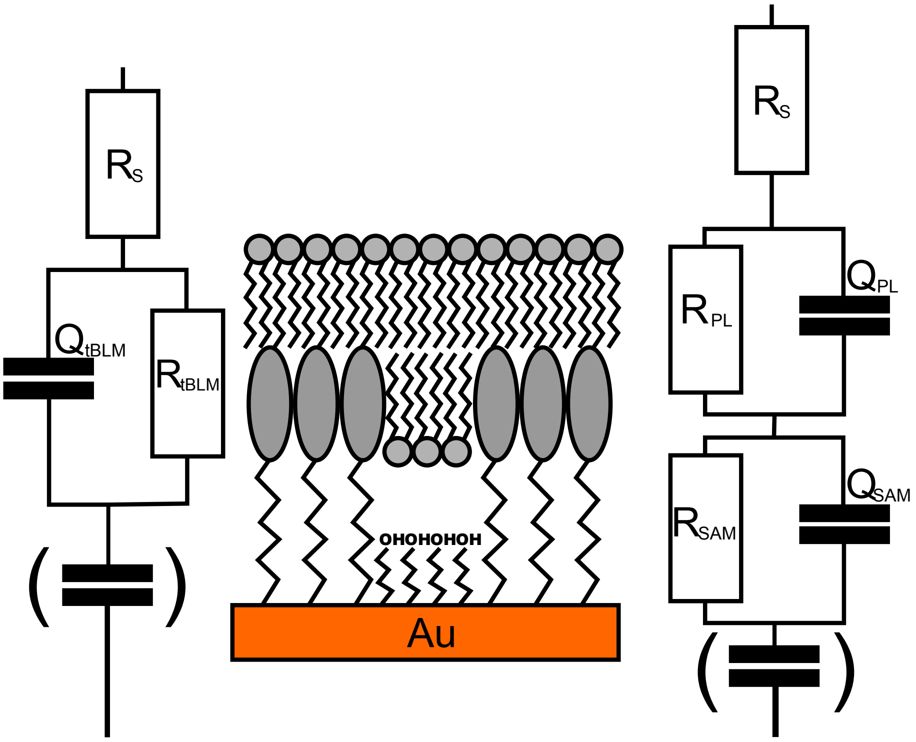

Figure 3.2: Equivalent circuits used in analysis of impedance data. The equivalent circuit described as $R_s(Q_{tBLM}R_{tBLM})$ was used for the majority of SAMs and tBLMs. $R_s(Q_{tBLM}R_{tBLM})(Q_{SAM}R_{SAM})$ was used in the case of tBLMs on 40% EO_3C mixed SAMs. R_s is solution resistance (electrolyte), Q_{tBLM} is capacitance of the entire tBLM modelled by a constant phase element (CPE) and R_{tBLM} is membrane resistance. Where Q_{SAM} and R_{SAM} are used they refer to the capacitance and resistance of accessible regions of the SAM. Capacitances enclosed in a bracket indicate that the element is not modelled as it is not observed in impedance spectra, but would be expected if measuring at lower frequencies.

the more resistant they become. Similarly, capacitors require lower frequencies to measure them as they increase. Given that the frequency range we are able to record in is restricted to a few mHz to a few MHz (due to technical issues at high frequencies and the practicalities of time needed per data point at low frequencies), this limits the components that we are able to measure.

The inter-domain resistances are expected to exceptionally high due to the lack of solvation in the EO_3C domain, however diffusion between the 6MH-bilayer and 6MH-transport domains is highly probable if they are connected. The underlying inner Helmholtz plane capacitors are expected to have capacitances of approximately 80 μF.cm^{-2} taking them far away from the size of the capacitances that we have observed thus far and likely beyond the range of EIS measurements. It is these capacitances that are included by themselves in brackets in some of the equivalent circuits throughout this thesis. The three membrane (RC) circuits can be grouped together as the resistance and capacitance can be treated as an average of the entire bilayer, while the three SAM (RC) circuits can also be grouped for similar reasons. This contraction gives us the R(RC)(RC) equivalent circuit that becomes R(QR)(QR) once capacitors have been replaced with CPEs. This equivalent circuit is used to represent cases where ion transport activity is apparent. The R(QR) form of the equivalent circuit is used when no ion transport activity is occurring beyond the background leak of the lipid bilayer. In this case the ion transport (RC) circuit can be ignored and although still present in theory, the lower (RC) circuit is overshadowed by the lipid bilayer (RC).

3.2.8 Cyclic Voltammetry

Ferricyanide

To characterise the electrodes, cyclic voltammetry with a ferrocyanide redox probe was employed. A three electrode set-up was used with a Ag/AgCl reference electrode, platinum wire counter electrode and the P2 electrodes as a working electrode. A solution of 4.0 mM $K_4Fe(CN)_6$, 0.1 M KCl and 0.05 M sodium phosphate buffer at pH 7.5 was used. The electrodes were cleaned as described but no SAM was formed. An EcoChemie PGSTAT30 was used in conjunction with the General Purpose Electrochemical System (GPES, version 4.9.007) provided. A potential window of 0.6 V to -0.2 V was scanned at rates of 4 mV/s, 16 mV/s and 49 mV/s (to check for diffusion dependence) in 0.5 mV potential steps. A linear potential profile was used. The ferrocyanide solution was degassed for 5 minutes prior to measurements with argon gas via a capillary tube. When degassing was completed the capillary tube was removed and argon gas allowed to flow over the surface of the solution to reduce the rate of O_2 dissolving back into it.

Ruthenium hexammonium

An alternative redox probe used was 10 mM $Ru(NH_3)_6Cl_2$ in 0.1 M KCl and 0.1 M phosphate buffer, pH 7.4. Potential was run from 0.2 V to -0.6 V and back to 0.2 V, at scan rates of 640 mV/s, 160 mV/s, 40 mV/s, 10 mV/s and 2.5 mV/s to check for diffusion dependence. The same potentiostat and software were used and the second scan was used for analysis.

Data Analysis

GPES was used to apply baselines and determine peak heights. The data were then used to calculate surface areas of the working electrode by rearranging the Randles-Sevcik equation from Section 2.2:

$$A = \frac{i_p}{0.4463nFC_R\sqrt{\frac{nF\nu D_R}{RT}}} \tag{3.2}$$

where I_p is the peak current, n is the number of electrons transferred (in this case one), F is Faraday's constant (96485.34 C/mol), A is the area of the working electrode, C_R is

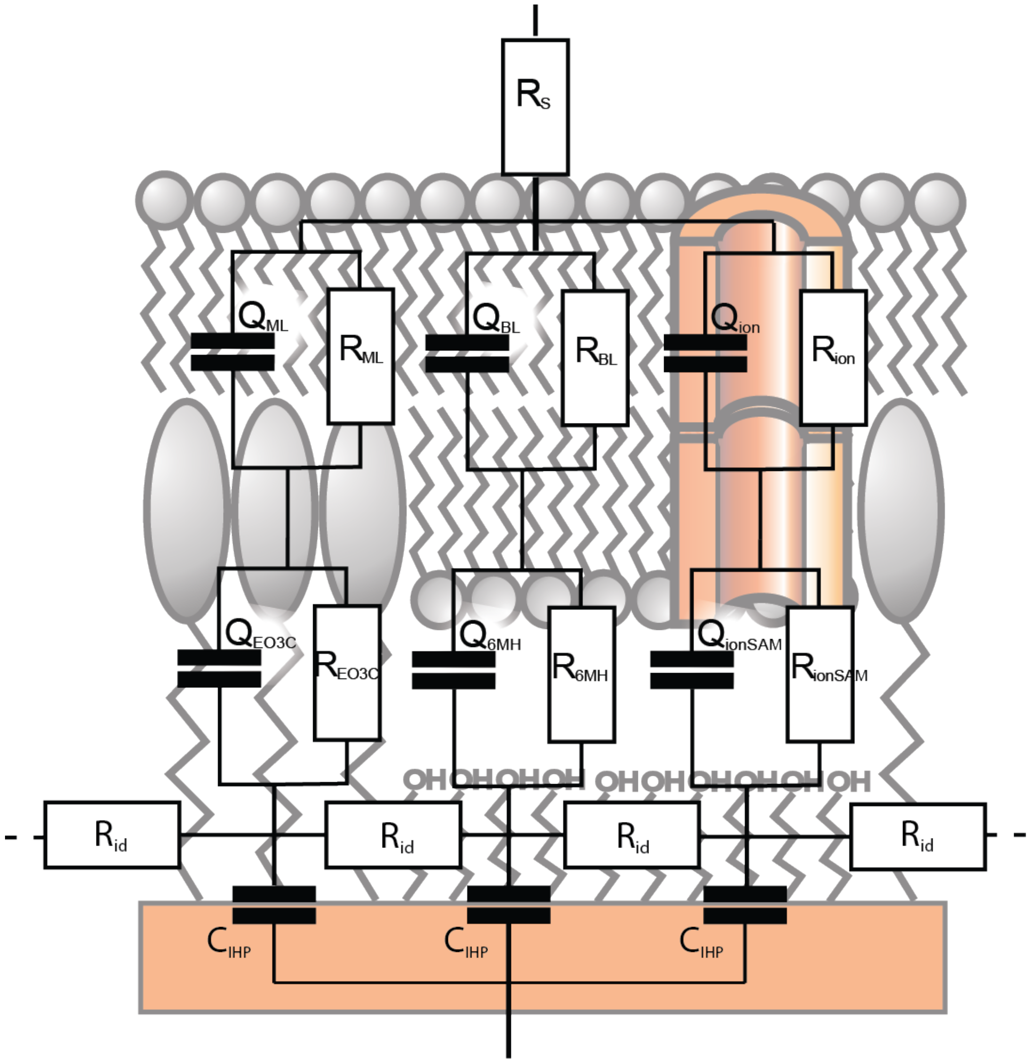

Figure 3.3: Complex equivalent circuit that R(QR) and R(QR)(QR) circuits are based on. ML refers to lipid monolayer, BL refers to lipid bilayer, ion refers to ion transporters, EO3C refers to the EO_3C SAM domains, 6MH refers to the 6MH SAM domains, ionSAM refers to the 6MH SAM domains exposed by ion transporters, R$_{\mathrm{id}}$$referstointerdomainresistance, andC_{\mathrm{IHP}}$ refers to the capacitance at the inner Helmholtz plane. Further details can be found in the text.

the concentration of the redox probe, υ is the scan rate, D_R is the diffusion constant of the redox probe used (7.1×10^{-6} $cm^2.s^{-1}$ for $K_4Fe(CN)_6$[Saji et al., 1975]; 8.3×10^{-6} $cm^2.s^{-1}$ for $Ru(NH_3)_6Cl_2$) and R is the universal gas constant (8.314 J/mol.K) and T is temperature (taken to be 298.15 K).

3.2.9 Scanning Electron Microscopy

Scanning electron microscopy was performed with a Thermo VG Scientific ESCALAB 250. Chamber pressure was kept below 5×10^{-9} mbar during measurements. An integrated FEG 1000 field emission source electron gun was used with a 100 nm spot size and 5 nA sample current.

3.2.10 X-Ray Photoemission Spectroscopy

X-ray photoelectron spectra were obtained with a Thermo VG Scientific ESCALAB 250. Chamber pressure was kept below 5×10^{-9} mbar during measurements. A monochromated Al KR X-ray source (15 kV, 150 W) was used to irradiate samples with a spot diameter of approximately 0.5 mm. Survey scans were taken in a range of 0 to 1380 eV, with high resolution scans being taken for certain peaks of interest including C 1s (279–289 eV), Au 4f (79–89 eV), O 1s (525–535 eV), S 2p3 (154–174 eV), Ti 2p (450–475 eV) and Ag 3d (362–382 eV) to investigate respective elements. High-resolution spectra were analysed using the Thermo VG software package for peak fitting and elemental composition, and all binding energies corrected vs 84.0 eV for Au $4f_{7/2}$.

3.2.11 Scanning Auger Emission Spectroscopy

Auger emission spectra were obtained with a Thermo VG Scientific ESCALAB 250. Chamber pressure was kept below 5×10^{-9} mbar during measurements. An integrated FEG 1000 field emission source electron gun was used with a 100 nm spot size and 5 nA sample current. Contrast maps were taken of Ag, Au, O, S, and Ti peaks. Peak measurements (P) were taken at 353.5 eV (Ag $M_5N_{45}N_{45}$), 69.8 eV (Au N_7VV), 506.8 eV (O KVV), and 381.0 eV (Ti LVV), with background measurements (B) being taken a few eV higher in each case. The maps were comprised of 128 x 128 points with the (P-B)/(P+B) contrast mode being used to minimise topographical effects.

3.2.12 Atomic Force Microscopy

A Multimode AFM on a Nanoscope IIIa (Digital Instruments, Veeco Metrology Group, Inc., CA) controller was used in contact mode in ambient conditions at 20°C. Silicon nitride cantilevers (NP-S, Veeco Metrology Group) with a spring constant of approximately 0.6 N/m were used. Images were flattened using a polynomial fit and a low-pass filter used for clarity.

For the study of P2 mkIII electrodes a NanoMan AFM (Digital Instruments, Veeco Metrology Group, Inc., CA) was used, in tapping mode.

3.2.13 Light Microscopy

A Nikon i90 epi-fluorescent microscope was used with 50:50 dichromic mirror and a 390-460 nm emission filter to block UV light for health and safety reasons.

Results

3.3 Initial Studies on the Cleaning of Gold Surfaces for the Formation of Tethered Bilayer Lipid Members Using Evaporated Gold Electrodes

Extensive work was done investigating cleaning protocols due to the sensitivity of surface supported BLMs to surface conditions[Naumann et al., 2003a]. It was important to study the effect of several methods on surface roughness and cleanliness as well as the reproducibility of the technique. Three cleaning regimes were investigated and compared to 'fresh' evaporated gold. 'Fresh' gold was defined as evaporated gold that was immediately immersed and stored in Milli-Q H_2O until used. '1x UV/O_3 ' refers to gold slides that are cleaned by exposure to UV radiation and O_3 for a period of 30 minutes prior to use. '4x UV/O_3 ' cleaned gold was subjected to four rounds of the cleaning regime described for '1x UV/O_3 ' gold, but with ODT SAMs being formed between each cleaning cycle. Finally, '4x UV/O_3 + EtOH' refers to samples that have been subjected to the same conditions as '4x UV/O_3 ' but with 1 hour immersed in ethanol after each round of UV/O_3 exposure. All samples were rinsed with propanol, followed by methanol and dried in a stream of nitrogen before use. Initial work done using contact angle measurements to compare the difference in surface conditions between UV/O_3 and dichloromethane (DCM) sonication and the effect on octadecanethiol (ODT) monolayer quality (results not shown). On this basis it was decided that the DCM sonication step had not improved the cleaning protocol and was removed.

3.3.1 X-Ray Photoelectron Spectroscopy (XPS)

XPS studies were conducted on the surfaces to assess the ability of Milli-Q water storage to keep gold surfaces clean ('fresh' sample) as well as UV/O_3 to clean a gold surface ('1× UV/O_3' sample), the extent to which UV/O_3 can remove a SAM ('4× UV/O_3' sample) and the effect that ethanolic reduction of UV/O_3 cleaned gold has ('4× UV/O_3 + EtOH' sample). Au 4f, C 1s, O 1s and S 2p peaks were examined (Figure 3.4) and normalised as a percentage of the Au $4f_{7/2}$ peak, see Table 3.2. Figure 3.4a indicates a variety of carbon species on the surface, most likely atmospheric contamination and the remains of degraded SAMs. The shift in the peak to a higher energy suggests a greater proportion of carbon-oxygen single (C-O) and double bonds (C=O), which are most likely due to oxidation of alkanethiols on the electrode surface. Additionally, the shoulder at approximately 286 eV is due to residual ethanol. A Soxhlet extractor was recently introduced, which should reduce the number of carbon contaminants left on the gold surface by purifying the ethanol. The remaining carbon contaminants are thought to be obtained from the atmosphere during transfer to the XPS apparatus. It should be noted that small carbon contaminants can quite often be displaced by thiol chemistry during SAM formation and are therefore not thought to pose a major issue.

Exposure to UV/O_3 results in a significant increase in surface oxidation, as seen in Figure 3.4b. Most notably is the shift in the O 1s peak after exposure to UV/O_3, from 533.0 eV, which indicates absorbed oxygen, to approximately 531 eV, which is indicative of gold oxides (Au_2O_3). The peak decreases in size and returns to 533.0 eV following ethanolic reduction, as suggested by Ron and Rubinstein [1994]; Ron et al. [1998] and Ron and Rubinstein [1998]. The fact that the peak moves to a higher energy compared to that of 'fresh' gold suggests than some gold oxides exist even before exposure to UV/O_3 for cleaning. Additionally, SiO_2 has a binding energy of 532-534 eV, and this likely contributes to the peaks in all the samples, but a higher proportion in 'fresh' samples and those which have been reduced with ethanol.

Sulphur contaminants were still found on the surface of all samples and do not increase drastically following UV/O_3 removal of a SAM (Figure 3.4c). The peak around 168.0 eV for the '1× UV/O_3' and '4× UV/O_3' samples indicate sulfoxide groups, a likely byproduct of UV/O_3 degradation of a SAM that results in an oxidised thiol group (SO_2) on the surface. The 'fresh' and '4× UV/O_3 + EtOH' samples however see peaks around 162 eV which suggests the presence of thiolates on the surface. These are likely to be intact alkanethiols ($CH_3(CH_2)nS$) in the case of the 'fresh' sample, or a reduced sulfoxide (SH) following oxidation of the alkanethiol and subsequent reduction by ethanol. While there are clearly contaminants on the electrode surface, these should be easily displaced by the formation of a new SAM.

Peak	Fresh (%)	1× UV/O_3 (%)	4× UV/O_3 (%)	4× UV/O_3 + EtOH (%)
C 1s	26.2	23.0	20.0	36.1
O 1s	13.8	26.7	25.6	13.3
S 2p3	5.0	4.9	8.8	6.5

Table 3.2: XPS data expressed as percentages relative to the Au $4f_{7/2}$ peak. Results are obtained from a single sample for each cleaning regimen. UV/O_3 cleaning decreases carbon contaminants and returns sulphur levels to near baseline levels, but increases surface oxidation. Ethanolic reduction can decrease the level of surface oxidation.

3.3.2 Atomic Force Microscopy (AFM)

To check for effects of cleaning on surface roughness, uncleaned evaporated gold was compared under AFM with UV/O_3 cleaning and UV/O_3 cleaning with ethanolic reduction. The roughness was measured using the root mean square (RMS) of images taken and these can be seen in Table 3.3. While there are some variation in the roughness of the electrodes throughout the process of exposure to UV/O_3 and ethanol reduction, these effects do not show a great deal of significance. Any significance in the data can be attributed to oxidation of the gold surface by UV/O_3 and subsequent etching of the gold oxides by ethanolic

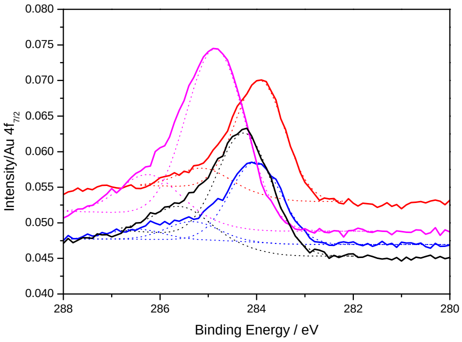

(a) C 1s

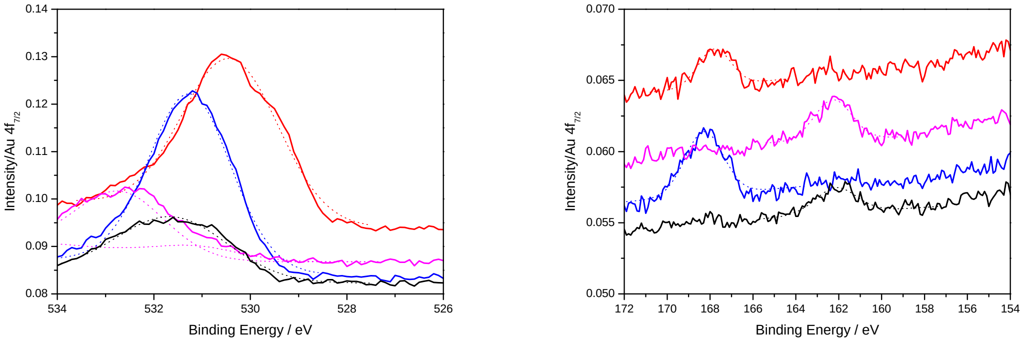

(b) O 1s

(c) S 2p

Figure 3.4: XPS spectra of several elemental positions for the study of cleaning protocols. Black = 'fresh' gold; red = '1× UV/O_3' cleaned gold; blue = '4× UV/O_3' cleaned gold; magenta = '4× UV/O_3' cleaned gold with ethanolic reduction (see text for further explanation of cleaning protocols). Peaks have been normalised against the Au 4f$_{7/2}$ peak for each sample and plotted as arbitrary units.

reduction, as suggested by literature[Ron et al., 1998; Tsuneda et al., 1999].

3.3.3 Electrochemical Impedance Spectroscopy (EIS)

Figure 3.5 shows the formation of SAMs on evaporated gold. While the impedance spectra of bare gold has not been included, the capacitances observed here for the SAMs (ODT = 1.04 ± 0.02 μF.cm^{-2}; 6MH = 5.91 ± 0.07 μF.cm^{-2}; EO$_3$C = 1.66 ± 0.16 μF.cm^{-2}) are far lower than literature values for bare gold (ranging from 25.36 μF.cm^{-2}[Subramanian and Lakshminarayanan, 2000] to 40 μF.cm^{-2}[Jenkins et al., 1998]) indicating that a well organised layer has been formed. The effect of ethanolic reduction on SAM quality was also examined by allowing various SAMs to form on UV/O_3 cleaned evaporated gold electrodes and interrogating by EIS. As can be seen from Figure 3.5 and equivalent circuit analysis in Table 3.4, ethanolic reduction leads to the formation of SAMs with far more reproducible characteristics, especially for EO$_3$C. Despite this improvement in the reproducibility of the SAMs they suffer from low resistances and, on the basis of α values and phase shift

Protocol	RMS (nm)
Fresh	2.57 ± 0.04
1x UV/O_3	2.99 ± 0.25
4x UV/O_3	2.52 ± 0.61
4x UV/O_3 + EtOH	2.44 ± 0.28

Table 3.3: Roughness as root mean square (RMS) values for the various cleaning protocols trialled on evaporated gold as measured with AFM, see text for further details. RMS (image R_q) from 3 samples per cleaning regimen measured over a 5.0 μm × 5.0 μm area, using Veeco Nanoscope 7.0 and mean average taken. For reference, TSG has an RMS of less than 1.0 nm over a 2.25 μm × 2.25 μm area.[Hegner et al., 1993]

maxima, SAM heterogeneities. It is likely that these are due to the roughness of the evaporated gold electrodes. These heterogeneities also give rise to a second capacitance semi-circle in the low frequency range that has been modelled in Table 3.4 by the parameter C_2.

On the basis of these results and the literature described previously [Ishida et al., 1997; Ron and Rubinstein, 1994, 1998; Ron et al., 1998; Tsuneda et al., 1999], a cleaning protocol was established involving UV/O_3 exposure followed by immersion in hot ethanol. This protocol has been used for the remainder of this thesis.

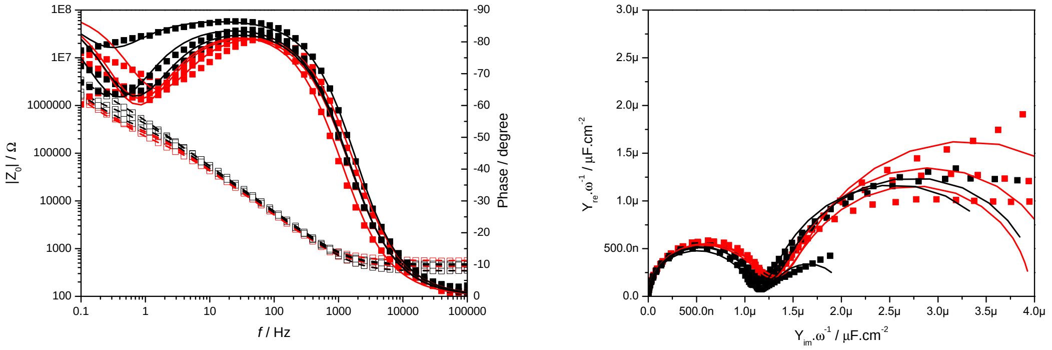

(a) ODT - Bode Plot

(b) ODT - Normalised Admittance Plot

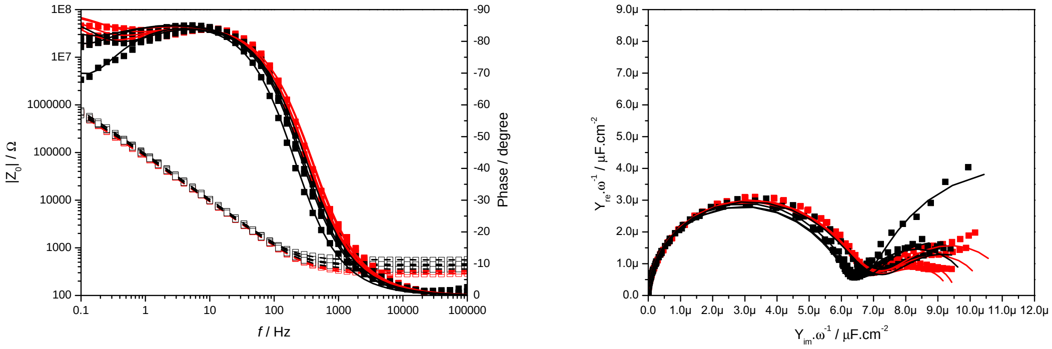

(c) 6MH - Bode Plot

(d) 6MH - Normalised Admittance Plot

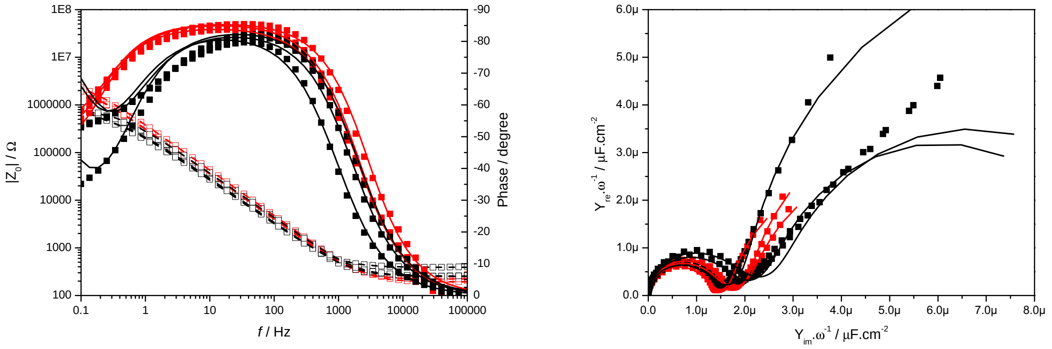

(e) EO$_3$C - Bode Plot

(f) EO$_3$C - Normalised Admittance Plot

Figure 3.5: EIS of SAMs on gold subjected to 30 minutes of UV/O$_3$ cleaning with or without 1 hour of ethanolic reduction. Black = no ethanolic reduction; Red = ethanolic reduction.

	ODT	ODT + EtOH	6MH	6MH + EtOH	EO_3C	EO_3C + EtOH
n	3	3	4	4	3	3
C_{SAM} (μF cm^{-2})	1.04 ± 0.02	1.15 ± 0.01	5.91 ± 0.07	6.18 ± 0.01	1.66 ± 0.16	1.38 ± 0.08
Q_{SAM} (μF cm^{-2})	3.06 ± 0.54	3.00 ± 0.17	24.01 ± 3.76	40.96 ± 4.45	3.96 ± 0.67	2.87 ± 0.22
α_{SAM}	0.929 ± 2.71e-3	0.919 ± 2.52e-3	0.905 ± 1.21e-2	0.864 ± 8.29e-3	0.914 ± 7.85e-3	0.938 ± 6.57e-3
R_{SAM} (kΩ cm^2)	105.84 ± 19.52	45.13 ± 8.87	48.62 ± 12.83	13.25 ± 2.61	105.95 ± 22.23	436.01 ± 26.07
C_2 (μF cm^{-2})	3.26 ± 0.63	4.46 ± 0.35	11.68 ± 1.25	10.10 ± 0.42	12.29 ± 2.49	8.08 ± 0.89

Table 3.4: Mean capacitances (taken at -45° phase shift), CPE values (Q and α) and resistances along with standard errors for SAMs of ODT, 6MH and EO_3C with and without ethanolic reduction after UV/O_3 cleaning. Values Q_{SAM}, α_{SAM}, R_{SAM} and C_2 are obtained from equivalent circuit modelling software EISFit using a R(QR)C circuit, where Q is the capacitance of a CPE, α is a parameter of the CPE that acts as an indicator of SAM roughness. R_{SAM} and C_2 are the resistance of the SAM and the capacitance value for the second semi-circle in the Normalised Admittance Plot (Figures 3.5b, 3.5d and 3.5f) as explained later. C_{SAM} obtained by taking the value of the first capacitance semi-circle peak in the Cole-Cole plot and doubling. All values normalised using an area of 0.242 cm^2. ODT capacitance in literature is 1.04 ± 0.05 μF cm^{-2}[Steinem et al., 1996].

3.3.4 Conclusions

UV/O_3 cleaning with ethanolic reduction has been investigated as a method for the removal of alkanethiol SAMs from Au electrodes, with the aim of reusing an electrode surface multiple times. XPS studies showed that exposure to UV/O_3 decreased the number of carbon moieties on the surface, while exposure to ethanol reduced the presence of oxygen containing species. AFM studies did not show any significant effect of the UV/O_3 and ethanolic reduction cleaning process, although literature suggests that UV/O_3 exposure roughens the surface of the electrode, while ethanolic reduction smoothens it[Ron et al., 1998; Tsuneda et al., 1999]. Meanwhile, EIS showed that reproducible SAMs were formed on gold electrodes, and that electrodes cleaned with UV/O_3 and ethanolic reduction are preferential for the formation of good quality SAMs, when compared to electrodes only cleaned with UV/O_3. While the results presented are not necessarily significant on an individual basis, when considered collectively they do show a trend that is consistent with literature[Ron et al., 1998].

It is thought that UV/O_3 breaks down alkanethiols and other carbon contaminants, while also producing gold oxides on the electrode surface. These oxides are then etched away by the ethanolic reduction process. This surface is more homogenous than the initial surface which will contain some gold oxides on the surface from atmospheric oxidation. In addition to the smoother electrode surface brought about by ethanolic etching, the decrease in surface heterogeneities makes for a superior surface for SAM formation. On the basis of these results and the literature described previously [Ishida et al., 1997; Ron and Rubinstein, 1994, 1998; Ron et al., 1998; Tsuneda et al., 1999], a cleaning protocol was established, involving UV/O_3 exposure followed by immersion in hot ethanol for a period at least twice as long as that used for UV/O_3 exposure.

Characterisation and Development of Array Format Electrodes

To aid the development of array-format membrane biosensors, Philips Research (UK) provided their expertise in the design and manufacture of electrodes on glass. Several geometries were tested in each series, with increasing complexity being added in each subsequent set of designs.

3.4 Philips Research Electrodes: Series 1

The first generation of Philips electrodes, hereafter referred to as P1 electrodes, were designed to test surface properties and edge effects. These include the morphology of pixel edges, surface roughness, perimeter:area ratios and potential problems such as residues from manufacture that need removing. Glass substrate used in the electrode designs measure 10 mm by 30 mm and have a single layer design on them. Glass was used as a substrate with a 20 nm layer of Ti as an adhesion layer prior to sputtering of 200 nm of Au. Electrode tracks were graduated from 20 μm for the region inside the electrochemical cell to 100 μm and terminating in 0.75 mm wide contact pads with a pitch of 1.0 mm for compatibility with PCI connectors. Five designs were created, all with an intended constant area of π mm^2 excluding exposed tracks (see Table 3.5, as well as Figures A.2, A.3, A.4, A.5 and A.6 in the Appendix). The designs were made such that different features could be examined. Design A consists of a single circular electrode with radius of 1 mm. Design B has 4 circular electrodes with radii of 0.5 mm. Design C has 9 circular electrodes with radii of 0.33 mm. In this case, 4 of the 9 electrodes have been interlinked with tracks such that they will be measured as a single electrode of $\frac{4}{9}\pi$ mm^2. Design D is essentially the same design as design C, but with square rather than circular electrodes. These electrodes measure 0.59 mm by 0.59 mm. Finally, design E is comprised of 100 electrodes each with a radius of 100 μm. The electrodes in design E have also been linked such that we have 6 regions made up of 1, 3, 5, 7, 9 and 76 electrodes, however these can be cross-linked to allow measurement with all 100 electrodes simultaneously.

Design	Number of Electrodes	Radius (mm)	Area (cm^2)	Perimeter (mm)	Ratio
A	1	1.0	3.14E-02	6.28	2.0
B	4	0.5	7.85E-03	3.142	4.0
C	9	0.33	3.42E-03	2.073	6.1
D	9 (square)	0.59	3.48E-03	2.36	6.8
E	100	0.1	3.14E-04	0.628	20.0

Table 3.5: Dimensions of Philips 1st generation (P1) electrodes. Areas and perimeters are given for individual electrodes, excluding tracks. Ratio is calculated as $\frac{\text{Perimeter (mm)}}{\text{Area (mm}^2\text{)}}$.

These designs are such that an understanding of edge effects linked to the perimeter:area ratios should become apparent. As we can see the perimeter : area ratio for a single electrode decreases with each design. Considering that in some of the designs the electrodes are linked we see slightly different ratios. The single layer morphology of the electrodes also come into play here as there is no insulating layer for the tracks. Taking the tracks into account, the 76-linked electrode region of design E has a 5% increase in area and a 22% increase in perimeter due to the tracks alone. This will influence results and indicates the strong need for an insulating layer to cover the tracks in later designs.

This effect is compounded when one considers that the electrodes are three dimensional, with 20 nm of titanium and 200 nm of gold rising above the glass substrate. Table 3.6 investigates the contribution that the sides of these electrode has on the total active surface area of the electrode in question. While the effect is negligible for designs A-C, it begins to become significant when looking at design E. Of greater concern is the effect calculated for an additional design, F, where due to the smaller dimensions of the electrode pixels the tracks and walls become a dominating influence.

3.4.1 Atomic Force Microscopy (AFM)

Figure 3.6 shows a comparison by AFM analysis between first generation Philips electrodes and evaporated gold electrodes such as those used in Section 3.3.2. The evaporated gold had a RMS of 3.0 nm while the sputtered gold used on the Philips electrodes had a RMS of 0.9 nm over a 4 μm^2 area. This indicates that Philips electrodes have a far smoother surface than the evaporated gold slides previously used. Template stripped gold from silicon of the type normally used at Leeds typically have a RMS of 0.4 nm, while mica (considered atomically flat) has a RMS of 0.1 nm. This should make the Philips electrodes a good surface for the formation of high quality tBLMs.

Design	Pixel Area	Track Area	Pixel Wall Area	Track Wall Area	Total Area	Design Area	Error (%)
A	3.142	0.006	0.001253	0.0001200	3.149	3.142	100.23
B	3.142	0.024	0.002497	0.0004800	3.169	3.142	100.86
C	3.079	0.054	0.003692	0.001200	3.138		101.91
E	3.142	0.600	0.01184	0.02172	3.775	3.142	120.17
F	0.03142	0.960	0.0005326	0.03475	1.027	0.03142	3268.09

Table 3.6: Table showing effect that tracks and electrode walls have on total surface area. Areas given are for the entire electrode. Track width taken to be 20 μm and wall height taken to be 200 nm. Error is the total area (pixel, track and electrode wall areas) divided by the design area, and expressed as a percentage where 100% signifies the electrode is as intended. As can be seen the degree of error encountered with the A, B and C designs is relatively small, however when E type electrodes are examined the error becomes significant, and overwhelming with the F type electrodes.

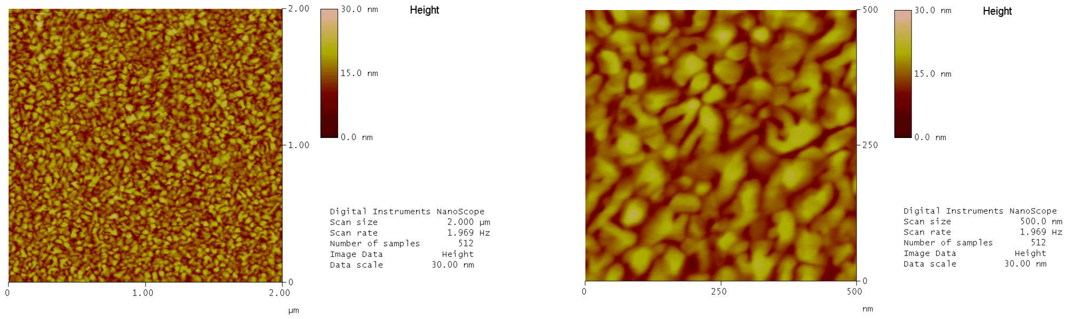

(a) Evaporated gold, 2 μm $\times$ 2 μm

(b) Evaporated gold, 0.5 μm $\times$ 0.5 μm

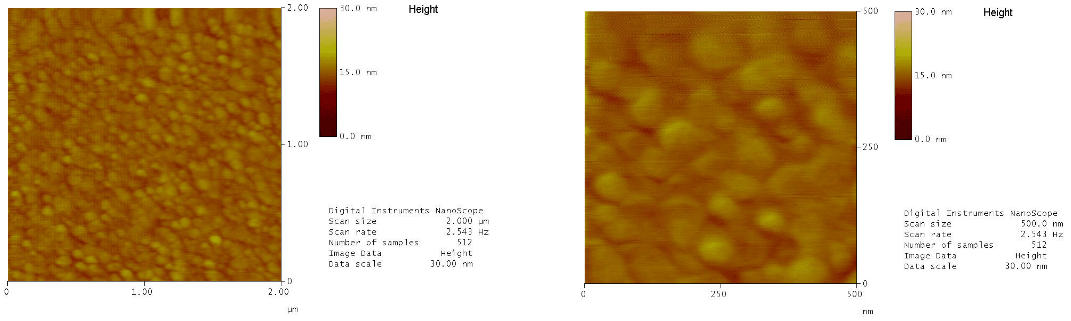

(c) Philips sputtered gold, 2 μm $\times$ 2 μm

(d) Philips sputtered gold, 0.5 μm $\times$ 0.5 μm

Figure 3.6: AFM analysis of evaporated gold and sputtered gold. Images taken in contact mode, Z-scale = 30 nm. Evaporated gold: RMS = 3.0 nm; Philips sputtered gold: RMS = 0.9 nm.

3.4.2 Cyclic Voltammetry

Cyclic voltammetry with a ferrocyanide probe was used to investigate the geometric area of the electrode surfaces.

The various electrode designs were compared by looking at a single pixel of each design (A-E) as shown in Figure 3.7. Peak currents decrease with each electrode design as would be expected, ranging from 8 μA for P1A electrodes to 290 nA for P1E electrodes. The geometric area of each electrode also decreases as can be seen in Table 3.7. Interestingly, the ratio between the area calculated using the Randles-Sevcik equation and the geometric area decreases with decreasing electrode size for designs A-C. However, the ratio increases dramatically with design E. Exposed tracks could account for calculated areas larger than those designed (such as with design E), however significantly smaller areas are unexpected. The peak separation observed in these CVs varies with scan rate and is always greater than the ideal 59 mV discussed in Section 2.2. This deviation can be attributed to one of two phenomena - ohmic drop, or quasi-reversible electron transfer.

A system usually suffers from ohmic drop when the electrode potential can not be fully controlled, either as a result of the electrolyte having a poor conductivity, the reference electrode being positioned too far away from the working electrode, or the working electrode itself possessing poor conductivity. In these experiments the reference electrode was positioned within 2 cm of the working electrode and the ferricyanide redox couple was supported in 0.1 M KCl, precluding both of these as factors. Poor electrode conductivity could be expected to present itself in electrochemical impedance spectroscopy experiments done later in this chapter (Figure 3.9 and Table 3.9), however there is no evidence to support this.

Quasi-reversible electron transfer is therefore the more likely option. While the ferri/ferrocyanide redox couple is reversible in nature, contaminants on the bare Au electrodes used here may slow electron transfer kinetics giving rise to quasi-reversible schemes. This could also explain the increased planar for design E, which approaches microelectrode dimensions resulting in a shift to a hemispherical diffusion scheme and greatly increasing the current density.

Electrode	Slope	Offset	Planar Area (cm^2)	Design Area (cm^2)	Ratio (%)
A	7E-05	1E-06	2.32E-02	3.14E-02	73.89
B	2E-05	9E-07	5.43E-03	7.85E-03	69.17
C	5E-06	3E-07	1.75E-03	3.42E-03	51.17
E	1E-06	2E-07	4.09E-04	3.14E-04	130.25

Table 3.7: Parameters from CV analysis for P1 electrodes. Slope and offset are obtained by plotting peak currents against the square root of the scan rate they were measured at. Planar area is calculated using slope in place of peak current in equation 2.16. Design area is the area of a single circle with the radius sum of circular regions, excluding tracks. Ratio is calculated as $\frac{\text{Planar Area}}{\text{Design Area}} \times 100$.

Further study of the E-type electrodes was conducted with each sub-array being mea-

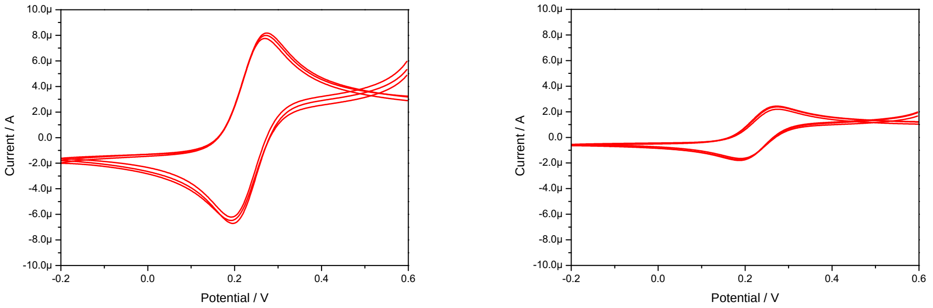

(a) P1A (b) P1B

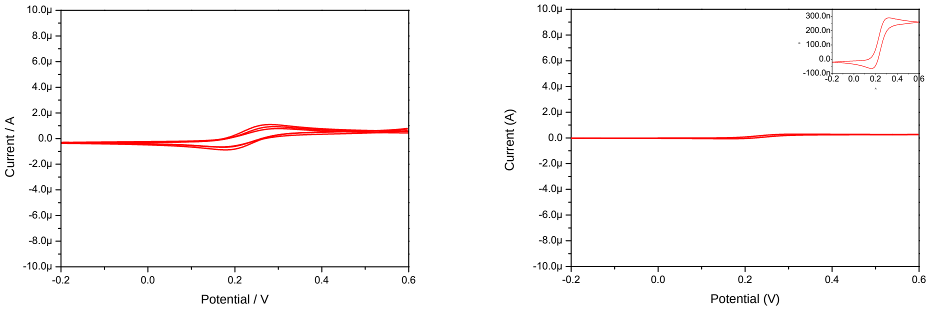

(c) P1C (d) P1E

Figure 3.7: Cyclic voltammograms showing probing of P1 electrodes using 4 mM potassium (II) ferrocyanide over a potential range of 0.6 V to −0.2 V at a scan rate of 10 mV/s. Figures 3.7a-3.7c are all shown on the same scale, while Figure 3.7d is enlarged for viewing clarity.

sured individually, as shown in Figure 3.8. Peak current was found to decrease with fewer electrodes and voltammogram morphology begins to change from planar-diffusion controlled showing redox peaks (Figure 3.8a) to a hybrid planar/hemispherical plot as shown in Figure 2.11 in Section 2.2.2 (Figure 3.8g). An interesting point to note here is that the P1E-100 plot presents planar diffusion dominant behaviour despite being made up of many electrodes the same size as the P1E-1 electrode, which by itself shows microelectrode dominant behaviour. This is most likely due to the layout of the electrodes, as discussed in Section 2.2.2. To recap, individual electrodes will have hemispherical diffusion layers, but when placed in proximity to each other these layers begin to merge and form a planar diffusion layer (Figure 2.14).

Peak current was recorded at several scan rates, with peak separation found to vary by only 20 mV in most cases. At slower scan rates, electrodes P1E1–9 showed far greater peak separation. However, this is due to flattening of the redox peaks causing the sigmoidal wave that is characteristic of a microelectrode's radial diffusion becoming the dominant feature. It should also be noted that the peak separation was at its lowest 80 mV, a significant deviation from the 59 mV separation that is characteristic of an ideal reversible system. This is indicative of the quasi-reversible electron transfer kinetics described earlier. As can be seen in Table 3.8, the measured surface areas (planar area) of the P1E electrodes are relatively close to their intended active areas (design area). Note that the perimeter : area ratios calculated in Table 3.5 compare designs A–E, where as Table 3.8 refers to the subelectrodes of design E.

Electrode	Slope	Offset	Planar Area (cm^2)	Design Area (cm^2)	Ratio (%)
E-100	9E-05	5E-06	3.07E-02	3.14E-02	97.64
E-76	6E-05	3E-06	2.05E-02	2.39E-02	85.57
E-9	7E-06	8E-07	2.39E-03	2.83E-03	84.31
E-7	6E-06	7E-07	2.05E-03	2.20E-03	92.96
E-5	5E-06	6E-07	1.70E-03	1.57E-03	108.55
E-3	3E-06	3E-07	1.02E-03	9.42E-04	108.55
E-1	1E-06	1E-07	3.41E-04	3.14E-04	108.48

Table 3.8: Results of ferrocyanide probing of P1E electrodes. Slope and offset are taken from a plot of peak current vs. square root of scan rate. Planar area is calculated using slope in place of current in Equation 2.16. Design area is sum of circular regions, excluding tracks. Ratio is calculated as $\frac{\text{Planar Area}}{\text{Design Area}} \times 100$.

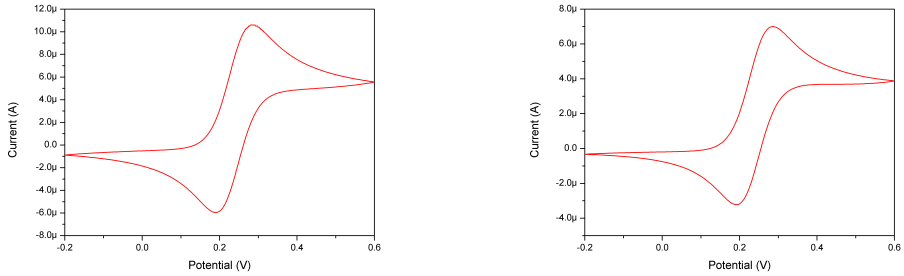

(a) P1E-100 (b) P1E-76

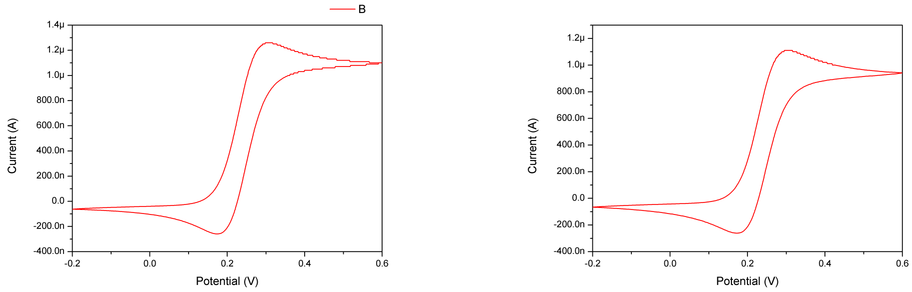

(c) P1E-9 (d) P1E-7

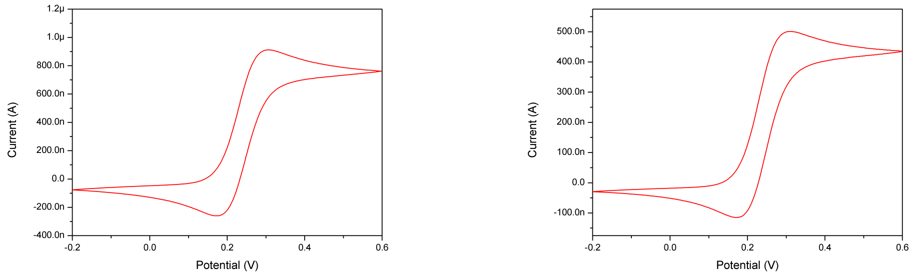

(e) P1E-5 (f) P1E-3

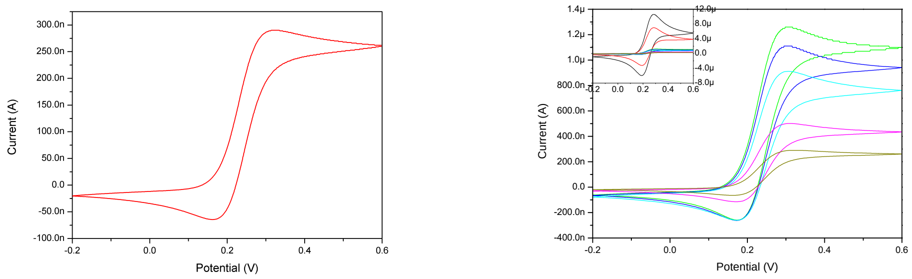

(g) P1E-1 (h) Overview

Figure 3.8: Cyclic voltammograms showing probing of P1E electrodes using 4 mM potassium (II) ferrocyanide over a potential range of 0.6 V to −0.2 V at a scan rate of 4 mV/s. Note that the voltammograms are on different scales with peak currents ranging from 11 μA for P1E-100 to 300 nA for P1E-1. This can be observed better in Figure 3.8h. Also of note is the transition from a redox peak character seen in Figures 3.8a and 3.8b to microelectrode-like behaviour seen in Figures 3.8c–3.8g.

3.4.3 Electrochemical Impedance Spectroscopy (EIS) of EO_3 Cholesterol and 6-Mercaptohexanol Self Assembled Monolayers

EO_3C and 6MH SAMs were formed on P1 electrodes and studied with EIS. EO_3C SAMs shown in Figures 3.9a and 3.9b can be seen to cluster into two populations. The lower set of SAM capacitances appears to be clustered around a limiting value equivalent to 1.04 μF cm^{-2}, while the upper set is closer to 1.37 μF cm^{-2}. When taken together these give an average capacitance of 1.22 ± 0.11 μF cm^{-2}. Equivalent circuit analysis (Table 3.9) shows the SAMs to be of high quality with α values of approximately 0.98 when modelled with a CPE, and a resistance of 2.38 ± 1.40 MΩ.cm^2. The lower value is likely to be representative of a true 100% EO_3C SAM, while the upper value is probably due to defects in the SAM. Previous studies by Jeuken et al. [2007b] found 100% EO_3C SAMs to have capacitances of approximately 1 μF.cm^{-2}, agreeing with the lower set of capacitance data.

6MH SAMs seen in Figures 3.9c and 3.9d present a more continuous distribution of capacitances, ranging from 3.22 μF cm^{-2} to 4.40 μF cm^{-2} and giving an average of 3.83 ± 0.13 μF cm^{-2}. These also have a reasonably high α value and SAM resistance, of approximately 0.99 and 5.56 ± 1.15 MΩ.cm^2 respectively, indicating high quality SAMs.

System	100% EO_3C	100% 6MH
n	4	11
C_{SAM} (μF cm^{-2})	1.22 ± 0.11	3.83 ± 0.13
Q_{SAM} (μF cm^{-2})	1.55 ± 0.24	4.44 ± 0.08
α_{SAM}	0.978 ± 7.62e-3	0.985 ± 2.04e-3
R_{SAM} (MΩ cm^2)	2.38 ± 1.40	5.56 ± 1.15

Table 3.9: EISFit parameters for 100% EO_3C and 100% 6MH SAMs formed on P1 electrodes. All SAMs fitted to a R(QR) equivalent circuit. C_{SAM} is obtained by doubling the height of the capacitance semi-circle in Normalised Admittance Plots (Figures 3.9b and 3.9d) and normalising by the electrode area. Q_{SAM} is taken from equivalent circuit fitting using the aforementioned R(QR) circuit.

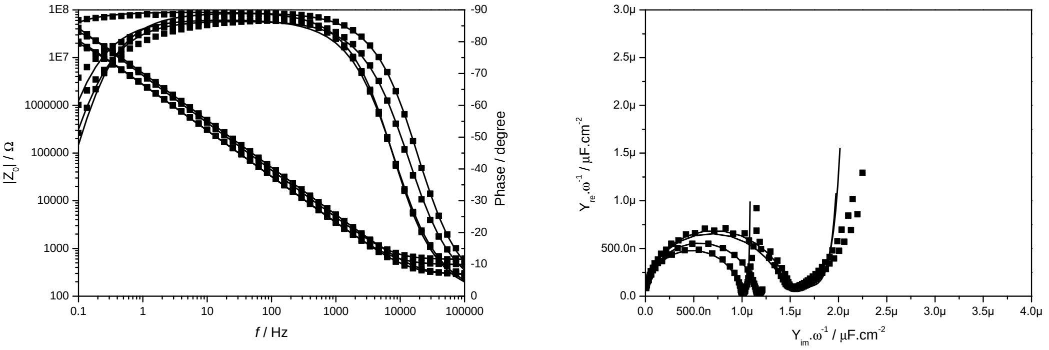

(a) EO_3C - Bode Plot

(b) EO_3C - Normalised Admittance Plot

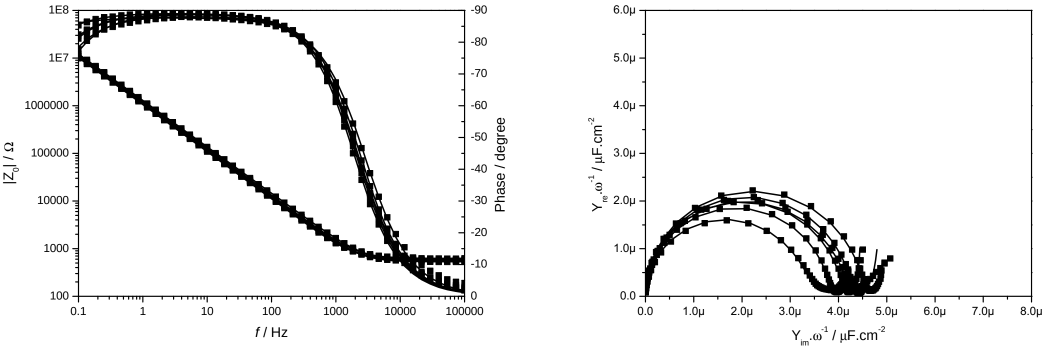

(c) 6MH - Bode Plot

(d) 6MH - Normalised Admittance Plot

Figure 3.9: EIS of P1 electrodes with 100% EO_3C or 100% 6MH SAMs. Modelled with EISFit using a R(QR) equivalent circuit

3.4.4 Formation of Tethered Bilayer Lipid Membranes

SAMs were formed by immersing electrodes in propanolic solutions of either 0.1 mM EO$_3$C, or approximately 0.11 mM EO$_3$C and 0.89 mM 6MH overnight. These were interrogated with EIS and the surface coverage of EO$_3$C calculated using Equation 3.1. The surface coverage of the electrodes varies with several factors thought to play a role in the SAM formation kinetics including relative concentrations of thiols, temperature, electrode surface topography and electrode surface chemistry[Jeuken et al., 2007b]. Given the difficulty in controlling these factors, SAMs are formed, interrogated and classified into three main groups which are studied below - 100% EO$_3$C (when using only EO$_3$C in solution), 80% EO$_3$C (calculated surface coverages of 60-90%, when forming a mixed SAM) or 40% EO$_3$C (calculated surface coverages less than 60%, when forming a mixed SAM). These three classifications have been made on the basis of ionophore activity experiments done in Chapter 4.

tBLMs were formed on these SAMs via the addition of *E. coli* polar lipid extract in the form of SUVs, together with 10 mM Ca^{2+}. The latter has been shown to be necessary to induce vesicle rupture leading to bilayer formation[Jeuken et al., 2005]. The resultant bilayer capacitances are a significant drop from that of the SAM and makes bilayer formation relatively easy to detect (Figure 3.10).

System	100% EO$_3$C	80% EO$_3$C	40% EO$_3$C
n	5	10	3
Circuit	R(QR)	R(QR)	R(QR)(QR)
C$_{\text{tBLM}}$ (μF cm^{-2})	0.72 ± 0.06	0.73 ± 0.01	0.76 ± 0.03
Q$_{\text{tBLM}}$ (μF cm^{-2})	1.34 ± 0.20	1.58 ± 0.12	4.03 ± 1.54
α_{tBLM}	0.945 ± 1.12e-2	0.926 ± 8.80e-3	0.964 ± 3.41e-2
R$_{\text{tBLM}}$ (MΩ cm^{2})	2.38 ± 1.40	1.35 ± 0.26	1.177e-2 ± 9.32e-3
Q$_{\text{SAM}}$ (μF cm^{-2})	-	-	4.13 ± 0.49
α_{SAM}	-	-	0.900 ± 2.29e-2
R$_{\text{SAM}}$ (MΩ cm^{2})	-	-	4.68 ± 0.59

Table 3.10: EISFit parameters for tBLMs formed on either 100%, 80% or 40% EO$_3$C SAMs with P1 electrodes. tBLMs are fitted to either R(QR) or R(QR)(QR) circuits. C$_{\text{tBLM}}$ is obtained by doubling the height of the capacitance semi-circle in Normalised Admittance Plots (Figures 3.10b, 3.10d and 3.10f) and normalising by the electrode area. Q$_{\text{tBLM}}$ is taken from equivalent circuit fitting using the aforementioned circuits.

100% EO$_3$C SAMs, as seen in Figure 3.10b, gave a bilayer capacitance of 0.72 ± 0.06 μF cm^{-2}, which agrees with previously quoted values between 0.6 and 0.8 μF cm^{-2}[Jeuken et al., 2007b]. Equivalent circuit analysis, shown in Table 3.10, gives the fitted circuit a high α value and a high resistance indicating a high quality tBLM with few defects. Due to the close-packed nature of the cholesteryl SAM, a phospholipid monolayer forms on the surface of the SAM. This arrangement is referred to as a hybrid BLM (hBLM) rather than a tethered BLM (tBLM) that is formed when a lipid bilayer is present, as described in Section 1.3.3. While this system has its uses, it is deemed unsuitable for the study of integral membrane proteins due to the fact that the close-packed EO_3C SAM does not provide room for protein to incorporate.

Mixed EO_3C:6MH SAMs with their hydrophilic 6MH recessed domains are likely to be more suited to the study of membrane proteins as there will be regions of the tBLM where a full lipid bilayer exists for the membrane protein to traverse, as well as a hydrophilic submembraneous environment to support extra-membraneous protein domains (see Chapter 4). tBLMs formed on SAMs of approximately 40% EO_3C, such as those shown in Figures 3.10e and 3.10f have a similar capacitance to the hBLMs formed on 100% EO_3C (0.76 ± 0.03 μF.cm^{-2}) and α values in the region of 0.96. Unlike the previously described hBLMs, they also present a second capacitance semi-circle as seen Figure 3.10f, which varies from 1.50 to 2.81 μF cm^{-2}. It is possible that this second semi-circle represents the capacitance of the SAM accessible via bilayer defects. The tBLM resistance is far lower than those formed on 100% EO_3C SAMs, as can be seen by the dip at 10–100 Hz in Figure 3.10e, using equivalent circuit analysis with the R(QR)(QR) circuit shown in Figure 4.2, this resistance is found to be 11.77 ± 9.32 kΩ.cm^2. This behaviour is due to the low proportion of the surface covered by EO_3C. Previous work done by Jeuken et al. [2007b] has shown that 60% surface area coverage with EO_3C is required to produce an optimum tBLM on template stripped gold.

tBLMs formed on 80% EO_3C SAMs presented only a single capacitance semi-circle equivalent to 0.73 ± 0.01 μF.cm^{-2} (Figure 3.10d). Equivalent circuit analysis showed the α value for the tBLM to be relatively low at 0.93. This is due to the heterogeneity of the mixed SAM, with domains of EO_3C and 6MH existing on various scales as has been shown by AFM[Jeuken et al., 2007b]. These heterogeneities are reflected in the lipid bilayer. The tBLM was also shown to have a resistance of 1.35 ± 0.26 MΩ.cm^2 - an increase by two orders of magnitude, compared to SAMs with only 40% EO_3C. This resistance is comparable to previous work on the same system using template stripped gold[Jeuken et al., 2007a, b], as well as other tBLM systems such as the yeast cell membranes of Jadhav et al. [2008] and diphatanoyl archae lipid analogues as used by Koper [2007]; Naumann et al. [2003a]; Terrettaz et al. [2003]; Vockenroth et al. [2007] and others, all of which gave membrane resistances in excess of 1 MΩ.cm^2 and in some cases exceeding 10 MΩ.cm^2. It should be noted that these systems are comprised of 100% tether SAM and should therefore be compared to the pure EO_3C system which had a bilayer resistance closer to 2.38 ± 1.40 MΩ.cm^2 and compares well. A review by Janshoff and Steinem [2006] gave membrane resistances in the range 0.1–10 MΩ.cm^2 as all being within normal limits.

Several P1 electrode designs were compared for their ability to host a good quality tBLM. As can be seen in Figure 3.11, there are some minor variations in the tBLM resistance across the range of electrode designs. To check the effect of electrode size on bilayer resistance, several electrodes of each design were tested by forming tBLMs on 80% EO_3C SAMs. Equivalent circuit analysis with a R(QR) circuit was used to estimate the tBLM resistance as shown in Figure 3.11. As can be seen the membrane resistance for the P1A and P1E electrodes show resistances of 1.21 ± 1.12 and 1.45 ± 0.87 $M\Omega.cm^2$, respectively, whereas the P1B and P1C present lower membrane resistances. It is hoped that the addition of an insulating layer across the tracks in later designs will improve the tBLM resistance further by removing the tracks as active regions. The number of replicates for each design is stated on the figure. As can be seen the number of replicates is small in some cases, and would benefit from a larger data set. The differences between electrodes A, B, C, and E are not very significant, however samples containing valinomycin have been added for comparison. As can be seen the tBLM resistance is significantly lower, approximately 15.9 $k\Omega.cm^2$. This shows that the tBLM resistance difference is large enough that ionophore-mediated ion transport will be detectable in the majority of tBLMs.

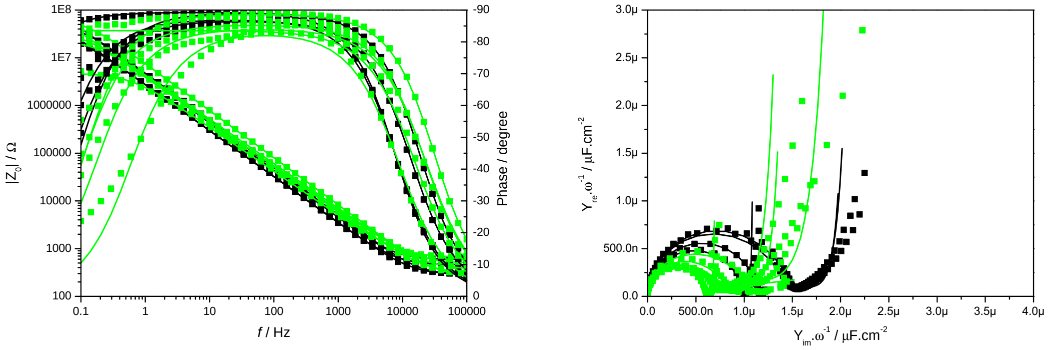

(a) 100% EO_3C - Bode Plot (b) 100% EO_3C - Normalised Admittance Plot

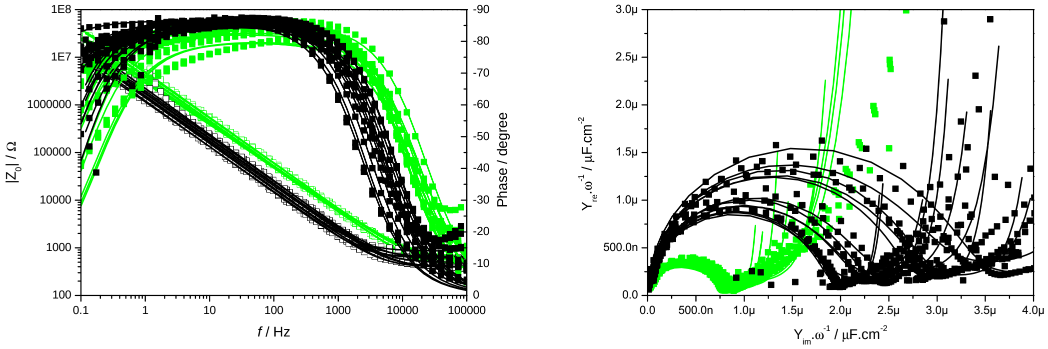

(c) 80% EO_3C - Bode Plot (d) 80% EO_3C - Normalised Admittance Plot

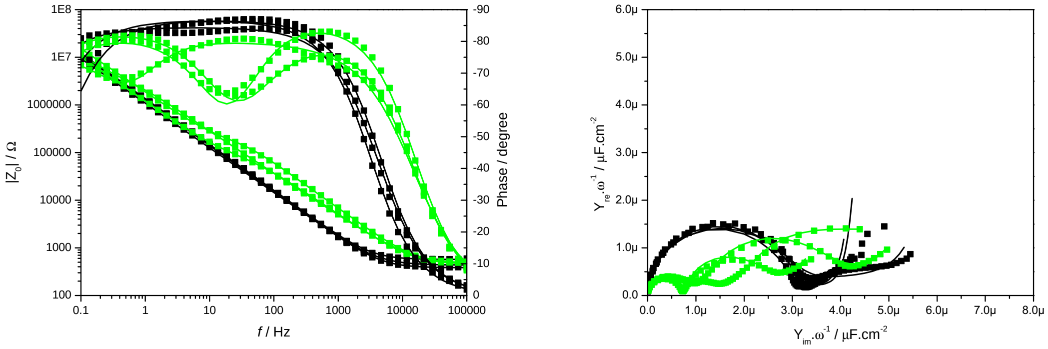

(e) 40% EO_3C - Bode Plot (f) 40% EO_3C - Normalised Admittance Plot

Figure 3.10: Cole-Cole and Bode plots showing the effect of BLM formation on 100% EO_3C surface coverage (hBLM) and mixed (40% or 80% EO_3C surface coverage, tBLM) SAM. Measured in 30 mM Na_2SO_4 buffer. Black = SAM; Green = Bilayer after washing.

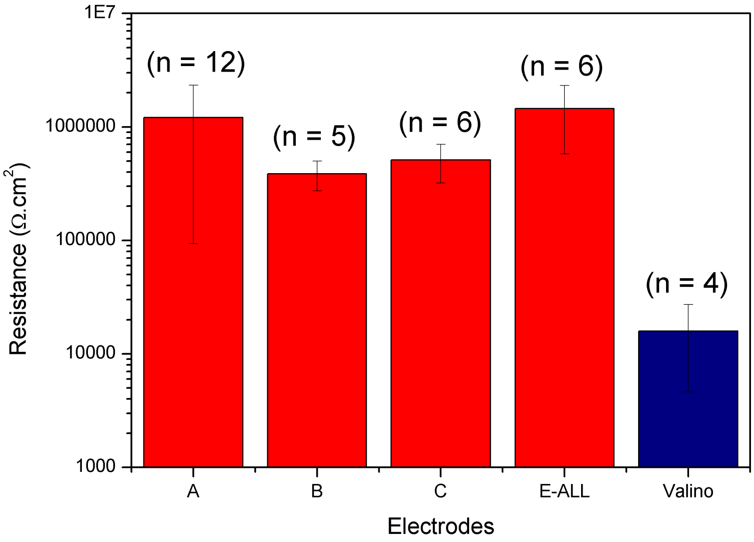

Figure 3.11: The average tBLM resistances measured for each electrode design. Resistance is normalised to electrode design area (see Table 3.5), Ω.cm^2, with error bars and shown on a logarithmic scale. Valinomycin resistance measured in buffer containing 30 mM K^+. Red = bilayer with no valinomycin in 30 mM Na_2SO_4 buffer; Blue = bilayer with valinomycin in 30 mM K_2SO_4 buffer. n is the number of replicates used in the figure.

3.4.5 Conclusions and alterations to be made

The first generation of Philips electrodes have been shown to be very effective in their role as a reusable surface for SAM and tBLM formation. AFM studies have shown that the surface is approaching the quality expected of template stripped gold, and a substantial improvement on the previously used evaporated gold.

EIS has been used to study the formation of EO_3C and 6MH SAMs, and shown both to be of high quality and with a good degrees of reproducibility. EIS has also been used to compare the tBLMs formed on EO_3C and mixed SAMs of varying EO_3C:6MH proportions. While tBLM capacitance remained around 0.75 μF.cm^{-2} in all cases, the tBLM resistance improved with increasing concentration of EO_3C. The difference between 100% and 80% EO_3C is comparatively small however when compared to that of tBLMs formed on 40% EO_3C SAMs. This highlights the importance of only using SAMs with a high proportion of EO_3C. Previous work by Jeuken et al. [2007b] has shown 60% EO_3C to be a reasonable lower limit in this regard. Furthermore, the tBLM resistances are comparable to others found in literature.

While these electrodes have been highly successful, I feel improvements can be made particularly with the addition of an insulating layer. This would limit the active electrode area to the pixel regions of the electrode by insulating the electrode tracks. Given that lipid bilayers can be formed on SiO_2 there is a possibility that tBLM resistance may be improved by minimising edge defects. The inclusion of on-chip counter and reference electrodes may also be of benefit in the future.

3.5 Philips Research Electrodes: Series 2 - MKI

This generation of electrodes was designed to include a 500 nm thick SiO_2 insulating layer that would be deposited over the top of the sputtered layers of 20 nm Ti and 200 nm Au as found in the previously studied generation. This would have the effect of restricting the 'active' electrode areas to just the gold pixels, rather than including any track areas that were previously exposed to the electrolyte. This insulating layer would also protect the 20 μm wide electrode tracks from damage that could affect measurements taken of the active areas. The basic design of the C and E type electrodes were brought forward, and a new F type electrode added based on the E type but with pixels an order of magnitude smaller. The design parameters of these designs can be found in Table 3.11. Additionally the connectors at the far end of the electrode were designed to use the same pitch as a PCI connector, thus providing a readily available connection to interrogate individual electrode pixels. To pave the way for the third generation of electrodes, space for on-chip secondary electrodes was also included. These secondary electrodes were envisaged to include a Pt track for use as a counter electrode, another Pt track for use as a high frequency pseudo-reference electrode as detailed by Ecochemie [2003], and an Ag track for use as a reference electrode following electrodeposition of AgCl.[Zhou et al., 2010]

Design	Number of Electrodes	Radius (mm)	Area (cm^2)	Perimeter (mm)	Ratio
C	9	0.33	3.42E-03	2.073	6.1
E	100	0.10	3.14E-04	0.628	20.0
F	100	0.01	3.14E-06	0.063	200.5

Table 3.11: Dimensions of Philips 2nd generation (P2) electrodes. Areas and perimeters are given for individual electrodes, excluding tracks. Ratio is calculated as $\frac{\text{Perimeter (mm)}}{\text{Area (mm}^2)}$.

In this generation, henceforth termed P2 MKI, the insulating layer was deposited directly on to the gold surface with the aim of better defining the electrode area. However, upon use in electrochemical experiments it became evident that the electrode surface was less well defined than the P1 electrodes, with large variations in the capacitance of SAM-modified electrodes and the currents measured with redox probes.

3.5.1 Electrochemical Impedance Spectroscopy of 6MH and EO_3C SAMs

The EO_3C and 6MH SAMs shown in Figure 3.12 were formed on these electrodes and found to have capacitances that deviated significantly from previously determined values. P1 electrodes with EO_3C SAMs had been determined to have a capacitance of 1.22 ± 0.11 $\mu F.cm^{-2}$, whereas when formed on P2 MKI electrodes the capacitance is much lower in all cases. Similarly, the capacitance of 6MH-modified P2 MKI electrodes varied greatly, as can be seen in Table 3.12, whereas the 6MH SAMs had previously been determined to have a capacitance of 3.83 ± 0.13 $\mu F.cm^{-2}$ on P1 electrodes.

This could suggest that the SAMs are forming improperly, or that the electroactive surface area is ill-defined. The cause of this variation was investigated further using several techniques detailed below.

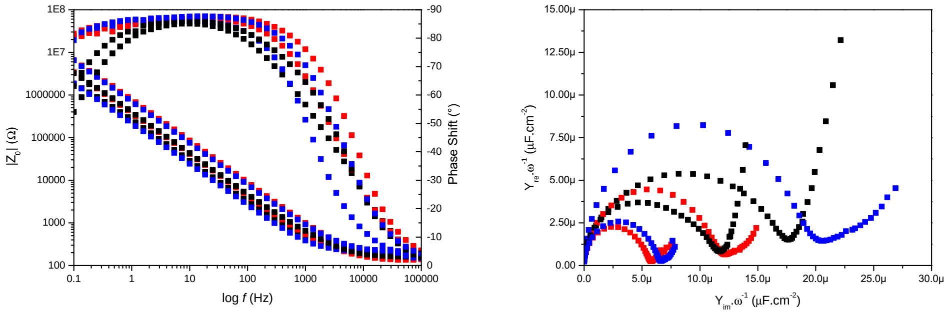

(a) 6MH - Bode Plot (b) 6MH - Normalised Admittance Plot

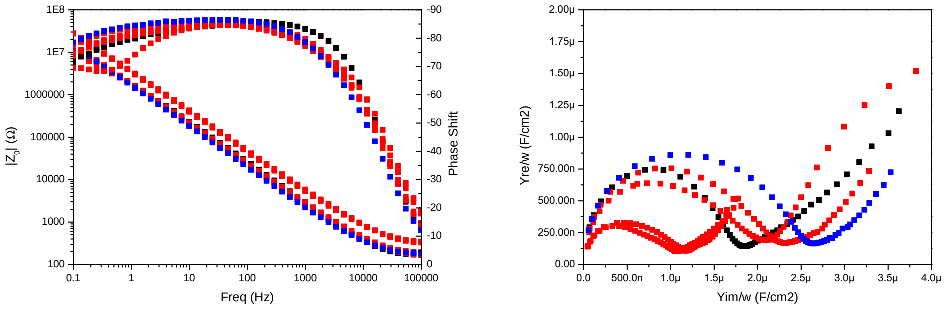

(c) EO3C - Bode Plot (d) EO3C - Normalised Admittance Plot

Figure 3.12: EIS of P2 MKI electrodes indicating a variable surface area. Black = not cleaned; Red = soaked in 4 M NaOH; Blue = sonicated in 4 M NaOH.

Sample	6MH	EO3C
Uncleaned	4.54 ± 1.20	0.744
NaOH	3.36 ± 1.55	0.506 ± 0.225
Sonicated	5.40 ± 4.00	0.861

Table 3.12: Comparison of cleaning methods and their effects on capacitance of 6MH and EO3C SAMs. 6MH was previously determined to have a normalised capacitance of 3.83 μF.cm^{-2}. EO3C was previously determined to have a normalised capacitance of 1.18 ± 0.24 μF.cm^{-2}.

3.5.2 Light microscopy

Viewing the electrodes under the light microscope gave an indication of the state of the electrode surface. As can be seen in Figure 3.13a, the SiO_2 insulating layer appears to be largely intact and overlaps the electrode surface by approximately 10 μm. Defects become apparent however upon inspection of the track regions in Figure 3.13b.

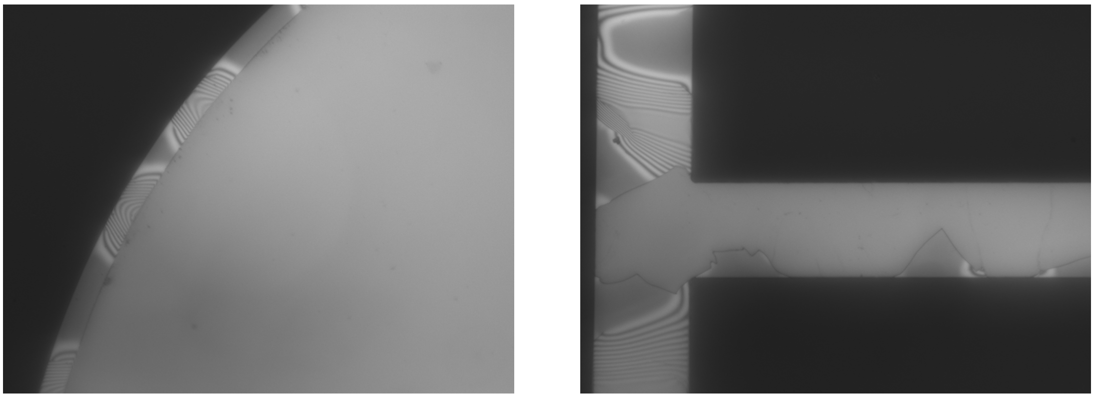

(a) Intact edge

(b) Delaminated track

Figure 3.13: Light microscope images of first iteration P2F electrodes suffering from delamination of the SiO_2 insulating layer.

3.5.3 Scanning Electron Microscopy and Scanning Auger Electron Spectroscopy

Following examination by light microscopy, the nature of the surface defects was examined by SEM and SAES. Figure 3.14 shows a comparison of electrodes before (Figures 3.14a and 3.14b) and after (Figures 3.14c and 3.14d) exposure to solvent. Figure 3.14c clearly shows areas of lighter contrast on the tracks in a manner that is very similar to that seen in Figure 3.13. The nature of these areas of contrast can be seen in Figure 3.14d, a scanning Auger electron spectroscopy contrast map of the O KVV peak between 505.0 eV and 508.7 eV. Light areas indicate regions of high levels of molecular oxygen, in this case associated with the SiO_2 insulating layer. The dark areas indicate very low levels or an absence of oxygen. As such it can be seen that regions of SiO_2 have been removed uncovering an underlying layer low in oxygen moieties. This is in all probability the Au layer. While the arms of the ‘cross’ to the top and right of the intersection have been removed, the arm to the left of the intersection appears to have begun delamination but the SiO_2 is still attached.

In comparison to Figures 3.14c and 3.14d, Figures 3.14a and 3.14b exhibit none of these features suggesting that the SiO_2 layer is undisturbed. Contrast can be seen in Figure 3.14b, however this is due to the central window in the SiO_2 insulation that defines the area of the active electrode.

3.5.4 Conclusions and alterations to be made

EIS analysis of EO_3C and 6MH SAMs showed them to be poorly reproducible on these electrodes. While the cause of this irreproducibility was uncertain, microscopy and Auger electron spectroscopy contrast mapping showed conclusively that delamination is observed on Au electrodes insulated with SiO_2. The delamination of the electrodes is particularly problematic given the asystematic nature of the process. This results in a highly variable active electrode area. Furthermore, delamination may occur following SAM formation, leading to areas of the electrode being exposed. These regions will be devoid of SAM, with the bare Au having a large influence on the capacitance recorded. A comparison between samples that have either been used as received, or immersed in solvent during the cleaning process, indictates that the observed delamination is a solvent-mediated effect. Given that exposure of the electrodes to solvent is required for cleaning protocols and electrochemical experiments, it is clear that steps must be made to prevent this process. The addition of an adhesion layer between the Au and SiO_2 layers should be sufficient to ensure the stability of the SiO_2 insulation layer.

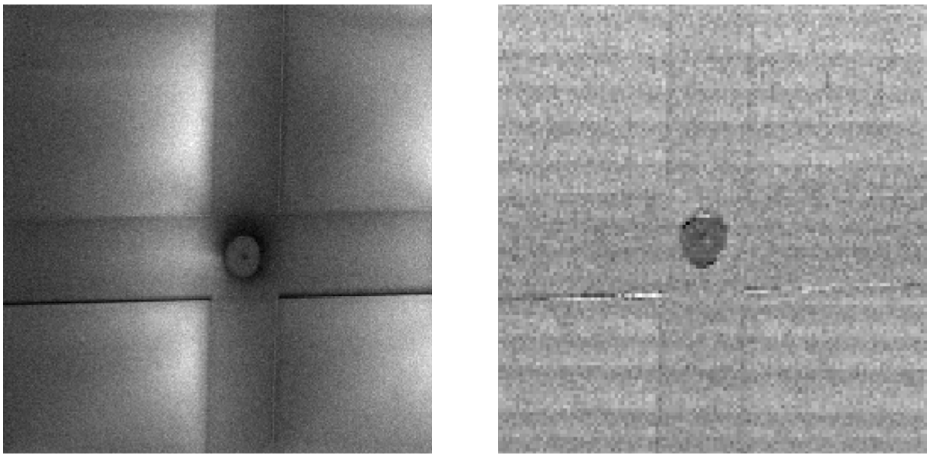

(a) SEM - Intact SiO_2 (b) SAES - Intact SiO_2

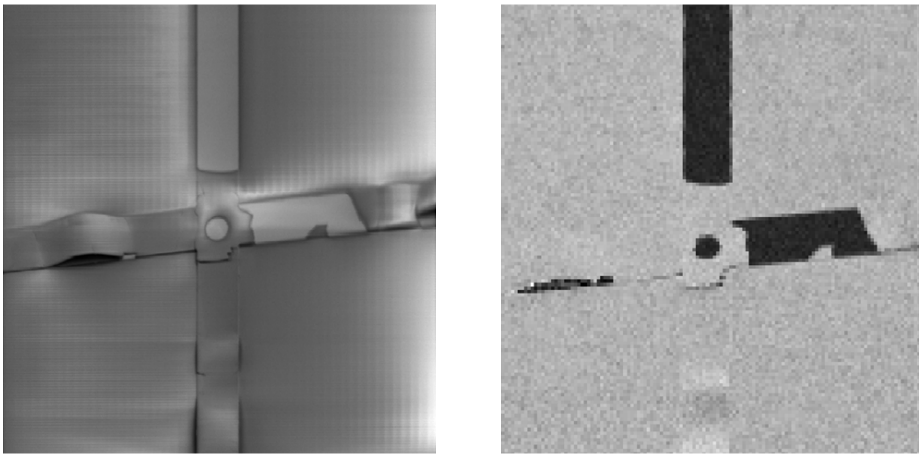

(c) SEM - Delaminated SiO_2 (d) SAES - Delaminated SiO_2

Figure 3.14: Scanning electron microscopy (SEM) and Scanning Auger emission spectroscopy (SAES) contrast maps of P2 MKI F electrodes. (a) and (b) Electrode prior to solvent exposure; (c) and (d) Electrode with solvent exposure. Contrast maps are generated from the O KVV peak intensity at 506.8 eV compared to the background intensity at 517.8 eV using the equation (Peak-Background)/(Peak+Background). White areas are indicative of the presence of atomic oxygen.

3.6 Philips Research Electrodes: Series 2 - MKII

Following analysis of the P2 MKI electrodes, a new batch of P2 electrodes was fabricated utilising a 20 nm thick Ti adhesion layer to prevent delamination of the SiO_2 insulation layer.

3.6.1 Cyclic Voltammetry

Electrodes were initially studied with cyclic voltammetry using a $Ru(NH_3)_6Cl_2$ redox probe. Black plots in Figure 3.15 show the electrochemical behaviour of the electrodes to be poor as detailed below. In an attempt to improve the electrodes they were incubated in 4 M NaOH. As can be seen from the red plots in Figure 3.15, this cleaning step has a huge effect on both the size of peaks and their positions indicating a change in the surface chemistry.

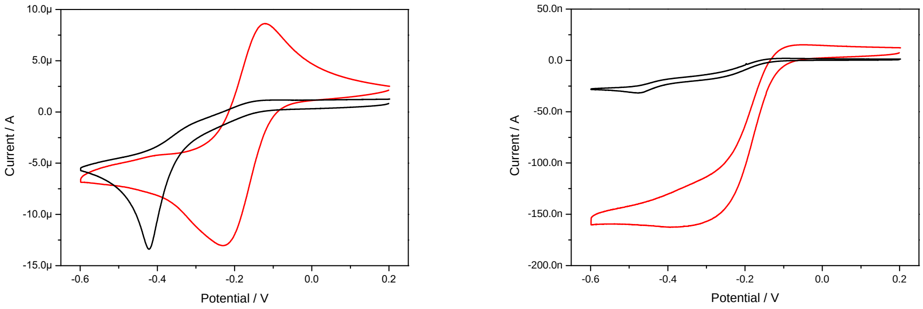

(a) P2 MKII C (b) P2 MKII F

Figure 3.15: CV of P2 MKII electrodes using the $Ru(NH_3)_6Cl_2$ redox probe at a scan rate of 640 $mV.s^{-1}$. Scans were taken to compare the effect of cleaning the electrodes with 4 M NaOH. Black = Cleaned according to established cleaning protocol; Red = Soaked in 4 M NaOH prior to established cleaning protocol.

Figure 3.15a shows the effect on P2MKII C electrodes. The reductive peak retains its amplitude, but the peak shifts from -420 mV (vs Ag/AgCl) to -230 mV following the NaOH cleaning step. Additionally, the morphology of the peak changes drastically. The oxidative peak is not visible prior to NaOH cleaning, however the expected peak shape develops with an amplitude of 8.62 μA at a potential of -121 mV following NaOH.

Figure 3.15b shows the effect on P2MKII F electrodes. Of immediate notice is the large difference in the size of the peaks with the NaOH cleaned electrode having an amplitude of 160 nA, compared to just 32 nA without NaOH cleaning. While the morphology of the uncleaned sample remains similar to that seen in Figure 3.15a, the NaOH cleaned sample has changed from peaks to waves that plateau, indicating microelectrode behaviour.

The stark contrast between voltammograms before and after the NaOH cleaning step indicates that a change is going on at the electrode surface. In Figure 3.15b, there are two peaks visible - the large reductive peak at -480 mV, and a smaller underlying wave around -280 mV which is at a similar potential to that seen in the NaOH cleaned sample in Figure 3.15a and is most a $Ru(NH_3)_6Cl_2$ peak. This could be attributed to an isolating substance on the surface that is removed by the NaOH cleaning step and/or it could be the result of a porous layer on the surface which affects the rate of diffusion between the active electrode surface and the bulk $Ru(NH_3)_6Cl_2$.

Additionally, the shift in voltammogram morphology from peaks to waves in Figure 3.15b is characteristic of a system unconstrained by diffusion. These electrodes are substantially smaller than the C and E type electrodes studied previously and approach the dimensions that are characteristic of microelectrodes as described in Section 2.2.2. A hemispherical diffusion profile results in access to a substantially larger amount of $Ru(NH_3)_6Cl_2$ such that the voltammograms adopt this non-diffusion limited behaviour. This also results in the large increase in the magnitude of the peaks as more $Ru(NH_3)_6Cl_2$ is accessible to the electrode surface following the NaOH cleaning step - further evidence to suggest that a barrier layer is found on the electrode surface, which is removed by NaOH.

3.6.2 EIS

Unused P2 MKII electrodes were immersed in 4 M NaOH for 3 hours prior to the established cleaning procedure described in Section 3.2.3 and ODT SAMs formed.

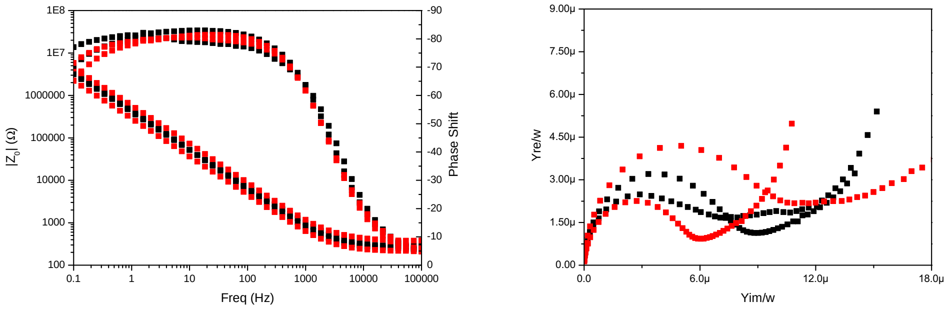

(a) ODT - Bode Plot (b) ODT - Normalised Admittance Plot

Figure 3.16: EIS of ODT SAMs formed on P2 MKII electrodes. Large variability between samples and v high capacitances suggests that incomplete SAMs are forming in an asystematic manner. Black = P2C; Red = P2E. Surface area for each is designed to be 0.03142 cm^2. Literature value for ODT capacitance $= 1.04 \pm 0.005$ $\mu F.cm^{-2}$.

As can be seen from Figure 3.16a, the SAMs have a maximal phase shift ranging between -80°and -83°suggesting a degree of surface heterogeneity. Total impedance at 100 mHz ranges from 2 MΩ to 5 MΩ, values which are within normal limits for this system. Figure 3.16b shows drastically changing capacitances ranging from 4.51 to 8.38 $\mu F.cm^{-2}$, a very substantial deviation from the literature value of 1.04 ± 0.05 $\mu F.cm^{-2}$, which was well reproduced in Section 3.3. This would suggest that SAMs are only forming on a portion of the total electrode area, with the remaining area most likely to be covered with material obstructing the underlying Au layer thus preventing SAM formation.

3.6.3 Microscope data

To investigate what was happening on the surface, an optical microscope fitted with a blue band-pass filter (wavelength 390-490 nm) was used. This indicated non-uniform surface properties on a macroscale as can be seen in Figure 3.17. This electrode was subjected to the standard UV/O_3 cleaning protocol. The electrode has a smooth grey appearance for a large proportion of its surface, with a small brighter patch near the bottom. On closer inspection of this bright region some darker material can be seen that appears to have peeled away from the electrode surface.

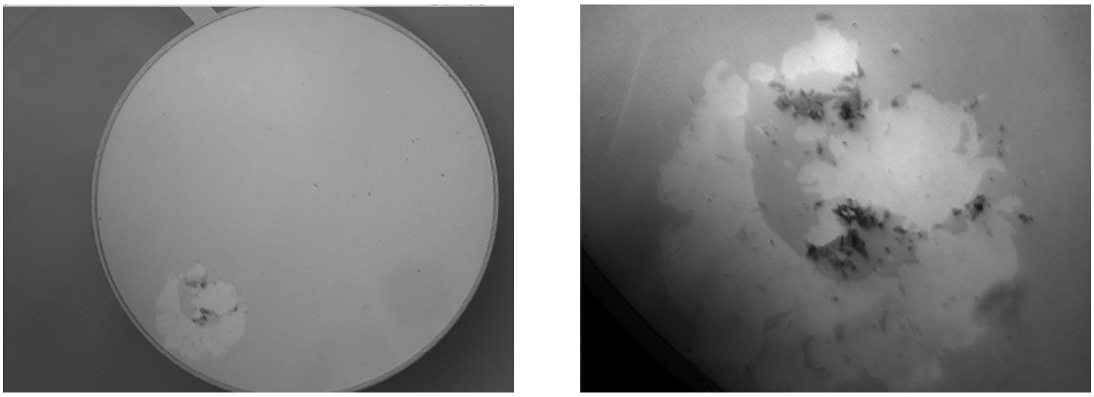

(a) x10 Magnification

(b) x40 Magnification

Figure 3.17: Initial state of electrodes.

Figure 3.18 shows another electrode submitted to 2 hours immersion in 4 M NaOH, followed by the standard cleaning protocol. The electrode still has a largely uniform grey surface, with brighter areas which are bordered by a similar peeling effect to that seen previously. The difference between these two samples is not sufficiently large to account for the drastic change seen in the electrochemistry experiments discussed earlier. A number of different parameters including immersion time, temperature and sonication were also explored but did not provide significant improvements.

Following initial trials with NaOH cleaning methods, more caustic methods were employed as can be seen in Figure 3.19. These included NoChromix, a chromate-free chromic acid analogue that provides a high degree of oxidising power (Figures 3.19a) and acetone (Figures 3.19b). Exposure to NoChromix solution for 20 hours resulted in severe pitting of the grey regions, with the bright areas remaining apparently unaffected. Despite this pitting effect there were only small gaps in the grey layer. Acetone proved to be reasonably effective with large areas of peeling occurring and fissures in the grey region appearing with bright areas being exposed. Longer exposure times were also investigated, but showed no visible improvement.

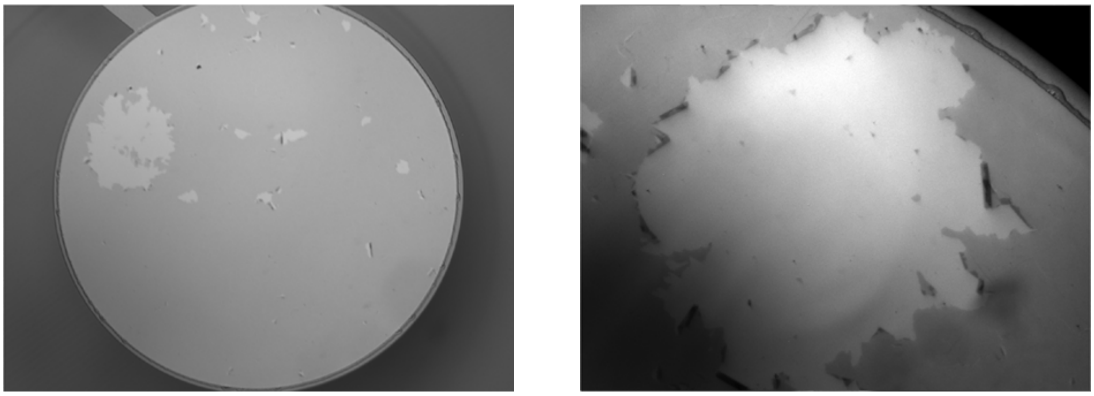

(a) x10 Magnification (b) x40 Magnification

Figure 3.18: Electrodes after 2 hours in 4 M NaOH.

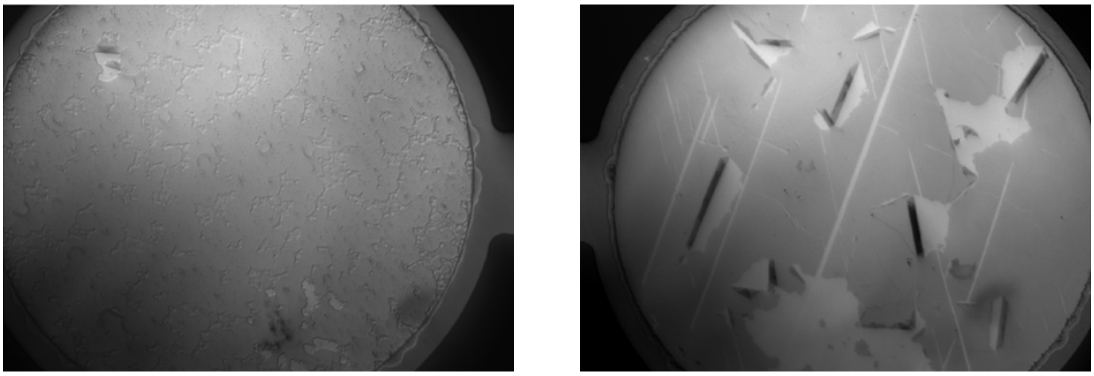

(a) 20 hours NoChromix, x10 Magnification (b) 20 hours Acetone, x10 Magnification

Figure 3.19: Electrodes following harsher cleaning methods.

3.6.4 XPS

X-ray photoelectron spectroscopy was employed to determine the chemical nature of the grey layer observed previously in Figures 3.17, 3.18 and 3.19. Two samples were studied - the first was subjected to the standard cleaning protocol, while the second was immersed in acetone for 20 hours prior to the standard cleaning protocol. The high resolution XPS peak data for these samples can be seen in Figure 3.20.

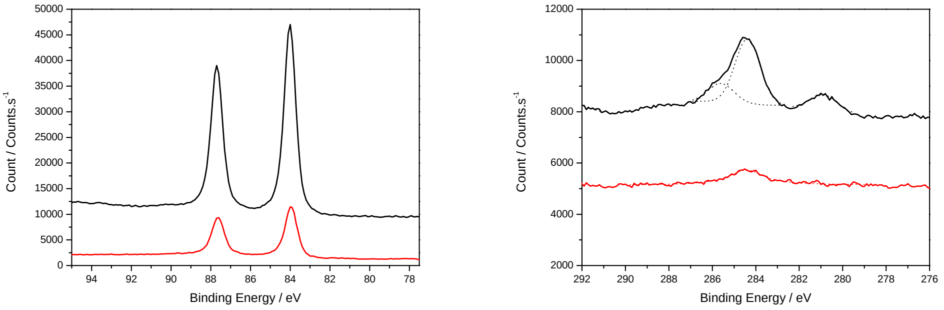

(a) Au 4f (b) C 1s

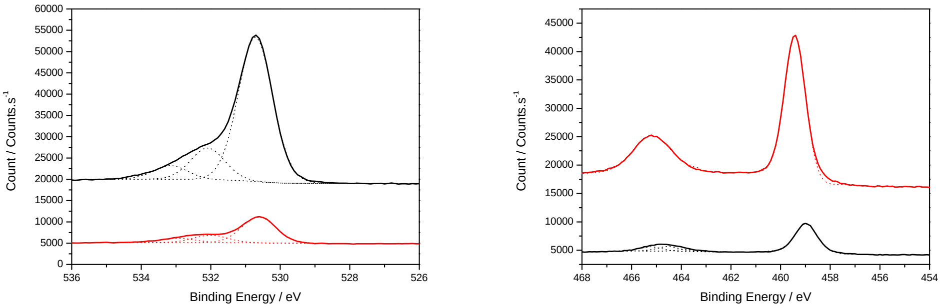

(c) O 1s (d) Ti 2p

Figure 3.20: XPS spectra of P2 MKII F electrodes before and after 20 hours exposure to acetone. Data show a large decrease in the size of the Ti 2p and O 1s peaks, but an increase as atomic percentage. Counts are much lower in acetone sample in general. Black = not cleaned; Red = following exposure to acetone for 20 hours. N.B. Intensities have not been normalised to the Au $4f_{7/2}$ peak.

Figure 3.20a shows the data for the Au 4f region of the X-ray photoemission spectrum from 77.0 - 95.0 eV. Two peaks can be seen in each sample at 84.0 eV and 87.7 eV, respectively. Of immediate interest is the substantial difference in the peak heights between the two samples. While there is always variation in the signal intensities between different samples due to the angle that the X-rays interact with the surface, how well focused they are on the sample and so on, the variation observed here is greater than normally expected. In light of the microscopy data obtained that shows substantial coverage of the electrode with a grey film despite the cleaning protocol it would be unwise to normalise the data according to the Au 4f peak as done in Figure 3.4. As such this analysis will not be considering the relative heights of the various peaks detected, only their positions. The peak at 84.0 eV, in Figure 3.20a, fits well with literature values for the Au $4f_{7/2}$ peak of Au which ranges from 83.7-84.3 eV. Similarly the peak at 87.7 eV correlates with the Au $4f_{5/2}$ peak of Au reported as ranging from 87.4-87.9 eV. Of particular note is the absence of a peak at 85.9 eV which would correspond to the Au $4f_{7/2}$ peak of Au_2O_3. This tells us that the surface contains metallic Au, but no traces of any Au oxides that could account for the poor SAM formation observed in EIS experiments.

Most notably, Figure 3.20d indicates dual peaks at 459-460 eV and 464.5-465.5 eV. These correlate well with literature values for the Ti $2p_{1/2}$ and Ti $2p_{3/2}$ peaks of TiO_2 at 464.3-464.7 eV and 458.3-459.2 eV, respectively. These are quite removed from the Ti $2p_{1/2}$ and Ti $2p_{3/2}$ peaks for metallic Ti which can be found at 460.0 eV and 453.2-454.3 eV respectively. The lack of any peaks in these regions suggests that the Ti is entirely in TiO_2 form.

Figure 3.20b investigates C 1s peaks in the range 276.0-292.0 eV. The predominant peak in both cases is the C 1s peak for atomic C at 284.6 eV, which has a range of 284.2-284.8 eV. A shoulder peak was also identified at 285.7 eV Additionally, the uncleaned sample contains a smaller peak at 281.0 eV, which correlates well with the C 1s peak of TiC, which covers a range of 281.4-281.7 eV. This suggests that there are a number of carbon contaminants, primarily in aspecific atomic forms, but also in small quantities as carbon contaminants in direct contact with titanium. When comparing the two samples it can be seen that the postulated TiC peak at 281.0 eV is only apparent in the sample not subjected to acetone cleaning. Whether this is a true indication of whether the acetone step has been of benefit is unclear, due to the low signal strength of the acetone cleaned sample, which could result in a potential TiC peak being drowned out by background noise as even the C peak is rather shallow.

Figure 3.20c shows the O 1s region, ranging from 526.0-536.0 eV. A peak is visible in both samples, being centred at 530.7 eV, with shoulder peaks present at 532 eV and 533 eV. The main peak correlates well with values for titanium oxide, TiO_2, which can be found in the range 529.7-530.2 eV, respectively. The O 1s peak for Au_2O_3 also can be found at 530.2 eV, which coincides with the main peak seen here. While Au_2O_3 signals could be overlapping with the titanium oxide signals, the lack of any gold oxide signals in Figure 3.20a suggests that this is unlikely. The shoulder peaks in the 532-533 eV region can be attributed to the SiO_2 insulating layer surrounding the electrode, which exists in the 532.0-534.3 eV part of the spectrum.

Based on the analysis conducted above, it is highly likely that the grey layer observed in Figures 3.17-3.19 is most likely due to TiO_2 deposits. The peaks observed in Figures

3.20b, 3.20c and 3.20d strongly indicates the presence of a TiO_2 layer.

To give some impression of the relative peak heights in a single sample, the ratio of the different peaks expressed as a percentage of the sum of these peaks can be found in Table 3.13. These ratios show little variation between the two samples suggesting that the acetone cleaning step is of limited use in removing the TiO_2 layer despite initial microscopy evidence shown in Figure 3.19a. The only benefit that can be observed is the previously discussed reduction in the relative magnitude of the C 1s peaks, particularly those associated with TiC, but even these could be an artefact of the low signal obtained.

Sample	Au 4f	C 1s	O 1s	Ti 2p
Not cleaned	14.58	16.05	47.66	21.72
Acetone	13.65	18.45	44.22	23.68

Table 3.13: XPS ratios of P2 MKII electrodes before and after cleaning with acetone. Ratios displayed as % of total counts.

3.6.5 Effect of HF Cleaning on Removal of TiO_2 Layer

Following the identification of the electrode surface contaminant as TiO_2, attempts were made to remove it as the TiO_2 layer as already explained in Section 3.6.3. XPS studies showed these attempts were unsuccessful and following discussions with Carl Glasse at Philips Research, it was decided that a harsh HF-based Ti etch may be of benefit in the removal of the TiO_2 layer. Fuming nitric acid (FNA) was used to remove organic material, followed by a Ti etch (7 H_2O : 2 FNA : 1 HF) heated to 48 °C for a several seconds. This mix was significantly more concentrated than that used originally in post-processing of the electrodes (165 H_2O : 5 FNA : 1HF).

The effects of this etching procedure were minimal, and these studies can be found in the appendices (Appendix B); however Martinez et al. [2010] provide evidence of the diffusion of Ti into Au when exposed to high temperatures (200 - 400°C). These temperatures are likely to have been achieved during the deposition of the SiO2 layer. Ti diffusion has been reported over distances of up to 260 nm making this a significant process that potentially results in Ti being dispersed throughout the Au layer. The paper further reports that this effect can be negated by replacing the Ti layer with TiN, which is more thermally resistant.

3.6.6 Conclusion

P2 MKI electrodes suffered from delamination of the SiO_2 insulating layer. However, the incorporation of a Ti adhesion layer resolved this issue. The new P2 MKII electrodes suffered from contamination of the Au electrode surface with Ti from the Ti adhesion layer. SAES showed widespread TiO_2 on the surface of the electrodes, leaving only very small patches of Au exposed. While attempts to remove this layer were made during manufacture of the electrodes, as well as following detailed analysis, it is hypothesised that Ti diffused into the Au layer. Based on the findings of Martinez et al. [2010], it is expected that Ti diffusion can be negated by replacing the use of Ti in the adhesion layer with TiN.

3.7 Philips Research Electrodes: Series 2 - MKIII

Following the Ti contamination issues faced with the P2 MKII electrodes, a new batch were manufactured utilising the higher melting point of titanium nitride (TiN). To protect the electrode surfaces during transit, a layer of photoresist was left on with acetone being recommended as a suitable solvent for its removal.

3.7.1 EIS of ODT SAM

Electrodes were immersed in acetone for 2 minutes or 2 hours, before further rinsing with acetone, propanol and methanol. The electrodes were then exposed to UV/O_3 and ethanol as per the established cleaning protocols.

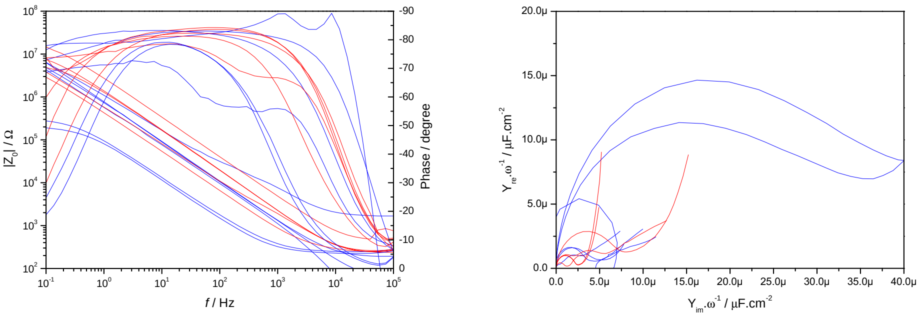

(a) ODT - Bode Plot

(b) ODT - Normalised Admittance Plot

Figure 3.21: EIS of ODT SAMs on P2 MKIII electrodes following acetone cleaning steps of varying lengths. Red = 2 minutes in acetone; Blue = 2 hours in acetone.

	2 mins	2 hours	Evap + EtOH
Circuit	R(QR)	R(QR)	R(QR)
n	5	6	5
C_{mean} (μF cm^{-2})	2.54 ± 1.86	11.66 ± 11.81	1.15 ± 0.02
Q_{mean} (μF cm^{-2})	7.30 ± 5.37	26.51 ± 28.81	3.05 ± 0.17
α_{mean}	0.905 ± 0.038	0.891 ± 0.075	0.986 ± 0.014
R_{mean} (kΩ cm^2)	2.94 ± 2.34	51.63 ± 70.57	3.25 ± 1.50

Table 3.14: EIS of ODT SAMs on P2 MKIII electrodes. Results for ODT SAM formed on evaporated Au ('Evap + EtOH') taken from Section 3.3 and shown for comparison. Values Q_{mean}, α_{mean} and R_{mean} obtained from equivalent circuit modelling software EISFit using a R(QR) circuit, where Q is the capacitance of a CPE and α is an indicator of SAM roughness. C_{mean} is obtained by doubling the height of the capacitance semi-circle in Normalised Admittance Plots (Figure **??**) and normalising by the electrode area. Q_{mean} is taken from equivalent circuit fitting using the aforementioned circuits. ODT capacitance in literature is 1.04 ± 0.05 μF cm^{-2}[Steinem et al., 1996].

As can been seen from Figure 3.21, acetone cleaning appears to have limited success in preparing the electrode surface for SAM formation. Figure 3.21b shows capacitances to vary wildly, while Figure 3.21a shows a range of defects including poor capacitor behaviour and low resistances.

3.7.2 XPS

XPS was used to follow the effect of acetone cleaning on the electrode, as well as to investigate any unexpected surface chemistry that may be interfering with SAM formation. Figure 3.22 shows the data collected of the Au 4f, C 1s, O 1s and Ti 2p peak regions of electrodes cleaned for varying lengths of time in acetone.

Figure 3.22a shows varying levels of Au, suggesting that the Au surface is initially blocked but exposed following an acetone cleaning step. Interestingly, the signal decreases in the ‘2 day’ sample suggesting that the surface has become occluded once more. In all cases, both the Au $4f_{5/2}$ and Au $4f_{7/2}$ transitions of metallic Au are visible at approximately 87.4 eV and 83.8 eV respectively. The lack of signal at 85.9 eV suggests no Au_2O_3 is present.

Figure 3.22b shows several peaks indicating carbon contaminations in a variety of chemical environments. The dominant peak in all samples is found at approximately 284.5 eV, the binding energy for the 1s transition of C with no affecting chemical environment. Additionally, in all samples there appears to be a second peak merged with the dominant peak at approximately 286.6 eV. The origin of this peak is undetermined. While the aforementioned peaks are present across all the samples, there are two further peaks seen in the uncleaned sample at 293.2 eV and 289.3 eV. These are not found in the ‘2 minute’ or ‘2 hour’ acetone cleaned samples, however the 289.3 eV peak reappears in the ‘2 day’ sample. While the identity of these peaks remain unclear, it is likely that they are due to C found in the complex chemical environment of a photoresist layer. This layer would be removed by acetone, however leaving the sample sitting in that same acetone/photoresist solution for a long period of time may result in a thinner photoresist layer being redeposited on the surface.

Figure 3.22c shows the region around the O 1s transitions. The uncleaned sample has a complex peak that can be deconvoluted to two peaks at 530.7/529.9 eV and 532.4/531.6 eV with peak fitting. These correspond to the 1s transitions of O in TiO_2 and SiO_2 respectively. After cleaning for 2 minutes or 2 hours these O 1s peaks have changed to a shallow hump that is most likely the product of two peaks at 533.0 eV and 531.3 eV. 533.0 eV is within the range expected for the 1s transition of O in SiO_2, but 531.3 eV is too high for TiO_2 (529.7-530.2 eV) or Au_2O_3 (530.2 eV). This leads me to look at other chemical environments of O with similar binding energies, of which there are a great many in this region including some organic compounds, metal oxides, hydroxides, carbonates and sulphates. None of these compounds standout as being highly likely, suggesting that this

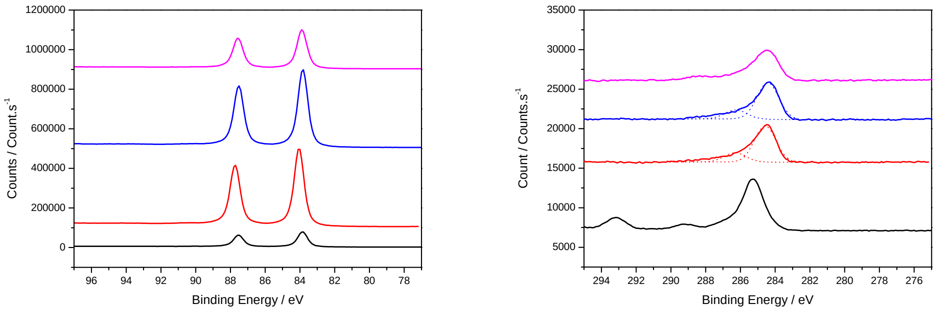

(a) Au 4f

(b) C 1s

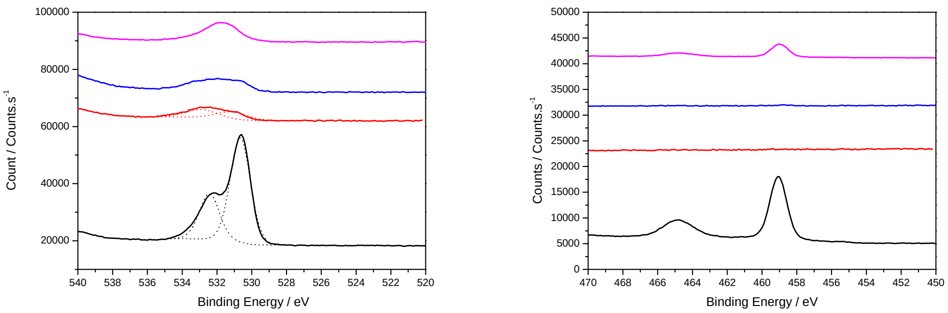

(c) O 1s

(d) Ti 2p

Figure 3.22: XPS spectra of P2MKIII electrodes following acetone cleaning steps of varying lengths. Black = 'No wash'; red = '2 mins'; blue = '2 hrs'; magenta = '2 days'.

peak is due to contamination. The source of contamination could be residue left over from removal of the proposed photoresist layer, which is masked by more substantial signals in the uncleaned sample, or picked up at some point through the cleaning process.

Figure 3.22d shows very well the effectiveness of acetone as a cleaning regime. The uncleaned sample shows the presence of TiO_2 based on the binding energies of the peaks shown. These peaks disappear entirely when cleaned for 2 minutes or 2 hours, but reappear between 2 hours and 2 days.

Sample	Au 4f	C 1s	O 1s	Ti 2p
Not cleaned	10.82	16.77	35.20	26.63
2 mins	69.68	9.85	5.12	0.00
2 hours	69.65	10.25	5.33	0.00
2 days	44.75	14.25	10.17	1.91

Table 3.15: XPS ratios as total %. Other peaks not shown which account for missing percentages.

These results indicate that there are surface contaminants that are easily removed by immersing in acetone for a period of 2 minutes to 2 hours, reducing counts for O and Ti significantly. However, when the sample is immersed in acetone for 2 days, these contaminants begin to reappear. This is most likely due to the dissolution of a photoresist layer remaining from the manufacturing process. The photoresist is easily removed after a short period of time, but on a longer timescale the solubilised photoresist begins to readsorb to the electrode surface.

3.7.3 AFM

Given the lack of any TiO_2 or any other significant surface chemistry detected with XPS, AFM imaging was used to study the surface topography.

Figures 3.23a, 3.23b and 3.23c show the surface of P2 MKIII C-type electrodes. Figures 3.23a and 3.23b shows a well defined surface with the majority of the electrode experiencing a height difference of approximately 20 nm, although there exists some surface debris in excess of 30 nm high. These images compare well to the evaporated Au electrodes used in Section 3.3.2 (Figures 3.6a and 3.6b).

Figure 3.23c sees a significantly larger height difference in the order of 200 nm, suggesting that it is not the electrode surface itself that is being measured but a contaminant on the surface. The lack of an ordered structure points to a polymeric substance, most likely the photoresist layer that has been discussed previously.

Figures 3.23d and 3.23e shows the smaller P2 MKIII E-type electrodes. While on first appearances the surfaces appear to be similar to those seen in Figures 3.23a and 3.23b, closer inspection of Figure 3.23e shows a grainier texture indicative of microscopic surface debris. These grains are approximately 50 nm in diameter, and are probably dust but their specific identity cannot be confirmed.

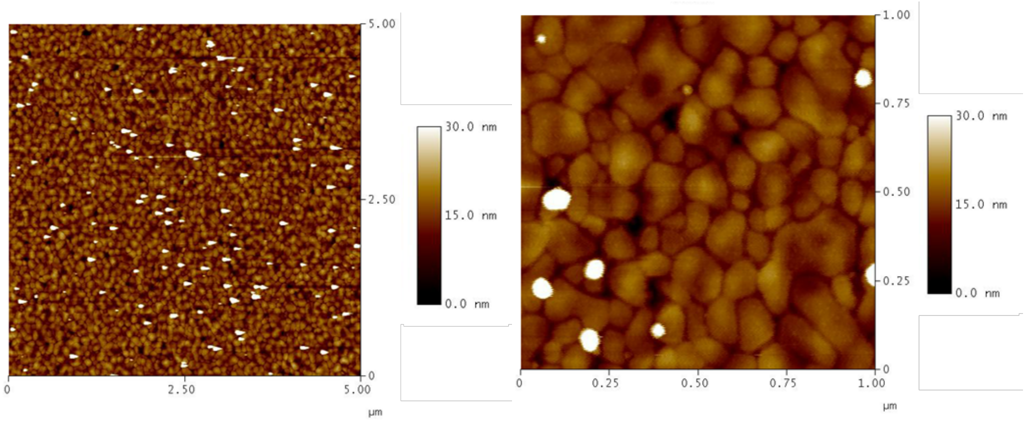

(a) P2C (5 μm x 5 μm) (b) P2C (1 μm x 1 μm)

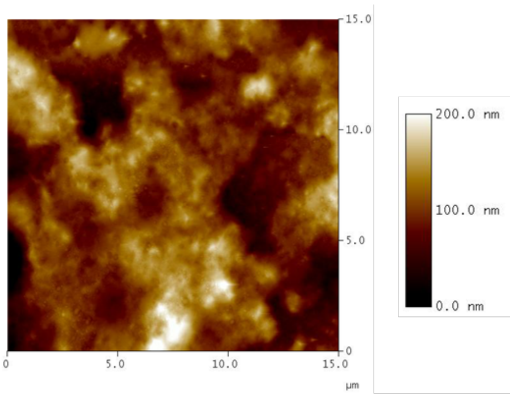

(c) P2C with photoresist contaminant (15 μm x 15 μm)

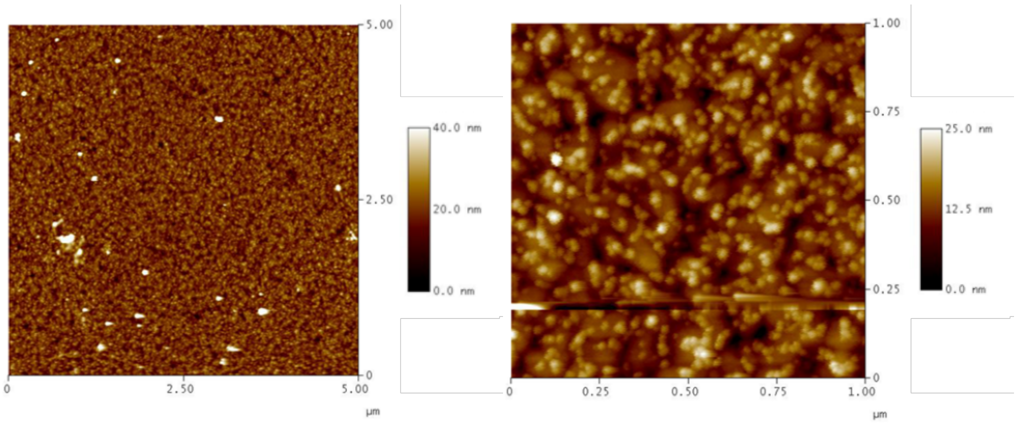

(d) P2E (5 μm x 5 μm) (e) P2E (1 μm x 1 μm)

Figure 3.23: AFM of P2 MKIII electrodes

3.7.4 Conclusions

P2 MKII electrodes suffered from diffusion of Ti into the Au layer, with substantial amounts of TiO_2 on the electrode surface. The replacement of Ti with TiN in the adhesion layer appears to have resolved these issues as XPS shows no Ti present after a short period of cleaning with acetone (Figure 3.22d). Despite these changes, the formation of an ODT SAM is still highly irreproducible making the electrodes unsuitable for use. AFM studies have shown the surface topography to be similar to evaporated Au used in the initial studies at the start of this chapter (Figure 3.6), rather than the superior quality of the P1 electrodes.

While this drop in quality is disappointing, it does not explain the difficulty experienced in forming stable ODT SAMs. This could be related to the change in lithography processes required to deposit and pattern the TiN and SiO_2 layers. Further analysis and refinement of the manufacturing workflow and cleaning protocols may be required to produce a suitable surface.

3.8 Conclusions & Discussions

The studies undertaken in Section 3.3 allowed a cleaning protocol to be established that minimises Au oxides and leads to more reproducible SAMs, as shown in Figure 3.5 and Table 3.4.

A series of patterned electrodes were designed in conjunction with Philips Research and MiPlaza. The first generation, P1, electrodes were a great success with AFM studies showing a vast improvement in the surface roughness compared to the previously used evaporated Au samples. High quality SAMs and tBLMs were formed on them, and they have been the primary electrodes used in Chapters 4, 5, and 6. Despite their excellent characteristics, the addition of an insulating layer, to confine the active electrode area to the pixel regions, was deemed to be of great benefit for several reasons discussed earlier.

A second generation of electrodes, P2, was thus designed. These electrodes were to incorporate the aforementioned insulating layer, as well as a slight redesign in the electrode layout to allow interfacing with a PCI port for an easy connection, as well as leaving space for the addition of onboard reference and counter electrodes in a proposed third generation of electrodes.

The addition of this insulating layer was met with numerous issues, however, as the initial batch, P2 MKI, suffered from delamination of the SiO_2 insulating layer when immersed in liquid. A Ti adhesion layer was added to overcome this issue, P2 MKII, but this addition led to contamination of the Au layer as the high temperatures experienced in SiO_2 deposition resulted in Ti diffusing into the Au layer and making the removal of a TiO_2 layer difficult. This effect has recently been described in literature, and the replacement of Ti with TiN as a more thermally stable material suggested [Martinez et al., 2010].

The P2 MKIII electrodes were then created making use of a TiN adhesion layer. This prevented delamination and avoided contamination of the Au layer with Ti. However, EIS showed SAM formation to still be an issue. AFM studies showed the electrode to have a surface roughness closer to the evaporated Au used in Section 3.3 than the P1 electrodes, however this difference does not explain the problems encountered. It is possible that the electrodes still have small amounts of photoresist or associated residues that prevent efficient formation of ODT SAMs. This may explain the small C and O signals still observed in XPS studies, despite the use of an acetone cleaning step. Further study with SAES may be beneficial in identifying if these contaminants are widespread or localised.

While the second generation electrodes studied here did not provide a suitable surface for the formation of tBLMs, the design principles remain sound. Further refinement of either the manufacturing process or the cleaning steps utilised in the removal of surface contaminants, will hopefully yield electrodes that can support a good quality SAM on which a tBLM with a higher membrane resistance than seen with the P1 electrodes. This is primarily due to the insulation of the track regions, which disproportionately affect the electrode area:perimeter ratio.

Chapter 4

Ionophores as Model Ion Transporters for the Characterisation of the EO$_3$C/6MH Tethered Bilayer Lipid Membrane System

4.1 Introduction

The EO$_3$ cholesterol/6-mercaptohexanol (EO$_3$C/6MH) tethered bilayer lipid membrane system that has been employed in this thesis and prior work [Becucci and Guidelli, 2009; Jenkins et al., 1998; Jeuken et al., 2008; Jeuken, 2008; Jeuken et al., 2005, 2006, 2007a, b; Weiss et al., 2008, 2009] has been well described thus far in Sections 1.3.4 and 3.4.4. To assess this system's use in the detection of ion transport activity, the ionophores valinomycin and gramicidin were employed as model cases to gain a better understanding of how their respective activities are influenced via electrochemical impedance spectroscopy, as well as providing further insight into how the EO$_3$C/6MH SAM influences the properties of the lipid bilayer.

Recently, two independent studies by the groups of Losche and Lipkowski have shown that pure monolayers of thiolipids, 20-tetradecyloxy-3,6,9,12,15,18,22-heptaoxahexatricontane-1-thiol (WC14) and 2,3-di-*O*-phytanyl-*sn*-glycerol-1-tetraethylene glycol-DL-α-lipoic acid ester (DPhyTL) , exclude water between the lipid bilayer and gold surface, which instead is occupied by the ethylenoxy groups of the tBLM system[Leitch et al., 2009; McGillivray et al., 2007]. A similar situation is likely to apply to EO$_3$C used in this system. Hydration can be introduced by mixing diluting thiols, in our case 6MH, into the tethering layer[McGillivray et al., 2007]. We have previously shown that EO$_3$C and 6MH phase separate on the surface creating nano-scale domains of 6MH[Jeuken et al., 2007b]. One

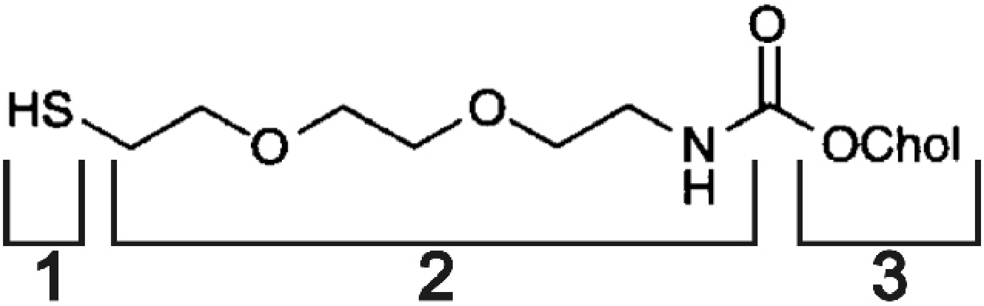

(a)

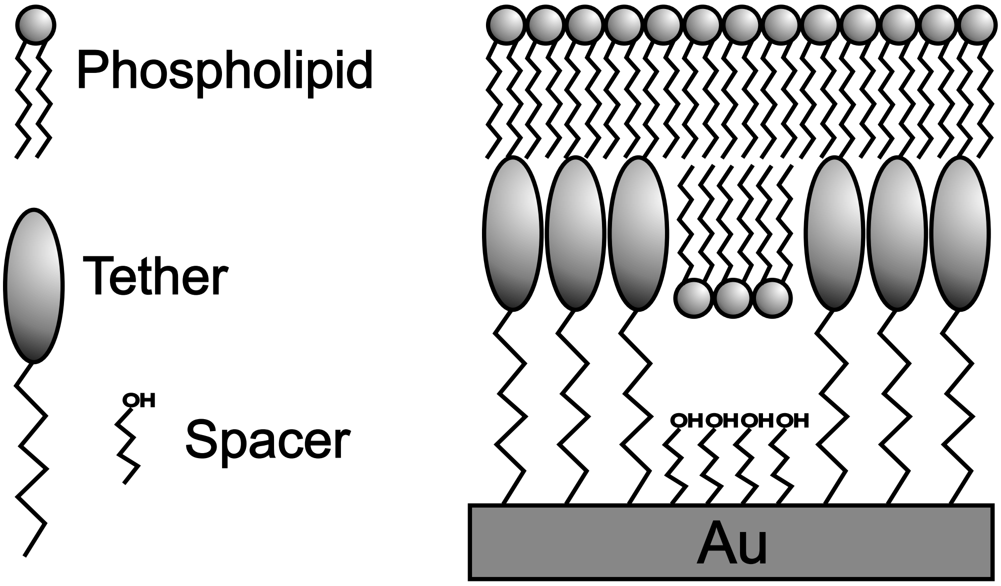

(b)

Figure 4.1: (a) Chemical structure of EO_3 cholesterol. (1) thiol group, (2) triethylenoxy linker, (3) cholesterol moiety[Boden et al., 1997]. (b) Schematic representation of a tBLM comprised of EO_3C tether and 6MH diluting thiols.

previous study has indicated that diluting thiols are necessary to observe ion-channel activity[He et al., 2005]. Thus, a generally held view is that hydration, in the form of ionic reservoirs, is necessary for the solvation of ions and that this is a requirement for ion transport through ion channels in the tBLM. Efforts have been made to investigate hydration via thiol density by Vockenroth *et al* by comparing the afore mentioned DPhyTL with a related, but bulkier molecule, di-phytanylglycerol-hexaethyleneglycol-di-lipoic acid (DPhyHDL)[Vockenroth et al., 2008a]. While DPhyTL was shown to produce a tBLM with excellent electrical properties, DPhyHDL was far less effective but showed a far more pronounced response to α-hemolysin addition. The use of mixed SAM in the tBLM system may thus be preferable and here, we show that without the presence of 6MH in our tBLM system, ion transport facilitated by valinomycin and gramicidin is not possible.

The ionophore valinomycin is a 12 residue cyclical peptide, which functions by co-ordinating ions and shielding their charge in such a way that they can diffuse across the membrane[Pullman, 1991]. Due to the requirement to coordinate to the K^+ ions, valinomycin exhibits high ion selectivity but relatively slow ion transport (approximately $10^2 - 10^4$ ions sec^{-1} $molecule^{-1}$)[Hladky et al., 1974]. Valinomycin has an affinity for K^+ ions that is 10^5 greater than Na^+ ions[Hladky et al., 1974]. In contrast, gramicidin is a half-channel pore-forming peptide which provides a much faster route for ion transport (approximately $10^7 - 10^8$ ions sec^{-1} $molecule^{-1}$)[Hladky et al., 1974]. It is able to adopt several conformations depending on its environment, but its active form is a right-handed single stranded $\beta^{6.3}$-helical head-to-head dimer which forms a membrane spanning channel that allows direct passage of cations across the membrane, subject to size and charge constraints[O'Connell et al., 1990]. Pore-forming peptides are capable of transporting a far wider range of ions than ion carriers. Gramicidin is able to transport most small monovalent cations, but binds divalent cations (such as Ba^{2+})[Bamberg and Lauger, 1977; Heitz and Gavach, 1983] and cannot transport anions [Andersen and Koeppe, 1992] or molecules larger than its internal pore diameter (4 Å[Andersen and Koeppe, 1992]) such as large organic cations including tetramethylammonium (TMA^+)[Roux, 1996].

4.2 Experimental Section

4.2.1 Materials

EO_3 cholesterol (EO_3C) was made as described previously[Boden et al., 1997]. *Escherichia coli* (*E. coli*) polar lipid extract (Avanti Polar Lipids Inc., Alabama, Alabaster), 6-mercaptohexanol (6MH, Sigma), isopropanol, methanol and ethanol (HPLC grade, Fisher), nitrogen and argon (BOC) were used as received. Water was obtained from an Elga PURELAB Prima water purification system to give 18.2 MΩ.cm resistance. Electrochemical experiments were performed in a range of buffers all containing MOPS buffer (3-(*N*-morpholino)propanesulfonic acid, Sigma, 20 mM) with either Na_2SO_4, K_2SO_4, $TMASO_4$, NaCl or $BaCl_2$ (Sigma, 30 mM in all cases) adjusted to pH 7.4 with H_2SO_4, NaOH, KOH, HCl, $Ba(OH)_2$ or TMAOH (Sigma), respectively, at 20 °C. Ethylenediaminetetraacetic acid (EDTA, Sigma) was adjusted to pH 7.4. $CaCl_2$ (Sigma) was made up to a 1 M stock solution. Valinomycin and gramicidin D (Sigma) were used from methanolic stock solutions.

4.2.2 Preparation of Electrodes

The majority of experiments were performed on P1 series patterned gold electrodes described in the previous chapter (Section 3.4) and cleaned using the following procedure developed in the same chapter. Electrodes were sonicated in propanol for 10 minutes to remove any remaining products from the manufacturing process and then exposed to a UV/O_3 generator (UVOCS Inc.) for at least 10 minutes to breakdown organic contaminants. The electrodes were then transferred to an ethanol Soxhlet extractor for at least twice as long. This should reduce any gold oxidised by the UV/O_3 cleaning back to metallic according to Ron et al. [1998] and Ishida et al. [1997], a claim that is supported by results presented in Section 3.3.

4.2.3 Vesicle Formation

Powdered *E. coli* polar lipid extract (100 mg) from Avanti Polar Lipids was dissolved in chloroform/methanol (5 mL, 1:1 ratio) and divided into 20 aliquots. These were then dried under a stream of nitrogen to remove the bulk of the solvent before drying further in a vacuum desiccator. Aliquots were stored under a nitrogen environment at −20 °C. 1 mL of 30 mM Na_2SO_4, 20 mM MOPS, pH 7.4 buffer was added to a single aliquot of dried lipid and agitated by vortex until all the lipid was resuspended in solution. The lipid solution was then tip sonicated (Banson Sonifier S-250A) at 4 °C for 30 minutes.

4.2.4 Formation of Self-Assembled Monolayers (SAMs)

Cleaned electrodes were immersed in a propanolic solution of either EO_3C (0.1 mM) or EO_3C and 6MH (0.11 mM:0.89 mM) thiols overnight. These gave SAMs of pure EO_3C or ∼80% EO_3C and ∼20% 6MH by surface area respectively, as previously described in detail by Jeuken et al. [2007b]. Before use, electrodes were thoroughly rinsed with propanol and methanol and dried under a stream of N_2.

4.2.5 Tethered Bilayer Lipid Membrane Formation

The modified gold electrode was housed in an electrochemical cell made of PTFE and glass, with rubber O-rings and covered in electrolyte (20 mM MOPS, 30 mM Na_2SO_4, pH 7.4). $CaCl_2$ was added to a working concentration of 10 mM, followed by vesicles to make a 0.5 mg/mL solution. The membrane was allowed to form over 1–2 hours during which time EIS measurements were taken every 10 minutes. After membrane formation, EDTA (10 mM) was added and the cell was rinsed 5 times in buffer solution. The tBLM was then characterised using EIS.

4.2.6 Ionophore Reconstitution and Measurement

The ionophores valinomycin and gramicidin were introduced into the electrolyte from a methanol stock solution, ensuring that the volume of methanol added did not exceed 1% (v/v). Valinomycin was used at 4.5 μM, while gramicidin was used at concentrations ranging from 0.58 nM to 15 μM. Ionophores were allowed to incorporate for an hour before rinsing the cell with fresh buffer. Buffers were exchanged to demonstrate ion selectivity as explained in the Results section. Na^+ buffer contained 30 mM Na_2SO_4, 20 mM MOPS; K^+ buffer contained 30 mM K_2SO_4, 20 mM MOPS; Ba^{2+} buffer contained 30 mM $BaCl_2$, 20 mM MOPS; and TMA^+ buffer contained 30 mM $TMASO_4$, 20 mM MOPS. The pH was set to pH 7.4 using NaOH, KOH, $Ba(OH)_2$ and TMAOH respectively.

4.2.7 Electrochemical Impedance Spectroscopy (EIS)

Data were analysed with the software EISFit, written by L.J.C. Jeuken. Two equivalent circuits were employed and are shown in Figure 4.2. The first equivalent circuit, $R_s(Q_{tBLM}R_{tBLM})$ (referred to as R(QR) for brevity), is composed of a resistor (R_s) in series with a constant phase element (CPE, Q_{tBLM}) and a second resistor (R_{tBLM}) in parallel. R_s simulates the resistance of the electrolyte. Q_{tBLM} simulates the capacitance of the double layer (the SAM or the lipid bilayer) with an additional factor, α, which is taken to be a measure of surface roughness or defects in the lipid bilayer. R_{tBLM} models the resistance of the lipid bilayer. The second equivalent circuit, $R_s(Q_{PL}R_{PL})(Q_{SAM}R_{SAM})$ (referred to as R(QR)(QR) for brevity), is similar to the first equivalent circuit but with the addition of a second (QR) element to account for high levels of ion transport as seen in the valinomycin-K^+ plot (Figure 4.3). Here Q_{tBLM} and R_{tBLM} are replaced by Q_{PL} and R_{PL}, where PL is means ‘polar lipid’. This is due to these parameters no longer representing the entire tBLM (SAM and polar lipid), but just the polar lipid added via vesicles, without the underlying SAM. The terms Q_{SAM} and R_{SAM} model the underlying SAM elements, which needs to be modelled when $R_{tBLM/PL}$ decreases due to K^+ transport. Both these equivalent circuits would normally terminate in a capacitor. However, the impedance spectra presented here do not extend to frequencies low enough to observe the effect of this ‘final’ capacitor and as such this element has been excluded during analysis.

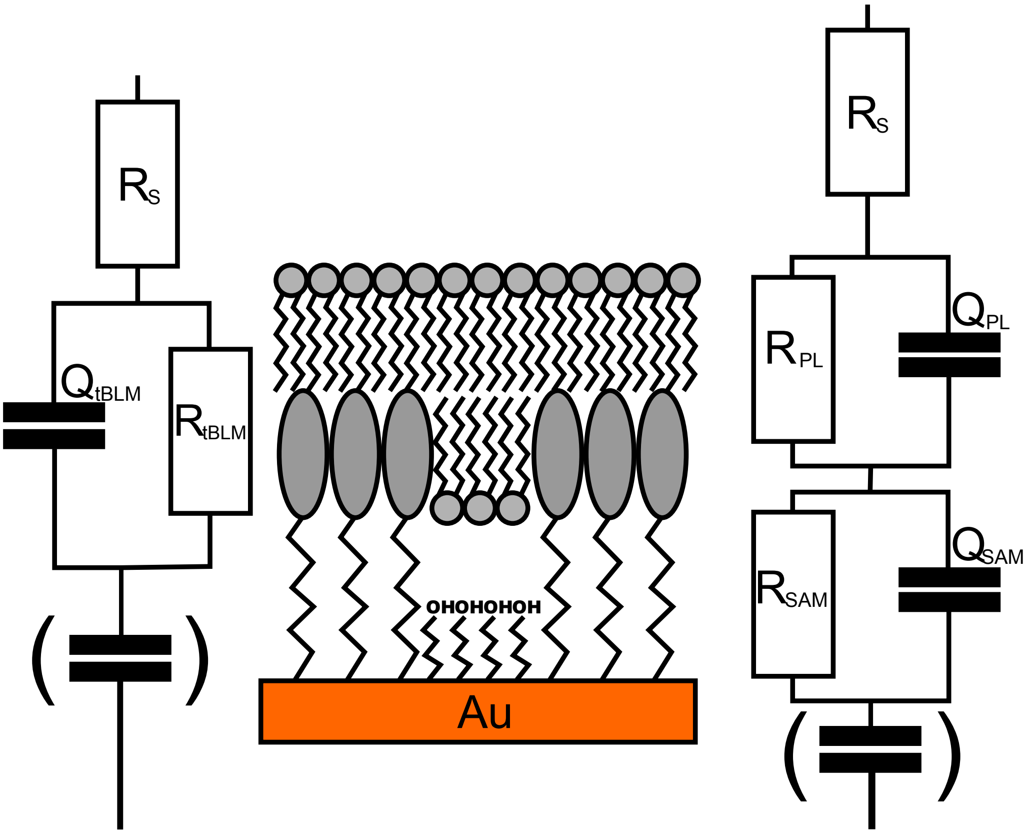

Figure 4.2: Equivalent circuits used in analysis of impedance data. (Left) The equivalent circuit described as R(QR) was used for SAMs, tBLMs, tBLM with valinomycin (Na^+) and tBLM with gramicidin (Na^+). (Right) The equivalent circuit described as R(QR)(QR) was used to model tBLMs with valinomycin (K^+) and gramicidin (Ba^{2+}) incorporated into them. R_s is solution resistance (electrolyte), Q_{tBLM} is double layer capacitance of the entire tBLM modelled by a constant phase element (CPE) and R_{tBLM} is membrane resistance. Where R(QR)(QR) is used Q_{PL} and R_{PL} are used to describe the capacitance (modelled by a CPE) and resistance of the polar lipid portion of the tBLM, while R_{SAM} represents the resistance of the tethering SAM and Q_{SAM} is the SAM capacitance modelled by a CPE. Capacitances enclosed in a bracket indicate that the element is not modelled as it is not observed in impedance spectra, but would be expected if measuring at lower frequencies.

4.2.8 Surface Plasmon Resonance (SPR)

SPR measurements were performed using a custom built SPR instrument based on a Kretschmann configuration, using a 5mW HeNe laser ($\lambda = 632.8$ nm). SPR spectra were simulated using a four layer model representing prism, gold, organic layer, and sub-phase with refractive indices of 1.84, 0.25-3.1, 1.45, and 1.33 respectively. Spectra were taken over a 16° range to include the critical angle and the minima for accurate modelling. All kinetic data were taken one degree, external angle, below the initially observed minima to give a maximum change in signal. SPR measurements were undertaken on Schott TiH53 high refractive index right angle prisms (Galvoptics, Essex, U.K.) with a 48 nm gold layer on the hypotenuse. The gold layer was deposited by electrothermal evaporation (rate 0.1–0.2 nm.s^{-1}, pressure 8×10^{-7} mbar) directly onto the prisms. A SAM was formed on the gold layer as described above.

The mixed SAM activated prism was incubated with the vesicle solution and the kinetics of adsorption followed in real time, by monitoring the change in reflectivity at a fixed angle below the resonance minimum. Upon reaching steady state conditions, the flow cell, which had a volume of 60 μL, was flushed with 8 times its volume to remove all vesicles from the solution as well as any nonspecifically surface bound vesicles. Gramicidin (0.56 μM) was then injected into the flow cell and the kinetics of binding and subsequent rinsing followed. Once collection of the kinetic data were completed, a reflectivity curve was taken and compared to the initial curve, thus giving a quantification of adsorbed layer thickness by modelling of the curves and the respective shift in the resonance minima. While SPR is very sensitive to changes in refractive index it must be remembered that these changes are not always specific to the process being investigated. Initial experiments with the gramicidin concentrations used in EIS experiments indicated that aggregation of gramicidin monomers was obstructing the production good quality data of gramicidin incorporating into the tBLM. To reduce the degree of change in refractive index brought about by the aggregation of gramicidin the concentration used for SPR experiments was decreased from 15 μM to 0.56 μM, a value at which capacitance changes were still observed. It should also be noted that the aggregation of gramicidin monomers at the surface of the tBLM is149 not expected to have had an effect on the EIS measurements at relevant concentrations.

1

4.3 Results

4.3.1 Formation of Tethered Bilayer Lipid Membranes

Tethered bilayer lipid membranes (tBLMs) were formed on sputtered gold electrodes modified with self-assembled monolayers (SAMs) of either pure EO_3 cholesterol (EO_3C) or mixed SAMs of EO_3C and 6-mercaptohexanol (6MH) with surface coverage ratio of approximately 80% EO_3C and 20% 6MH (Figure 4.1b). tBLMs were formed by incubating these surfaces with vesicles of *E. coli* polar lipid extract in the presence of $CaCl_2$ (10 mM). It is believed that the divalent calcium cations negate the net negative charge of the vesicles and promote rupture and fusion into a planar bilayer[Jeuken et al., 2005]. The formation of the tBLM was followed using electrochemical impedance spectroscopy (EIS) and indicated by a drop in capacitance (Figure 4.3). The resistance of the tBLM was determined by fitting EIS data to an equivalent circuit as described in Methods. The full set of EIS parameters for tBLMs formed on pure EO_3C and mixed SAMs can be found in Tables 4.1 and 4.2, respectively.

4.3.2 Valinomycin

Figures 4.3a & b show the effect of addition of valinomycin (4.5 μM) to tBLMs prepared from pure EO_3C SAMs. The effects of valinomycin, in Na^+ or K^+, on the tBLM resistance are negligible (Table 4.1). In contrast, tBLMs formed on mixed SAMs of 80% EO_3C and 20% 6MH show a very different behaviour. Addition of valinomycin to the tBLM in the presence of Na^+ buffer does not significantly change the membrane resistance (Table 4.2). However, when the electrolyte is exchanged for K^+ buffer, a drop in resistance is seen as shown by the large dip in phase at around 20 Hz (Figure 4.3c). The differences in resistance indicate that valinomycin has a 200-fold preference for the transport of K^+ over Na^+, which is in agreement with other studies performed on similar systems[Naumann et al., 2003b; Rose and Jenkins, 2007; Schiller et al., 2003]. This drop moves to higher frequencies as valinomycin or K^+ concentration is increased or to lower frequencies when decreased, and moves to far lower frequencies when K^+ is completely replaced by Na^+. This confirms that the tBLM resistance is due to valinomycin-mediated K^+ transport. No significant change is observed in the primary capacitance of tBLMs formed on either pure EO_3C or mixed SAMs (Figures 4.3b and d, Tables 4.1 and 4.2). However, a secondary capacitance which can be linked to the afore mentioned drop in resistance is visible in Figure 4.3d when K^+ is present. The occurrence of this secondary capacitance made it necessary to use a different equivalent circuit to fit the data as described in Methods and shown in Figure 4.2. The capacitance determined from this second semi-circle is similar to the capacitance of 6MH in the mixed SAM prior to tBLM formation, as will be explained in the discussion.

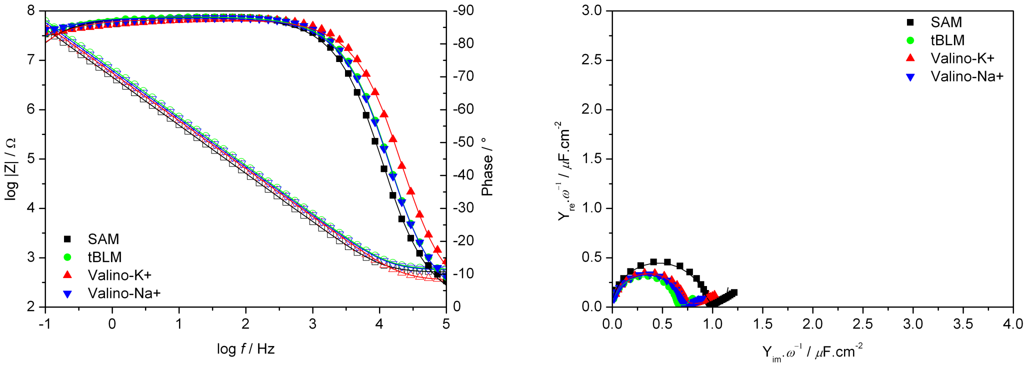

(a) Pure EO_3C SAM - Bode Plot (b) Pure EO_3C SAM - Normalised Admittance Plot

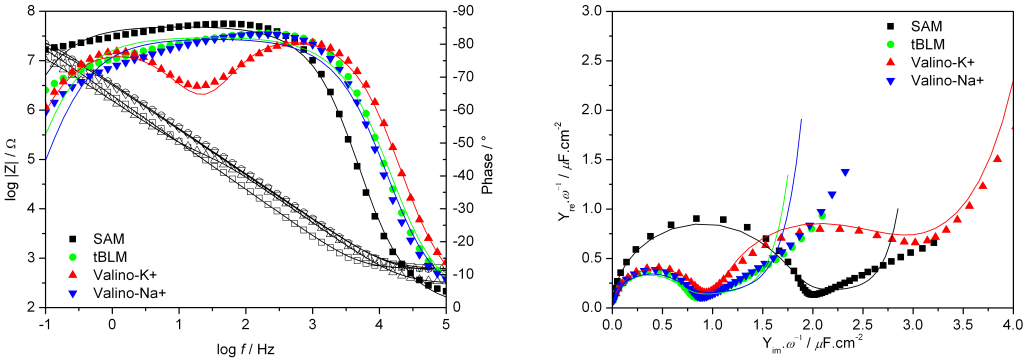

(c) Mixed SAM - Bode Plot (d) Mixed SAM - Normalised Admittance Plot

Figure 4.3: Impedance data for tBLMs formed on either a pure EO_3C SAM (a and b), or a mixed EO_3C:6MH SAM (c and d) with 4.5 μM valinomycin. Black squares = SAM; Green circles = tBLM; Red up Triangle = 4.5 μM valinomycin in K^+ buffer; Blue down triangle = 4.5 μM valinomycin in Na^+ buffer. Bode Plots - Solid shapes = Phase shift; Open shapes = Absolute impedance. Lines are fits using equivalent circuits as described in Methods and Figure 4.2. R(QR)(QR) was used to model the K^+ plot in the case of mixed SAMs. R(QR) was applied in all other cases. Na^+ buffer contained 30 mM Na_2SO_4, 20 mM MOPS buffer, pH 7.4. K^+ buffer contained 30 mM K_2SO_4, 20 mM MOPS, pH 7.4.

4.3.3 Gramicidin

Unexpectedly and in contrast to the valinomycin results, addition of gramicidin increases the overall double layer capacitance of the tBLM. Following the formation of a tBLM on a mixed SAM, gramicidin is added from methanolic stock solution to the electrolyte in the range 0.58 nM - 15 μM. Instead of a decrease in membrane resistance, the addition of gramicidin leads to a gradual increase in capacitance tending towards that of the underlying SAM (Figure 4.5 and inset). Replacing Na^+ with Ba^{2+} - which is not transported by gramicidin - reverts the double layer capacitance to approximately that of a tBLM (Figure 4.4d). However, in the presence of Ba^{2+} a drop in resistance can also be observed (Figures 4.4c and 4.4d, Table 4.2). Figure 4.4d shows the double layer capacitance when TMA^+ is used and resides between the capacitance values for Na^+ and Ba^{2+}. The membrane resistance with TMA^+ is higher than with K^+ or Ba^{2+} ions, although this is more clearly seen in Table 4.2.

Interestingly, and following a similar trend to the valinomycin results, no major changes in resistance or capacitance are seen upon addition of gramicidin to a tBLM formed on pure EO_3C (Figures 4.4a, 4.4b, and Table 4.1) with the exception of a mild increase in the double layer capacitance. This may be indicative of ion transport into small defects of the underlying EO_3C SAM. This lack of gramicidin activity agrees well with the valinomycin data presented here, showing that gramicidin is only able to function, or incorporate in tBLMs, when suspended over ionic reservoirs such as those produced by 6MH domains in our phase separated SAMs.

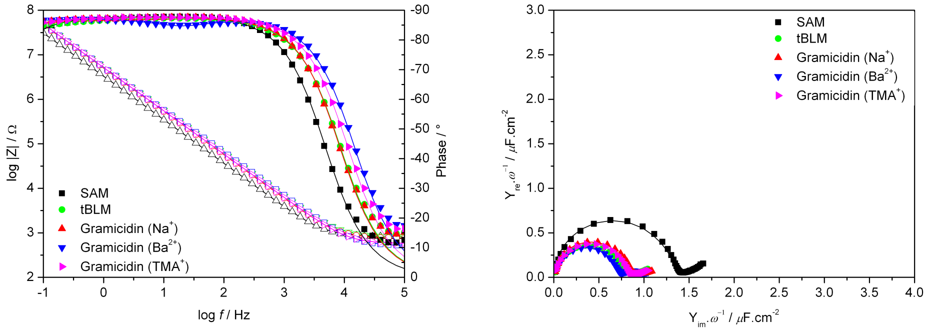

(a) Pure EO_3C SAM - Bode Plot (b) Pure EO_3C SAM - Normalised Admittance Plot

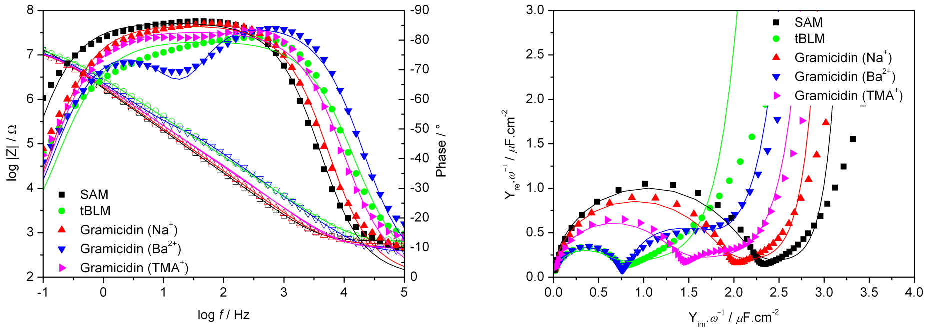

(c) Mixed SAM - Bode Plot (d) Mixed SAM - Normalised Admittance Plot

Figure 4.4: Impedance data for tBLMs formed on either an EO_3C SAM (a and b), or a mixed SAM (c and d) with 15 μM gramicidin. Black squares = SAM; Green circles = tBLM; Red up triangle = 15 μM gramicidin in Na^+ buffer; Blue down triangle = 15 μM gramicidin in Ba^{2+} buffer; Magenta right triangle = 15μM gramicidin in TMA^+ buffer. Bode Plots - Solid shapes = Phase shift; Open shapes = Impedance. Lines are plots of the equivalent circuits as calculated using EISFit as described in Methods. R(QR)(QR) was used to model the Ba^{2+} data. R(QR) was used in all other cases. Na^+ buffer contained 30 mM Na_2SO_4, 20 mM MOPS buffer, pH 7.4. Ba^{2+} buffer contained 30 mM $BaCl_2$, 20 mM MOPS, pH 7.4. TMA^+ buffer contained 30 mM $TMASO_4$, 20 mM MOPS, pH 7.4.

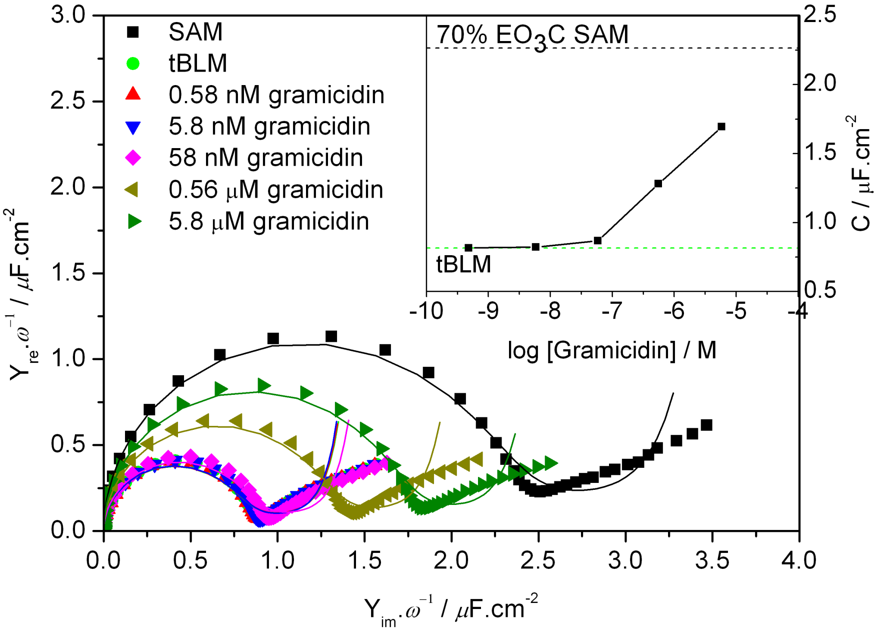

Figure 4.5: (Main) Impedance data for tBLMs formed on a mixed EO_3C:6MH SAM, measured in Na^+ buffer. Gramicidin is added from methanolic stock to give various solution concentrations. Square = SAM; Circle = tBLM; Up Triangle = 0.58 nM gramicidin; Down Triangle = 5.8 nM gramicidin; Diamond = 58 nM gramicidin; Left Triangle = 560 nM gramicidin; Right Triangle = 5.8 μM gramicidin. Lines are fits calculated by EISFit using the R(QR) equivalent circuit. (Inset) Summary of the effect of gramicidin concentration on the capacitance of the tBLM. The capacitance of the SAM (approximate surface coverages of 70% EO_3C and 30% 6MH) and the tBLM prior to gramicidin are also shown as annotated dashed lines. Na^+ buffer contained 30 mM Na_2SO_4, 20 mM MOPS, pH 7.4.

Surface Plasmon Resonance (SPR)

The issue of incorporation and whether or not the tBLM could be disrupted by gramicidin was addressed using surface plasmon resonance (SPR). Analysis showed that following incubation with *E. coli* polar lipid extract vesicles and $CaCl_2$ (10 mM) a tBLM is formed. On a mixed SAM (75% EO_3C:25% 6MH) the lipid layer is 34±1 Å thick, while on a 100% EO_3C SAM the lipid layer has a thickness of 27±1 Å. These values compare well to studies done previously[Jeuken et al., 2006; Williams et al., 1997]. A thinner layer is expected for 100% EO_3C SAMs as only a monolayer of lipid is deposited to form the tBLM, as opposed to the bilayer of lipid that forms on the mixed SAM. Subsequent addition of gramicidin (0.56 μM) led to a gradual increase in organic layer thickness, which, after a rinsing step, is calculated to be 4.3 Å thick for the tBLM on a mixed SAM and 5.8 Å on the tBLM on a 100% EO_3C SAM.

EIS parameters for tBLMs on pure EO_3C SAMs

System	tBLM (Na^+)	Valinomycin (Na^+)	Valinomycin (K^+)	Gramicidin (Na^+)	Gramicidin (Ba^{2+})	Gramicidin (TMA^+)
Circuit	R(QR)	R(QR)	R(QR)	R(QR)	R(QR)	R(QR)
n	7	4	4	3	2	3
C_{tBLM} (μF.cm^{-2})	0.67 ± 0.02	0.66 ± 0.01	0.68 ± 0.02	0.80 ± 0.01	0.67 ± 0.01	0.74 ± 0.02
Q_{tBLM}	0.89 ± 0.05	0.95 ± 0.04	1.12 ± 0.07	1.06 ± 0.07	1.04 ± 0.01	1.07 ± 0.08
α_{tBLM}	0.97 ± 0.01	0.96 ± 0.01	0.95 ± 0.01	0.98 ± 0.01	0.96 ± 0.01	0.97 ± 0.01
R_{tBLM} (MΩ.cm^2)	11.7 ± 4.6	5.6 ± 4.4	4.8 ± 3.0	39.6 ± 4.9	> 40	31.1 ± 22.1

Table 4.1: The tBLM capacitance and resistance for valinomycin and gramicidin-doped tBLMs formed on EO_3C SAMs. Valinomycin was used at 4.5 μM. Values given for gramicidin are at a concentration of 15 μM. Data were modelled using a R(QR) equivalent circuit as described in Methods. C_{tBLM} is obtained by doubling the height of the capacitance semi-circle in Normalised Admittance Plots (Figures 4.3b and 4.4b) and normalising by the electrode area. Q_{tBLM} is taken from equivalent circuit fitting using the aforementioned circuits. All other parameters were taken from EIS fits using the equivalent circuits indicated, as described in Methods.

EIS parameters for tBLMs on mixed SAMs

System	tBLM (Na^+)	Valinomycin (Na^+)	Valinomycin (K^+)	Gramicidin (Na^+)	Gramicidin (Ba^{2+})	Gramicidin (TMA^+)
Circuit	R(QR)	R(QR)	R(QR)(QR)	R(QR)	R(QR)(QR)	R(QR)
n	17	4	4	5	5	4
$C_{tBLM/PL}$ ($\mu F.cm^{-2}$)	0.75 ± 0.01	0.77 ± 0.01	0.80 ± 0.01	1.64 ± 0.11	0.73 ± 0.02	1.25 ± 0.11
$Q_{tBLM/PL}$	1.59 ± 0.08	1.87 ± 0.05	2.84 ± 0.08	2.73 ± 0.12	2.80 ± 0.47	2.86 ± 0.59
$\alpha_{tBLM/PL}$	0.93 ± 0.01	0.91 ± 0.01	0.97 ± 0.01	0.94 ± 0.01	0.97 ± 0.02	0.92 ± 0.01
$R_{tBLM/PL}$ ($M\Omega.cm^2$)	1.58 ± 0.52	1.00 ± 0.08	0.006 ± 0.003	0.38 ± 0.02	0.009 ± 0.004	0.558 ± 0.432
Q_{SAM}	-	-	3.89 ± 0.02	-	2.63 ± 0.09	-
α_{SAM}	-	-	0.91 ± 0.01	-	0.92 ± 0.01	-
R_{SAM} ($M\Omega.cm^2$)	-	-	0.77 ± 0.07	-	0.43 ± 0.01	-

Table 4.2: The tBLM capacitance and resistance for valinomycin and gramicidin-doped tBLMs formed on mixed SAMs. Valinomycin was used at 4.5 μM. Values given for gramicidin are at a concentration of 15 μM. Data were modelled using either a R(QR), or R(QR)(QR) equivalent circuit as described in Methods. C_{tBLM} is obtained by doubling the height of the capacitance semi-circle in Normalised Admittance Plots (Figures 4.3d and 4.4d) and normalising by the electrode area. Q_{tBLM}, and Q_{SAM} where applicable, are taken from equivalent circuit fitting using the aforementioned circuits. All other parameters were taken from EIS fits using the equivalent circuits indicated, as described in Methods.

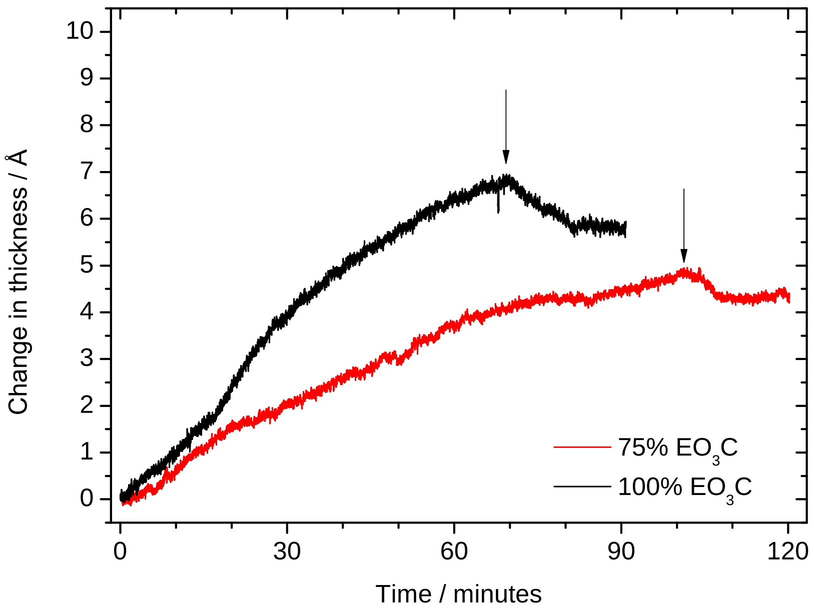

Figure 4.6: SPR kinetic profiles after addition of 0.56 μM gramicidin to *E. coli* polar lipid tBLMs formed on 75% EO$_3$C:25% 6MH (grey) and 100% EO$_3$C (black) SAM-covered gold surfaces. Reflectivity data has been converted to thickness in Å. Gramicidin was dissolved in methanol and added to 20 mM MOPS, 30 mM Na$_2$SO$_4$, pH 7.4 to give 1% methanolic solution containing 1.2 μg/ml gramicidin (0.56 μM). Gramicidin containing buffer was added at time 0, and incubated at 20°C for at least one hour, before rinsing with 20 mM MOPS, 30 mM Na$_2$SO$_4$, pH 7.4 as indicated with arrows.

4.4 Discussion

The membrane resistances of tBLMs formed on both the mixed and pure EO_3C SAMs compare well with other all-tether systems such as the yeast membranes used by Jadhav et al. [2008] (1.6 MΩ.cm^2) and the diphytanyl archaeal lipid analogues used by Koper, Knoll and others (2–15 MΩ.cm^2)[Andersson et al., 2008; Becucci et al., 2008; He et al., 2005; Naumann et al., 2003a, b; Schiller et al., 2003]. While the 2006 review by Janshoff and Steinem [2006] gave normal membrane resistances being 0.1–10.0 MΩ.cm^2, the resistances found here fall short of the 10.0 MΩ.cm^2 limit at which single channel measurements can be made. The resistances for the tBLMs formed on pure EO_3C SAMs are significantly higher than those obtained with mixed SAMs. The stark contrast in the impedance spectra for both valinomycin- and gramicidin-doped tBLMs indicates the importance of the presence of 6MH in the SAM for either the occurrence or detection of ion transporting activities. I have considered the possibility that the lack of ion transport in ionophore-doped tBLMs formed on pure EO_3C SAMs is due to an inability of the ionophores to incorporate into the phospholipid monolayer. However, studies done on lipid monolayers on mercury electrodes show that incorporation of gramicidin monomers is possible[Becucci et al., 2005; Rueda et al., 1999]. Further to this, I have undertaken SPR experiments that show a change in the reflectivity of the tBLM formed on mixed or 100% EO_3C SAMs equivalent to an increase in tBLM thickness by 4 ± 1 Å and 6 ± 1 Å respectively, which agree with literature values[Zhang et al., 2000]. The increased thickness observed in the pure EO_3C tBLM compared to that of the mixed SAM may in part be due to gramicidin monomers adopting a different position in which they protrude more from the lipid layer due to an inability to insert into the bottom leaflet occupied by the pure EO_3C SAM.

While it is possible that the capacitance changes observed following the addition of gramicidin are due to the large scale incorporation of gramicidin and the resultant change in the permittivity of the lipid bilayer, this can be shown to be unlikely by examining a few calculations. If we take the relative permittivities (ϵ_r) of lipid and protein as 4 and 20 respectively, and take the lengths of gramicidin and a lipid bilayer as 3 nm and 4 nm respectively, then we can calculate approximate capacitances for layers of each using the equation $C = \frac{\epsilon_r \epsilon_0}{d}$.

$$\begin{aligned} C_{\text{gramicidin dimer}} &= \frac{\epsilon_0 20}{3 \times 10^{-9}} \\ &= 6.20 \mu F.cm^{-2} \end{aligned}$$

or 12.40 μF.cm$^{-2} foragramicidinmonomer$or 12.40 μF.cm$^{-2} foragramicidinmonomer$or 12.40 μF.cm^{-2}

To gain a sense of how much gramicidin has been incorporated into the bilayer, we can use the increase in the average thickness of the bilayer as observed in the SPR experiment (Figure 4.6). A 5 Å increase was observed for the 75% EO_3C tBLM, and a 7 Å increase for the 100% EO_3C tBLM. Given that the actual length of the gramicidin dimer is 30 Å, we find that gramicidin must account for $\frac{1}{6}$ and $\frac{1}{2}$ the bilayer in 75% and 100% EO_3C tBLMs respectively (

$$\begin{aligned} C_{75\%\text{ top layer}} &= 75\% \times C_{\text{lipid monolayer}} + 25\% C_{\text{lipid bilayer}} + \frac{1}{6}(75\% \times C_{\text{gramicidin monomer}} + 25\% \times C_{\text{gramic}} \\ &= 75\% \times 2 \times 0.885\mu\text{F.cm}^{-2} + 25\% \times 0.885\mu\text{F.cm}^{-2} + \frac{1}{6}(75\% \times 12.40\mu\text{F.cm}-2 + 25\% \times 6.20\mu\text{F.c} \\ &= 3.4\mu\text{F.cm}^{-2} \end{aligned}$$

$$\begin{aligned} C_{100\%\text{ top layer}} &= C_{\text{lipid monolayer}} + \frac{1}{2}C_{\text{gramicidin dimer}} \\ &= 2 \times 0.885\mu\text{F.cm}^{-2} + \frac{1}{2} \times 12.40\mu\text{F.cm}-2 \\ &= 8\mu\text{F.cm}^{-2} \end{aligned}$$

It is clear that the incorporation of gramicidin has greatly altered the capacitance of these lipid layers, increasing it by more than 5 times in the case of the 100% EO_3C top layer. To get a view of the effect on the total capacitance these ‘top layer’ capacitances can then be added to those of their respective SAMs.

$Whenexaminingthedataforvalinomycin - orgramicidin - mediatediontransportwiththeirrespecti$

While this is a somewhat simplistic model of the tBLM system, it does support the hypothesis that only the ionic reservoirs created by the 6MH SAM regions are capable of detecting ion transport. Furthermore, the measured capacitance is dependant on the concentration of ionophore added as demonstrated in Figure 4.5 suggesting that the ionophores permeate the tBLM over the 6MH reservoirs in an incremental fashion. A very similar effect is seen with the capacitance changes observed after gramicidin addition (Figure 4.5). In this case, however, the ionophore activity results in a substantial increase in double-layer capacitance from 0.75 μF.cm^{-2} to 1.64 μF.cm^{-2}. The membrane resistance decreased from 1.58 MΩ.cm^2 to 0.38 MΩ.cm^2, which is a relatively small change compared to the far more significant drop to 0.006 MΩ.cm^2 produced by valinomycin. While capacitance changes were observed in the presence of Na$^+$, a change to Ba^{2+} caused the capacitance to return to 0.73 μF.cm^{-2}, a value very close to that of the tBLM prior to gramicidin exposure. This indicates that the tBLM retains its structural integrity even upon addition of large quantities of gramicidin, as supported by SPR. The use of smaller concentrations of gramicidin resulted in smaller increases in capacitance, however no changes to resistance were observed as can be seen from Figure 4.5. When the buffer is changed to Ba^{2+}, a residual signal of gramicidin activity is found in the form of a second capacitance semi-circle and an associated 'dip' in the phase shift as seen in Figures 4.4c and 4.4d.

Gramicidin channels are well documented as being impermeable and blocked by divalent cations, such as Ba^{2+}, which bind to a site found at the mouth of the pore. This blocking behaviour has been reported to reduce the single channel conductance, such that permeant ions present may be able to traverse the channel albeit at a reduced rate[Bamberg and Lauger, 1977]. The decrease in resistance could be caused by several factors including protons, which at the buffer pH of 7.4 would exist in concentrations of approximately 40 nM and be transported along a proton wire at a far higher rate than other ions[Pomes and Roux, 1996, 2002], and traces of K^+ leaking from the Ag/AgCl reference electrode. In support of the possibility that protons are responsible, the data look similar to effects observed previously on the addition of a proton ionophore, carbonyl cyanide m-chlorophenyl hydrazone (CCCP)[Jeuken et al., 2006]. SPR experiments shown in Figure 4.6 do not indicate any loss of lipid from the tBLM, however, we cannot exclude the possibility that the addition of gramicidin has degraded the tBLM allowing non-specific ion leakage to occur.

The increased capacitance and slight dip in phase angle around 50 Hz observed in the TMA^+ data is suggestive of rate-limited ion transport. The double layer capacitance is larger than that for Ba^{2+}, but lower than for Na^+, indicating that ion transport is occurring and the sub-membrane ionic reservoirs are being accessed. That the capacitance is lower than for Na^+ may suggest that this does not occur uniformly with ions being transported at either a reduced rate compared to Na^+ or only at a proportion of the gramicidin-permeated regions. The small secondary capacitance seen in Figure 4.4d, and accompanying dip in phase angle around 50 Hz in Figure 4.4c, resemble the effect observed with Ba^{2+}-mediated block. However in this case, the secondary capacitance is smaller than the primary capacitance whereas it is usually the secondary capacitance that is larger. When attempts are made to model the data using an appropriate equivalent circuit this smaller secondary capacitance cannot be fitted. It is thought that this is due to the unidirectional effect of TMA^+ observed by Bokvist and Sandblom [1992], who reported that a facilitory effect is observed when TMA^+, and other quaternary ammonium ions, are added to a supporting electrolyte of 10 mM HCl. While TMA^+ ions themselves are unable to pass through the gramicidin pore, it was hypothesised that the binding of TMA^+ to an external binding site resulted in the lowering of internal energy barriers which resulted in H^+ ions being able to transit more readily[Eisenman and Sandblom, 1983a, b]. They also reported that this effect was unidirectional when asymmetric solutions were used in a planar BLM setup. The asymmetric ion transport rates across the gramicidin dimer pore would result in a 'diode-like effect' with net transport being in favour of transport from bulk electrolyte into the sub-membrane environment. This diode behaviour would in theory affect the resistance of the gramicidin channel. Although resistance changes have been shown to have an effect on capacitance with the Na^+ and Ba^{2+} data, the capacitance changes seen with TMA^+ do not fit with simulations done to examine this effect. While a diode does have its own capacitance, the effect that this would have on the overall system would be negligible given that the change would be confined to the gramicidin channels themselves and not the substantially larger ionic reservoirs that lie beneath the permeated bilayer.

There is a large body of literature relating to work on gramicidin in lipid environments. As may be expected, there are a large number of variables amongst these in terms of the surface, lipids, tethers, gramicidin concentrations and bias potentials. Some examples of this include work by Becucci et al. [2002, 2005] on phospholipid monolayers and hybrid bilayer lipid membranes (hBLMs) on hanging drop mercury electrodes, Nelson [2001] on phospholipid monolayers on hanging drop mercury electrodes, Jadhav et al. [2008] on hBLMs on gold electrodes and the 'Ion Channel Switch' biosensor of Cornell et al. [1997], which included gramicidin covalently bound to antibody fragments in a tBLM system. The findings presented here best resemble those shown by Becucci and Guidelli [2009], where the addition of gramicidin and application of negative potentials allowed the sub-structure of the DPTL SAM to be identified by the distribution of K^+ ions as identified by capacitance. Where they were able to interpret their measured capacitances as various chemical groups of DPTL, we have interpreted our results referring to nanoscale domains of 6MH as explained below.

The contrasting behaviour between valinomycin and gramicidin is most likely due to the difference in ion transport rates (10^2–10^3 ions sec^{-1} molecule^{-1} cf. 10^7–10^8 ions sec^{-1} dimer^{-1}, respectively) and the phase-separated nature of the EO_3C:6MH SAM resulting in nanoscale domains (10-100 nm diameter) of 6MH over which tBLMs are suspended, forming local ionic reservoirs (see Figure 4.1b for a schematic illustration)[Jeuken et al., 2007b]. The capacity of these reservoirs to store ions is severely limited. The incorporation of a gramicidin dimer into one of these regions provides the underlying ionic reservoir with access to the bulk electrolyte. The large conductance of gramicidin dimers reduce the resistance of the tBLM/6MH nano-domain to such an extent that we do not measure a substantial drop in membrane resistance, but instead causes the double layer capacitance to revert back to the value measured without the lipid bilayer. The compartmentalised nature of the tBLM is also believed to have ramifications when electric fields are applied. It has previously been observed that at potentials below -0.25 V vs Ag/AgCl, nanoscale domains lift off the surface up to 15 nm high[Jeuken, 2008]. It is now believed that the nanoscale domains correspond to the 6MH areas on the SAM surface, and water is accumulated in these areas 'pushing' up the lipid bilayer locally.

4.5 Conclusions

In summary, it has been shown that ion transport through tBLMs prepared with cholesterol tethers is only observed when the tethering SAM is diluted such that the layer between the electrode and the lipid bilayer does not solely consist of ethylenoxy linkers. As pure EO_3C SAMs show no changes in resistance or capacitance upon addition of ionophores we propose that they are incapable of solvating ions due to the ethylenoxy linker layer being largely dehydrated. This is supported by independent infrared reflection absorption spectroscopy studies by Leitch et al. [2009] and McGillivray et al. [2007] on similar tethering molecules. However, we expect the degree of dehydration found will be worse due to the lower cross-sectional area of cholesterol (32 $Å^2$)[Rothman and Engelman, 1972] versus these lipids (69 $Å^2$ for DPhyPC)[Pownall et al., 1987]. As such, in our case a functional tBLM will require a balance between tethering units for high membrane resistivity and hydrophilic diluents to allow ion transport.

Unexpectedly, it was shown that ion transport activity does not always result in a decrease in membrane resistance when tBLMs are used. Although slow transport (valinomycin-mediated K^+ and gramicidin-mediated at nanomolar concentrations of $H^+/Na^+/K^+$) results in resistance changes, fast transport (gramicidin-mediated Na^+) is seen as a change in double layer capacitance of the tBLM. Mixed SAMs phase separate creating 6MH nanoscale domains,[Jeuken et al., 2007b] which we hypothesise to be associated with ionic reservoirs. Incremental capacitance change based on gramicidin titration suggests that these ionic reservoirs are not continuous but isolated by the surrounding regions covered in EO_3C. This has been summarised in Figure 4.7.

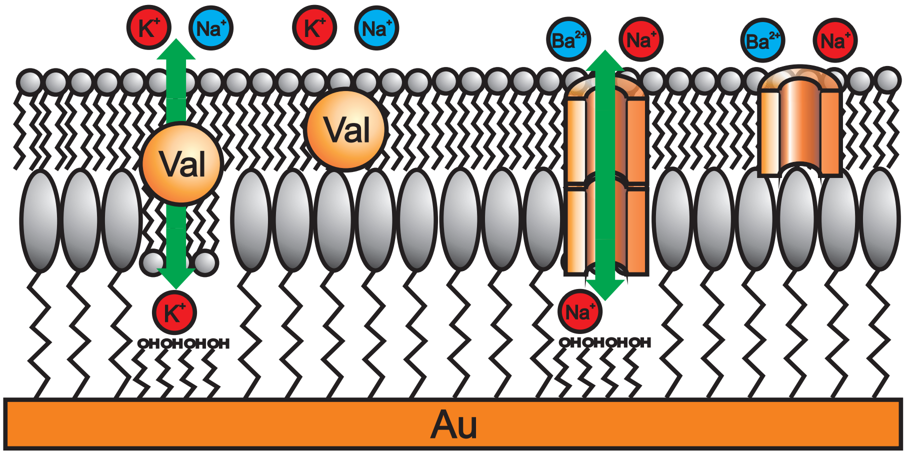

Figure 4.7: Schematic of ionophore transport in different regions of a tBLM formed on a mixed EO_3 cholesterol/6-mercaptohexanol SAM.

Chapter 5

TRPC5

5.1 Introduction

Ion channels, like ionophores, are capable of transporting ions across a lipid bilayer. While ionophores are generally small peptides of 10-20 amino acids, ion channels are much larger ranging from 160 amino acids (KcsA) to in excess of 973 amino acids (TRPC5). In addition to the size difference their ion transport activities are markedly different also. Whereas ionophores can generally be said to be simple carriers, often used by bacteria as toxins to breakdown ionic gradients across membranes, ion channels operate in a more discrete way. The vast majority of ion channels have their ion conductance controlled by a gating mechanism. This usually involves an external stimulus, be it a molecule, light, pH, membrane potential, or mechanical forces, which the protein reacts to resulting in a movement of key transmembrane helices. This movement causes the channel to open allowing ions of a certain size and charge to pass across the membrane. Which ions pass is dependent on the selectivity filter that varies between ion channels[Hille, 2001].

TRPC5 is a member of the TRP channel family discussed in Section 1.4.3. This family is comprised of ligand-gated Ca^{2+} channels. The physiological role that TRPC5 plays is not well defined. It is expressed across the central and peripheral nervous systems[Gomis et al., 2008], as well as in the heart and lungs[Riccio et al., 2002]. Suggested roles have included an osmo- (stretch) sensor protein[Gomis et al., 2008], as well as functions relating to vascular remodelling[Kumar et al., 2006; Xu et al., 2006]. TRP channels form tetramers as shown in Figure 1.25b, with the subunit composition varying from channel to channel. Each subunit has 6 transmembrane domains, several extramembranous loops and cytosolic C- and N-termini (Figure 1.25a). Transmembrane helices 1–4 and some of the connecting loops are most likely responsible for gating and regulatory functions, while transmembrane regions 5 and 6, as well as the loop connecting the two, form a cation-conducting pore that allows passage of Ca^{2+}.

TRPC5 is has been shown to be activated by a number of compounds. Some of these will open the pore at very low concentrations of ligand resulting in the flux of millions of cations per second with single channel studies giving a chord conductance of 41.3 ± 1.1 pS at -60 mV[Jung et al., 2003]. Much work has been done investigating the behaviour of TRPC5 in presence of its ligands including the lanthanides, especially La^{3+} and Gd^{3+}[Jung et al., 2003]; several reducing agents, namely Tris (2-carboxyethyl) phosphine (TCEP) and dithiothreitol (DTT)[Xu et al., 2008]; and a number of lipids[Beech et al., 2009]. Additionally, its inhibition by 2-aminoethoxydiphenyl borate (2-APB) has also been well documented[Xu et al., 2005].

Activation by the lanthanides is thought to be dependent upon Glu^{543} and $Glu^{595/598}$, which can be found at the start and end of the pore forming loop between transmembrane helices 5 and 6. When these residues are mutated La^{3+} and Gd^{3+} have no effect on the conductance properties of TRPC5. In wild type TRPC5 however La^{3+}has been reported by Jung et al. [2003] to increase TRPC5 currents at concentrations as low as 1 μM and achieve maximal effect between 10 μM and 1 mM. However, at concentrations greater than 1 mM this potentiating effect declines and begins to assert an inhibitory effect instead. TRPC5 also responded positively to as little as 1 mM TCEP, as well as 10 mM DTT or 5 mM MTSET[Xu et al., 2008]. These reduce a disulphide bond between a pair of cysteines, Cys^{553} and Cys^{558}. These residues are positioned in an extracellular loop by the mouth of the pore, and when these cysteines are mutated the channel no longer responds to Gd^{3+}. 2-APB is a well known inhibitor of Ca^{2+}-permeant channels and has been used at a concentration of 75 μM in several publications[Beech, 2007; Jung et al., 2003; Xu et al., 2008].

Given that these channels are only found in eukaryotes, for the best chance of success they need to be overexpressed in an eukaryotic expression system such as yeast or, preferably, a mammalian cell line which will have a better chance of faithful reproduction of the functional protein. Here the *trpc5* gene has been inserted into a HEK293 cell line via a plasmid[Zeng et al., 2004]. It has already been shown that bacterial cell membrane extracts can be immobilised on a gold surface functionalised with EO_3C[Jeuken et al., 2005] and yeast cell membrane fractions have been immobilised using 1,2-dipalmitoyl-*sn*-glycero-phosphothioethanol as a lipid tether[Jadhav et al., 2008]. In this chapter we will explore the feasibility of tethering HEK293 cell membranes containing TRPC5 to an EO_3C:6MH tBLM. This will be examined using EIS, as well as IonGate electrophysiology (as described in Section 2.3).

5.2 Experimental Section

5.2.1 Materials

Except where stated otherwise, all chemicals in this section were obtained from Sigma. Electrochemical experiments were performed in a range of buffers all containing MOPS buffer (3-(N-morpholino)propanesulfonic acid, 20 mM) with either Na_2SO_4, K_2SO_4, $TMASO_4$, NaCl or $BaCl_2$ (30 mM in all cases) adjusted to pH 7.4 with NaOH, KOH, HCl, $Ba(OH)_2$ or TMAOH, respectively, at 20 °C. Ethylenediaminetetraacetic acid (EDTA) was adjusted to pH 7.4. $CaCl_2$ was made up to a 1 M stock solution. *trpc5*$^+$ and *trpc5*$^-$ HEK-293 cells were kindly donated by D.J. Beech, University of Leeds[Zeng et al., 2004]. T175 cell culture flasks (Sarstedt) were used as received. Fetal bovine serum (FBS), penicillin, and streptomycin were added to Dulbecco's Modified Eagle's Medium-F12+GlutaMAX (Invitrogen) prior to use. Blasticidin, zeocin, tetracycline, trypsin-EDTA, sucrose, Tris-Cl, Na_2CO_3, glucose, HEPES, $MgCl_2$, DTT, TCEP, La^{3+}, and glycerol were used as received, as was 'Complete' protease inhibitor (Roche). Bovine serum albumin (BSA), sodium bicinchoninic acid, sodium-potassium tartrate, NaOH, $NaHCO_3$ and $CuSO_4$ were used as received. IonGate reagents (SensorPrep A and SensorPrep B), as well as IonGate electrodes were used as per manufacturers instructions.

5.2.2 Cell Culture

HEK-293 cells contained the pcDNA4/TO plasmid vector with human *trpc5* cDNA inserted between the *kpn* I and *xho* I sites.[Zeng et al., 2004] Cells were grown in Dulbecco's modified Eagle's medium-F12+GlutaMAX, to which 10% fetal bovine serum (FBS) was added, along with penicillin (50 units/mL) and streptomycin (0.5 mg/mL). Flasks were split at approximately 70% confluence (as determined by microscope examination). For this cell medium was removed and the cells rinsed with 1 mL of trypsin-EDTA. Trypsin-EDTA was repeatedly pipetted over the cells to cleave from the flask surface before transferring to new T175 flasks (Sarstedt) and adding 10 mL of cell medium. Cells stably expressing TRPC5 were selected by 5 μg/mL blasticidin and 400 μg/mL zeocin (Invitrogen). Cells were grown at 37°C under 5.2% CO_2.

5.2.3 Expression of TRPC5

HEK293 cells were grown for one day before inducing expression of TRPC5 with 1 μg/mL tetracycline for 24 hours. Cells were then allowed to grow to approximately 80% confluence as determined by optical microscopy. Cell medium was removed and cells were rinsed with 2 mL of PBS before being removed also. Cells were removed from flask surface using 2 mL trypsin-EDTA, before adding 2 mL of cell medium with FBS to inactivate trypsin. Contents of two flasks were pooled into a single 15 mL Falcon tube before centrifuging at 100 rpm for 2 minutes. Supernatant was discarded and cell pellet was resuspended in 1 mL of buffer 2 (20 mM MOPS, 30 mM Na_2SO_4, 1 mM EDTA, pH 7.4). The contents of three 15 mL Falcon tubes were pooled into a 50 mL Falcon tube and topped up with 42 mL of buffer 2, along with 1 mM of the protease inhibitor PMSF.

5.2.4 Protein Preparation

Membrane samples were prepared using a protocol provided by IonGate Biosciences that has been specifically designed for the isolation of HEK293 cell membranes[Ion, 2008]. Cell suspension was defrosted and pelleted by low speed centrifugation at 3000 x g for 10 minutes. A minimum of 2 mL of packed cell volume (PCV) was required for the protocol. The 2 mL pellet was resuspended in 250 mM sucrose and 10 mM Tris buffered to pH 7.5 with 'Complete' protease inhibitor (Roche). The cells were centrifuged again at 800 x g for 5 minutes and then resuspended in 5 mL of 1 mM Na_2CO_3 at room temperature. The cell suspension was diluted with more 1 mM Na_2CO_3 to give a total volume of 40 mL and shaken strongly. The change in osmolarity between the sucrose buffer and Na_2CO_3 solution results in osmotic swelling and rupture of the cell membranes. The homogenate was then centrifuged at 800 x g for 10 minutes to remove cell debris and nuclei. The supernatant was collected and centrifuged at 100000 x g for 30 minutes in a Ti45 rotor at 4°C to pellet the plasma membranes (including some intracellular membranes). This membrane pellet was then resuspended in 500 μL of 10 mM Tris at pH 7.5. The membrane suspension was mixed with 3.75 mL of 70% (w/v) sucrose in a Ti45 centrifuge tube and layers of 9 mL 45% (w/v) sucrose, 9 mL 31% (w/v) sucrose and 6 mL 9% (w/v) sucrose were stacked on top to produce a sucrose density gradient. The gradient was centrifuged at 100000 x g overnight with the brake off at 4°C. The sucrose fractions were collected separately, diluted 3 fold with a storage buffer of 134.3 mM NaCl, 5 mM KCl, 8 mM glucose, 10 mM HEPES, 1.2 mM $MgCl_2$ and 1.5 mM $CaCl_2$ adjusted to pH 7.4 with NaOH. The diluted fractions were then centrifuged at 100000 x g for 30 minutes in a Ti45 rotor. The supernatant was discarded and the pellet resuspended in approximately 200 μL of the storage buffer with 10% (v/v) glycerol and 0.2 mM DTT added. Small aliquots of 50 μL of each fraction were taken for testing and the remainder of the sample frozen in liquid N_2 and stored at -80°C.

5.2.5 BCA Assay

A BCA assay was used to determine protein concentration in samples. A range of BSA standards was used for calibration, ranging from 0.2–1.0 μg. Given approximate concentrations expected from the IonGate purification protocol, the quantity of sample to be added was approximated and diluted with SDS (1% w/v) to give concentrations within the range of the BSA standards. BCA reagents A (1.0% sodium bicinchoninic acid, 2.0% Na_2CO_3, 0.16% NaK tartrate, 0.4% NaOH, 0.95% $NaHCO_3$ adjusted to pH 11.25 with 50% NaOH) and B (4% $CuSO_4$) were mixed in a 50:1 ratio and then added and incubated at 37°C for 30 minutes, before being read in a plate reader at 562 nm.

5.2.6 SDS-PAGE

A 7.5% polyacrylamide gel was made. Samples were diluted with Milli-Q water to give an approximate mass of 10 μg of protein per well using the protein concentrations obtained from the BSA assay. Loading buffer, including SDS and DTT were also added to the sample. A marker (Precision Plus Protein Standards, 250 kD–20kD Unstained; BioRad) was used as a reference. The gel was loaded into an electrophoresis chamber and 120 V was applied for approximately 1 hour, or until the marker dye in the wells reached the bottom of the gel. The gel was removed from the chamber, washed and incubated in Coomassie blue for several hours before being rinsed in Milli-Q water and transferred to destain overnight. The gel was then rinsed in Milli-Q water again and imaged in white light.

5.2.7 Western Blot

A second gel for Western blotting was performed at the same time as the SDS-PAGE in the same conditions, however a dual colour marker (Precision Plus Protein Standards, 250 kD–20 kD Dual Colour; BioRad) was used and the gel was not stained with Coomassie blue. Instead, the gel and a nitrocellulose membrane were sandwiched between several sheets of filter paper and clamped together, put into an electrophoretic transfer chamber and an electrical current of 50 mA passed through the plane of the gel to transfer proteins to the membrane for 80 minutes. The membrane was removed and blocked with 5% (w/v) milk powder in TBST for 2 hours at 4°C. The membrane was then washed with TBST twice for 15 minutes each before incubating in 2.5% (w/v) milk in TBST with 1 μg/mL rabbit anti-TRPC5 primary antibody at 4°C for 1 hour. The membrane was then washed in TBST three times as previously described, before adding the HRP-conjugated goat anti-rabbit secondary antibody and incubating for 1 hour at room temperature. The membrane was then washed another three times in TBST as previously described, before finally adding 400 μL of Pierce SuperSignal Femto substrate (a chemiluminesence marker) and incubating for 5 minutes at room temperature in the absence of light. The membrane was dried and transferred to a dark room where it was exposed to photographic film for 30 seconds. The photographic film was then immersed in developer for 2 minutes, washed in water for 1 minute, then immersed in fixer for a minute before finally washing in water and hanging up to dry. Further images were produced with varying exposure times. The photographic film was overlaid on the Western blot and the coloured markers traced onto the photographic film.

5.2.8 IonGate

IonGate Electrode Preparation

IonGate electrodes were prepared according to the manufacturer's protocol. IonGate electrodes were incubated with 50 μL of IonGate SensorPrep A for 15 minutes to form a

SAM. The electrode was then rinsed four times with isopropanol before drying under a stream of N_2 and leaving for 30 minutes to allow any residue isopropanol to evaporate. 3 μL, of SensorPrep B1 was then added, immediately followed by 50 μL, of non-activating TRP buffer (137 mM NaCl, 5 mM KCl, 10 mM HEPES, 1.2 mM $MgCl_2$, 1.5 mM $CaCl_2$, pH 7.4) with 0.2 mM DTT. This was left for 45 minutes to allow hybrid BLM formation. Membrane preparations were diluted in non-activating TRP buffer with 0.2 mM DTT and then added to the electrode surface. Electrodes were then centrifuged at 2500 rpm for 45 minutes at 4°C. Great care was take throughout not to touch the electrode surface with the pipette tip.

IonGate Measurements

Solid-supported membrane electrophysiology was used to examine whether TRPC5 could be incorporated into a solid-supported membrane. In these experiments the sample is kept hydrated in a resting electrolyte when not being studied. The measurement starts with the replacement of the resting electrolyte with the non-activating electrolyte under constant flow conditions. This non-activating electrolyte contains Ca^{2+}, TRPC5's conducting ion, but not TRPC5's activating ligand, La^{3+}. The sample is kept in non-activating electrolyte for 2 seconds allowing a baseline to be established, before replacing it with activating electrolyte containing both Ca^{2+} and La^{3+}. The response to this change is measured for a further 2 seconds before reverting back to the non-activating electrolyte, recording for a final 2 seconds, and putting the electrode back into resting electrolyte. The concentration of $LaCl_3$ in the activating electrolyte was incremented from 1 to 100 μM, before adding 2-APB to inhibit channel function.

Resting electrolyte contained 141.5 mM NaCl, 5 mM KCl, 10 mM HEPES, 1.2 mM $MgCl_2$. Non-activating electrolyte contained 137 mM NaCl, 5 mM KCl, 10 mM HEPES, 1.2 mM $MgCl_2$, 1.5 mM $CaCl_2$. Activating electrolyte contained 137 mM NaCl, 5 mM KCl, 10 mM HEPES, 1.2 mM $MgCl_2$, 1.5 mM $CaCl_2$ and 1-100 μM $LaCl_3$. The concentrations used here were selected to mimic the bathing electrolyte used in patch clamp experiments, while also ensuring that the ionic strength of the electrolyte was kept as constant as possible. The increase in ionic strength calculated for the addition of μM quantities of $LaCl_3$ was deemed small enough to be considered negligible.

5.2.9 Electrochemical Impedance Spectroscopy

Preparation of P1 Electrodes

As described previously in Chapter 4.

Formation of SAMs

As described previously in Chapter 4.

5.2.10 Formation of Mixed Proteoliposomes

Following the determination of protein concentration, a sample is then diluted with *E. coli* polar lipid extract. A suspension of *E. coli* vesicles is made up and extruded through 200 nm pores 11 times. To this vesicle suspension, the HEK293 membrane sample is added to give a concentration of 10% (w/w) protein concentration from HEK293 membranes. The solution is then subjected to two cycles of freeze-thawing in liquid nitrogen, which has been reported to lead to fusion of vesicles. The membranes are then split into 200 μL, aliquots, frozen in liquid nitrogen and stored at -80 °C. When used they are diluted in buffer and again extruded through 200 nm pores 11 times.

Formation of tBLM

As described previously in Chapter 4.

EIS Measurements

As described previously in Chapter 4.

Additionally, the measurement of TRPC5 channels requires the presence of Ca^{2+} as the permeant ion and the addition of La^{3+} as the gating ligand. SAMs were measured in 30 mM Na_2SO_4, 20 mM MOPS buffer at pH 7.4 to determine SAM coverage. 200 μL of membrane preparation and 10 mM $CaCl_2$ added to 1780 μL of electrolyte buffer and incubated for 1 hour to allow the tBLM to form. The tBLM was then rinsed with 50 mM EDTA, and four times with Na_2SO_4/MOPS buffer. A measurement was then taken to determine the tBLM capacitance in MOPS buffer for comparison to *E. coli* polar lipid tBLM capacitances recorded in Chapters 3 and 4.

TRPC5 buffer (134.3 mM NaCl, 5 mM NaCl, 8 mM glucose, 10 mM HEPES, 1.2 mM $MgCl_2$ and 1.5 mM $CaC._2$, adjusted to pH 7.4 with NaOH) was used from here on out. MOPS buffer was exchanged for TRPC5 buffer by rinsing the cell a minimum of 5 times, before taking a second measurement of the tBLM to determine the membrane characteristics. La^{3+} was then added at concentrations of 1 μM, 5 μM, 10 μM, and 100 μM. Measurements were taken at each step with time being given for the La^{3+} to exert its effect. The cell was then rinsed thoroughly with fresh TRPC5 buffer and remeasured for a further hour.

Data were analysed with the software EISFit, as described previous using two equivalent circuits were used - $R_s(Q_{tBLM}R_{tBLM})$ and R_sQ_{tBLM}, referred to as R(QR) and RQ, respectively (Figure 5.1).

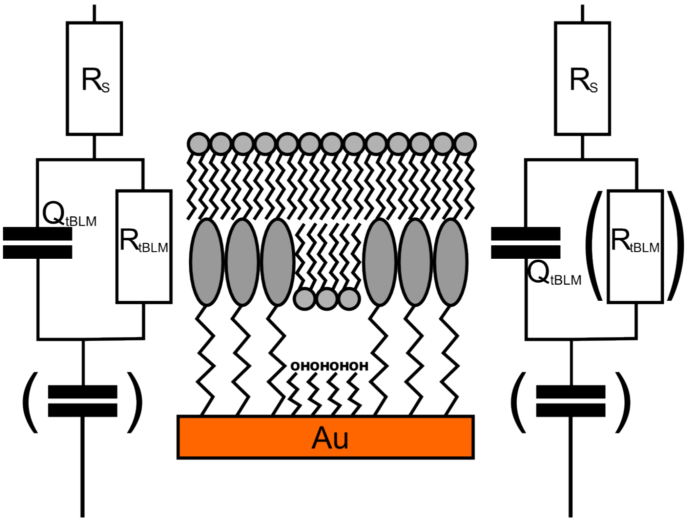

Figure 5.1: Equivalent circuit used in analysis of impedance data. (left) The equivalent circuit described as R(QR), used for SAMs and tBLMs. (right) The equivalent circuit described at RQ, used to analyse La^{3+} control experiments for reasons discussed later. R_s is solution resistance (electrolyte), Q_{tBLM} is capacitance of the entire tBLM modelled by a constant phase element (CPE) and R_{tBLM} is membrane resistance. Components enclosed in a bracket indicate that the element is not modelled as it is not observed in impedance spectra, but would be expected if measuring at lower frequencies.

5.3 Results

5.3.1 Protein Expression

Plasma membranes were ‘released’ from HEK293 cells by osmotic swelling as described in Section 5.2.4[Ion, 2008]. Following the lysis it became apparent that the nuclear membrane had ruptured releasing DNA into the sample. Attempts were made to avoid this by centrifuging the sample at 1000 x g to form a loose pellet of the DNA. The supernatant was transferred to a three-layer sucrose density gradient and subjected to ultracentrifugation, which gave three fractions all of which were harvested and tested for protein content using a BCA assay. The three fractions were calculated to contain 0.178 mg, 1.298 mg and 1.512 mg protein in the top (9%), middle (31%) and bottom (45% sucrose) fractions, respectively. A 100 μL sample taken prior to the sucrose gradient, assumed to be essentially the total membrane fraction, was also tested and found to contain 0.499 mg protein.

Protein content normalised SDS-PAGE and Western Blots were made of these samples as shown in Figures 5.2 and 5.3. The SDS-PAGE gel, Figure 5.2, shows numerous bands in all 4 samples. The total membrane fraction contains all of the bands found in the three separated fractions as one would expect. Particularly prominent bands can be found at approximately 40 kDa, 50 kDa, 60 kDa, 90 kDa, 100 kDa and 140 kDa. Additionally, there are also a number of bands between 50–100 kDa, as well as some higher molecular weight bands around 250 kDa. The bottom fraction has a band at approximately 100 kDa that is significantly more intense than in the top and middle fractions, while containing marginally less of the proteins that make up the sub-100 kDa bands predominantly seen in middle fraction. The top fraction contains fewer clear bands, and those that are visible tend to be in the sub-100 kDa range. This shows that while the membrane proteins have been fractionated to an extent, there is still substantial mixing of the samples as can be seen by the presence of the majority of proteins in each fraction. The fractionation protocol may require further refinement.

The two Western Blots (Figures 5.3a and 5.3b) clearly show that TRPC5 is found in all four lanes at approximately 100 kDa. 10 seconds exposure time highlights these bands at 100 kDa as being the predominant form of TRPC5, while a longer exposure of 30 seconds in Figure 5.3b shows the presence of some other bands. Two high molecular weight bands are visible at 250 kDa and larger than 250 kDa. These are likely to be TRPC5 aggregates and are most prevalent in the middle and total membrane fractions. The middle membrane fraction also appears to have a low molecular weight band at 75 kDa, which is not present in the other lanes. This confirms the earlier conclusion that while some fractionation has occurred, there is still a broad distribution of certain species throughout all fractions. As such, it was decided to continue with the middle fraction in accordance with the IonGate protocol.

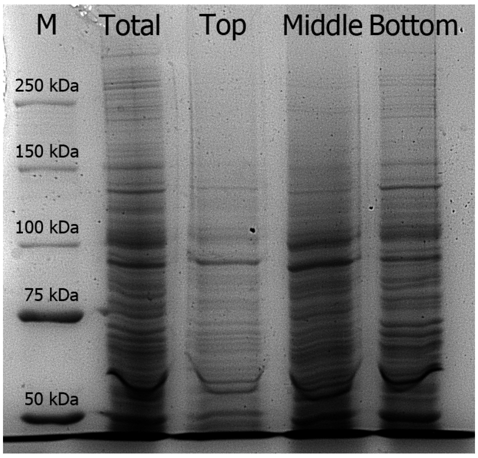

Figure 5.2: SDS-PAGE stained with Coomassie Blue. Lanes from left to right are marker, total membrane fraction, top membrane fraction, middle membrane fraction, bottom membrane fraction.

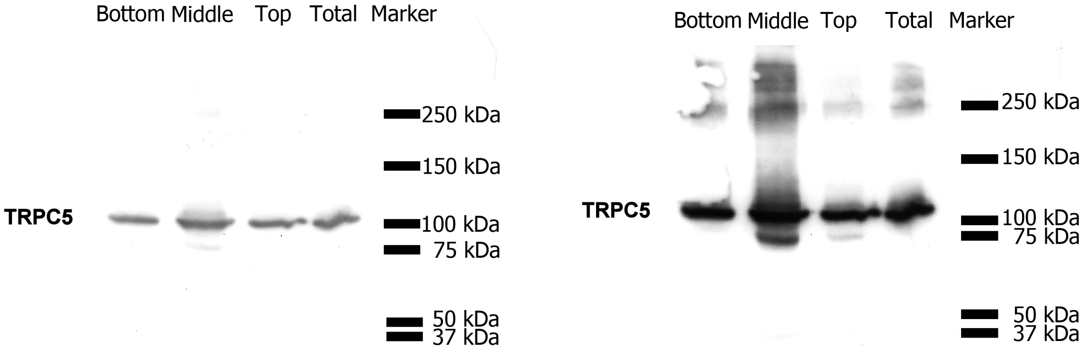

(a) 10 second exposure

(b) 30 second exposure

Figure 5.3: Western Blot. Lanes from left to right are bottom membrane fraction, middle membrane fraction, top membrane fraction, total membrane fraction, marker. The membrane was incubated with rabbit anti-TRPC5 antibody, followed by HRP-conjugated goat anti-rabbit antibody. Detection was achieved using a chemiluminescent marker and exposing to photographic film.

5.3.2 IonGate Solid-Supported Membrane Electrophysiology

Solid-supported membrane electrophysiology was used to examine whether TRPC5 could be incorporated into a solid-supported membrane. The effect of La^{3+} on ion channel activity was studied, as was the effect of a 2-APB, a known inhibitor of TRPC5.

Figure 5.5 shows a small selection of a large number of experiments carried out in parallel with each other. It should be noted that the results obtained varied greatly from sample to sample - the cause of these variations is not clear, but is expected to relate to inconsistent concentrations or incorporation rates of TRPC5 channels in the samples used. Attempts have been made in later figures to use normalised data for comparison between such samples.

Figure 5.5a shows a sample obtained from HEK293 cells expressing TRPC5 (*trpc5*$^+$), while Figure 5.5b shows a sample obtained from HEK293 cells without the TRPC5 gene (*trpc5*$^-$). These experiments consist of 4 phases - a resting phase, an equilibration phase, an activation phase, and a washout phase (Figure 5.4).

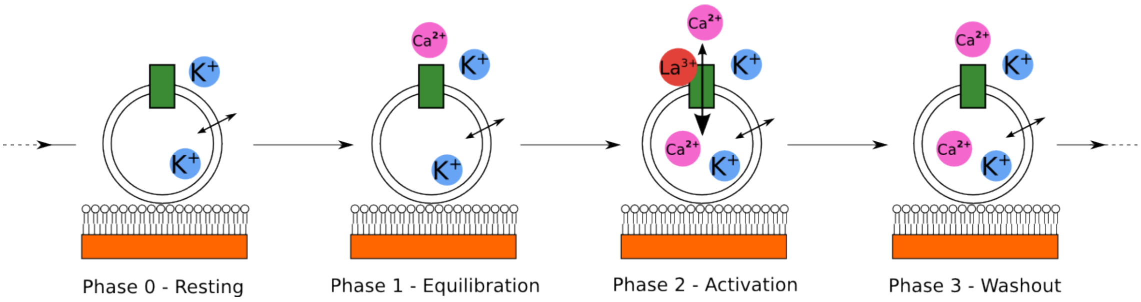

Figure 5.4: Schematic representation of the flux of ions at each phase of the IonGate experimentspresented in Figures 5.5, 5.7 and 5.9. TRPC5 is represented by the green rectangle, ions by coloured circles annotated with their identity, and arrows represent the movement of ions. The small arrow on the right hand side of each vesicle represents leak of ions, a trait commonly associated with vesicles in such systems.

Figures 5.5, 5.7 and 5.9 are divided into 3 phases, corresponding to phases 1-3 that start at time 0.0 s, 2.0 s, and 4.0 s, respectively. Phase 0 occurs between phase 3 and phase 1. In phase 1, the resting buffer (containing no Ca^{2+} or La^{3+}) is replaced with non-activating buffer (containing Ca^{2+}, but no La^{3+}). The binding of Ca^{2+} to the SSM results in a small signal as the system equilibrates. This effect is found in both the presence and absence of TRPC5, suggesting it is due to non-specific binding. Phase 2 sees the addition of varying concentrations of La^{3+} as part of the activation buffer. While the effect of La^{3+} on *trpc5*$^-$ samples is greatly diminished, a small peak remains. It is likely that this is also due to non-specific binding, similar to that observed for Ca^{2+} in phase 1. Addition of 5 μM La^{3+} results in small increases in peak height in samples derived from *trpc5*$^+$ HEK293 cells, while the *trpc5*$^-$ sample in Figure 5.5b shows a greatly diminished effect. Similarly, further additions of La^{3+} to 25 μM, 50 μM and 100 μM resulted in large increases with *trpc5*$^+$ samples (Figure 5.5a); but not for *trpc5*$^-$ samples (Figure 5.5b), which saw only marginal increases to 0.75 nA for 100 μM vs. 4.5 nA for *trpc5*$^+$

(Figure 5.5). The addition of 2-APB in phase, following the addition of 100 μM La^{3+}, led to significant decreases in response in each case with peak height dropping to 1.0 nA and 0.1 nA for *trpc5*$^{+}$ and *trpc5*$^{-}$, respectively. Phase 3 sees a negative signal as La^{3+}, and 2-APB, are washed out and replaced with non-activating buffer. When TRPC5 is present, these negative signals increase in line with the La^{3+} concentration used in phase 2. When TRPC5 is absent a small negative signal remains but its size remains constant.

These effects can be seen in greater detail in Figure 5.6, where the peak heights (open symbols) and integrals (closed symbols) are plotted against the concentration of La^{3+}. The effect of La^{3+} on *trpc5*$^{+}$ samples (marked with circles and squares) exhibit a sharp increase in the measured current both as a function of peak height (open) and peak integral (closed). The *trpc5*$^{-}$ control sample (triangles), however, does not experience such a response. Furthermore, the addition of 2-APB results in a drop in current in all cases. This small drop in response in the *trpc5*$^{-}$ sample, suggests that 2-APB may elicit some manner of response in the lipid bilayer that is not restricted to its action on TRPC5.

In Figure 5.6b, the magnitude of the off peaks (from phase 3) has been subtracted from that of the on peaks (phase 2). Doing this for both peak height and peak integral presents a better view of what is happening in terms of ion flux. The peak integral is the total charge measured; that is, the charge required to counter the influx of ions to the vesicles as shown in Figure 5.4 (phase 2). As can be seen in Figure 5.6b this reaches a plateau following addition of 25 μM La^{3+} for both *trpc5*$^{+}$ samples. This represents the point at which intra- and extra-vesicular electrolytes reach equilibrium, and the difference between samples relates to the number of surface bound vesicles undergoing equilibration. Peak height however increases with La^{3+} concentration and is related to the rate at which charge builds. In terms of ion channels this can be attributed at least in part to the frequency and length of channel opening events. As such a TRPC5-containing vesicle exposed to 100 μM La^{3+} will reach equilibrium quicker than one exposed to 25 μM La^{3+}. Interestingly, at concentrations of 5 μM La^{3+}, the integral is significantly lower suggesting that the vesicle does not reach equilibrium. Given the small peak height it is likely that this is due to a slow rate of ion transfer in weakly activated channels. With longer time periods one could expect equilibrium to be reached, however in these experiments each phase only lasts 2 seconds. In samples where TRPC5 is not present a slight increase in peak integral and height is seen with increasing La^{3+} concentration, however, the extent of this is far smaller that that observed with *trpc5*$^{+}$ samples and the ‘jump’ in activity observed between 0 and 25 μM La^{3+} is not detected. This may indicate a La^{3+}-lipid interaction that was not accounted for by subtracting the off peak. Unexpectedly, the TRPC5 inhibitor 2-APB had an inhibitor effect on this non-TRPC5 La^{3+}-mediated response. This suggests that 2-APB’s mode of action is not necessarily confined to a specific interaction with TRPC5, but may exert its effect by changing physico-chemical properties of the lipid bilayer.

Figure 5.7 shows experiments, performed in series on the same sample, showing the effect of La^{3+} titration when 2-APB is added to both the non-activating and activating electrolytes. These experiments are subtly different from those shown in Figure 5.5 where 2-APB was only added to the activating buffer. Adding the inhibitor in phases 1-3 should remove any influence it may have on the activating peak (phase 2) besides an inhibitory effect, as any initial reactions should have stabilised. In addition to this, it ensures that the inhibitor has time to exert its effect. Figure 5.7a shows the La^{3+} titration without the presence of 2-APB at every phase. Here, smaller responses to La^{3+} addition are measured than seen in Figure 5.5a, however, the response does increase with La^{3+} concentration suggesting the lower activity can most likely be attributed to a variation in the amount of active channels available in each membrane preparation used. While the increases in peak height are only small, the slowed rate of signal decay leads to a large increase in the peak integral, as is shown in Figure 5.8.

Figure 5.7b show the same experiment, but with 75 μM 2-APB added to both the non-activating and activating electrolytes such that it is present throughout the experiment (phases 1-3), with the exception of the resting phase (phase 0). Under these conditions there are negligible changes in the peak height, while the peak decays more rapidly than before resulting in a smaller peak integral than that observed in the absence of 2-APB, which is also unresponsive to changes in La^{3+} concentration. Furthermore, the response observed when changing from activating to non-activating electrolyte, 4 seconds into the experiment, has no negative component unlike that seen without 2-APB.

Figure 5.9 shows the effect of another of TRPC5's ligands, the membrane impermeable disulphide reducing agent Tris (2-carboxylethyl) phosphine hydrochloride (TCEP). As can be seen by the black plot, the change from non-activating electrolyte to activating electrolyte with 0 mM TCEP is similar to that observed in Figure 5.5a. However when 1 mM TCEP was added to the activating electrolyte, the peak amplitude increased massively to 2.5 nA. This was a rapid, but short lived response that rapidly decayed and transitioned into a negative phase with an amplitude of -1.25 nA before slowly returning to the baseline. Exchanging the activating electrolyte for non-activating electrolyte repeated the response with a rapid negative peak 2.0 nA in height and a positive trough with an amplitude of approximately 1.2 nA. Addition of 75 μM 2-APB and subsequent measurements with no TCEP or 2-APB in the activating electrolyte, saw no significant change in peak heights or rates of signal decay.

It is possible that the addition of TCEP (a disulphide reducing agent) resulted in a modification of the SAM layer causing permanent change to the system. Additionally, TCEP itself is electroactive with a reduction potential of -0.25 V (vs Ag/AgCl). As a result of these complications TCEP studies were not taken further.

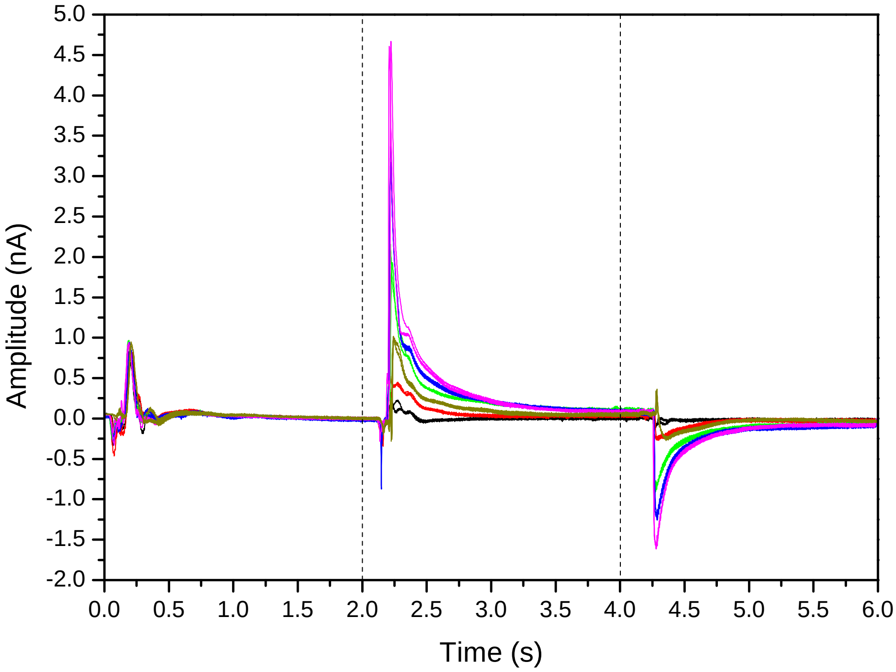

(a) *trpc5*$^+$ sample

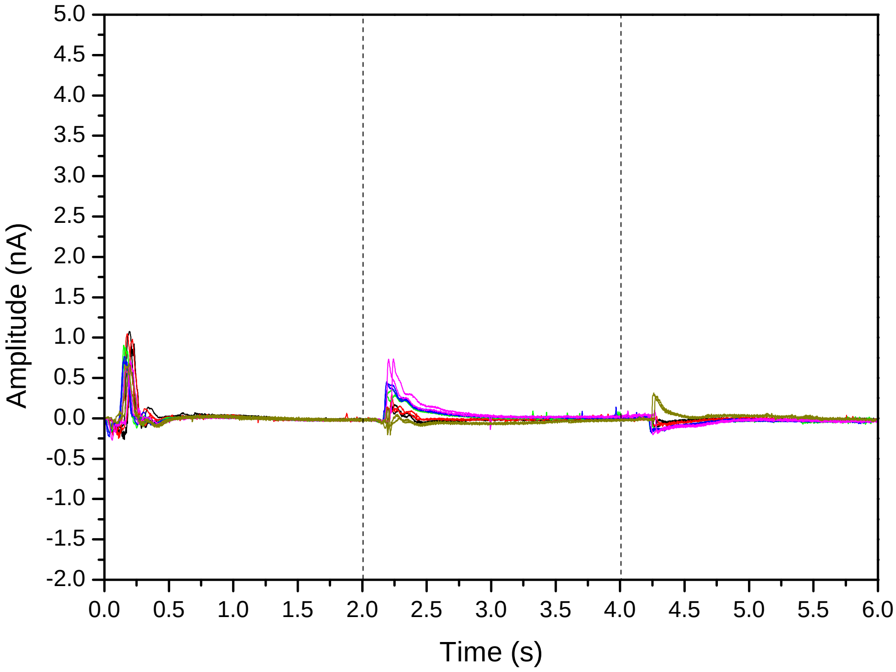

(b) *trpc5*$^-$ control sample

Figure 5.5: IonGate data showing titration with La^{3+}. Black = 0 μM La^{3+}; Red = 5 μM La^{3+}; Green = 25 μM La^{3+}; Blue = 50 μM La^{3+}; Magenta = 100 μM La^{3+}; Mustard = 100 μM La^{3+} + 75 μM 2-APB.

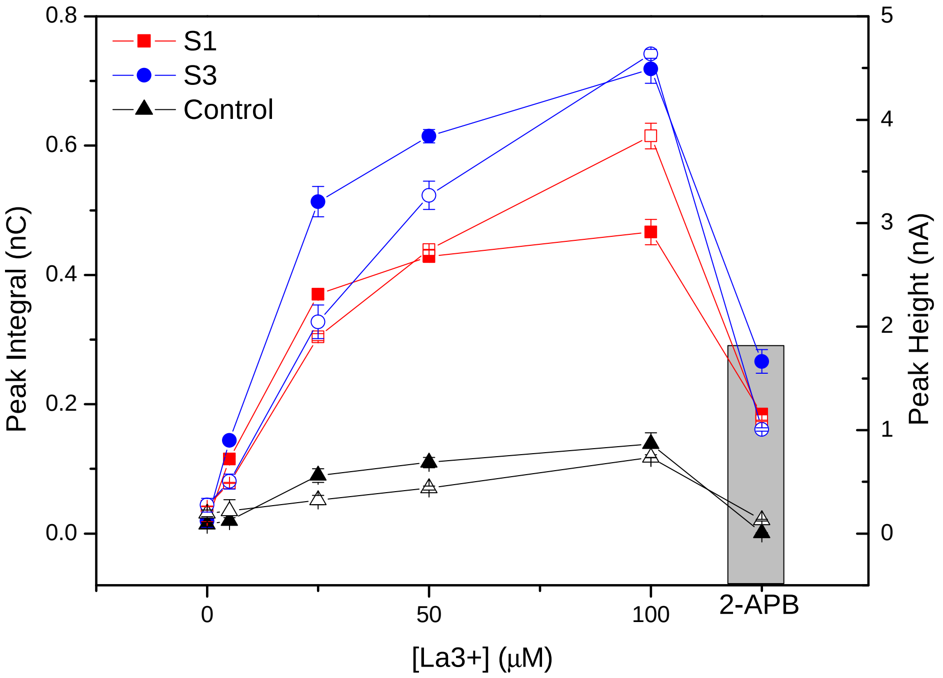

(a) On

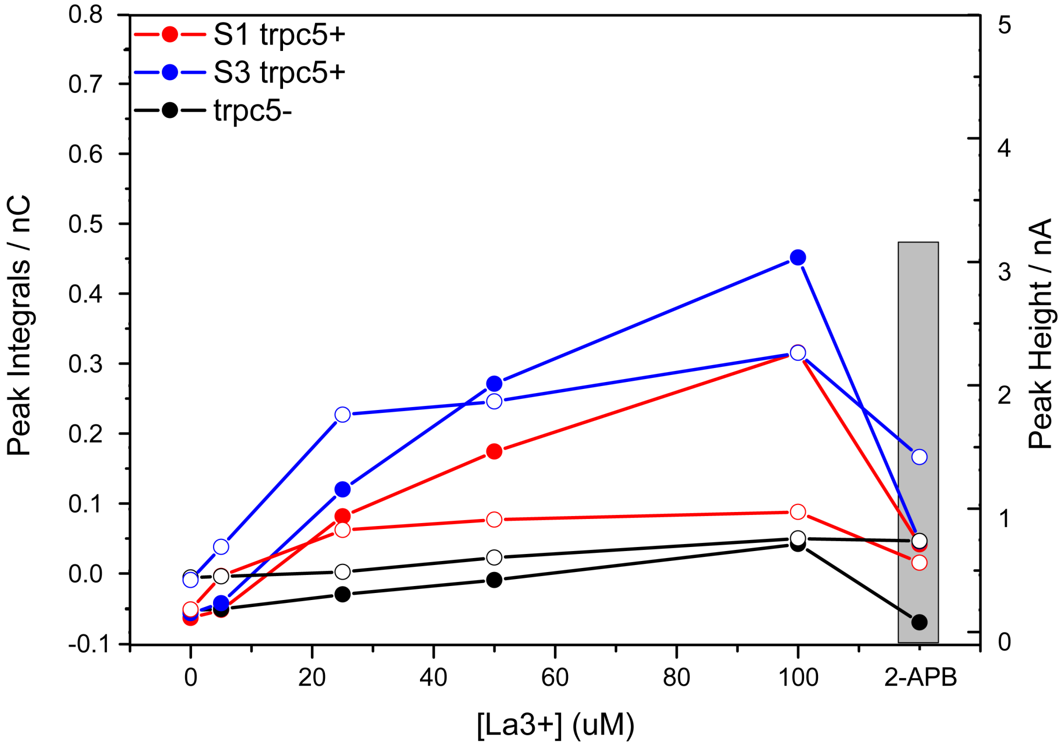

(b) On - Off

Figure 5.6: Response of TRPC5 IonGate system to La^{3+}-titration displayed as (a) peak height and integral vs [La^{3+}], and (b) difference between phase 2 (on) and phase 3 (off) peaks for height and integral. Peak height represented by open shapes, peak integral by solid shapes. Black = *trpc5*$^{-}$ control; Red = *trpc5*$^{+}$ (S1); Blue = *trpc5*$^{+}$ (S3).

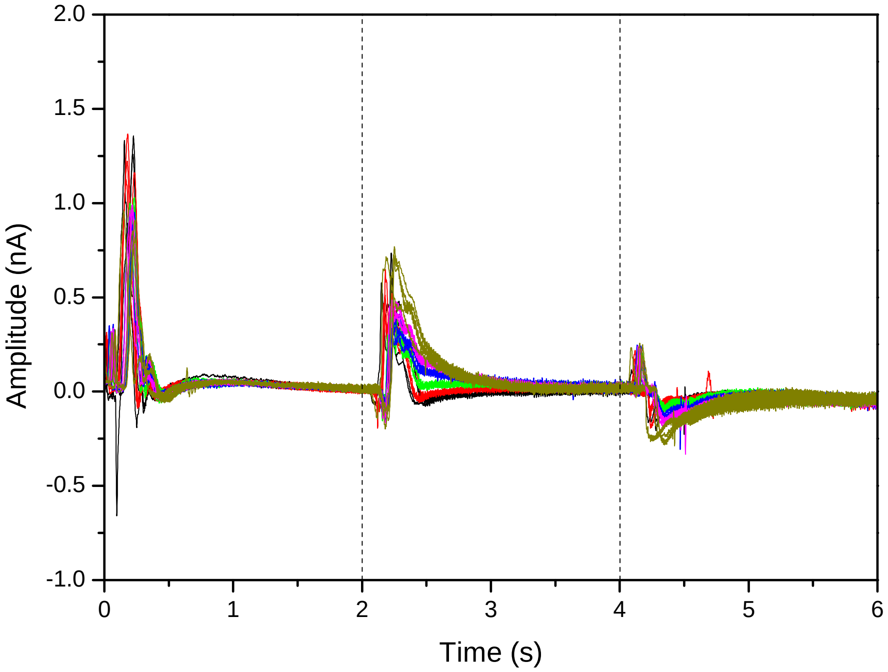

(a) No APB

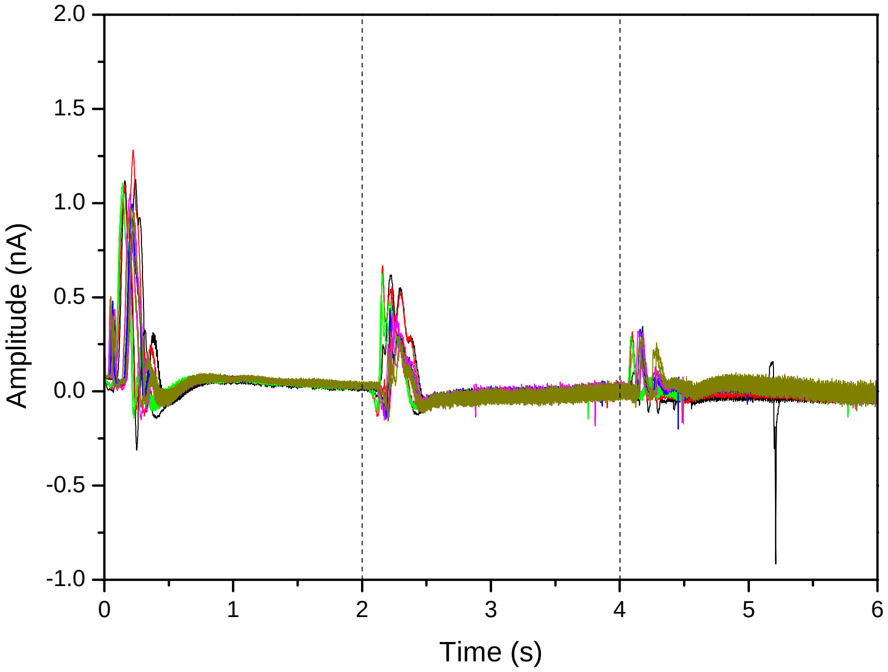

(b) With APB

Figure 5.7: TRPC5 IonGate control data showing La^{3+} titration with and without presence of 2-APB inhibitor. Black = 0 μM La^{3+}; Red = 5 μM La^{3+}; Green = 10 μM La^{3+}; Blue = 25 μM La^{3+}; Magenta = 50 μM La^{3+}; Mustard = 100 μM La^{3+}.

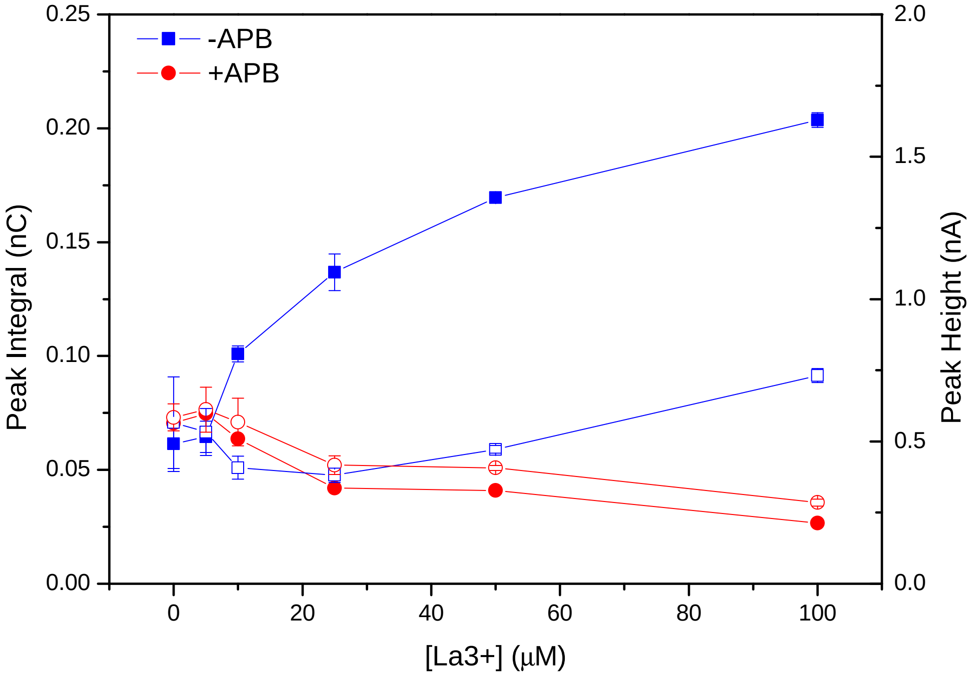

Figure 5.8: Response of TRPC5 IonGate system to La^{3+}-titration in the presence and absence of Ca^{2+}-channel inhibitor 2-APB. Peak height represented by open shapes (left axis), peak integral by solid shapes (right axis). Blue = *trpc5*$^{+}$ - 2-APB; Red = *trpc5*$^{+}$ + 2-APB.

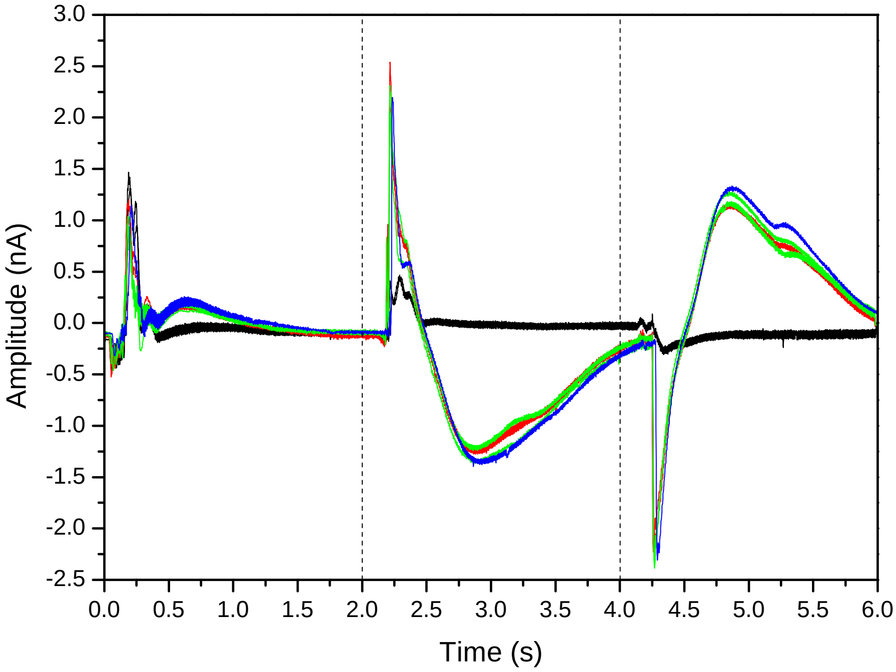

Figure 5.9: TRPC5 IonGate data showing titration with 1 mM TCEP, followed by 75 μM 2-APB. Black = 0 mM TCEP; Red = 1 mM TCEP; Green = 1 mM TCEP + 75 μM 2-APB; Blue = Wash.

5.3.3 Electrochemical Impedance Spectroscopy

Following the successful measurement of TRPC5 activity with the IonGate workstation, EIS was used to study TRPC5-containing tBLMs on P1C electrodes. Membrane fragments were added to *E. coli* polar lipid extract, which had been extruded through 200 nm pores, at a concentration of 10% (w/w). The mixture was then subjected to two rounds of freeze-thaw, before being extruded a further 11 times through 200 nm pores to produce TRPC5-containing proteoliposomes. Mixed membranes are used in this case, as prior work with *E. coli* membranes has shown that undiluted membranes do not form high quality tBLMs[Weiss et al., 2009]. It is thought that this is due to the high proportion of membrane proteins preventing EO_3C from interfacing with the lipid bilayer.

Figure 5.10 shows a mixed SAM with 82% EO_3C coverage and a capacitance of 1.69 $\mu F/cm^{-2}$. Addition of TRPC5 proteoliposomes resulted in the capacitance dropping to 0.96 $\mu F/cm^{-2}$, which is within the expected range for a tBLM containing proteins[Weiss et al., 2009]. Titration of La^{3+} caused minor fluctuations in the capacitance and a noticeable decrease in the resistance of the membrane from 1.2 $M\Omega.cm^2$ to 0.43 $M\Omega.cm^2$, an effect that could potentially be linked to activation of the channel. These effects can be better seen in Table 5.1.

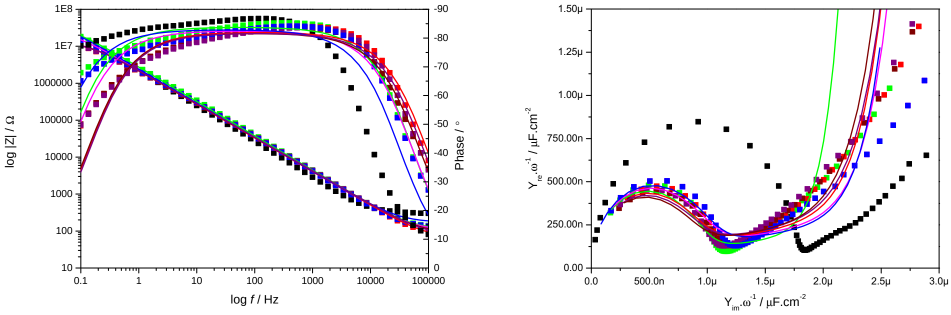

(a) (b)

Figure 5.10: EIS data for TRPC5-containing tBLM with La^{3+} addition. Black = 82% SAM. Green = Bilayer formed from TRPC5 proteoliposomes. Magenta = 1 μM La^{3+}; Red = 5 μM La^{3+}; Wine = 10 μM La^{3+}; Purple = 100 μM La^{3+}. Blue = wash out in Na^+.

Attempts to reproduce this activity were unsuccessful, in part due to the varying capacitances observed with La^{3+} addition, as explained below.

La^{3+} Controls

Figure 5.11 shows a control experiment to investigate the effects of La^{3+} addition on the lipid content of the tBLM. The tBLM was formed on a mixed SAM, with 85% EO_3C coverage, using only *E. coli* polar lipids. The double layer capacitance of the tBLM was 0.65 $\mu F.cm^{-2}$, which is within the range expected of a tBLM with no protein. Figure

System	tBLM (Na^+)	TRPC5 (1 μM)	TRPC5 (5 μM)	TRPC5 (10 μM)	TRPC5 (100 μM)	TRPC5 (Na^+)
Circuit	R(QR)	R(QR)	R(QR)	R(QR)	R(QR)	R(QR)
C_{tBLM} (μF.cm^{-2})	0.958	1.010	0.943	0.885	0.905	1.010
Q_{tBLM} (μF.cm^{-2})	2.078	2.565	2.683	2.677	2.632	2.419
α_{tBLM}	0.932	0.918	0.913	0.909	0.909	0.922
R_{tBLM} (MΩ.cm^2)	1.219	0.883	0.424	0.446	0.427	1.643

Table 5.1: The capacitance and resistance for TRPC5-containing tBLMs formed on mixed SAMs. Data were modelled using a R(QR) equivalent circuit as described in Methods. C_{tBLM} is obtained by doubling the height of the capacitance semi-circle in Normalised Admittance Plots (Figure 5.10b) and normalising by the electrode area. Q_{tBLM} is taken from equivalent circuit fitting using the aforementioned circuit. All other parameters were taken from EIS fits using the equivalent circuits indicated, as described in Methods.

5.11a shows a slow but steady decline in phase, and as such no distinct resistance can be attributed. For this reason a RQ equivalent circuit has been used. The cause of this decline is uncertain, but is most likely associated with surface heterogeneities resulting in non-uniform behaviour of the tBLM. Despite modelling with a RQ circuit, the R_{tBLM} can be estimated to be in excess of 2 MΩ.cm^2, on the basis of prior work. La^{3+} was added to concentrations of 1 μM and 5 μM. These additions resulted in substantial increases in the double layer capacitance, 1.05 μF.cm^{-2} and 0.99 μF.cm^{-2} respectively. Repeated washing of the tBLM with fresh electrolyte resulted in the capacitance dropping back to a value of 0.81 μF.cm^{-2}. These capacitance variation are far larger than would normally be expected due the course of an experiment with a tBLM containing only *E. coli* polar lipids (C_{tBLM} for tBLM formed on 80% EO_3C SAM as shown in Figure 3.10d was 0.73 ± 0.01 μF.cm^{-2}). These variations are due to the presence of La^{3+}, and the effects exerted will be discussed in detail later.

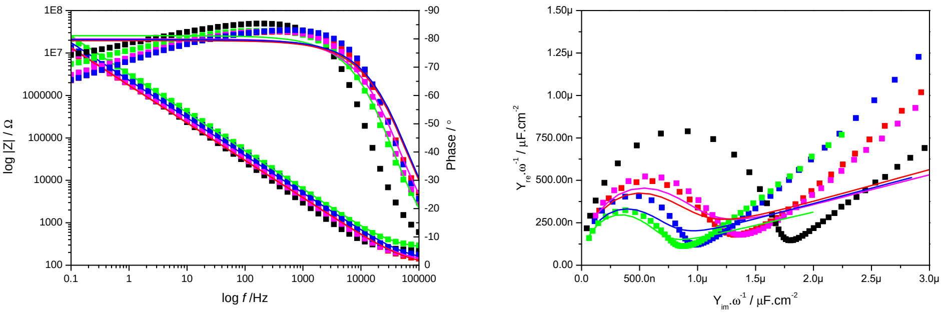

Figure 5.11: Impedance data for the effect of La^{3+} on tBLM containing no TRPC5 formed on a 85% EO_3C SAM. Black = 85% EO_3C SAM; Green = *E. coli* Lipid Bilayer tBLM; Magenta = 1 μM La^{3+}; Red = 5 μM La^{3+}; Blue = Washed out La^{3+}.

System	tBLM (Na^+)	tBLM (1 μM)	tBLM (5 μM)	tBLM (Na^+)
Circuit	RQ	RQ	RQ	RQ
C_{tBLM} (μF.cm^{-2})	0.648	1.045	0.990	0.814
Q_{tBLM} (μF.cm^{-2})	1.929	3.530	3.657	2.743
α_{tBLM}	0.901	0.888	0.882	0.886

Table 5.2: The capacitance and resistance for tBLMs devoid of TRPC5 formed on mixed SAMs. Data were modelled using a RQ equivalent circuit as described in Methods. C_{tBLM} is obtained by doubling the height of the capacitance semi-circle in Normalised Admittance Plots (Figure 5.11b) and normalising by the electrode area. Q_{tBLM} is taken from equivalent circuit fitting using the aforementioned circuit. All other parameters were taken from EIS fits using the equivalent circuits indicated, as described in Methods.

5.4 Discussion

5.4.1 Membrane Preparation

The HEK293 cells were lysed via osmotic shock as detailed in the Experimental Section. On inspection of the lysate a loose pellet was found following a low speed centrifugation step. This has been attributed to DNA released following rupture of the nuclear membrane. The most likely cause for this is inadequate cryo-preservation steps taken following harvesting of the HEK293 cells, as a cell lysis method as gentle as osmotic lysis should not rupture the nuclear membrane. The protocol suggested either a two or three phase sucrose density gradient, as the cell membranes should collect at the interfaces. No distinct material was found at any of the interfaces, however the middle phase was cloudy, suggesting the presence of membrane fragments. As such the three fractions were collected and treated individually, however had a two phase gradient been utilised it could be expected that the material found in the middle phase would have been concentrated at the interface instead. It should be noted that no pellet was observed, providing further evidence that major organelles such as the nuclei had most likely been ruptured and pooled with the cell membrane. All three fractions yielded pellets following ultracentrifugation and were analysed with a BCA assay, SDS-PAGE with Coomassie blue staining and Western Blotting.

The Coomassie blue stained SDS-PAGE gel of the IonGate samples (Figure 5.2) gives us some idea of how the sucrose density gradient has separated the various fractions in the samples. While all lanes received approximately 10 μg of protein as determined by BCA assay, the SDS-PAGE suggests the top membrane fraction actually had less than 10 μg protein. The middle membrane fraction appears to contain the highest concentration of a protein with a size of 110 kDa, which I presume to be TRPC5. Furthermore, the fractionation is only partial. This may be linked to the protocol's method of stacking the sucrose gradient on top of the sample. We have been advised that this is a practice used for the purification of mitochondrial proteins, and given that the principle of a sucrose density gradient is that the proteins should reach equilibrium positions in the gradient based on their relative densities, it was assumed that this would not pose an issue. However, given that standard practice is to load the sample on top of the gradient perhaps this has some how limited the movement of material. This would explain why the top membrane fraction contains the lowest protein concentration as determined by BCA assay, as well as apparently having a smaller distribution of proteins compared to the bottom membrane fraction which is rich is protein variety and total protein concentration. Despite this, a co-worker using the same protocol for a separate experiment has recently obtained good results using the same protocol, albeit with some minor variations.

Figures 5.3a and 5.3b show the Western Blot of a second gel performed at the same time as the Coomassie blue stained SDS-PAGE gel mentioned previously. In the 10 second exposure, Figure 5.3a, TRPC5 can be clearly identified as having a mass of slightly over

100 kDa. A longer exposure of 30 seconds, Figure 5.3b, makes other species visible that are still detected by the anti-TRPC5 primary antibody. Higher molecular weight species can be found in all four lanes at 250 kDa, as well as a second band in excess of 250 kDa. These are assumed to be aggregates, however they are clearly shown to be in the minority. Another band can be found at 75 kDa in the middle membrane fraction lane, which could be a truncated form of TRPC5. Its presence here, however, is unexplained. The middle membrane fraction also displays a consistent smearing throughout the lane. This middle fraction was used for the production of proteoliposomes due to the visible presence of membrane fragments in the middle fraction following ultracentrifugation and the suggested partial purification observed by proteins passing from the initial site of the cell lysate at the bottom of the tube, through the bottom fraction and into the middle fraction.

5.4.2 IonGate - Solid-Supported Membrane Electrophysiology

The data presented in Figure 5.6 demonstrates the ability of La^{3+} to elicit elevated currents. These currents increase with the concentration of La^{3+} added in a manner that concurs with the sigmoidal behaviour observed by Jung et al. [2003]. While this behaviour is observed in both TRPC5 and control samples, the magnitude of the response is far greater in TRPC5-containing samples. The initial positive signal following addition of La^{3+} in phase 2 is due to a combination of the influx of Ca^{2+} ions into the proteoliposomes and the La^{3+} binding to the lipid membranes. This is mirrored by the negative response following the switch back to non-activating electrolyte in phase 3, which is due to the dissociation of La^{3+} from the membrane. Interestingly, the negative response is of a smaller magnitude to the La^{3+} mediated positive response as can be seen in Figure 5.6. The opening of the TRPC5 channel allows the facilitated diffusion of Ca^{2+} ions across the membrane. Assuming that there is no Ca^{2+} efflux upon removal of La^{3+}, the difference in the positive and negative response peaks is most likely attributable to the influx of Ca^{2+}. Whilst the binding effects of La^{3+}account for the remainder of the signal in phase 2. This binding effect has been studied previously by Garcia-Celma et al. [2007], who showed that charge translocation occurred upon the interaction of ions with a solid-supported membrane. The effect elicited varied depending on the lipid headgroup and the valency of the ion, with La^{3+} having a far greater effect than K^+.

To check that the hypothesised Ca^{2+} influx is a La^{3+}-mediated effect due to TRPC5 activity, an inhibitor of TRPC5, 2-aminoethoxydiphenyl borate (2-APB)[Beech, 2007], was added. This resulted in a significant reduction in measured currents, both in terms of height and integral. While the addition of 2-APB resulted in a marked reduction in currents with the *trpc5*$^+$ sample, the effect on the *trpc5*$^-$ control sample was negligible. This provides strong evidence that the responses recorded were at least in part due to specific TRPC5 activity, as opposed to just a La^{3+}-mediated artefact.

Additional experiments were performed to demonstrate the effectiveness of 2-APB as shown in Figures 5.7 and 5.8. These show a clear difference in the kinetics of the peak in phase 2 dependent on the presence of 2-APB. When it is present the peak decays far more rapidly, suggesting that inhibition of channel activity is occurring at all concentrations of La^{3+}. Futhermore, the washout peak in phase 3, which I attribute to La^{3+} release from the membrane, is not observed when 2-APB is present (Figure 5.7). The lack of negative response is likely to be an artefact brought about by the rinsing of 2-APB from the system, with similar responses being observed in Figures 5.5a and 5.5b. This may indicate that 2-APB inhibits La^{3+} binding to the membrane, in addition to the specific effects it has on Ca^{2+}-permeable channels. The fact that there is still a positive component in phase 2 even when 2-APB is present, suggests that besides reversible binding of La^{3+} to the membrane an additional factor contributes to the signal. The putative La^{3+}-lipid interactions may result in a shift in phase transitions of the lipid bilayer, resulting in an increase in membrane permeability to La^{3+}, Ca^{2+} and Cl^{-}, as reported by Cheng et al. [1999] in their work on erythrocyte cell membranes.

The data obtained through activation of TRPC5 with TCEP, Figure 5.9, are clearly very different to those obtained with La^{3+} addition. While there is a clear change in the signal on addition of TCEP, the large negative component and its lack of response to the addition of 2-APB or washing of the electrode suggests that the effect is not related to the biological activity of TRPC5. More likely is either a chemical reaction with the SAM formed on the electrode surface, or an electrochemical reaction (TCEP is reduced at -0.25 V vs Ag/AgCl[Kizek et al., 2004]).

5.4.3 Electrochemical Impedance Spectroscopy

With the biological activity of the TRPC5 sample verified, and the measurement of ion channels in a solid-supported membrane system confirmed as a viable option, steps were taken to incorporate TRPC5 into the tBLM system described in Chapter 4. While a significant drop in membrane resistance was observed following the addition of La^{3+}, this behaviour was found to be irreproducible.

Control experiments were performed many times in addition to those shown in Figure 5.11, however significant variation in the capacitance and estimated resistance of *E. coli* polar lipid extract tBLMs was observed. In some cases capacitance increased on addition of La^{3+}, as was shown in Figure 5.11, while in other cases the capacitance decreased or the membrane resistance fluctuated. The lack of correlation between La^{3+} concentration and EIS parameters, other than significant fluctuations, precludes the use of La^{3+} in EIS studies.

The multitude of effects that multivalent cations have on the properties of lipid bilayers have been reported in a number of publications. Chanturiya and Nikoloshina [1994] found that La^{3+} had an effect on the capacitance of an egg PC and cholesterol BLM, while several groups have reported on La^{3+} ability to affect the phase that various lipids exist in[Chowdhry et al., 1984; Hwang et al., 1996; Lehrmann and Seelig, 1994], as well as the formation of domains[Lehrmann and Seelig, 1994; Seelig et al., 1995]. Meanwhile, Cheng et al. [1999] report on the effects of lanthanides on red blood cells, which include binding of Gd^{3+} to lipids and membrane proteins, resulting in changes in phase transitions and protein conformations. These effects lead to domain formation and perforation of the membrane, allowing the diffusion of lanthanides across the membrane (as well as Ca^{2+} and Cl^{-}). While these effects are important and of interest to further the understanding of how La^{3+} stimulates the TRPC5 channel, the substantial difficulties that they present when interrogating the channel meant that this line of investigation was ultimately deemed unlikely to produce results.

In addition to the issues presented by La^{3+}'s effects, it is also thought that the frequently observed lack of activity may have been due to fundamental difficulties in incorporating TRPC5 into the tBLM system. The limited dimensions of the sub-membrane reservoirs are thought to have a cross-sectional area in the low nm^2 range[Jeuken et al., 2007b] and an estimated depth of 1-2 nm. With this in mind it is not hard to imagine that the comparatively large N- and C-termini of TRPC5 may not be well accommodated in a functional form. This is less of a problem with the IonGate system, which makes use of compound membranes and adsorbed vesicles both of which have the potential for substantial sub-membrane/intra-vesicular regions.

TRPC channels have been reported to be affected by a wide variety of lipids[Beech et al., 2009]. It is possible that either lipids in the *E. coli* polar lipid extract are inhibiting TRPC5's activity, or that essential lipids present in the HEK293 cell membrane are lacking from the tBLM. The use of an alternative lipid composition may improve the chances of detecting TRPC5 activity, as well as limiting the extent of La^{3+} effects in control experiments.

Finally, the experiments shown in Figure 5.10 were performed on P1C electrodes. Progressing to smaller electrode geometries increase the absolute membrane resistance and in theory the likelihood of being able to detect smaller currents, such as those associated with ion channel activity. TRPC5 is reported to have a single channel conductance in the region of 40 pS at -60 mV[Jung et al., 2003]. In order to measure this conductance for a single channel, above the background leak currents that are experienced, the tBLM would need to have a resistance of at least 25 GΩ. This would mean that, if interrogating a single pixel of a P1C electrode, a membrane resistance of 85.5 $M\Omega.cm^2$ would be required, a property far out of reach of even the best tBLM systems. Despite this Keizer et al. [2007] and Andersson et al. [2007] have reported single-channel behaviour of gramicidin A, M2δ peptide, and the BK potassium channel can be observed in a DPTL tBLM system when studied with patch-clamp electrophysiology. These tBLMs have been reported to have resistances of 1.5-17 GΩ on 100 μm × 100 μm electrodes (equal to 0.15-1.7 $M\Omega.cm^2$), and the channels have conductances of 67 pS (gramicidin A), 15 pS (M2δ peptide), and 37 pS (BK K^+ channel) according to the studies[Andersson et al., 2007; Keizer et al., 2007]. Given that a 17 GΩ resistance translates to a 59 pS conductance, one would imagine that the background leak current would mask these unitary conductances.

While single channel activity is apparently detectable using certain proteins in specific systems, two of these are better classified as pore-forming peptides (gramicidin A and M2δ). Furthermore, the authors note that BK conductance is significantly lower than those reported in literature (37 ps *cf.* >200 pS), suggesting that channel function may be restricted. Although single channel measurements have not yet been obtained in the EO_3C:6MH system used in this thesis, the work of Keizer et al. [2007] and Andersson et al. [2007] would suggest that it is possible - the challenge encountered is the mode of detection. While the aforementioned authors used patch-clamp techniques on their tBLMs, here I have attempted to use EIS. Electrophysiology's high time resolution allows these channel conductance events to be identified as peaks of constant amplitude; however, due to the nature of EIS as a time-resolved technique, much starker differences in tBLM resistance need to occur for activity to be detected above the background leak currents. While single channel systems are very appealing due to their high time resolution, and their applications in stochastic sensors[Bayley and Cremer, 2001], for the majority of biosensing applications they are not required and as such multiple channel systems are perfectly adequate in many cases. These systems should be easier to realise, due to higher measurable currents and the possibility for marginally lower channel densities. With this in mind, it should be possible to detect large changes in tBLM capacitance or resistance with EIS.

5.5 Conclusion

TRPC5 was expressed and harvested from HEK293 cells successfully. The sample produced was shown to be biologically active using the IonGate system, with channel activation being observed upon titration of La^{3+}, and subsequent inhibition occurring after the administration of 2-APB. A second ligand, TCEP, was also trialled. However, it was deemed incompatible with the chemistry of the IonGate system.

While TRPC5 was studied with some success using the IonGate system, issues were encountered when attempts were made to incorporate the channel into a tBLM for study with EIS. Irreproducible results and highly variable control data made characterisation of the system excessively difficult and ultimately the decision was made to terminate work with the channel.

5.5.1 Future Ion Channel Candidates

The initial promise of TRPC5, such as the results shown in Figure 5.10 shows that the detection of ion channel activity in a tBLM system is most likely possible. The issues faced have allowed a number of criteria for the selection of future potential targets to be established.

The use of ionic ligands, such as La^{3+}, is rife with issues and as such they should be avoided where possible. Additionally, other ligands which have noticeable effects on the characteristics of control tBLMs should also be avoided.

- To minimise the risk of sub-membrane reservoir volumes impinging on channel function, target channels should have small extramembranous domains.
- As the tBLM system has been well characterised using *E. coli* polar lipids, it is presumably advantageous to select channels which are native to, or have previously been reported to show activity in the membranes of, *E. coli* and other bacterial species.
- Finally, while any channel is theoretically detectable given a large enough quantity of them and a high enough membrane resistance, some effort can be saved by utilising channels with larger conductances. Channelrhodopsins (ChR1, ChR2 and VChR1), while interesting in their ability to be activated by light, have low conductances in the fS range, presenting an additional obstacle to their use. MthK on the other hand has a large conductance of 160 pS[Parfenova et al., 2006; Zadek and Nimigean, 2006] that should make detection far easier.

A number of ion channels were assessed for their suitability in future studies using EIS. The aforementioned MthK was of interest due to its well characterised nature and high conductance. However, it is activated by Ca^{2+} which may interfere with measurements and contains substantial extramembranous RCK domains that are essential to its gating mechanism.

Two channels were eventually selected - KcsA and $\mathrm{Na_vCbt}$. KcsA from *S. lividans*, is a very well characterised $\mathrm{K^+}$-permeable bacterial channel. It is gated by pH change, a parameter that has previously been investigated in our system suggesting that control experiments should be relatively straight forward. It is very compact, forming a tetramer with each subunit containing just 2 membrane spanning helices, a half helix that forms the pore filter and limited extramembranous architecture. Its zero-voltage conductance is approximately 97 pS[LeMasurier et al., 2001], which is large in comparison to many other channels.

$\mathrm{Na_vCbt}$ from *C. thermarum*, is a postulated voltage-gated $\mathrm{Na^+}$ channel from a thermophilic bacterium. It shows a strong sequence homology with the better characterised NaChBac from *B. halodurans*. Previous work with biological samples has shown the channel to be highly stable, appearing to be in a similar state after several days at room temperature as a fresh sample in a gel. Based on a sequence analysis it is thought to be a pentamer with six transmembrane helices per subunit and minimal extramembranous domains.

Chapter 6

Incorporation of Prokaryotic Ion Channels: KcsA and $\mathrm{Na_V}$Cbt

6.1 Introduction

Following the attempts to incorporate TRPC5 in the previous chapter several criteria were identified that may aid the incorporation of functional ion channels into my system. These included small extra-membraneous domains, compatibility with bacterial lipids (preferably *E. coli* lipids), and high unitary conductances. Using these criteria, I selected two ion channels as being good candidates for further study - KcsA and $\mathrm{Na_v}$Cbt.

6.1.1 KcsA

KcsA is a very well characterised pH-gated K^+-channel from a bacterial species (*Streptomyces lividans*). Its precise function is unclear, but it affects colony growth in terms of growth rate and myceliar density[Schrempf et al., 1995]. The channel is a tetramer formed from four identical subunits, each 17.6 kDa in size. These subunits are comprised of 160 amino acids with two hydrophobic regions of approximately 30 amino acids each, corresponding to two membrane spanning helices. Both the C- and N-termini reside in the cell interior[Schrempf et al., 1995]. KcsA expresses well in large quantities and can be purified comparatively easily[Heginbotham et al., 1998]. Furthermore, the channel forms a stable tetramer in many detergents and is stable till at least 50°C[Cortes and Perozo, 1997]. Figure 6.1 shows KcsA's sequence aligned to that of several other K^+ channels from numerous species, both prokaryotic and eukaryotic. As can be seen, it shares a high level of homology to several of these channels, but especially so with the S5, H5 and S6 regions of eukaryotic voltage-gated K^+ *Shaker* channels ($K_v\alpha1$.x, Figure 6.2a), as well as the M1 and M2 regions of inward rectifying K^+ channels (K_{ir}x.x/$K_v\alpha11$.x, Figure 6.2b)[Schrempf et al., 1995]. These regions constitute the channel pore forming helices; KcsA however lacks regions S1-S4 of $K_v\alpha1$.x channels, which are thought to be responsible for the channels' voltage-gating properties[Hille, 2001].

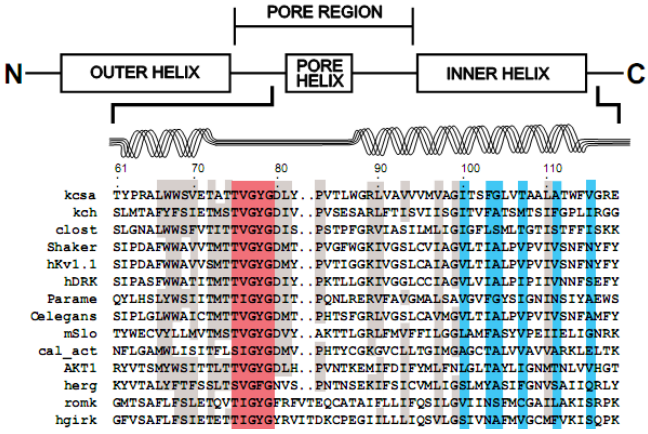

```
    kcsa  TYPRALWWSVETATTVGYGDLY..PVTLWGRLVAVVVMVAGITSFGLVTAALATWFVGRE
     kch  SLMTAFYFSIETMSTVGYGDIV..PVSESARLFTISVIISGITVFATSMTSIFGPLIRGG
   clost  SLGNALWWSFVTITTVGYGDIS..PSTPFGRVIASILMLIGIGFLSMLTGTISTFFISKK
  Shaker  SIPDAFWWAVVTMTTVGYGDMT..PVGFWGKIVGSLCVIAGVLTIALPVPVIVSNFNYFY
  hKv1.1  SIPDAFWWAVVSMTTVGYGDMY..PVTIGGKIVGSLCAIAGVLTIALPVPVIVSNFNYFY
    hDRK  SIPASFWWATITMTTVGYGDIY..PKTLLGKIVGGLCCIAGVLVIALPIPIIVNNFSEFY
   Parame  QYLHSLYWSIITMTTIGYGDIT..PQNLRERVFAVGMALSAVGVFGYSIGNINSIYAEWS
Celegans  SIPLGLWWAICTMTTVGYGDMT..PHTSFGRLVGSLCAVMGVLTIALPVPVIVSNFAMFY
    mSlo  TYWECVYLLMVTMSTVGYGDVY..AKTTLGRLFMVFFILGGLAMFASYVPEIIELIGNRK
 cal_act  NFLGAMWLISITFLSIGYGDMV..PHTYCGKGVCLLTGIMGAGCTALVVAVVARKLELTK
    AKT1  RYVTSMYWSITTLTTVGYGDLH..PVNTKEMIFDIFYMLFNLGLTAYLIGNMTNLVVHGT
    herg  KYVTALYFTFSSLTSVGFGNVS..PNTNSEKIFSICVMLIGSLMYASIFGNVSAIIQRLY
    romk  GMTSAFLFSLETQVTIGYGFRFVTEQCATAIFLLIFQSILGVIINSFMCGAILAKISRPK
   hgirk  GFVSAFLFSIETETTIGYGYRVITDKCPEGIILLLIQSVLGSIVNAFMVGCMFVKISQPK
```

Figure 6.1: Sequence alignment of KcsA with various K^+ channels. Red, selectivity filter; blue, cavity and inner pore lining; grey, residues where nature of side chain is conserved (> 50% similarity). Sequences are kcsa, *S. lividans*; kch, *E. coli*; clost, *C. acetobutylicum*; Shaker, *D. melanogaster*; hKv1.1, *H. sapiens*; hDRK, *H. sapiens*; Parame, *P. tetraaurelia*; Celegans, *C. elegans*; mSlo, *M. musculus*; cal_act, *H. sapiens*; AKT1, *A. thaliana*; herg, *H. sapiens*; romk, *R. norvegicus*; hgirk, *H. sapiens*[Ren et al., 2001].

(a)

(b)

Figure 6.2: Schematic representations of (a) $K_v\alpha1.x$, and (b) $K_{ir}x.x/K_v\alpha11.x$ channels[Ionovation].

It was the first ion channel to have its structure solved[Doyle et al., 1998], and has been instrumental in our understanding of how ion channels function. Its tetrameric structure can be seen in Figures 6.3a and 6.3b [Cortes and Perozo, 1997]. The two membrane spanning helices (the inner and outer helices) are connected by a loop region (the turret) with a short helix (selectivity filter), which sits inside the pore lumen.

The channel lumen is 45 Å long and varies in diameter along its length as can be seen in Figure 6.4b, but reaches a maximum diameter of 10 Å in the centre of the channel. Figure 6.4a highlights the chemical nature of surface exposed residue side chains along the lumen wall. At either end of the channel there exist a dense ring of negatively charged residues which repel anions and attract cations. This is thought to improve ion conductance rates by increasing the local concentration of cations[Ren et al., 2001]. The channel lumen narrows and is lined with polar residues that form the selectivity filter. This selectivity filter contains a short amino acid sequence Thr-Val-Gly-Tyr-Gly, which has been identified as being responsible for determining which ions are allowed to pass through the pore by coordinating dehydrated cations as they transit the channel lumen[Ren et al., 2001].

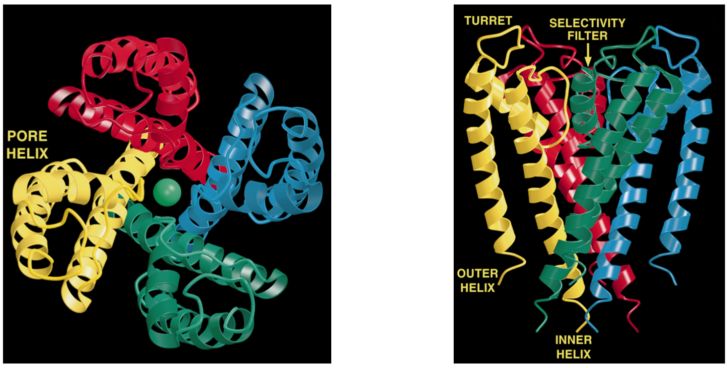

(a) (b)

Figure 6.3: Structure of KcsA as determined by X-ray crystallography. (a) Top down view of the channel depicting the four subunits and a central K^+ ion; (b) Side on view highlighting key structural features[Ren et al., 2001].

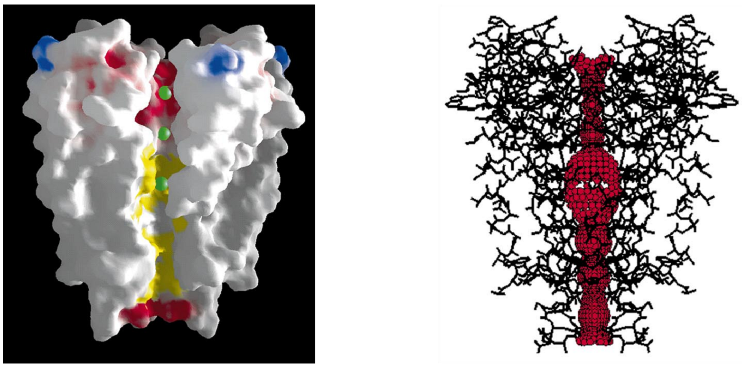

(a) (b)

Figure 6.4: The KcsA lumen. (a) Space filling cross-section of the channel showing the average position of K^+ ions undergoing transit, model has been colour coded to represent residue side chain character - blue (positive), red (negative), yellow (hydrophobic); (b) Wireframe model of the channel with the lumen wall highlighted in red[Ren et al., 2001].

Two ions can be found at either end of the selectivity filter, where the side chains of polar residues coordinate dehydrated ions. By dehydrating the ions prior to passage through the selectivity filter, the channel can have finer control over which ions it allows to pass. LeMasurier et al. [2001] found that the channel presented a selectivity sequence of $K^+ > Rb^+/NH_4{}^+/Tl^+ >> Cs^+/Na^+/Li^+$ in symmetrical solutions, with the channel exhibiting over 150-fold greater rates of conductance for K^+ than for Na^+. Na^+ has a radius of 0.95 Å whereas K^+ has a radius of 1.33 Å. Because Na^+ is slightly smaller, the channel side chains can't efficiently coordinate the ion. This makes the ion's passage energetically unfavourable, resulting in a lower conductance for Na^+. K^+ on the other hand is of an optimal size resulting in very rapid transport. Rb^+ has a radius of 1.48 Å, which is of a sufficiently similar size to have a similar conductance as K^+. Cs^+, meanwhile, is slightly larger at 1.69 Å - while this is not an optimal size it is far more favourable than that of Na^+. Multivalent cations, anions and large organic cations are all unable to pass the selectivity filter due to charge or gross incompatibilities in the size of the ion.

Once the ion passes the selectivity filter it passes into the large central cavity. This is located in the middle of the lipid bilayer presenting a sizeable energy barrier, due to a lack of polarizable material[Parsegian, 1975]. KcsA overcomes this by stabilising ions in this cavity with helix dipoles and rehydrating the ions. The carboxy-end of each pore helix is orientated towards the centre of the cavity. This produces a dipole effect, which despite being positioned 8 Å away from the cavity centre, produces a negative electrostatic potential that is favourable for the cations as demonstrated in Figure 6.5. The lumen in this cavity, and the rest of the channel from here to the intracellular exit, is lined with hydrophobic residues as indicated by yellow colouring in Figure 6.4a. While lining these regions with polar residues would aid the stabilisation of transient ions, it would do so too efficiently thus impeding ion conductance. The use of helix dipoles and rehydration stabilises the ion, while the hydrophobic lumen ensures a rapid transit which maintains high conductances throughout the channel[Ren et al., 2001].

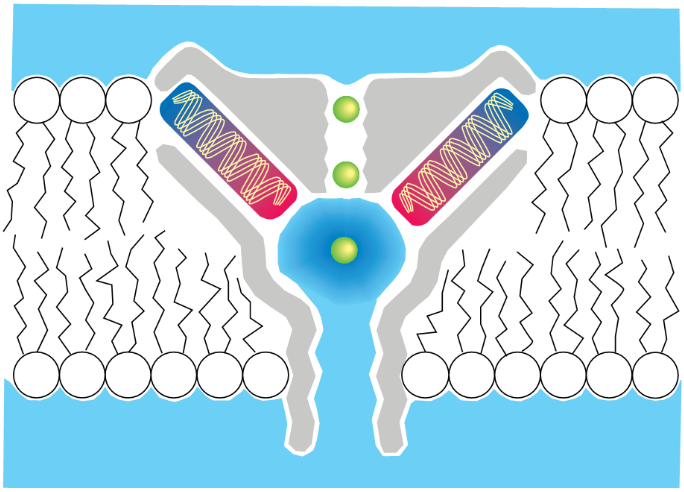

Figure 6.5: Schematic representation of how KcsA stabilises ions in the central cavity using helical dipoles[Ren et al., 2001].

Initial studies of KcsA were under steady state conditions typically used in electrophysiological experiments. KcsA channels incorporated into BLMs exhibit preferential orientation such that an inside-out arrangement is usually being studied[Cuello et al., 1998; Heginbotham et al., 1999]. The conductance of K^+ at 0 mV is 97 pS, but exhibits low open channel probabilities (often around 0.2[Cordero-Morales et al., 2006]) under steady state conditions, even at low pH[Cuello et al., 1998; Heginbotham et al., 1999; LeMasurier et al., 2001]. This low opening probability has been attributed to a voltage-modulated inactivation mechanism[Cordero-Morales et al., 2006; Gao et al., 2005]. While a jump from high to low pH will activate the channel on the time scale of a few milliseconds, this is followed by an inactivation phase that occurs over several seconds and once inactivated the channel exhibits poor recovery. This inactivation mechanism explains the low open channel probabilities observed under steady state conditions. Several approaches have been taken to slow the inactivation phase including voltage-modulation[Cuello et al., 1998; Heginbotham et al., 1999], increasing the extracellular K^+ concentration[Cordero-Morales et al., 2006; Lopez-Barneo et al., 1993], adding permeant ions with long channel residency times such as Rb^+[LeMasurier et al., 2001; Lopez-Barneo et al., 1993] and mutagenesis of various residues in the channel[Cordero-Morales et al., 2006; Lopez-Barneo et al., 1993].

Glu71 has been identified as a key residue involved in the inactivation mechanism[Cordero-Morales et al., 2006]. Glu71Ala mutants have been particularly effective at severely handicapping the inactivation mechanism, and making study of the channel gating kinetics far clearer[Chakrapani et al., 2007a, b].

Chakrapani et al. [2007a] used Glu71Ala mutants for detailed studies of KcsA activity at both macroscopic[Chakrapani et al., 2007a] and single-channel[Chakrapani et al., 2007b] levels. A pH-pulse protocol was used on wild-type and Glu71Ala KcsA to prevent the channel from being inactivated. This required switching from pH 8.0 to a low pH (3.0-4.75) for a duration of approximately 250 ms, before returning to pH 8.0. No significant changes in macroscopic current were detected above pH 5.0. However, below this point, the decreasing pH resulted in larger current, which were reached more rapidly. When examined at single-channel resolution, ion conductivity is due to channel opening during burst phases with individual opening events lasting 10-100 ms[Chakrapani et al., 2007b]. Voltage was shown to have no effect on the activation kinetics using Glu71Ala mutants, but effects were detected in wild-type samples suggesting voltage affects the inactivation kinetics, as had been previously suggested by Cuello et al. [1998] and Heginbotham et al. [1999]. Closer examination of single-channel data indicated that increasing the applied voltage leads to longer burst phases, primarily due to longer mean open times[Chakrapani et al., 2007b].

To summarise - KcsA is activated by low pH; if the channel is left at low pH for more than a couple of hundred milliseconds, the channel enters an inactivation state. However, if the pH is raised the channel will be deactivated. Inactivation is associated with a poor recovery rate, and does not respond well to further pH jumps, leading to reduced ion conductance. Deactivation on the other hand is an idling state from which the channel is responsive to further pH jumps. By using a pH-pulse protocol the channels can be switched between activated and deactivated states, while for the large part avoiding inactivation states. This allows channel currents and open channel probabilities to be maintained. The use of Glu71Ala mutants greatly reduces the probability of a channel entering an inactivation state[Cordero-Morales et al., 2006], and as such is of great use where pH-pulse protocols are impractical.

6.1.2 Na$_v$Cbt

The second channel studied in this chapter is a putative voltage-gated Na$^+$ channel from the alkalithermophilic bacteria *Caldalkalibacillus thermarum*. The channel is tetrameric, with each monomer subunit being comprised of 298 amino acid residues arranged into 6 transmembrane helices and a 65 amino acid C-terminal domain as shown in the SOSUI plot in Figure 6.6. However, while Na$_v$Cbt remains comparatively unstudied a close homolog, NaChBac, has been studied in great depth[Ito et al., 2004; Koishi et al., 2004; Kuzmenkin et al., 2004; Nurani et al., 2008; Ouyang et al., 2007; Ren et al., 2001; Studer et al., 2011; Yue et al., 2002]. Given the limited information available for Na$_v$Cbt, this introduction will look at the literature of its homologs to provide an overview of voltage-gated Na$^+$ channels in general.

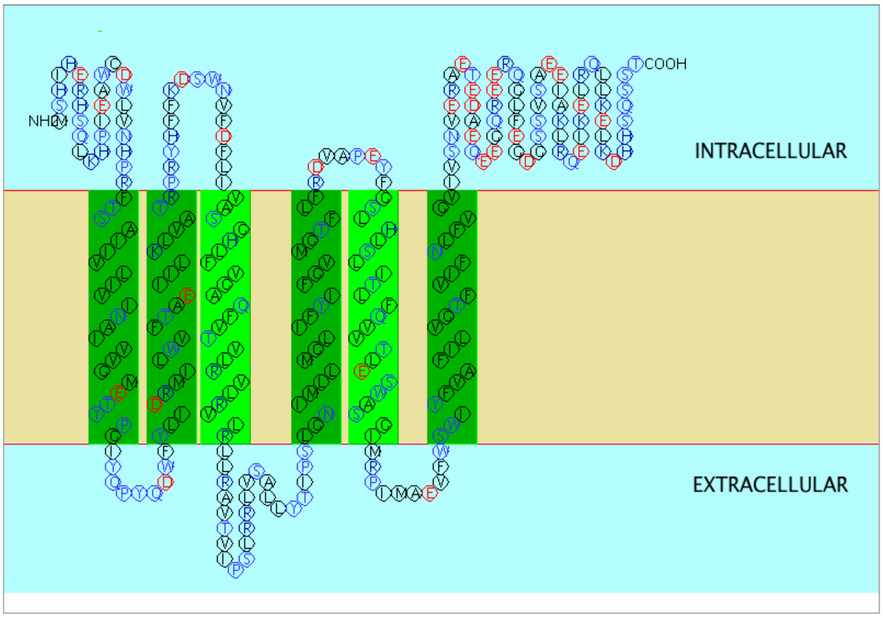

Figure 6.6: SOSUI plot showing predicted structure of Na$_v$Cbt.

NaChBac is comprised of 274 amino acid residues and approximately 31 kDa in size. It originates from the halophilic bacterium *B. halodurans*, which lives in high salt, high alkaline conditions (as high as 1 M salt and pH 11). These parameters would indicate high degrees of Na$^+$ influx. This and the tendency of alkaliphilic *Bacillus* to use Na$^+$ to drive their flagella motors[Atsumi et al., 1992; Imae and Atsumi, 1989; Ito et al., 2004; Krulwich et al., 2001; Yorimitsu and Homma, 2001] has led to suggestions that NaChBac may play a role in *B. halodurans* motility[Ren et al., 2001]. In addition to a role in motility, Na$_v$BP - a NaChBac homolog from another alkaliphilic *Bacillus* - has been linked to chemotaxis and pH homeostasis[Ito et al., 2004]. It is possible that these roles could also extend to NaChBac. While Na$_v$Cbt is not from a *Bacillus*, it is from an alkaliphilic prokaryote and as such it is likely to share similar characteristics.

Like KcsA, NaChBac also contains a short sequence of amino acids (LESWAS/Lys-Glu-Ser-Tyr-Ala-Ser) that has been identified as a selectivity filter which shows strong selectivity for Na^+ over Ca^{2+} despite the channel's similarity to Ca_v channels. Additionally, the channel shows an inability to transport anions[Ren et al., 2001; Yue et al., 2002]. Hydropathy analysis suggests the channel has six transmembrane regions, with region 4 containing positively charged residues that are frequently associated with voltage-sensing domains of voltage-gated ion channels.

Current-voltage curves suggest that NaChBac opens between potentials of -50 mV and 50 mV, with peak conductance being reached at approximately -20 mV[Kuzmenkin et al., 2004; Ren et al., 2001; Yue et al., 2002]. Single-channel studies indicate a unitary conductance of 12 ± 1 pS and comparatively slow activation times ($\tau_{\mathrm{act}} = 10 \pm 3.5$ ms[Ren et al., 2001]) *cf.* Na_v channels ($\tau_{\mathrm{act}} < 2$ ms[Hille, 2001]). Slow inactivation times were also identified with $\tau_{\mathrm{inact}} = 203 \pm 43$ ms[Ren et al., 2001] *cf.* $\tau_{\mathrm{inact}} < 10$ ms[Hille, 2001].

A study of NaChBac in BLMs presented slightly different channel characteristics, including a single-channel conductance of 120 pS[Studer et al., 2011]. The authors of a similar study with a different channel found a large difference between the conductances measured with traditional patch-clamp and BLM[Perez et al., 1994]. The authors of this study attributed this to the lipid composition of the BLM and an increased ion concentration, which are suggested to increase the local ion concentration at the BLM surface resulting in elevated conductances[Rostovtseva et al., 1998].

NaChBac is sensitive to a number of blocking agents - specifically Cd^{2+}, Co^{2+}, La^{3+} and dihydropyridines (nifedipine and nimodipine in particular), as well as mibefradil and Ni^{2+} to a much lesser extent[Ren et al., 2001]. The channel is unresponsive to ω-conotoxin GVIA, ω-agatoxin IVA and tetrodotoxin (TTX). This pattern of pharmacology is interesting as it is more similar to that of eukaryotic Ca^{2+} channels than that of eukaryotic Na^+ channels.

While NaChBac is the most well studied prokaryotic Na^+ channel, a study by Koishi et al. [2004] found several other homologs in prokarya. While these share 22-54% sequence homology and very similar structures are proposed, their character in terms of voltage-gating and kinetics is diverse.

6.2 Experimental Section

6.2.1 Materials

KcsA plasmid was kindly provided by Prof. A. Sivaprasadarao (University of Leeds, UK), and was comprised of a pET28a plasmid backbone (*kanR*$^+$) with the *kcsa* gene inserted under the control of an IPTG promoter. Na$_v$Cbt plasmid (pDG102) was provided by Dr. D. McMillan (University of Leeds, UK), and was constructed using a pTrc99A plasmid backbone (*ampR*$^+$)with the *navcbt* gene inserted under the control of an IPTG promoter. LB medium was made from 10 g/L Tryptone, 5 g/L Yeast extract, and 10 g/L NaCl, adjusted to pH 7 with NaOH. This was turned into agar by the addition of 15 g/L agar and heating prior to pouring plates. SOC medium contained 20 g/L Tryptone, 5 g/L Yeast extract, 0.584 g/L NaCl, 0.186 g/L KCl, 0.952 g/L $MgCl_2$, 1.204 g/L $MgSO_4$ and 3.603 g/L glucose, adjusted to pH 7 with NaOH. Other materials were as described in Chapter 4.

6.2.2 Ion Channel Production

Transformation, growth, overexpression and purification of KcsA and Na$_v$Cbt were all conducted by Dr. D. McMillan.

Transformation of Bacteria

1 μL of KcsA plasmid (unknown concentration) was transformed into *E. coli* strain BL21 using standard heat shock treatment. Transfection was induced by incubation at 42°C for 45 seconds. Cells were cooled for 2 minutes on ice, and then bathed in 1 mL of SOC medium before incubating on a shaker at 37°C for 1 hour. Cells were plated for overnight incubation on LB agar treated with kanamycin (50 μg/L) in aliquots of 100-300 μL.

Transformation of cells with *navcbt*-containing pDG102 was performed under the same conditions, but with 100 μg/L carbenicillin used instead of kanamycin.

Growth and Over Expression of Ion Channels

A colony of transformed cells was used to inoculate 5 mL of LB medium (50 μg/L kanamycin) and incubated overnight at 200 rpm in a shaker at 37°C. This culture was used to inoculate two 500 mL flasks containing 100 mL of LB medium and incubated overnight. This provided 8 mL aliquots which inoculated 8 large 2 L baffled flasks made up to 400 mL of LB medium. Cells were grown at 37°C at 200 rpm in a shaker until an OD_{600} of approximately 0.65 was reached. Growth was monitored at 30 minute intervals for two flasks and similar growth in all flasks was assumed. At OD_{600} 0.65, over expression was induced with 200 μg/mL, of IPTG for a 4 hour period.

Growth and expression were the same for Na$_v$Cbt, but with the cells being grown on 0.5× LB medium (100 μg/L carbenicillin).

Purification of KcsA from Membranes

Cells were harvested by centrifugation (10 min, 7000 x *g*). Pellets were resuspended in 50 mL of W1 buffer (20 mM MOPS, 5 mM $MgSO_4$, 30 mM KCl, pH 7.4) with PMFS at a final concentration 0.1 mM. 0.1 mg/mL of pancreatic DNase was added to the preparation prior to two cycles of cell disruption at 30000 psi using a cell disruptor (Constant Systems Ltd.).

Broken cells were removed by low speed centrifugation (10 min, 8000 x *g*). Supernatant containing bacterial membranes was pelleted by centrifugation (45 min, Ti50.2 rotor, 45000 rpm, 4°C). Membranes were resuspended and washed by diluting in 20 mL of W1 buffer and pelletted by centrifugation (45 min, Ti50.2 rotor, 45000 rpm, 4°C). Pellets were resuspended again in W1 buffer. The suspension was then diluted to a concentration of 3-4 mg/mL protein in solubilisation buffer (20 mM Tris.HCl, 5 mM $MgSO_4$, 300 mM KCl, 20 mM imidazole, 10% glycerol, 1% DDM, pH 8.0) and PMSF was added to a final concentration of 0.1 mM. This was incubated for 1 hour on a spiromax at 4°C, before centrifugation (45 min, Ti70 rotor, 45 000 rpm, 4°C). The supernatant containing solubilised KcsA and other membrane proteins was collected for purification.

A 2mL Nickel sepharose bench column was used. The column was washed with Milli-Q water then equilibrated with buffer A (20 mM Tris.Cl, 5 mM $MgSO_4$, 250 mM KCl, 0.1 mM PMFS, 0.05% DDM and 20 mM imidazole). The solubilised membrane proteins were applied to the column and the flow through collected. The column was re-equilibriated with buffer A and flow through collected. Buffer B, C and D only differed from buffer A by its increasing imidazole concentration. The column was washed with Buffer B (40 mM imidazole) and flow through collected. KcsA was eluted with Buffer C (200 mM Imidazole) and collected in 1 mL fractions. A final wash with Buffer D (400 mM imidazole) was applied to remove any remaining proteins and this flow through was collected.

Purification of Na_vCbt from Membranes

Purification of Na_vCbt was as for KcsA, but with K^+ in buffers being replaced with Na^+.

Reconstitution of Ion Channels into *E. coli* Polar Lipid Vesicles

5 mg of dried Avanti *E. coli* polar lipid extract was resuspended in 250 μL buffer (300 mM KCl, 5 mM $MgSO_4$, 20 mM Tris-HCl pH 7.4) and extruded through 200 nm polycarbonate track-etched membranes with an Avanti Mini-Extruder to produce 200 nm diameter small unilamellar vesicles.

225 μL of these vesicles (20 mg/mL) were then mixed with 35 μL of 10% octylglucoside (OG) until the solution clarified. The clarified vesicles were then mixed with 30 μL of 3 mg/mL purified KcsA, or 60 μL of 2 mg/mL purified Na_vCbt (both in 0.05% DDM). The reconstituted mix was incubated on ice for 15 minutes and added to 25 mL of ice cold buffer (30 mM KCl, 20 mM Tris-HCl, pH 7.4 for KcsA, or 30 mM NaCl, 20 mM Tris-HCl, pH 7.4 for Na_vCbt) in a Ti50.2 ultracentrifuge tube. The tube and its

contents were spun at 41,000 rpm in a Ti50.2 rotor for 1 hour at 4°C. The supernatant was discarded and the pellet resuspended in 1 mL of ice cold potassium or sodium buffer (for KcsA and Na_vCbt, respectively) prior to extrusion through 400 nm and 200 nm membranes to produce small unilamellar vesicles. Reconstituted vesicles were stored on ice and used within 2 days.

6.2.3 Protein Determination

BCA assay, SDS-PAGE and Western Blot were all used to characterise the protein content throughout the purification process. These techniques were used as described in Chapter 5, apart from the exceptions mentioned below.

During immunoblotting, purified protein was subjected to 12% SDS-polyacrylamide gel electrophoresis (SDS-PAGE) followed by electroblotting in a semi-dry blotter (Biorad) onto a polyvinylidene difluoride (PVDF) membrane using 0.5% SDS as the running buffer. Detection was achieved using a penta-His antibody conjugate (Qiagen) directed against the N-terminal hexa-histidine tag used for purification. The antibody-specific bands were visualised using the SuperSignal West Pico chemiluminescence system.

6.2.4 Formation of Tethered Bilayer Lipid Membranes

Electrodes were prepared and tBLMs formed as described previously in Chapter 4. Proteoliposomes containing reconstituted ion channels were used in place of *E. coli* polar lipid vesicles.

6.2.5 EIS Measurements

EIS measurements were performed as has been described previously in Chapter 4. KcsA experiments were conducted in electrolytes of either 200 mM K_2SO_4 or 200 mM Na_2SO_4, with 20 mM MOPS. These electrolytes were adjusted to pH 4.5 or pH 7.8 using KOH and NaOH, respectively. Na_vCbt experiments were conducted in electrolytes of either 30 mM Na_2SO_4 or 30 mM $BaCl_2$, with 20 mM MOPS adjusted to pH 7.4 with either NaOH or $Ba(OH)_2$, respectively. Gating measurements were taken at bias potentials of +100 mV, 0 mV and -200 mV vs SCE. Electrolytes were replaced 5 times when changing from one to the other.

The equivalent circuit, $R_s(Q_{tBLM}R_{tBLM})$ (referred to as R(QR) for brevity and shown in Figure 6.7), was used to analyse all results and is composed of a resistor (R_s) in series with a constant phase element (CPE, Q_{tBLM}) and a second resistor (R_{tBLM}) in parallel. R_s represents the resistance of the electrolyte. Q_{tBLM} represents the capacitance of the electrode surface (the SAM or the lipid bilayer) with an additional factor, α, which is taken to be a measure of surface roughness or defects in the SAM or lipid bilayer. R_{tBLM} models the resistance of the SAM or lipid bilayer.

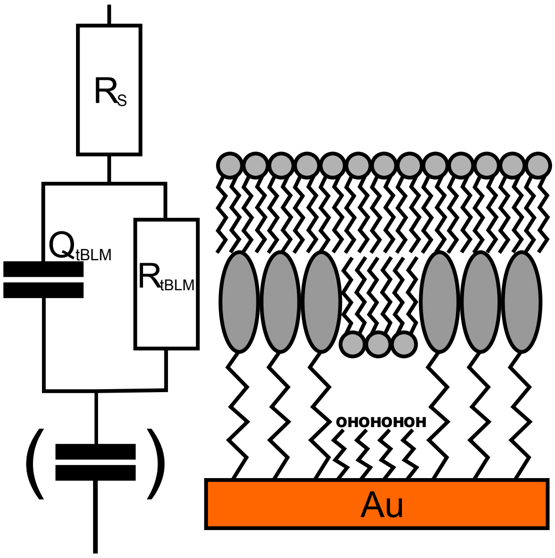

Figure 6.7: Equivalent circuit used in analysis of impedance data of KcsA and Na_vCbt. The equivalent circuit described as R(QR) was used for SAMs, tBLMs formed from KcsA-containing proteolipsomes and Na_vCbt-containing proteoliposomes. R_s is solution resistance (electrolyte), Q_{tBLM} is double layer capacitance of the entire tBLM modeled by a constant phase element (CPE) and R_{tBLM} is membrane resistance. Capacitances enclosed in a bracket indicate that the element is not modelled as it is not observed in impedance spectra, but would be expected if measuring at lower frequencies.

6.3 Results

6.3.1 KcsA

Protein Preparation

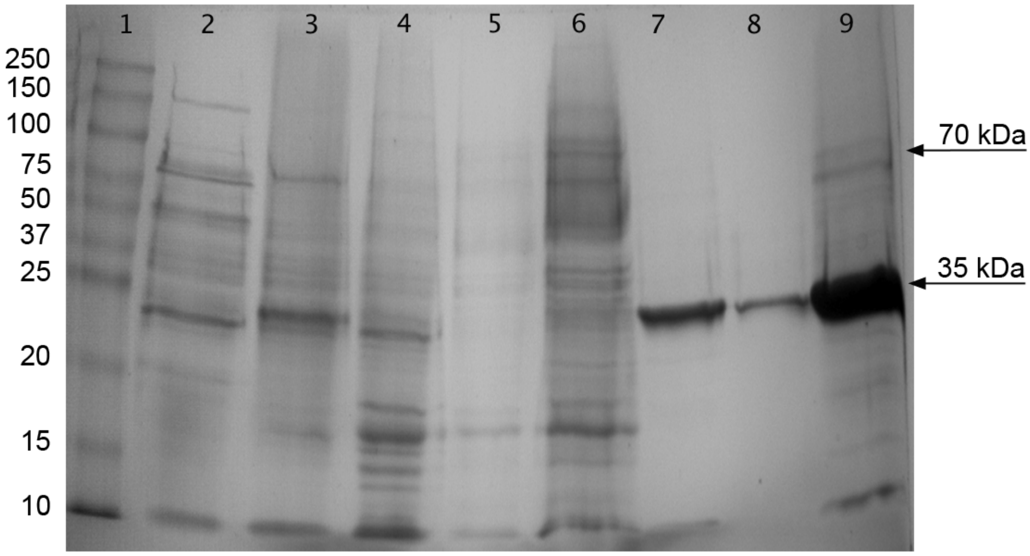

Figure 6.8: SDS-PAGE gel of KcsA purification products. Cytoplasmic, membrane, and insoluble fractions were loaded into lanes 2, 3, and 4 respectively. Lanes 5 and 6 are the first wash and the flow through, not shown in chronological order of the procedure. Lanes 7, 8 and 9 were loaded successively with extracts from fraction 3, the final wash and concentrated KcsA. The lane 1 is the molecular ladder.

Figure 6.8 shows a SDS-PAGE gel of materials collected throughout the purification of KcsA. A clear band can be seen in many of the lanes, just below the 42 kDa marker in lane 1. Given KcsA's 17.6 kDa subunit size, this is most likely its dimeric form (approximately 35.2 kDa). The dimer is relatively stable, being found in samples taken from the cytoplasm, membrane and insoluble fractions of cell lysis, as well as in the third fraction obtained from the nickel-sepharose column following elution with imidazole. Smaller quantities were also found in the final wash step (400 mM imidazole) suggesting that the protein was very well bound to the column. A very clear band can be found in lane 9 which corresponds to eluted KcsA that has been run through a concentration column. A very faint band can also be seen in lane 10 at approximately 70 kDa, which may be very small quantities of KcsA in a tetrameric form.

Western blotting was used to confirm the identity of these bands.

EIS of KcsA

EIS was used to measure the properties of KcsA-containing tBLMs at pH 4.5 and pH 7.8, as well as with both Na^+ and K^+ containing electrolytes. Figures 6.9a and 6.9b show the results of these experiments, and equivalent circuit fits modelled to a R(QR) circuit. The parameters of these fits have been compiled into Table 6.1.

As can be seen in Figure 6.9b, the majority of the data separates into two main groups with different capacitances. K^+ at pH 4.5 (red open circles) are clustered together with an average capacitance of 1.66 μF.cm^{-2}, while the majority of the other measurements are clustered around 0.96 μF.cm^{-2}. This is a distinct difference suggesting that there is an ion-specific pH-dependent effect on the capacitance, similar to that observed with gramicidin in Chapter 4.

Equivalent circuit parameters were also found to cluster in two groups. Of the CPE parameters, α_{tBLM} shows very little variation staying at around 0.94. Q_{tBLM}, however, shows considerable variation along similar lines to that of C_{tBLM}, as expected (see Table 6.1). While the variation for K^+ at different pHs is expected, the value for pH 7.8 is far lower than that observed for Na^+. One would expect a small amount of K^+ transport to occur at higher pH whereas Na^+ transport should be universally lower. A similar issue is encountered when examining R_{tBLM} values, which, when measured in Na^+, are lower than average for a tBLM when compared to a non-protein containing tBLM such as those studied in Section 3.4 (see Table 3.10).

However, visual inspection of the fits (Figure 6.9a) indicates certain caution has to be taken with interpreting R_{tBLM}. The raw data do not exhibit the decrease in phase shift at low frequency that is characteristic of a resistor parallel to a capacitor. Instead the (negative) phase shows a gradual decrease towards lower frequency suggesting complex and heterogeneous surfaces. This might be due to the incorporation of KcsA disrupting the insulating nature of the tBLM.

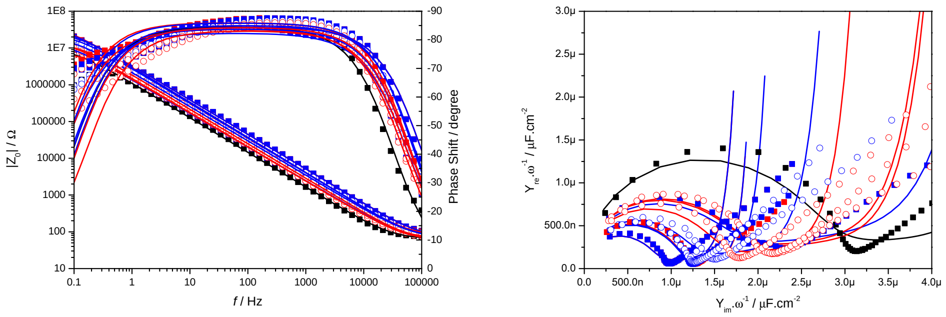

(a) (b)

Figure 6.9: EIS of tBLM formed from reconstituted proteoliposomes containing KcsA, where potential ion transport activity has been detected. Black = SAM, Na^+; Blue = Na^+; Red = K^+; Closed shapes = pH 7.8; Open shapes = pH 4.5.

While ion transport activity has potentially been identified in Figure 6.9, this is just one success amongst several other experiments that were less successful. One such experiment is shown in Figure 6.10. As can be seen, there are no clear differences been K^+ and Ba^{2+}, nor between pH 4.5 and pH 7.8.

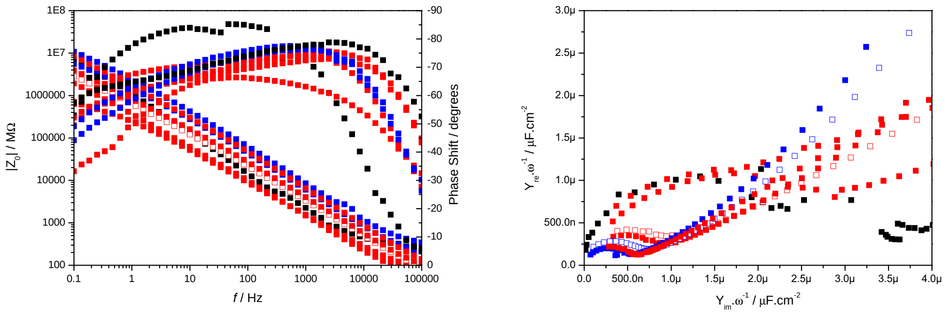

(a) (b)

Figure 6.10: EIS of tBLM formed from reconstituted proteoliposomes containing KcsA, where no clear patterns are observed. Black = SAM, Ba^{2+}; Blue = Na^+; Red = K^+; Closed shapes = pH 7.8; Open shapes = pH 4.5.

	K^+		Na^+	
	pH 4.5	pH 7.8	pH 4.5	pH 7.8
Model	R(QR)	R(QR)	R(QR)	R(QR)
n	3	2	2	3
C_{tBLM} (μF.cm^{-2})	1.661 ± 0.072	0.951 ± 0.135	1.140 ± 0.051	1.190 ± 0.252
Q_{tBLM} (μF.cm^{-2})	3.633 ± 0.304	1.157 ± 0.662	2.335 ± 0.301	2.610 ± 0.858
α	0.932 ± 0.004	0.949 ± 0.008	0.939 ± 0.007	0.937 ± 0.011
R_{tBLM} (MΩ.cm^2)	0.418 ± 0.097	1.817 ± 0.470	0.706 ± 0.064	0.848 ± 0.192

Table 6.1: EISFit parameters for KcsA-containing tBLMs formed on mixed SAMs. Measurements taken at pH 4.5 and pH 7.8 in electrolytes containing K^+ or Na^+. Data were modelled using a R(QR) equivalent circuit as described in Methods. C_{tBLM} is obtained by doubling the height of the capacitance semi-circle in Normalised Admittance Plots (Figure 6.9b) and normalising by the electrode area. Q_{tBLM} is taken from equivalent circuit fitting using the aforementioned circuit. All other parameters were taken from EIS fits using the equivalent circuits indicated, as described in Methods

6.3.2 Na_vCbt

Protein Preparation

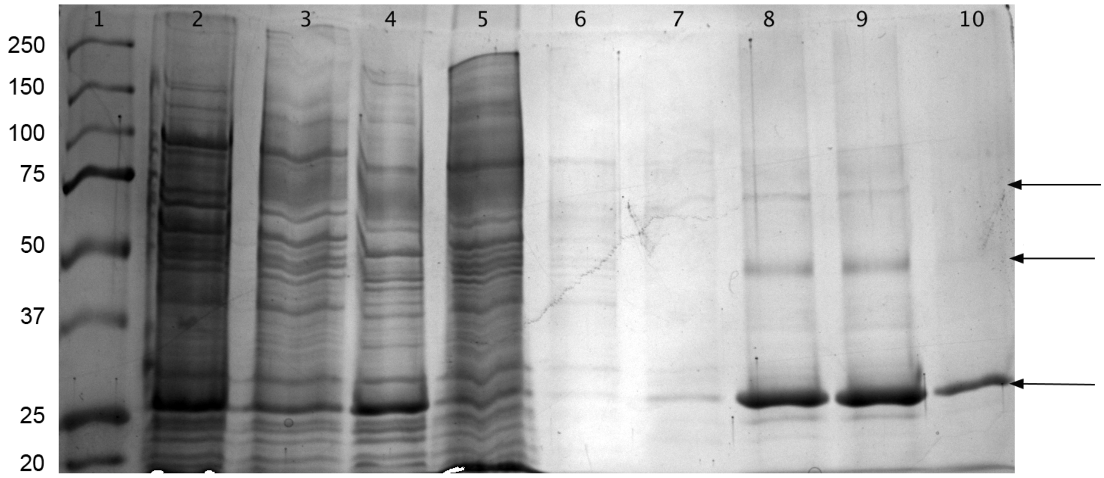

Figure 6.11: SDS-PAGE gel of Na_vCbt purification products. Cytoplasmic, membrane, and insoluble fractions were loaded into lanes 2, 3, 4, and 5 respectively. Lanes 6 and 7 are the first wash and the flow through, not shown in chronological order of the procedure. Lanes 8, 9 and 10 were loaded successively with extracts from fraction 3, the final wash and concentrated Na_vCbt. The first lane is the molecular ladder.

Figure 6.11 shows a SDS-PAGE gel of materials collected throughout the purification of Na_vCbt. A clear band can be seen in many of the lanes, just above the 25 kDa marker in lane 1. This is most likely the 34 kDa subunit of Na_vCbt. A further two bands can be found in lanes 8 and 9 between 50 kDa and 75 kDa, as well as between 75 kDa and 100 kDa - these are likely to be dimeric (68 kDa) and trimeric forms (102 kDa) respectively. A very clear band can be found in lane 10 which corresponds to the eluted Na_vCbt monomer that has been run through a concentration column. A Western blot was used to confirm the identity of these bands.

EIS of Na_vCbt

Figure 6.12 shows EIS scans of representative of tBLMs containing Na_vCbt at concentrations of 2.8% (w/w) with respect to lipid. Na_vCbt is thought to be voltage-gated based on its homology to NaChBac, and as such scans have been taken at +100 mV, 0 mV and -200 mV vs SCE.

In each case no significant changes in capacitance (C_{tBLM}) were observed, and changes to CPE parameters (Q_{tBLM} and α_{tBLM}) were minimal as can be seen in Table 6.2 and Figures 6.12b, 6.12d and 6.12f. More significant changes were seen in the tBLM resistances. These changes in activity were detected at 0 mV and -200 mV only, in line with literature for the closely related ion channel NaChBac[Ren et al., 2001]. At these potentials the tBLM resistance decreased under Na^+ conditions, but remained largely the same in the presence of Ba^{2+} (Table 6.2). This can be seen in Figures 6.12c and 6.12e as an increasing deviation of phase for Na^+ from that for Ba^{2+}. In contrast, the measurements taken at +100 mV (Figure 6.12a) showed minimal variation (less than 1 MΩ.cm^2 difference). This lack of activity at +100 mV provides strong evidence for Na$_v$Cbt being a voltage-gated ion channel.

To check that this potential-dependent effect was indeed due to the activity of Na$_v$Cbt, and not due to aspecific effects of applying a potential to the tBLM, control experiments were conducted. This control tBLM was formed from *E. coli* polar lipid vesicles with no protein content. As can be seen from Table 6.3 and Figure 6.13 there are only minor variations between each measurement. Capacitance and CPE parameters change very little irrespective of electrolyte or potential remaining in the region of 0.97 μF.cm^{-2}, 1.08 μF.cm^{-2} and 0.99 respectively. Resistance shows slightly more variation, but does not drop below 4 MΩ.cm^2 regardless of electrolyte or potential. The only exception to this is with the addition of 8.8 μM nifedipine in DMSO, which reduces resistance to 2.187 ± 1.878 MΩ.cm^2 at -200 mV vs SCE yet has no affect on any other parameters. The use of nifedipine had been planned due to its inhibitory effect on NaChBac activity, which was expected to be observed with Na$_v$Cbt also. However, these results preclude its use in further EIS studies as is explained in the discussion.

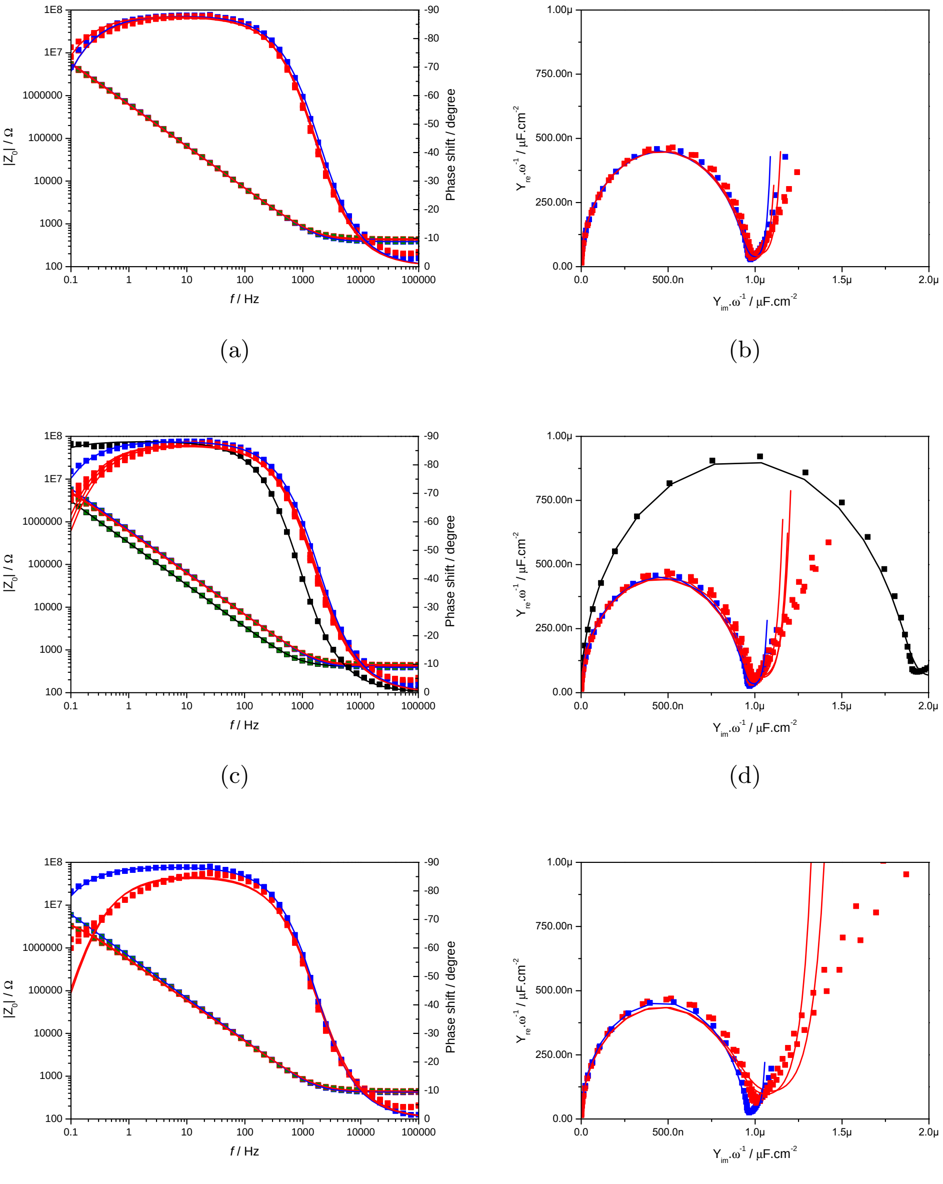

(a) (b)

(c) (d)

(e) (f)

Figure 6.12: EIS of Na_vCbt activation. tBLM formed from proteoliposomes containing 2.8% (w/w) Na_vCbt. (a) and (b) +100 mV vs SCE; (c) and (d) 0 mV vs SCE; (e) and (f) -200 mV vs SCE. Black = 82% EO_3C SAM, Red = Na^+, Blue = Ba^{2+}.

	+100 mV		0 mV		-200 mV	
	Na^+	Ba^{2+}	Na^+	Ba^{2+}	Na^+	Ba^{2+}
Model	R(QR)	R(QR)	R(QR)	R(QR)	R(QR)	R(QR)
n	4	2	6	2	4	2
C_{tBLM} (μF.cm^{-2})	0.980 ± 0.007	0.945 ± 0.028	0.983 ± 0.005	0.944 ± 0.027	0.990 ± 0.004	0.940 ± 0.023
Q_{tBLM} (μF.cm^{-2})	1.197 ± 0.050	1.148 ± 0.069	1.240 ± 0.034	1.127 ± 0.065	1.416 ± 0.039	1.118 ± 0.070
α_{tBLM}	0.971 ± 0.004	0.976 ± 0.004	0.967 ± 0.002	0.978 ± 0.004	0.950 ± 0.002	0.979 ± 0.005
R_{tBLM} (MΩ.cm^2)	3.702 ± 0.739	3.708 ± 0.307	2.492 ± 0.096	5.183 ± 1.110	1.069 ± 0.109	5.030 ± 3.164

Table 6.2: EISFit parameters for mixed SAM tBLMs formed from proteoliposomes containing Na_vCbt. tBLM formed from *E.coli* polar lipid vesicles containing either 2.8% (w/w) or 5.6% (w/w) Na_vCbt. Potential was modulated between +100 mV, 0 mV and -200 mV (vs Ag/AgCl), and Na^+ or Ba^{2+}-containing electrolytes were used. Data were modelled using a R(QR) equivalent circuit as described in Methods. C_{tBLM} is obtained by doubling the height of the capacitance semi-circle in Normalised Admittance Plots (Figures 6.12b, 6.12d and 6.12f) and normalising by the electrode area. Q_{tBLM} is taken from equivalent circuit fitting using the aforementioned circuit. All other parameters were taken from EIS fits using the equivalent circuits indicated, as described in Methods.

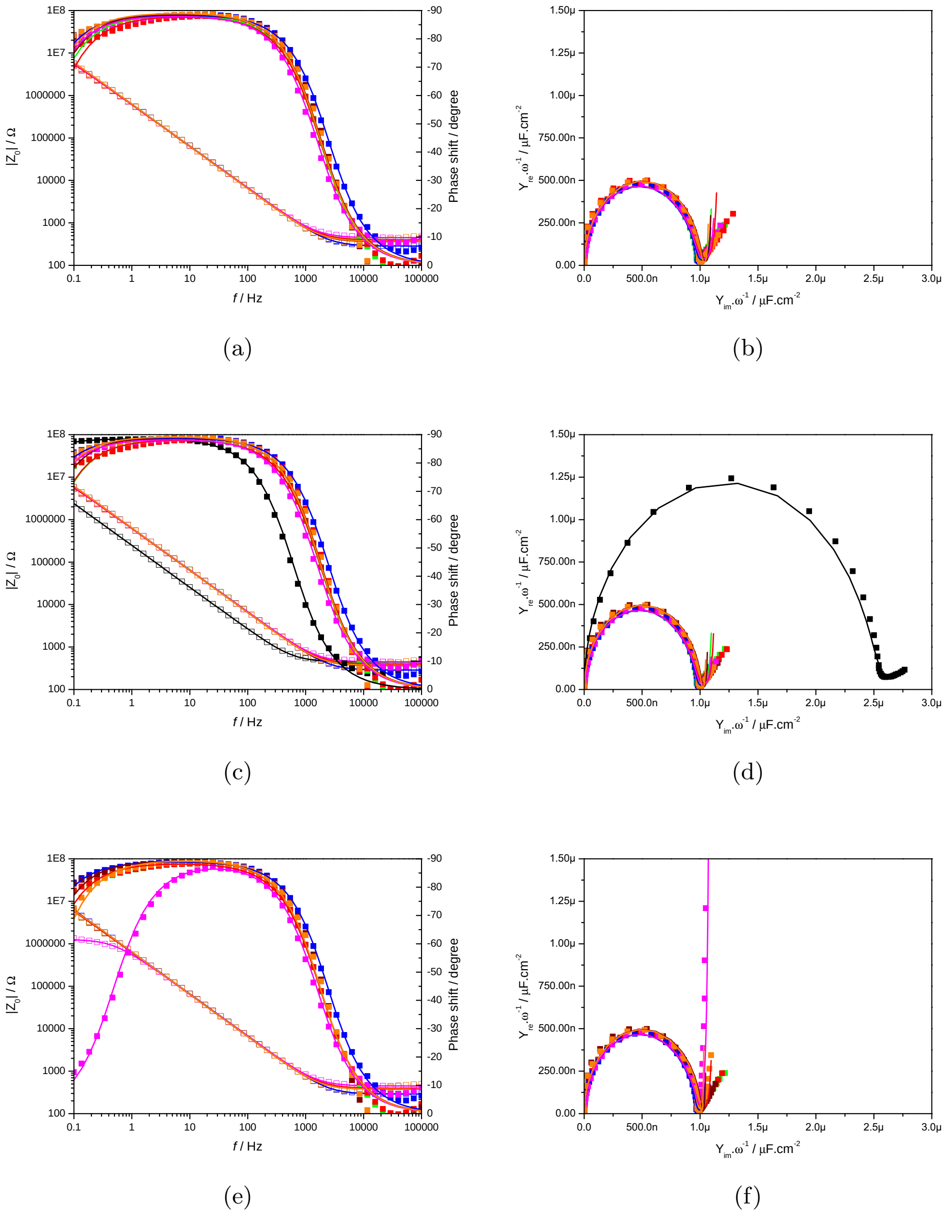

(a) (b)

(c) (d)

(e) (f)

Figure 6.13: EIS of Na_vCbtcontrol experiment. tBLM was formed from *E. coli* polar lipid extract vesicles only, with no reconstituted Na_vCbtpresent. (a) and (b) +100 mV vs SCE; (c) and (d) 0 mV vs SCE; (e) and (f) -200 mV vs SCE. Black = 66% EO_3C SAM, Red = Na^+, Blue = Ba^{2+}, Magenta = Na^+ with nifedipine, Orange = Na^+ following nifedipine washout.

	+100 mV			0 mV			-200 mV		
	Na^+	Ba^{2+}	Nif. (Na^+)	Na^+	Ba^{2+}	Nif. (Na^+)	Na^+	Ba^{2+}	Nif. (Na^+)
Model	R(QR)	R(QR)	R(QR)	R(QR)	R(QR)	R(QR)	R(QR)	R(QR)	R(QR)
n	2	1	2	3	1	2	2	1	2
C_{tBLM} ($\mu F.cm^{-2}$)	0.980 ± 0.019	0.947	0.978 ± 0.016	0.971 ± 0.013	0.946	0.975 ± 0.015	0.975 ± 0.021	0.941	0.972 ± 0.014
Q_{tBLM} ($\mu F.cm^{-2}$)	1.109 ± 0.023	1.084	1.088 ± 0.021	1.085 ± 0.014	1.059	1.066 ± 0.021	1.067 ± 0.021	1.037	1.058 ± 0.028
α_{tBLM}	0.985 ± 0.005	0.985	0.987 ± 0.005	0.987 ± 0.003	0.987	0.981 ± 0.003	0.990 ± 0.005	0.990	0.990 ± 0.006
R_{tBLM} ($\mu F.cm^2$)	4.917 ± 0.838	8.190	6.752 ± 0.214	6.099 ± 0.797	12.513	9.676 ± 0.073	6.370 ± 0.795	9.970	2.187 ± 1.878

Table 6.3: EISFit parameters for control tBLMs formed from *E. coli* polar lipid vesicles on mixed SAMs. Potential was modulated between +100 mV, 0 mV and -200 mV (vs Ag/AgCl), and Na^+ or Ba^{2+}-containing electrolytes were used. Nifedipine (Nif.) was added as a channel inhibitor. Data were modelled using a R(QR) equivalent circuit as described in Methods. C_{tBLM} is obtained by doubling the height of the capacitance semi-circle in Normalised Admittance Plots (Figures 6.13b, 6.13d and 6.13f) and normalising by the electrode area. Q_{tBLM} is taken from equivalent circuit fitting using the aforementioned circuit. All other parameters were taken from EIS fits using the equivalent circuits indicated, as described in Methods.

6.4 Discussion

6.4.1 KcsA

Two distinct data sets are presented here in Figures 6.9 and 6.10. While, the distinct separation of data into two clusters in Figure 6.9b is reminiscent of the results obtained with gramicidin-mediated ion transport in Chapter 4 (Figure 4.4), there are no such trends in Figure 6.10b. Bearing in mind that the data presented in Figure 6.9 was only obtained on one occasion, and that further replicates will be necessary to bring weight to the results and any conclusions that can be drawn, a more detailed examination of this data follows.

The similarity between the data in Figure 6.9 and the work done with gramicidin, indicates that KcsA may be facilitating rapid ion transport under low pH conditions. It is suggested that this is presented as a capacitance change, rather than a change to resistance, as was described in Chapter 4. The capacitances in Na^+ electrolytes, while significantly lower than that for K^+ at pH 4.5, are not as low as that for K^+ at pH 7.8. Literature reports the permeability of KcsA for Na^+ to be approximately 150-fold smaller than for K^+[LeMasurier et al., 2001], suggesting that the effect of Na^+ on KcsA should be minimal. The cause of this discrepancy is uncertain, however, Zakharian and Reusch [2004] have shown that a strong outward K^+ gradient can cause channel activation irrespective of pH. If we assume that some K^+ is trapped in the sub-bilayer ionic reservoirs following the opening of the channel at low pH, one can imagine a strong K^+ gradient would be set up when the bulk electrolyte is replaced with Na^+. While it is unlikely that this is a dominant cause, due to the small dimensions of these sub-membrane reservoirs and any residual K^+ in the sub-membrane environment being replaced, the effect is still worth noting given the lack of other explanations. This decreased signal can be seen in the capacitance of Na^+ plots at pH 4.5 and pH 7.8, which at approximately 1.2 μF.cm^{-2} is significantly lower than 1.7 μF.cm^{-2} for an open channel transporting K^+ at pH 4.5, but higher than the closed channel at pH 7.8. The negligible difference between the Na^+ signals for pH 4.5 and pH 7.8 indicates that pH is not playing a role in the activation of the channel under these conditions - a finding that agrees with those of Zakharian and Reusch [2004], as well as Negoda et al. [2009]. Resistances obtained via modelling of the $R_s(Q_{tBLM}R_{tBLM})$ equivalent circuit also follow a similar pattern, with K^+ at pH 4.5 giving a similar resistance to that seen with gramicidin-permeated tBLMs in Na^+ (Table 4.2, Chapter 4) or activated TRPC5 channels in Chapter 5 (Table 5.1). Resistances in Na^+, or K^+ at high pH, were closer to those of unmodified tBLMs as shown in Table 3.10.

6.4.2 Na_vCbt

Na_vCbt does not experience capacitance changes, but as can be seen in Figures 6.12c and 6.12e, as well as Table 6.2, significant deviations in tBLM resistance are detected in the presence of Na^+ when compared to Ba^{2+}. These changes in activity were detected at 0 mV and -200 mV only, in line with literature for the closely related ion channel NaChBac[Ren et al., 2001]. They constitute small but significant results that are dependent on the bulk ion of the electrolyte and the applied potential - an effect that is not seen in control experiments (Figure 6.13).

The appearance of ion transport as a small resistance change suggests a rate of ion transport that is slower than valinomycin (which was shown to exhibit a resistance in the order of 10 $k\Omega.cm^2$), and significantly slower than gramicidin or KcsA (both of which show their response in dramatic capacitance changes). KcsA has been reported to have a unitary conductance of 97 pS[Cordero-Morales et al., 2006], and Studer et al. [2011] measured NaChBac unitary conductance to be 120 pS. KcsA is well reported to demonstrate good functionality following over-expression, purification and reconstitution[Chakrapani et al., 2007b; Gao et al., 2005; Roux and Mac, 1999]. Na^+ channels, such as Na_vCbt and NaChBac, have not shown as great success. While the effect that tBLM have on ion channel function is not fully understood it is possible that the comparatively low level of activity is related to the channel density (between 2.8% and 5.6% for Na_vCbt *cf.* 1.0% for KcsA), availability of permeant ions (30 mM Na_2SO_4 for Na_vCbt *cf.* 200 mM KCl for KcsA), or restriction of the protein's conformational change. Additionally, it is possible that the optimum gating voltage for the system was not reached. A more comprehensive study examining a greater range of potentials at smaller intervals may allow the creation of a curve of tBLM resistance vs applied potential that correlates well with traditional patch-clamp I-V curves.

The addition of nifedipine (in DMSO) appears to have a deleterious effect on the resistance of the tBLM at -200 mV. Prior work done by myself (unpublished) with DMSO has shown that quantities greater than the 10 μL used here are necessary to disrupt the bilayer and thus DMSO is not the cause of this effect. However, nifedipine has been shown to have electroactive properties[Hazard et al., 1991], as have other related compounds (nitrosoaromatics and a photodegradation product of nifedipine[Bollo et al., 2007; Nunez-Vergara et al., 2002]). It is likely that the results seen here are not an indication of loss of membrane resistance, but the occurrence of Faradaic processes as electrons are exchanged between nifedipine and the electrode. As a drop in resistance is only seen at -200 mV in control tBLMs (Figure 6.13f), the use of nifedipine was deemed unsuitable for use in further studies.

6.5 Conclusion

Two ion channels of prokaryotic origin have been purified, reconstituted and incorporated into tBLMs. While more detailed studies are required, the results thus far correlate with findings in literature and indicate that there may be functional ion channels that have been incorporated into the tBLM.

pH-mediated capacitance changes have been identified in a KcsA-containing sample. While electrophysiology of KcsA often finds its low open probability (due to inactivation kinetics) problematic[Chakrapani et al., 2007a], the longer timescales involved with EIS protocols may prove to be advantageous in allowing an average channel activity to be observed. This channel activity was identified through changes in tBLM capacitance, in a similar manner those observed in the gramicidin experiments described in Chapter 4.

Conversely, the presence of $\mathrm{Na_vCbt}$ has been shown to have a noticeable effect on the resistance of the tBLM. While the degree to which the resistance changes upon $\mathrm{Na_vCbt}$ activation is not as substantial as with valinomycin as used in Chapter 4, it is likely that this is due to the lower number of molecules capable of facilitating diffusion of permeant ions across the tBLM. These ion channels probably adopt a mixture of orientations, which may also have an effect on how they affect tBLM properties. Both $\mathrm{Na^+}$ and $\mathrm{Ba^{2+}}$ were compared, giving a stark difference in resistance at certain potentials indicating an ion-specific voltage-gated behaviour.

The use of the ion channel blocker nifedipine was trialled in the case of $\mathrm{Na_vCbt}$, however it was shown to be electroactive in this system making genuine changes in resistance due to channel activity hard to separate from Faradaic electrode transfer, which presents itself in a similar manner. Clearly, the use of channel blockers or inhibitors would of great benefit in showing that the ion transport activities observed here are due to the biological activity of ion channels as supposed to modulation of the tBLM's properties - an issue that was encountered in Chapter 5 with $\mathrm{La^{3+}}$.

While the results presented in this chapter are promising, it should be noted that the data collected comes from a small number of experiments that do not always concur with each other. As such the conclusions drawn would benefit greatly from the robustness provided by repeating them. Furthermore, these experiments could be extended following the initial study of their basic parameters.

The range of pH values KcsA has been studied at could be extended below 4.5, with which one may expect to see even greater increases in capacitance. The specific activity of the channel could be checked via the use of a verified ion channel blocker such as $\mathrm{TEA^+}$ (tetraethylammonium)[LeMasurier et al., 2001] or $\mathrm{Ba^{2+}}$[Heginbotham et al., 1998, 1999; Zakharian and Reusch, 2004]. While a non-ionic blocker would be preferable, I have so far been unable to find any that in literature are confirmed inhibitors.

Studies of $\mathrm{Na_vCbt}$ could be furthered by examining the potentials at which gating occurs. Investigating at 10 mV intervals and extending the window may help define an optimum potential. Given that Na_vCbt is thought to be homologous to NaChBac, one would expect the two to share similar gating properties. Both channels originate in halophilic bacteria (*Caldalkalibacillus thermarum* and *Bacillus halodurans*, respectively), however, *C. thermarum* is also thermophilic, and as such exploration the channel's temperature range may provide interesting results. Ren et al. [2001] details the use of several other antagonists that have an effect on NaChBac, including Cd^{2+}, Ni^{2+}, nimodipine and mibefradil. Based on previous work with multivalent cations, it is likely that Cd^{2+} or Ni^{2+} would prove problematic due to their effect on the structure of the tBLM and electric double layer. Other organic channel antagonists may be of use, however nimodipine (a compound closely related to nifedipine) has been reported to exhibit similar electrochemistry[Alvarez-Lueje et al., 1994; Gupta et al., 2011]. Another compound used by Ren et al. [2001], mibefradil may yet be of use as to the best of my knowledge there are no reports on its electrochemistry, or lack there of.

Chapter 7

General Discussion and Conclusion

The overall aim of this thesis was the incorporation of functional ion channels into tBLMs, as a proof of principle for an impediametric ion channel-based biosensor. To this end electrodes were designed and their suitability for the formation of tBLMs and detection of ion transport assessed.

Electrodes produced by Phillips Research were tested, and shown to be suitable for the formation of high quality SAMs and tBLMs. Two generations were created. The first of these was used for the characterisation of the model ionophore system. This yielded excellent results, providing further insight into the sub-structure of the EO_3C/6MH tBLM as described in Chapter 4. The two ionophores used here were a mobile ion carrier, valinomycin, and a pore-forming peptide, gramicidin. At the concentrations used in Chapter 4, their respective conductances were exhibited in two distinct manners. Valinomycin-mediated ion transport resulted in a decreased membrane resistance, whereas gramicidin-mediated ion transport saw the tBLM capacitance increase. These varied characters were attributed to the large difference in the rate of ion transduction for each molecule.

Following on from the ionophore studies, attempts were made to study a ligand-gated eukaryotic ion channel - TRPC5. While the studies in Chapter 5 were able to show TRPC5 activity in the IonGate ssBLM system, detection of the channel's activity in tBLM using EIS proved to be elusive. A reconsideration of the factors that may have adversely affected the ability to detect TRPC5 presented several features that I considered desirable in an ion channel to provide the best possible chance of detection with EIS. Suggestions included selection of channels with small extramembraneous domains, originating in bacteria and of high conductance. Additionally channels gated by multivalent cations were avoided.

With these criteria in mind I selected two channels for future study - KcsA and Na_vCbt. Two different responses were seen along similar lines to those for valinomycin and gramicidin in Chapter 4. KcsA experienced pH-mediated ion selective capacitance changes, while $\mathrm{Na_vCbt}$ saw voltage-mediated ion selective resistance changes. These results shows similar trends to literature in terms of ion selectivity and gating conditions, but in terms of how ion transport presents itself, the results remain unexplained.

Data from Chapter 4 would suggest that this is due to a difference in transport rates. This cannot be explained by the relative concentrations of each channel as this merely affects the magnitude of the effect seen. The difference in transport rates between valinomycin and gramicidin was approximately 5 orders of magnitude, however, the difference in channel conductances for KcsA and a $\mathrm{Na_vCbt}$ homolog, NaChBac, are negligible at 97 pS[Cordero-Morales et al., 2006] and 120 pS[Studer et al., 2011], respectively. It is possible that the tBLM affects the function of the channels via gating or effective diffusion/transport rates. Further study of $\mathrm{Na_vCbt}$ with alternative techniques such as patch clamp electrophysiology may provide insight into the channel's transport kinetics.

In addition to the first generation electrodes, a second generation was also designed and fabricated. While the first generation have proven themselves to be of great use, one of the aims of this thesis has been to develop electrodes that are better suited to the detection of ion channel activity. In the pursuit of this goal, a key parameter that was investigated was the size of the electrodes. This required the addition of an insulating layer to better define their area by burying tracks.

While the active electrode area was indeed restricted, the deposition of a stable insulating layer proved problematic. Problems that were encountered included delamination due to the lack of an adhesion layer (P2 MKI) and amalgamation of the subsequent Ti adhesion layer with the underlying gold electrode (P2 MKII). Changing the material used for the adhesion layer from Ti to TiN resolved the issues with amalgamation and delamination (P2 MKIII), however a high quality surface was still not attained. The reasons for this inability to form a good quality SAM remain uncertain, however, surface roughness would appear to not be a problem. Contamination of the electrode surface with photoresist could not be excluded, although XPS did not indicate large carbon deposits on the surface. Examination of the surface with SAES may provide clues to what the issue is.

As can be seen from Chapters 5 and 6, the incorporation of ion channels into tBLMs and subsequent measurement with EIS is not a trivial matter, and pose several technical hurdles that must be overcome. There are many criteria that need to be taken into account when considering a target ion channel and these have the potential to preclude many interesting channels. Such criteria include large extramembranous domains (e.g. TRP channels[Voets et al., 2005], MthK[Jiang et al., 2002]), low channel unitary conductance (e.g. channel rhodopsins[Nagel et al., 2005], viral ion channels[Fischer and Sansom, 2002]), and gating compounds that interfere with the membrane properties (e.g. multivalent ions).

The sub-membrane reservoirs described in Chapter 4, and depicted in Figure 4.1b, provide a limited volume for the extramembraneous domains of proteins to exist. This causes two main problems, lack of space for the protein and restriction of channel movement. Clearly if the space available is 1 nm^3 and the extramembraneous domain requires 2 nm^3 the protein will not fit. This can be thought to lead to two outcomes - either the protein does not inhabit that region, or it distorts the surrounding regions. Given that SAMs are generally reasonably well packed this distortion would most likely come from pushing the lipid bilayer away from the surface. If the channel is able to incorporate, it will probably be in rather confined conditions, limiting the extent to which conformation changes can occur. These restrictions are likely to impede channel function.

Producing highly insulating lipid bilayers can be challenging, and the GΩ 'gold standard' that lipid bilayer resistance is measured against is only obtained via the use of small electrode areas. In order to detect the activity of a single channel above the background leak current requires large unitary conductances, preferably above 100 pS.

The gating stimulus also needs to be carefully considered, as demonstrated by the effect of La^{3+} on the capacitance of *E. coli* polar lipid tBLMs (Figure 5.11), and the large currents experienced with TCEP (Figure 5.9). As such it would be very helpful to know the effect of the gating stimulus on the tBLM prior to working with the ion channel. Several supported-membrane systems have had their resilience to voltage changes studied[Kresak et al., 2009; Zagnoni et al., 2007], including the EO_3C system used in this thesis[Jeuken, 2008]. The effect of multivalent cations on lipid phase transitions and membrane capacitance are also well reported[Chanturiya and Nikoloshina, 1994; Garcia-Celma et al., 2007; Hwang et al., 1996; Lehrmann and Seelig, 1994; Picas et al., 2009; Schulz et al., 2009; Tanaka et al., 2001].

Additionally, several ion channels exhibit complex gating properties - KcsA for example is gated by low pH or high K^+ gradient. TRP channels are even more complicated with a range of gating modulators including a wide range of compounds, ions, lipids, temperature and membrane properties such as curvature. Additionally these ion channels can rarely be approached with a uniform methodology, and substantial optimisation of the expression, purification and reconstitution may be required.

While the work presented here has shown some success in the incorporation and measurement of ion channels, there are several successful examples in literature. The large conductance mechanosensitive channel (MscL) of *E. coli* was reconstituted into a DPhyTL-based tBLM by Andersson et al. [2008]. They were able to show a voltage-gating activity below -300 mV (vs Ag/AgCl) with a conductance of 0.2 nS. This is lower than the 3.0 nS reported in literature, and is attributed to the tethered nature of the membrane preventing the mechanical stress usually associated with this channel's activity.

Vockenroth et al. [2007] took M2 peptides that form the pore of nAChR and incorporated them into DPhyTL and DPhyHDL-based tBLMs. These two tethers are very similar with the main difference being the length of the linker between the diphytanol moiety and the thiol group - 4 ethylene glycol units for DPhyTL, and 6 for DPhyHDL. This system was studied with EIS and showed selectivity for K^+ over TMA^+, with resistances rising from approximately 3 MΩ.cm^2 to 15 or 35 MΩ.cm^2 for DPhyTL and DPhyHDL, respectively. Although nAChR is an ion-channel, the M2 peptide can be considered to be in the same class as small peptide antibiotics, such as gramicidin.

The OmpF porin was reconstituted into a DPhyTL-based tBLM on a mercury electrode by Becucci et al. [2006]. Measurements were taken between -300 and -950 mV (vs SCE) with the results indicating a voltage-gating effect with peak activity occurring between -350 and -600 mV. More recent studies have linked these voltages to the transmembrane potential of the tBLM, showing that peak activity occurs at a zero transmembrane potential and rapidly inactivates either side of this[Becucci et al., 2010]. Inhibition of the channel's activity by ampicillin has also been shown. The authors note, as with the work of Andersson et al. [2008] on MscL, that the tethering environment affects the channel conductance. In this case the channel openings occur less frequently, are shorter and have greater amplitude than those recorded in BLM systems. These have been attributed to the small sub-membrane environment which is energetically less favourable than the aqueous environment of the bulk solution, as well as the local potential difference in the tether layer which actively pull ions across the channel until saturation is reached.

In terms of the criteria suggested above, MscL, M2 and OmpF are all be considered compatible with tBLMs. While the M2 peptide of nAChR is largely confined to the membrane itself, the extramembraneous domains of MscL[Chang et al., 1998] and OmpF[Basle et al., 2004; Muller and Engel, 1998] are slightly larger but not substantially so. OmpF has short intracellular loops, and longer extracellular ones[Muller and Engel, 1998], while MscL has short extracellular loops and cytoplasmic α-helices[Chang and Zen, 2006]. But, as already mentioned, both of these proteins have exhibited deminished functionality when incorporated into tBLM systems and the authors have attributed this effect to the restricted movement of the channels.

Their conductances range from 37 ± 2 pS for the M2 peptide[Opella et al., 1999], 0.1-2.6 nS for OmpF[Brink and Fan, 1989; Conlan et al., 2000], and 3.0 nS for MscL[Levina et al., 1999] (although Andersson et al. [2008] reported a maximum conductance of 0.2 ns). While these are lower than preferable, it demonstrates that unitary conductances as low as 35 pS are detectable in tBLMs. In the case of the M2 peptide this may be due to a greater number of channels that can be accommodated due to their smaller size. The gating stimulus used in each of these examples was voltage-gating. While not neccesarily the primary stimulus of the protein (MscL is activated by lateral membrane pressure caused by swelling of the cell) these channels did display voltage-gated behaviour.

Another issue to consider is the suitability of EIS for ion channel biosensors. Traditionally, ion channels have been studied with electrophysiology techniques such as patch clamp or BLM. These utilise two electrode setups and measure current at a given potential. These techniques are capable of studying channel events on an ensemble or single-channel basis, with individual opening events visible as increases in current on a millisecond timescale.

The nature of EIS entails measurements over much longer time scales. The EIS measurements made in this thesis are taken between 100 kHz and 100 mHz, resulting in measurement periods of at least 10 μseconds and 10 seconds, respectively. For the range and number of frequencies used here, this led to each data set taking approximately 5 minutes to record.

The frequencies at which key values such as peak capacitance are recorded vary according to several factors, including the size of the electrode. For the ion channels studied in Chapter 6 electrode sizes of 0.242 cm^2 and 0.03142 cm^2 were used. This results in capacitances being recorded at approximately 1-5 kHz and 10-100 kHz respectively. While these capacitance changes are comparatively easy to follow on short timescales, resistance changes are typically observed at much lower frequencies. The approximate frequency the resistance (R) is detected at related to the membrane capacitance (C) according to

$$f \approx \frac{1}{C \times R} \tag{7.1}$$

In Chapter 4, EIS of valinomycin-doped tBLMs measured resistances of 6 kΩ.cm^2 and capacitances of 0.80 μF.cm^{-2} on a 0.03142 cm^2 electrode in the presence of K$^+$, or 0.77 μF.cm^{-2} and 1.0 MΩ.cm^2 for Na$^+$. Using Equation 7.1 this gives an approximate detection frequency of 200 Hz in K$^+$ or 1 Hz in Na$^+$. Comparing this with the actual detection frequencies in Figure 4.3c, we find the phase reaches a local minima at 20 Hz in K$^+$ and below 100 mHz in Na$^+$. As such the actual detection frequency is approximately 1 order of magnitude lower than that of the frequency calculated with Equation 7.1.

Using this equation we can also calculate the approximate electrode dimensions required to detect a single ion channel conductance. Assuming a 100 pS unitary conductance, and a desired millisecond time resolution (i.e. a detection frequency in the low kHz range), we find a capacitance of < 0.1 pF would be desirable. Given that tBLM capacitances where membrane proteins have been incorporated are approximately 1.0 μF.cm^{-2}, this corresponds to an electrode radius of < 2 μm. The smallest electrodes produced in this thesis have radii of 10 μm. It is clearly very difficult to use EIS to study single-protein conductance of ion-channels.

The real strength of EIS lies in its ability to detect larger scale changes to the lipid bilayer. Capacitance changes, such as those observed with gramicidin and KcsA (Figures 4.4 and 6.9, respectively), provide clear indicators of ensemble channel activity. These are due to their higher apparent conductances, which push the frequency that activity is measured at from the range of R$_{\mathrm{tBLM}}$, to that that of C$_{\mathrm{tBLM}}$.

Resistance changes, when visible, are present as a slowly declining phase angle as can be seen in Figure 5.10a. This slow decline is due to the heterogeneity of the surface and the effect on transport resulting in a multitude of resistance changes occurring at different frequencies, and overlapping on the Bode plot.

A specific frequency can be selected to monitor these changes over time as experimental conditions change, however, the frequency required is not always the same. This approach is well demonstrated by Terrettaz and Vogel [2005], who follow the activity of a synthetic ligand-gated ion channel (SLIC) at 10 mHz.

An alternative approach has been put forward by Yang et al. [2006], who developed a new mathematical treatment for the calculation of EIS parameters that are independent of the frequency periods being used. As such each frequency can be measured with a time resolution of 20 ms, an decrease in measurement time of three orders of magnitude at 100 mHz.

For these reasons the development of ion channel based biosensors is likely to be more arduous than the other common types discussed in Section 1.2. In this regard the greatest strength of the ion channel's application to biosensing becomes one of its greatest weaknesses. As a result, care must be taken to either control the presence of possible gating compounds in the analyte sample or to limit the selection of ion channels to a range which have singular, or controllable, gating conditions to minimise false positives. An alternative is the development of ionophore-based biosensors, such as the Ion Channel Switch from Cornell et al. [1997] discussed in Chapter 1.

The construction of the Ion Channel Switch took advantage of well understood ionophores coupled to antibodies that have been selected for specific analytes. This provides the high specificity experienced with antibody-antigen reactions, combined with a well characterised system that requires minimal optimisation. While attempts to commercialise this particular system by AMBRI Biosensors were unsuccessful, the thinking behind the approach has been carried on by others.

Bayley's group in particular have done a substantial amount of work with α-hemolysin developing stochastic sensors for a variety of stimuli[Bayley, 1995; Bayley and Cremer, 2001], including genetically engineering the pore to be gated by Zn^{2+}[Russo et al., 1997; Walker et al., 1994]; detection of protein-ligand[Howorka et al., 2004] or protein-inhibitor[Cheley et al., 2006] interactions; detection of TNT over other nitroaromatics[Guan et al., 2005]; detection of inositol 1,4,5-trisphosphate (IP_3, a secondary messenger)[Kang et al., 2007]; use of non-covalent molecular adaptors to alter the pore's ion selectivity, as well as providing the ability to detect analytes with prolonged dwell times[Wu et al., 2007]; and the detection of soluble proteins via interaction with a freely moving polyethylene glycol chain[Movileanu et al., 2000]. With this wide range of functionalities, Bayley and coworkers have constructed a diverse toolkit from which biosensors can be assembled. Furthermore, by utilising a variety of these in an array it would be possible to build an electronic 'nose', with various compounds having a distinct signature dependant on how they react with individual pores[Bayley and Cremer, 2001].

One increasingly popular system is that of pore-spanning BLMs, variants of which are also referred to as mixed hybrid BLMs (mixed hBLMs)[Favero et al., 2002], and nanopore-spanning BLMs (npsBLMs)[Kresak et al., 2009]. The small size of these pores (generally

1 μm or less) provide the stability and lifetimes of days to weeks associated with tBLMs, with the much larger extramembranous environments present in traditional BLM systems. Variations on this approach have been put to good use by several groups who have studied the activity of various ionophores, as well as an ionotropic glutamate receptor ($GluR_0$)[Favero et al., 2005], NaChBac[Studer et al., 2011], KcsA[Zagnoni et al., 2007], and bacteriorhodopsin[Schmitt et al., 2008]. The approach used by Favero et al. [2005] is the polycarbonate track-etched nanopore filter described in Section 1.3.4. Schmitt et al. [2008] meanwhile made use of a EO_3C-based tBLM on porous alumina. Studer et al. [2011] utilised a nanopore array in a Si_3N_4 chip, while Zagnoni et al. [2007] made use of a 100 μm aperture in a PMMA/PTFE film. All these approaches provided ample space for incorporation of membrane proteins, with many displaying significant improvements in robustness over traditional BLM systems.

In spite of this assessment, the tBLM system used here continues to be relevant in the field of biosensing. Various features of the system can be employed, such as the bilayer's capacity to host a range of membrane proteins that is not limited to ion channels. Work has already been published on cytochrome bo_3[Jeuken, 2008; Jeuken et al., 2006; Weiss et al., 2008, 2009], and work in the Jeuken group continues to explore other redox proteins such as CymA[Cheetham et al., 2011] and flavin monooxidase 3 (FMO3)[Catucci et al., 2011]. The lipid bilayer itself can also be the key feature of the sensor. Nanotoxicological studies of the cell membrane can be assisted with bilayer permeation data provided by EIS studies of bilayer-nanoparticle interactions[Mu et al., 2011], similar to that reported for BLM-like systems[de Planque et al., 2011].

Bibliography

URL `www.avantilipids.com`.

URL `http://eaps4.iap.tuwien.ac.at/~werner/qes_tut_interact.html`.

A. Abdelghani, J.M. Chovelon, J.M. Krafft, N. Jaffrezic-Renault, A. Trouillet, C. Veillas, C. Ronot-Trioli, and H. Gagnaire. Study of self-assembled monolayers of n-alkanethiol on a surface plasmon resonance fibre optic sensor. *Thin Solid Films*, 284-285:157–161, 1996.

A. Alvarez-Lueje, L.J. Nunez-Vergara, and J.A. Squella. Voltammetric behavior of 1,4-dihydropyridine calcium antagonists. *Electroanalysis*, 6:259–264, 1994.

O.S. Andersen and R.E. Koeppe. Molecular determinants of channel function. *Physiological Reviews*, 72:S89–S158, 1992.

M. Andersson, H.M. Keizer, C. Zhu, D. Fine, A. Dodabalapur, and R.S. Duran. Detection of single ion channel activity on a chip using tethered bilayer membranes. *Langmuir*, 23:2924–2927, 2007.

M. Andersson, G. Okeyo, D. Wilson, H.M. Keizer, P. Moe, P. Blount, D. Fine, A. Dodobalapur, and R.S. Duran. Voltage-induced gating of the mechanosensitive mscl ion channel reconstituted in a tethered lipid bilayer membrane. *Biosens. Bioelectron.*, 23:919–923, 2008.

Anon. *Structural Biochemistry.* WikiBooks, 2010. URL `http://en.wikibooks.org/wiki/Structural_Biochemistry/Lipids/Lipid_Rafts`.

F. Ashcroft. The state of ion channel research in 2004. *Nature Reviews Drug Discovery*, 3:239–278, 2004.

V. Atanasov, N. Knorr, R.S. Duran, S. Ingebrandt, A. Offenhausser, W. Knoll, and I. Koper. Membrane on a chip: A functional tethered lipid bilayer membrane on silicon oxide surfaces. *Biophys. J*, 89:1780–1788, 2005.

T. Atsumi, L. McCartert, and Y. Imae. Polar and lateral flagellar motors of marine *Vibrio* are driven by different ion-motive forces. *Nature*, 355:182–184, 1992.

C.D. Bain and G.M. Whitesides. Molecular-level control over surface order in self-assembled monolayer films of thiols on gold. *Science*, 240:62–63, 1988.

C.D. Bain, J. Evall, and G.M. Whitesides. Formation of monolayers by the coadsorption of thiols on gold: Variation in the head group, tail group, and solvent. *Journal of the American Chemical Society*, 111:7155–7164, 1989.

E. Bamberg and P. Lauger. Blocking of the gramicidin channel by divalent cations. *J. Membrane Biol.*, 35(1):351–375, 1977.

L.T. Banner, A. Richter, and E. Pinkhassik. Pinhole-free large-grained atomically smooth au(111) substrates prepared by flame-annealed template stripping. *Suface and Interface Analysis*, 41:49–55, 2008.

A.J. Bard and L.R. Faulkner. *Electrochemical Methods: Fundamentals and Applications.* John Wiley & Sons, Inc., New York, second edition edition, 2001.

G. Bartolommei, F.T. Buoninsegni, and M.R. Moncelli. Calcium transport by sarcoplasmic reticulum ca^{2+}-atpase can be investigated on a solid-supported membrane. *Bioelectrochemistry*, 63:157–160, 2004.

A. Basle, R. Qutub, M. Mehrazin, J. Wibbenmeyer, and A.H. Delcour. Deletions of single extracellular loops affect ph sensitivity, but not voltage dependence, of the *Escherichia coli* porin ompf. *Prote*, 17:665–672, 2004.

H. Bayley. Pore-forming proteins with built-in triggers and switches. *Bioorganic Chemistry*, 23:340–354, 1995.

H. Bayley and P.S. Cremer. Stochastic sensors inspired by biology. *Nature*, 413:226–230, 2001.

G. Beamson and D. Briggs. *High resolution XPS of organic polymers*, chapter C 1s, page 119. John Wiley & Sons, Ltd., 1992.

L. Becucci and R. Guidelli. Equilibrium distribution of k$^+$ ions in the hydrophilic spacer of tethered bilayer lipid membranes. *Soft Matter*, 5:2294–2301, 2009.

L. Becucci, M. R. Moncelli, and R. Guidelli. Thallous ion movements through gramicidin channels incorporated in lipid monolayers supported by mercury. *Biophys. J.*, 82(2): 852–864, 2002.

L. Becucci, R. Guidelli, C. Peggion, C. Toniolo, and M. R. Moncelli. Incorporation of channel-forming peptides in a hg-supported lipid bilayer. *J. Electroanal. Chem.*, 576(1): 121–128, 2005.

L. Becucci, M.R. Moncelli, and R. Guidelli. Impedance spectroscopy of ompf porin reconstituted into a mercury-supported lipid bilayer. *Langmuir*, 22:1341–1346, 2006.

L. Becucci, M. Innocenti, E. Salvietti, A. Rindi, I. Pasquini, M. Vassalli, M.L. Foresti, and R. Guidelli. Potassium ion transport by gramicidin and valinomycin across a ag(111)-supported tethered bilayer lipid membrane. *Electrochim. Acta*, 53:6372–6379, 2008.

L. Becucci, M. D'Amico, S. Daniele, M. Olivotto, A. Pozzi, and R. Guidelli. A metal-supported biomimetic micromembrane allowing the recording of single-channel activity and of impedance spectra of membrane proteins. *Bioelectrochemistry*, 78:176–180, 2010.

D.J. Beech. Canonical transient receptor potential 5. *Handbook of Experimental Pharmacology*, 179:109–123, 2007.

D.J. Beech, Y.M. Bahnasi, A.M. Dedman, and E. Al-Shawaf. Trpc channel lipid specificity and mechanisms of lipid regulation. *Cell Calcium*, 45:583–588, 2009.

A. Bentley, A. Atkinson, J. Jezek, and D.M. Rawson. Whole cell biosensors - electrochemical and optical approaches to ecotoxicity testing. *Toxicity in Vitro*, 15:469–475, 2001.

G. Binnig, C.F. Quate, and C. Gerber. Atomic force microscope. *Phys. Rev. Lett.*, 56(9): 930–933, 1986.

N. Boden, R.J. Bushby, S. Clarkson, S.D. Evans, P.F. Knowles, and A. Marsh. The design and synthesis of simple molecular tethers for binding biomembranes to a gold surface. *Tetrahedron*, 53(31):10939–10952, 1997.

K. Bokvist and J. Sandblom. Mechanisms of faciliation and blocking in gramicidin channels by impermeant ions. *J Membrane Science*, 66:157–168, 1992.

S. Bollo, S. Finger, J.C. Sturm, L.J. Nunez-Vergara, and J.A. Squella. Cyclic voltammetry and scanning electrochemical microscopy studies of the heterogeneous electron transfer reaction of some nitrosoaromatic compounds. *Electrochimica Acta*, 52:4892–4898, 2007.

D. Boltovskoy. Radiolaria. In D. Boltovskoy, editor, *Atlas del Zooplancton del Atlantico Sudoccidental y metodos de trabajo con el zooplancton marino*, pages 261–316. Publicacin Especial del Instituto Nacional de Investigacin y Desarrollo Pesquero, Mar del Plata., 1981.

D. Boltovskoy, S. Bender Kotzian, and F.L. Pedrozo. Some new techniques for the preparation and illustration of polycystina (radiolaria). *Micropaleontology*, 29:382–390, 1983.

I.R. Booth, M.D. Edwards, and S. Miller. Bacterial ion channls. *Biochemistry*, 42:10045–10053, 2003.

O. Braha, B. Walker, S. Cheley, J.J. Kasianowicz, L. Song, J.E. Goux, and H. Bayley. Designed protein pores as components for biosensors. *Chemistry and Biology*, 4:497–505, 1997.

C.M.A Brett and A.M.O Brett. *Electrochemistry: Principles, Methods and Applications.* Oxford University Press, Oxford, 1993.

A.A. Brian and H.M. McConnell. Allogeneic stimulation of cytotoxic t cells by supported planar membranes. *Proceedings of the National Academy of Sciences, USA*, 81:6159–6163, 1984.

P.R. Brink and S-F. Fan. Patch clamp recording from membranes which contain gap junction channels. *Biophysical Journal*, 56:579–593, 1989.

C. Burzik, G. Kaim, P. Dimroth, E. Bamberg, and K. Fendler. Bioenergetics-charge displacements during atp-hydrolysis and synthesis of the na$^+$-transporting f0f1-atpase of llyobacter tartaricus. *Biophysical Journal*, 85:2044–2054, 2003.

J. Cai and M.S. DuBow. *Biodegradation*, 8:105, 1997.

W.B. Caldwell, K. Chen, B.R. Herr, C.A. Mirkin, J.C. Hulteen, and R.P. Vun Duyne. Self-assembled monolayers of ferrocenylazobenzenes on au(111)/mica films: Surface-enhanced raman scattering response vs surface morphology. *Langmuir*, 10:4109–4115, 1994.

R.F. Carvalhal, R.S. Freire, and L.T. Kubota. Polycrystalline gold electrodes: A comparative study of pretreatment procedures used for cleaning and thiol self-assembly monolayer formation. *Electroanalysis*, 17:1251–1259, 2005.

E.T. Castellena and P.S. Cremer. Solid supported lipid bilayers: From biophysical studies to sensor design. *Surface Science Reports*, 61:429–444, 2006.

G. Catucci, L.J.C. Jeuken, G. Gianfranco, and S. Sadeghi. Molecular modelling and protein engineering of a soluble and active human flavin containing monooxygenase 3. *Submitted*, 2011.

O. Chailapakul and R.M. Crooks. Interactions between organized, surface-confined monolayers and liquid-phase probe molecules. 4. synthesis and characterisization of nanoporous molecular assemblies: Mechanism of probe penetration. *Langmuir*, 11: 1329–1340, 1995.

S. Chakrapani, J.F. Cordero-Morales, and E. Perozo. A quantitative description of kcsa gating i: Macroscopic currents. *Journal of General Physiology*, 130:465–478, 2007a.

S. Chakrapani, J.F. Cordero-Morales, and E. Perozo. A quantitative description of kcsa gating ii: Single-channel currents. *Journal of General Physiology*, 130:479–496, 2007b.

G. Chang, R.H. Spencer, A.T. Lee, M.T. Barclay, and D.C. Rees. Structure of the mscl homolog from *Mycobacterium tuberculosis*: a gated mechanosensitive ion channel. *Sci*, 282:2220–2226, 1998.

J-L. Chang and J-M. Zen. Fabrication of disposable ultramicroelectrodes: Characterization and applications. *Electrochem. Comm.*, 8:571–576, 2006.

A.N. Chanturiya and H.V. Nikoloshina. Correlations between changes in membrane capacitance induced by changes in ionic environment and the conductance of channels incorporated into bilayer lipid membranes. *J. Membrane Biol.*, 137:71–77, 1994.

D.L. Chapman. A contribution to the theory of electrocapillarity. *Phil. Mag.*, 25:475–481, 1913.

M.R. Cheetham, J.P. Bramble, D.G.G. McMillan, L. Kreminski, X. Han, B.R.G. Johnson, R.J. Bushby, P.D. Olmsted, L.J.C. Jeuken, S.J. Marritt, J.N. Butt, and S.D. Evans. Concentrating membrane proteins using asymmetric traps and ac electric fields. *Journal of the American Chemical Society*, 133:6521–6524, 2011.

S. Cheley, H. Xie, and H. Bayley. A genetically encoded pore for the stochastic detection of a protein kinase. *ChemBioChem*, 7:1923–1927, 2006.

Y. Cheng, H. Yao, H. Lin, J. Lu, L. Rongchang, and K. Wang. The events relating to lanthanide ions enhanced permeability of human erythrocyte membrane: binding, conformational change, phase transition, perforation and ion transport. *Chemico-Biological Interactions*, 121:267–289, 1999.

F.G. Chevallier, L. Jiang, T.G.J. Jones, and R.G. Compton. Mathematical modelling and numerical simulation of cyclic voltammetry at an electrode covered with an insulating film containing cylindrical micropores. *Journal of Electroanalytical Chemistry*, 587:254–262, 2006.

B.Z. Chowdhry, G. Lipka, A.W. Dalziel, and J.M. Sturtevant. Effect of lanthanum ions on the phase transitions of lecithin bilayers. *Biophysical Journal*, 45:633–635, 1984.

D.E. Clapham, L.W. Runnels, and C. Strubing. The trp ion channel family. *Nature Reviews Neuroscience*, 2(6):387–396, 2001.

Leland C. Jr. Clark. Membrane polarographic electrode system and method with electrochemical compensation, 1970.

Leland Jr. Clark and Champ Lyons. Electrode systems for continuous monitoring in cardiovascular surgery. *Ann. NY Acad. Sci.*, 102:29–45, 1962.

S. Conlan, Y. Zhang, S. Cheley, and H. Bayley. Biochemical and biophysical characterization of ompg: A monomeric porin. *Biochemistry*, 39:11845–11854, 2000.

J.F. Cordero-Morales, L.G. Cuello, Y. Zhao, V. Jogini, D.M. Cortes, B. Roux, and E. Perozo. Molecular determinants of gating at the potassium-channel selectivity filter. *Nature Structural & Molecular Biology*, 13:311–318, 2006.

B.A. Cornell, V.L.B. Braach-Maksvytis, L.G. King, P.D.J. Osman, B. Raguse, L. Wieczorek, and R.J. Pace. A biosensor that uses ion-channel switches. *Nature*, 387:580–583, 1997.

D.M. Cortes and E. Perozo. Structural dynamics of the streptomyces lividans k$^+$ channel (skc1): Oligomeric stoichiometry and stability. *Biochemistry*, 36:10343–10352, 1997.

R.F. Costello, I.R. Peterson, J. Heptinstall, and D.J. Walton. Improved gel-protected bilayers. *Biosens. Bioelectron.*, 14(3):2650271, 1999.

S.E. Creager and J. Clarke. Contact-angle titrations of mixed ω-mercaptoalkanoic acid/alkanethiol monolayers on gold. reactive vs nonreactive spreading, and chain length effects on surface pka values. *Langmuir*, 10:3675–3683, 1994.

S.E. Creager, L.A. Hockett, and G.K. Rowe. Consequences of microscopic surface roughness for molecular self-assembly. *Langmuir*, 8:854861, 1992.

L.G. Cuello, J.G. Romero, D.M. Cortes, and E. Perozo. ph-dependent gating in the *Streptomyces lividans* k$^+$ channel. *Biochemistry*, 37:3229–3236, 1998.

W.R. Cullen and K.J. Reimer. Arsenic speciation in the environment. *Chemical Reviews*, 89:713–764, 1989.

S. Daunert, G. Barrett, J.S. Feliciano, R.S. Shetty, S. Shrestha, and W. Smith-Spencer. Genetically engineered whole-cell sensing systems: Coupling biological recognition with reporter genes. *Chemical Reviews*, 100:2705–2738, 2000.

R. de Levie. On impedance measurements: The determination of the double layer capacitance in the presence of an electrode reaction. *Electrochimica Acta*, 10:395–402, 1965.

M.R.R. de Planque, S. Aghdaei, T. Roose, and H. Morgan. Electrophysiological characterization of membrane disruption by nanoparticles. *ACS Nano*, 5:3599–3606, 2011.

R.F. DeBono, G.D. Loucks, D. Dellamanna, and U.J. Krull. *Canadian Journal of Chemistry*, 74:677–688, 1996.

A. Demoz and D.J. Harrison. *Langmuir*, 9:1046, 1993.

E. den Dekker, J.G.J. Hoenderop, B. Nilius, and R.J.M. Bindels. The epithelial calcium channels, trpv5 & trpv6: From identification towards regulation. *Cell Calcium*, 33(5-6): 497–507, 2003.

D. Deng, N. Jiang, S-J Hao, H. Sun, and G-J. Zhang. Loss of membrane cholesterol influences lysosomal permeability to potassium ions and protons. *Biochimica et Biophysica Acta - Biomembranes*, 2008.

C. Dhal and J. Dhal. *Biology of Cholesterol*, chapter 7. CRC Press, Boca Raton, FL., 1988.

P. Diao, D. Jiang, X. Cui, D. Gu, R. Tong, and B. Zhong. Studies of structural disorder of self-assembled thiol monolayers on gold by cyclic voltammetry and ac impedance. *Journal of Electroanalytical Chemistry*, 464:61–67, 1999.

N.W. Downer, J. Li, E.M. Penniman, L.W. DeLuca, and H.G. Smith. Surface-bound biomembranes incorporating receptors: electrochemical and structural characterisation. *Biosensors and Bioelectronics*, 7:429–440, 1992.

D.A. Doyle, J.M. Cabral, R.A. Pfuetzner, A. Kuo, J.M. Gulbis, S.L. Cohen, B.T. Chait, and R. MacKinnon. The structure of the potassium channel: Molecular basis of k^+ conduction and selectivity. *Science*, 280:69–77, 1998.

R. Dutzler, E.B. Campbell, M. Cadene, B.T. Chait, and R. MacKinnon. X-ray structure of a clc chloride channel at 3.0 å reveals the molecular basis of anion selectivity. *Nature*, 415:287–294, 2002.

Ecochemie. Reference electrodes and their usage. Technical Report 038, 2003.

K. Edinger, A. Golzhauser, K. Demota, C. Woll, and M. Grunze. Formation of self-assembled monolayers of n-alkanethiols on gold: A scanning tunneling microscopy study on the modification of substrate morphology. *Langmuir*, 9:4–8, 1993.

G. Eisenman and J. Sandblom. *Physical Chemistry of Transmembrane Ion Motions*, chapter Energy Barriers in Ionic Channels: Data for Gramicidin A Interpreted Using a Single-File (3B4S”) Model Having 3 Barriers Separating 4 Sites, pages 329–348. Elsevier Science Publishers, Amsterdam, 1983a.

G. Eisenman and J. Sandblom. *The Physiology of Excitable Cells*, chapter TEA and TMA Alter the I-V Characteristics of the Gramicidin Channel As If They Bind to Channel Sites At Differing Depths In The Potential Field But Do Not Cross, pages 191–204. Alan Liss Inc., 1983b.

Y. Fang, A.G. Frutos, and J. Lahiri. Membrane protein microarrays. *J. Am. Chem. Soc.*, 124(11):2394–2395, 2002.

G. Favero, A. D’Annibale, L. Campanella, R. Santucci, and T. Ferri. Membrane supported bilayer lipid membranes array: Preparation, stability and ion-channel insertion. *Anal. Chim. Acta*, 460:23–34, 2002.

G. Favero, L. Camanella, S. Cavallo, A. D’Annibale, M. Perrella, E. MAttei, and T. Ferri. Glutamate receptor incorporated in a mixed hybrid bilayer lipid membrane array, as a sensing element of a biosensor working under flowing conditions. *Journal of the American Chemical Society*, 127:8103–8111, 2005.

H. Finklea, D. Snider, J. Fedyk, E. Sabatani, Y. Gafni, and I. Rubinstein. Characterisation of octadecanethiol-coated gold electrodes as microarray electrodes by cyclic voltammetry and ac impedance spectroscopy. *Langmuir*, 9:3660–3667, 1993.

H.O. Finklea. *Electroanalytical Chemistry, Vol. 19*, volume 19, chapter Electrochemistry of Organized Monolayers of Thiols and Related Molecules on Electrodes, pages 109–335. Marcel Dekker, NewYork, 1996.

H.O. Finklea. *Encyclopedia of Analytical Chemistry*, chapter Self-Assembled Monolayers on Electrodes. John Wiley & Sons, Inc., 2006.

W.B. Fischer and M.S.P. Sansom. Viral ion channels: structure and function. *Biochemica et Biophysica Acta*, 1561:27–45, 2002.

A.C. Fisher. *Electrode Dynamics*. Oxford Chemistry Primers. Oxford University Press, Oxford, 1996.

J.P. Folkers, P.E. Laibinis, G.M. Whitesides, and J. Deutch. Phase behavior of two-component self-assembled monolayers of alkanethiolates on gold. *Journal of Physical Chemistry*, 98:563–571, 1994.

C. Frubose and K. Doblhofer. *Journal of the Chemical Society - Faraday Transactions*, 91:1949–1953, 1995.

T. Gallant. Gallant's biology stuff, 2008.

H. Gao, G. Luo, J. Feng, A.L. Ottova, and Tien. H.T. Photoelectric conversion properties of bilayer lipid membranes self-assembled on an ito substrate. *J. Electroanal. Chem.*, 496:158–161, 2001.

I. Gao, X. Mi, V. Paajanen, K. Wang, and Z. Fan. Activation-coupled inactivation in the bacterial potassium channel kcsa. *Proceedings of the National Academy of Sciences USA*, 102:17630–17635, 2005.

J.J. Garcia-Celma, L. Hatahet, W. Kunz, and K. Fendler. Specific anion and cation binding to lipid membranes investigated on a solid supported membrane. *Langmuir*, 23: 10074–10080, 2007.

S. Geibel, N. Flores-Herr, T. Licher, and H. Vollert. Establishment of cell-free electrophysiology for ion transporters: Application for pharmacological profiling. *Journal of Biomolecular Screening*, 11:262–268, 2006.

R.B. Gennis. *Biomembranes*. Springer Advanced texts in chemistry. Springer-Verlag, New York (USA), 1989.

G. Gillen, S. Wight, J. Bennett, and M.J. Tarlov. Patterning of self-assembled alkanethiol monolayers on silver by microfocus ion and electron beam bombardment. *Applied Physics Letters*, 65:534–536, 1994.

H.H. Girault. *Analytical and Physical Electrochemistry.* EPFL Press, Lausanne, 2004.

H-Z. Goh, M. Broccio, S. Shenoy, F. Heinrich, J.A. Mindell, and M. Losche. Functional incorporation of kcsa into tethered lipid bilayer membranes. *Biophysical Journal*, 98: 537a, 2010.

Y. Golan, L. Margulis, and I. Rubinstein. Vacuum-deposited gold films i. factors affecting film morphology. *Surface Science*, 264:312–326, 1992.

A. Gomis, S. Soriano, C. Belmonte, and F. Viana. Hypoosmotic- and pressure-induced membrane stretch activate trpc5 channel. *Journal of Physiology*, 586:5633–5649, 2008.

J.J. Gooding, P. Erokhin, D. Losic, W. Yang, V. Policarpio, J. Liu, F.M. Ho, M. Situmorang, D.B. Hibbert, and J.G. Shapter. Parameters important in fabricating enzyme electrodes using self-assembled monolayers of alkanethiols. *Analytical Sciences*, 17:3–9, 2001.

G. Gouy. On the constitution of the electric charge at the surface of an electrolyte. *Compt. Rend.*, 149:654–657, 1909.

G. Gouy. Constitution of the electric charge at the surface of an electrolyte. *J. Phys.*, 9: 457, 1910.

D.C. Grahame. The electrical double layer and the theory of electrocapillarity. *Chem. Rev.*, 41(3):441–501, 1947a.

D.C. Grahame. New techniques in the measurement of the capacity of the electrical double layer. *Physical Review*, 72(6):522, 1947b.

M. Grandbois, M. Beyer, M. Rief, H. Clausen-Schaumann, and H.E. Gaub. How strong is a covalent bond? *Science*, 283:1727–1730, 1999.

R.J. Green, R.A. Frazier, K.M. Shakesheff, M.C. Davies, C.J. Roberts, and S.J.B. Tendler. Surface plasmon resonance analysis of dynamic biological interactions with biomaterials. *Biomaterials*, 21:1823–1835, 2000.

D.E. Grigoriadis, S.R.J. Hoare, S.M. Lechner, D.H. Slee, and J.A. Williams. Drugability of extracellular targets: Discovery of small molecule drugs targetting allosteric , functional and subunit-selective sites on gpcrs and ion channels. *Neuropsychopharmacology*, 34: 106–125, 2009.

L. Q. Gu, O. Braha, S. Conlan, S. Cheley, and H. Bayley. Stochastic sensing of organic analytes by a pore-forming protein containing a molecular adapter. *Nature*, 398(6729): 686–690, 1999.

X. Guan, L-Q. Gu, S. Cheley, O. Braha, and H. Bayley. Stochastic sensing of tnt with a genetically engineered pore. *ChemBioChem*, 6:1875–1881, 2005.

L-H. Guo, J.S. Facci, G. McLendon, and R. Mosher. Effect of gold topography and surface pretreatment on the self-assembly of alkanethiol monolayers. *Langmuir*, 10:4588–4593, 1994.

V.K. Gupta, R. Jain, M.M. Antonijevic, H. Khani, M.N. Siddiqui, A. Dwivedi, R. Mishra, and S. Agarwal. Assay of nimodipine - an anti hypertensive drug, in bulk form and pharmaceutical formulations by cathodic adsorptive stripping voltammetry. *International Journal of Electrochemical Science*, 6:37–51, 2011.

T.H. Haines. Do sterols reduce proton and sodium leaks through lipid bilayers? *Progress in Lipid Research*, 40:299–324, 2001.

B. Hassler, R.M. Worden, A. Mason, P. Kim, N. Kohli, J.G. Zeikus, M. Laivenieks, and R. Ofoli. Biomimetic interfaces for a multifunctional biosensor array microsystem. In D. Rocha, P.M. Sarro, and M.J. Vellekoop, editors, *IEEE Sensors 2004 Conference*, pages 991–994, Vienna Univ Technol, Vienna, AUSTRIA, 2004.

W.M. Haynes and D.R. Lide, editors. *CRC Handbook of Chemistry and Physics: A Ready-Reference Book of Chemical and Physical Data.* CRC Press, 91 edition, 2011.

R. Hazard, J.P. Hurvois, C. Moinet, A. Tallec, J.L. Burgot, and G. Eon-Burgot. On the electrochemical behaviour of nifedipine and related compounds: Instability of the reduction products in protic media. *Electrochimica Acta*, 36:1135–1141, 1991.

L. He, J.W.F Robertson, J. Li, I. Karcher, S.M. Schiller, W. Knoll, and R. Naumann. Tethered bilayer lipid membranes based on monolayers of thiolipids mixed with a complementary dilution molecule. 1. incorporation of channel peptides. *Langmuir*, 21(24): 11666–11672, 2005.

L. Heginbotham, L. Kolmakova-Partensky, and C. Miller. Functional reconstitution of a prokaryotic k^+ channel. *Journal of General Physiology*, 111:741–749, 1998.

L. Heginbotham, M. LeMasurier, L. Kolmakova-Partensky, and G. Miller. Single *Streptomyces lividans* k^+ channels: functional assymetries and sidedness of proton activation. *Journal of General Physiology*, 114:551–560, 1999.

M. Hegner, P. Wagner, and G. Semenza. Ultralarge atomically flat template-stripped au surfaces for scanning probe microscopy. *Surface Science*, 291:39–46, 1993.

F. Heinrich, T. Ng, D.J. Vanderah, P. Shekhar, M. Mihailescu, H. Nanda, and M. Losche. A new lipid anchor for sparsely tethered bilayer lipid membranes. *Langmuir*, 25:4219–4229, 2009.

F. Heitz and C. Gavach. Ca^{2+}-gramicidin a interactions and blocking effects on the ionic channel. *Biophy. Chem.*, 18:153–163, 1983.

H.L.F. von Helmholtz. Ueber einige gesetze der vertheilung elektrischer strome in koperlichen leitern mit anwendung auf die thierisch-elektrischen versuche. *Ann. Physik*, 89: 211–233, 1853.

P. Hildebrandt, S. Keller, A. Hoffmann, F. Vanhecke, and B. Schrader. Enhancement factor of surface-enhanced raman scattering on silver and gold surfaces upon near-infrared excitation. indication of an unusual strong contribution of the chemical effect. *Journal of Raman Spectroscopy*, 24:791–796, 1993.

B. Hille. *Ion Channels of Excitable Membranes.* Sinauer, 2001.

P. Hinterdorfer and Y.F. Dufrene. Detection and localization of single molecular recognition events using atomic force microscopy. *Nature Methods*, 3:347–355, 2006.

S.B. Hladky, L.G.M. Gordon, and D.A. Haydon. Molecular mechanisms of ion transport in lipid membranes. *Annu. Rev. Phys. Chem.*, 25:11–38, 1974.

J. C. Hoogvliet, M. Dijksma, B. Kamp, and W. P. van Bennekom. Electrochemical pretreatment of polycrystalline gold electrodes to produce a reproducible surface roughness for self-assembly: A study in phosphate buffer ph 7.4. *Analytical Chemistry*, 72:2016–2021, 2000.

S. Howorka, J. Nam, H. Bayley, and D. Kahne. Stochastic detection of monovalent and bivalent protein-ligand interactions. *Angewandte Chemie International Edition*, 43:842–846, 2004.

C.A. Hubner and T.J. Jentsch. Ion channel diseases. *Human Molecular Genetics*, 11: 2435–2445, 2002.

F. Hwang, D-Q. Zhao, J-W. Chen, X-H. Chen, and J-Z. Ni. Effect of lanthanum ions on the lipid polymorphism of phosphatidylethanolamines. *Chem. Phys. Lipids*, 82:73–77, 1996.

A. Ihs and B. Liedberg. Infrared study of ethyl and octyl xanthate ions adsorbed on metallic and sulfidized copper and silver surfaces. *Langmuir*, 10:734–740, 1994.

Y. Imae and T. Atsumi. Na^+-driven bacterial flagellar motors. *Journal of Bioenergetics and Biomembranes*, 21:705–716, 1989.

Membrane Preparation from Hek Cells - Swelling Method. IonGate Biosciences GmbH, 29/09/2008 2008.

Ionovation. Kcsa - the nobel potassium channel (bilayer application note 03).

T. Ishida, S. Tsuneda, N. Nishida, M. Hara, H. Sasabe, and W. Knoll. Surface-conditioning effect of gold substrates on octadecanethiol self-assembled monolayer growth. *Langmuir*, 13:4638–4643, 1997.

M. Ito, H. Xu, A.A. Guffanti, Y. Wei, L. Zvi, D.E. Clapham, T.A. Krulwich, and H.R. Kaback. The voltage-gated na$^+$ channel na$_V$bp has a role in motility, chemotaxis, and ph homeostasis of an alkaliphilic bacillus. *PNAS*, 101:10566–10571, 2004.

S.R. Jadhav, D. Sui, R.M. Garavito, and R.M. Worden. Fabrication of highly insulating tethered bilayer lipid membrane using yeast cell membrane fractions for measuring ion channel activity. *J. Colloid Interface Sci.*, 322(2):465–472, 2008.

A. Janshoff and C. Steinem. Transport across artificial membranes - an analytical perspective. *Anal. Bioanal. Chem.*, 385:433–451, 2006.

A.T.A. Jenkins, R.J. Bushby, N. Boden, S.D. Evans, P.F. Knowles, Q. Liu, R.E. Miles, and S.D. Ogier. Ion-selective lipid bilayers tethered to microcontact printed self-assembled monolayers containing cholesterol derivatives. *Langmuir*, 14(17):4675–4678, 1998.

T-J. Jeon, N. Malmstadt, and J.J. Schmidt. Hydrogel-encapsulated lipid membranes. *J. Am. Chem. Soc.*, 128:42–43, 2005.

L. J. C. Jeuken, S. A. Weiss, P. J. F. Henderson, S. D. Evans, and R. J. Bushby. Impedance spectroscopy of bacterial membranes: Coenzyme-q diffusion in a finite diffusion layer. *Anal. Chem.*, 80(23):9084–9090, 2008.

L.J.C. Jeuken. Afm: Study on the electric-field effects on supported bilayer lipid membranes. *Biophys. J.*, 94:4711–4717, 2008.

L.J.C. Jeuken, S.D. Connell, M. Nurnabi, J. O'Reilly, P.J.F. Henderson, S.D. Evans, and R.J. Bushby. Direct electrochemical interaction between a modified gold electrode and a bacterial membrane extract. *Langmuir*, 21:1481–1488, 2005.

L.J.C. Jeuken, S.D. Connell, P.J.F. Henderson, R.B. Gennis, S.D. Evans, and R.J. Bushby. Redox enzymes in tethered membranes. *J. Am. Chem. Soc.*, 128:1711–1716, 2006.

L.J.C. Jeuken, R.J. Bushby, and S.D. Evans. Proton transport into a tethered bilayer lipid membrane. *Electrochem. Comm.*, 9:610–614, 2007a.

L.J.C. Jeuken, N.N. Daskalakis, X. Han, K. Sheikh, A. Erbe, R.J. Bushby, and S.D. Evans. Phase separation in mixed self-assembled monolayers and its effect on biomimetic membranes. *Sensors and Actuators B*, 124:501–509, 2007b.

Y. Jiang, A. Lee, J. Chen, M. Cadene, B.T. Chait, and R. MacKinnon. Crystal structure and mechanism of a calcium-gated potassium channel. *Nature*, 417:515–522, 2002.

J.B. Jorcin, M.E. Orazem, N. Pebere, and B. Tribollet. Cpe analysis by local electrochemical impedance spectroscopy. *Electrochimica Acta*, 51:1473–1479, 2006.

H. Jung, S. Tebbe, R. Schmid, and K. Jung. Unidirectional reconstitution and characterization of purified na$^+$/proline transporter of escherichia coli. *Biochemistry*, 37: 11083–11088, 1998.

S. Jung, A. Muhle, M. Schaefer, R. Strotmann, G. Schultz, and T. Plant. Lanthanides potentiate trpc5 currents by an action at extracellular sites close to the pore mouth. *J. Biol. Chem.*, 278(6):3562–3571, 2003.

A. Junghans and I. Koper. Structural analysis of tethered bilayer lipid membranes. *Langmuir*, 26:11035–11040, 2010.

X-F. Kang, S. Cheley, A.C. Rice-Ficht, and H. Bayley. A storable encapsulated bilayer chip containing a single protein nanopore. *Journal of the American Chemical Society*, 129:4701–4705, 2007.

D.S. Karpovich and G.J. Blanchard. Direct measurement of the adsorption kinetics of alkanethiolate self-assembled monolayers on a microcrystalline gold surface. *Langmuir*, 10:33153322, 1994.

H.M. Keizer, B.R. Dorvel, M. Andersson, D. Fine, R.B. Price, J.R. Long, A. Dodabalapur, I. Kper, W. Knoll, P.A. Anderson, and R.S. Duran. Functional ion channels in tethered bilayer membranes - implications for biosensors. *ChemBioChem*, 8:1246–1250, 2007.

J.K.R. Kendall, B.R.G. Johnson, P.H. Symonds, G. Imperato, R.J. Bushby, J.D. Gwyer, C. van Berkel, S.D. Evans, and L.J.C. Jeuken. Effect of the structure of cholesterol-based tethered bilayer lipid membranes on ionophore activity. *ChemPhysChem*, 11:2191–2198, 2010.

Y-T. Kim, R.L. McCarley, and A.J. Bard. *Langmuir*, 8:1941–1944, 1993.

R. Kizek, J. Vacek, L. Tmkova, and F. Jelen. Cyclic voltammetric study of the redox system of glutathione using the disulfide bond reductant tris(2-carboxyethyl)phosphine. *Bioelectrochemistry*, 63:19–24, 2004.

W. Knoll, I. Koper, R. Naumann, and E-K. Sinner. Tethered bimolecular lipid membranes - a novel model membrane platform. *Electrochimica Acta*, 53:6680–6689, 2007.

R. Koishi, H. Xu, D. Ren, B. Navarro, B.W. Spiller, Q. Shi, and D.E. Clapham. A superfamily of voltage-gated sodium channels in bacteria. *J. Biol. Chem.*, 279:9532–9538, 2004.

I. Koper. Insultating tethered bilayer lipid membranes to study membrane proteins. *Molecular BioSystems*, 3:651–657, 2007.

O. Koster, W. Schuhmann, H. Vogt, and W. Mokwa. Quality control of ultramicroelectrode arrays using cyclic voltammetry, electrochemical impedance spectroscopy and scanning electrochemical microscopy. *Sensors and Actuators B*, 76:573–581, 2001.

P.M. Kovach, W.L. Caudill, D.G. Peters, and Wightmanm R.M. Faradaic electrochemistry at microcylinder, band, and tubular band electrodes. *Journal of Electroanalytical Chemistry and Interfacial Electrochemistry*, 185:285–295, 1985.

S. Kresak, T. Hianik, and R. Naumann. Giga-seal solvent-free bilayer lipid membranes: from single nanopores to nanopore arrays. *Soft Matter*, 5:4021–4032, 2009.

T.A. Krulwich, M. Ito, and A.A. Guffanti. The na^{+}-dependence of alkaliphily in *Bacillus*. *Biochimica et Biophysica Acta (BBA) - Bioenergetics*, 1505:158–168, 2001.

B. Kumar, K. Dreja, S.S. Shah, A. Cheong, S.-Z. Xu, P. Sukumar, J. Naylor, A. Forte, M. Cipollaro, D. McHugh, P.A. Kingston, A.M. Heagerty, C.M. Munsch, A. Bergdahl, A. Hultgrdh-Nilsson, M.F. Gomez, K.E. Porter, P. Hellstrand, and D.J. Beech. Upregulated trpc1 channel in vascular injury in vivo and its role in human neointimal hyperplasia. *Circulation Research*, 98:557–563, 2006.

A. Kuzmenkin, F. Bezanilla, and A.M. Correa. Gating of the bacterial sodium channel, nachbac: Voltage-dependent charge movement and gating currents. *J. Gen. Phys.*, 124: 349–356, 2004.

P.E. Laibinis and G.M. Whitesides. Self-assembled monolayers of n-alkanethiolates on copper are barrier films that protect the metal against oxidation by air. *Journal of the American Chemical Society*, 114:9022–9028, 1992a.

P.E. Laibinis and G.M. Whitesides. ω-terminated alkanethiolate monolayers on surfaces of copper, silver and gold have similar wettabilities. *Journal of the American Chemical Society*, 114:1990–1995, 1992b.

P.E. Laibinis, C.D. Bain, and G.M. Whitesides. Attenuation of photoelectrons in monolayers of n-alkanethiols adsorbed on copper, silver, and gold. *Journal of Physical Chemistry*, 95:7017–7021, 1991a.

P.E. Laibinis, G.M. Whitesides, D.L. Allara, Y-T. Tao, A.N. Parikh, and R.G. Nuzzo. Comparison of the structures and wetting properties of self-assembled monolayers of n-alkanethiols on the coinage metal surfaces, cu, ag, au. *Journal of the American Chemical Society*, 113:7152–7167, 1991b.

Y. Lange and T.L. Steck. *Current Opinions in Structural Biology*, 88:435–439, 1998.

R. Lehrmann and J. Seelig. Adsorption of ca^{2+} and la^{3+} to bilayer membranes: measurement of the adsorption enthalpy and binding constant with titration calorimetry. *Biochimica et Biophysica Acta*, 1189:89–95, 1994.

Jay Leitch, Julia Kunze, John D. Goddard, Adrian L. Schwan, Robert J. Faragher, Renate Naumann, Wolfgang Knoll, John R. Dutcher, and Jacek Lipkowski. In situ pm-irras studies of an archaea analogue thiolipid assembled on a au(111) electrode surface. *Langmuir*, 25(17):10354–10363, 2009.

M. LeMasurier, L. Heginbotham, and C. Miller. Kcsa: It's a potassium channel. *Journal of General Physiology*, 118:303–314, 2001.

N. Levina, S. Totemeyer, N.R. Stokes, P. Louis, M.A. Jones, and I.R. Booth. *EMBO*, 18: 1730–1737, 1999.

F. Loglio, M. Schweizer, and D.M. Kolb. In situ characterization of self-assembled butanethiol monolayers on au(100) electrodes. *Langmuir*, 19:830–834, 2003.

S.B. Long, E.B. Campbell, and R. MacKinnon. Crystal structure of a mammalian voltage-dependent *Shaker* family k^+ channel. *Science*, 309:897–903, 2005a.

S.B. Long, E.B. Campbell, and R. MacKinnon. Voltage sensor of kv1.2: Structural basis of electromechanical coupling. *Science*, 309:903–908, 2005b.

S.B. Long, X. Tao, E.B. Campbell, and R. MacKinnon. Atomic structure of a voltage-dependent k^+ channel in a lipid membrane-like environment. *Nature*, 450:376–382, 2007.

J. Lopez-Barneo, T. Hoshi, S.H. Heinemann, and R.W. Aldrich. Effects of external cations and mutations in the pore region on c-type inactivation of *Shaker* potassium channels. *Receptors and Channels*, 1:61–71, 1993.

D. Losic, J.G. Shapter, and J.J. Gooding. Influence of surface topography on alkanethiol sams assembled from solution and by microcontact printing. *Langmuir*, 17:3307–3316, 2001.

J. Lummis, J. Rusconi, and S. Hornibrook, editors. *Life Science: Part 1*. Beyond-Books.com, 2005. URL `http://www.beyondbooks.com/lif71/4b.asp`.

S.N. Magonov and M-H. Whangbo. *Surface Analysis with STM and AFM: Experimental and Theoretical Aspects of Image Analysis*. VCH Verlagsgesellschaft mbH, 1996.

W.E. Martinez, G. Gregori, and T. Mates. Titanium diffusion in gold thin films. *Thin Solid Films*, 518:2585–2591, 2010.

J.C. Mathai, G.D. Sprott, and M.L. Zeidel. *Journal of Biological Chemistry*, 276:266, 2001.

D.J. McGillivray, G. Valincius, D.J. Vanderah, W. Febo-Ayala, J.T. Woodward, F. Heinrich, J.J. Kasianowicz, and M. Losche. Molecular-scale structural and functional characterization of sparsely tethered bilayer lipid membranes. *Biointerphases*, 2(1):21–33, 2007.

D.J. McGillivray, G. Valincius, F. Heinrich, J.W.F. Robertson, D.J. Vanderah, W. Febo-Ayala, J. Ignatjev, M. Losche, and J.J. Kasianowicz. Structure of functional *Staphylococcus aureus* α-hemolysin channels in tethered bilayer lipid membrane. *Biophysical Journal*, 96:1547–1553, 2009.

K. Meyer-Lipp, C. Ganea, T. Pourcher, G. Leblanc, and K. Fendler. Sugar binding induced charge translocation in the melibiose permease from escherichia coli. *Biochemistry*, 43: 12606–12613, 2004.

H. Min, J-W. Park, H.K. Shon, D.W. Moon, and T.G. Lee. Tof-sims study on the cleaning methods of au surface and their effects on the reproducibility of self-assembled monolayers. *Applied Surface Science*, 255:1025–1028, 2008.

A. Miyazawa, Y. Fujiyoshi, and N. Unwin. Structure and gating mechanism of the acetylcholine receptor pore. *Nature*, 423:949–955, 2003.

M. Montal and P. Mueller. Formation of bimolecular membranes from lipid monolayers and a study of their electrical properties. *Proc. Natl. Acad. Sci. U. S. A.*, 69(12): 3561–3566, 1972.

L. Movileanu, S. Howorka, O. Braha, and H. Bayley. Detecting protein analytes that modulate transmembrane movement of a polymer chain within a single protein pore. *Nature Biotechnology*, 18:1091–1095, 2000.

Q. Mu, N. Hondow, L. Kreminski, A. Brown, L.J.C. Jeuken, and M. Routledge. Membrane binding and non-endocytotic uptake of genotoxic silica nanoparticles. *Submitted*, 2011.

P. Mueller, D.O. Rudin, H.T. Tien, and W.C. Wescott. Reconstitution of cell membrane structure in vitro and its transformation into an excitable system. *Nature*, 194(4832): 979–980, 1962.

D.J. Muller and A. Engel. Voltage and ph-induced channel closure of porin ompf visualized by atomic force microscopy. *Journal of Molecular Biology*, 285:1347–1351, 1998.

U. Muller and K. Hartung. Properties of three different ion channels in the plasma membrane of the slime mold *Dictyostelium discoideum. Biochimica et Biophysica Acta*, 1026: 204–212, 1990.

M. Murata, J. Peranen, R. Schreiner, F. Wieland, T.V. Kurzchalia, and K. Simons. *Proceedings of the National Academy of Sciences USA*, 92:10339–10343, 1995.

B. Muskal, I. Turyan, A. Shurky, and D. Mandler. *Journal of the American Chemical Society*, 117:1147, 1995.

G. Nagel, T. Szellas, S. Kateriya, P. Hegemann, and E. Bamberg. Channelrhodopsins: directly light-gated cation channels. *Biochemical Society Transactions*, 33:863–866, 2005.

R. Naumann, S.M. Schiller, F. Giess, B. Grohe, K.B. Hartman, I. Krcher, I. Kper, J. Lbben, K. Vasilev, and W. Knoll. Tethered lipid bilayers on ultraflat gold surfaces. *Langmuir*, 19:5435–5443, 2003a.

R. Naumann, D. Walz, S.M. Schiller, and W. Knoll. Kinetics of valinomycin-mediated k^+ ion transport through tethered bilayer lipid membranes. *J. Electroanal. Chem.*, 550-551: 241–252, 2003b.

A. Negoda, E. Negoda, M. Xian, and R.N. Reusch. Role of polyphosphate in regulation of the *Streptomyces lividans* kcsa channel. *Biochimica et Biophysica Acta*, 1788:608–614, 2009.

A. Nelson. Conducting gramicidin channel activity in phospholipid monolayers. *Biophys. J.*, 80(6):2694–2703, 2001.

L.J. Nunez-Vergara, S. Bollo, J. Fuentealba, J.C. Sturm, and J.A. Squella. Electrochemical and spectroelectrochemical behaviour of the main photodegradation product of nifedipine: The nitrosopyridine derivative. *Pharmaceutical Research*, 19:522–529, 2002.

G. Nurani, M. Radford, K. Charalambous, A.O. O'Reilly, N.B. Cronin, S. Haque, and B.A. Wallace. Tetrameric bacterial sodium channels: Characterization of structure, stability, and drug binding. *Biochemistry*, 47:8114–8121, 2008.

R.G. Nuzzo and D.L. Allara. Adsorption of bifunctional organic disulfides on gold surfaces. *J. Am. Chem. Soc.*, 105(13):4481–4483, 1983.

A.M. O'Connell, R.E. Koeppe, and O.S. Andersen. Kinetics of gramicidin channel formation in lipid bilayers: Transmembrane monomer association. *Science*, 250(4985):1256–9, 1990.

S.J. Opella, F.M. Marassi, J.J. Gesell, A.P. Valente, Y. Kim, M. Oblatt-Montal, and M. Montal. Structures of the m2 channel-lining segments from nicotinic acetylcholine and nmda receptors by nmr spectroscopy. *Nature Structural Biology*, 6, 1999.

T.F. Osborne and J.M. Rosenfeld. *Current Opinions in Lipidology*, 9:137–140, 1998.

A. Ottova-Leitmannova and H.T. Tien. Bilayer lipid membranes: An experimental system for biomolecular electronic devices development. *Progress in Surface Science*, 41(4):337–434, 1992.

W. Ouyang, T-Y. Jih, T-T. Zhang, A.M. Correa, and H.C. Hemmings Jr. Isoflurane inhibits nachbac, a prokaryotic voltage-gated sodium channel. *Journal of Pharmacology and Experimental Thermapeutics*, 322:1076–1083, 2007.

J.P. Overington, B. Al-Lazikani, and A.L. Hopkins. How many drug targets are there? *Nature Reviews*, 5:993–996, 2006.

W. Pan, C. J. Durning, and N. J. Turro. Kinetics of alkanethiol adsorption on gold. *Langmuir*, 12:4469–4473, 1996.

A. Papanikolaou, A. Papafotika, C. Murphy, T. Papamarcaki, O. Tsolas, M. Drab, T.V. Kurzchalia, M. Kasper, and S. Christoforidis. *Journal of Biological Chemistry*, 280: 26406, 2005.

L.V. Parfenova, B.M. Crane, and B.S. Rothberg. Modulation of mthk potassium channel activity at the intracellular entrance to the pore. *Journal of Biological Chemistry*, 281: 21131–21138, 2006.

V.A. Parsegian. *Annals of the New York Academy of Science*, 264:161, 1975.

J. Payandeh, T. Scheuer, N. Zheng, and W.A. Catterall. The crystal structure of a voltage-gated sodium channel. *Nature*, 475:353–359, 2011.

C. Pennetta, V. Akimov, E. Alfinito, L. Reggiani, T. Gorojankina, J. Minic, E. Pajot-Augy, M-A. Persuy, R. Salesse, I. Casuso, G. Errachid, A. andl Gomila, O. Ruiz, J. Samitier, Y. Hou, G. Jaffrezic, N. Ferrari, L. Fumagalli, and M. Sampietro. Towards the realization of nanobiosensors based on g-protein-coupled receptors. In C. Kumar, editor, *Nanodevices for the Life Sciences*, Nanotechnology for the Life Sciences, pages 217–240. Wiley-VCH Verlag GmbH & Co. KGaA, Weinheim, 1st edition, 2006.

G. Perez, A. Lagrutta, J.P. Adelman, and L. Toro. *Biophysical Journal*, 66:1022–1027, 1994.

K.A. Peterlinz and R. Georgiadis. *Langmuir*, 12:4731–4740, 1996.

R.J. Petrie, P.P. Schnetkamp, K.D. Patel, M. Awasthi-Kalia, and J.P. Deans. *Journal of Immunology*, 165:1220, 2000.

K. Picas, M.T. Montero, A. Morros, M.E. Cabana, B. Seantier, P-E. Milhiet, and J. Hernandez-Borell. Calcium-induced formation of subdomains in phosphatidylethanolamine/phosphatidylglycerol bilayers: A combined dsc, 31p nmr, and afm study. *Journal of Physical Chemistry B*, 113:4648–4655, 2009.

J. Pintschovius and K. Fendler. Charge translocation by the na$^+$/k$^+$-atpase investigated on solid supported membranes: cytoplasmic cation binding and release. *Biophysical Journal*, 76:814–826, 1999.

A.L. Plant. Self-assembled phospholipid/alkanethiol biomimetic bilayers on gold. *Langmuir*, 9(11):2764–2767, 1993.

R. Pomes and B. Roux. Structure and dynamics of a proton wire: A theoretical study of h$^+$ translocation along the single-file water chain in the gramicidin a channel. *Biophys. J.*, 71:19–39, 1996.

R. Pomes and B. Roux. Molecular mechanism of h$^+$ conduction in the single-file water chain of the gramicidin channel. *Biophys. J.*, 82(5):2304–2316, 2002.

J.A. Porter, K.E. Young, and P.A. Beachy. *Science*, 274:255–259, 1996.

H.J. Pownall, Q. Pao, H.L. Brockman, and J.B. Massey. Inhibition of lecithin-cholesterol acyltransferase by diphytanoyl phosphatidylcholine. *J. Biol. Chem.*, 262(19):9033–9036, 1987.

A. Pullman. Contribution of theoretical chemistry to the study of ion transport through membranes. *Chem. Rev.*, 91:793–812, 1991.

S. Ramanathan, W. Shi, B.P. Rosen, and S. Daunert. *Analytical Chemistry*, 69:3380, 1997.

I.S. Ramsey, M.M. Moran, J.A. Chong, and D.E. Clapham. A voltage-gated proton-selective channel lacking the pore domain. *Nature*, 440:1213–1216, 2006.

S. Raunser, M. Appel, C. Ganea, U. Geldmacher-Kaufer, K. Fendler, and W. Kuhlbrandt. Structure and function of prokaryotic glutamate transporters from *Escherichia coli* and *Pyrococcus horikoshii*. *Biochemistry*, 45:12796–12805, 2006.

P. Reisberg. *Membrane Transport*, volume 2008. Wellesley College, 01/04/1999 1999.

D. Ren, B. Navarro, H. Xu, L. Yue, Q. Shi, and D.E. Clapham. A prokaryotic voltage-gated sodium channel. *Science*, 294:2372–2375, 2001.

A. Riccio, A.D. Medhurst, C. Mattei, R.E. Kelsell, A.R. Calver, A.D. Randall, C.D. Benham, and M.N. Pangalos. mrna distribution analysis of human trpc family in cns and peripheral tissues. *Brain Research and Molecular Brain Research*, 109:95–104, 2002.

F.F. Roberto, J.M. Barnes, and D.F. Bruhn. Evaluation of a gfp reporter gene construct for environmental arsenic detection. *Talanta*, 58:181–188, 2002.

H. Ron and I. Rubinstein. Alkanethiol monolayers on preoxidized gold. encapsulation of gold oxide under an organic monolayer. *Langmuir*, 10:4566–4573, 1994.

H. Ron and I. Rubinstein. Self-assembled monolayers on oxidized metals. 3. alkylthiol and diakyl disulfide assembly on gold under electrochemical conditions. *J. Am. Chem. Soc.*, 120:13444–13452, 1998.

H. Ron, S. Matlis, and I. Rubinstein. Self-assembled monolayers on oxidized metals. 2. gold surface oxidative pretreatment, monolayer properties, and depression formation. *Langmuir*, 14:1116–1121, 1998.

L. Rose and A.T.A. Jenkins. The effect of the ionophore valinomycin on biomimetic solid supported lipid dppte/epc membranes. *Bioelectrochemistry*, 70:387–393, 2007.

T.K. Rostovtseva, V.M. Aguilella, I. Vodyanoy, S.M. Bezrukov, and V.A. Parsegian. *Biophysical Journal*, 75:1783–1792, 1998.

J.E. Rothman and D.M. Engelman. Molecular mechanism for interaction of phospholipid with cholesterol. *Nature - New Biology*, 237(71):42–4, 1972.

B. Roux. Valence selectivity of the gramicidin channel: A molecular dynamics free energy perturbation stud. *Biophysical Journal*, 71:3177–3185, 1996.

B. Roux and Mac. The cavity and pore helices in the kcsa k+ channel: electrostatic stabilization of monovalent cations. *Science*, 285:100–102, 1999.

M. Rueda, I. Navarro, G. Ramirez, R.F. Prieto, C. Prado, and A. Nelson. Electrochemical impedance study of tl$^+$ reduction through gramicidin channels in self-assembled gramicidin-modified dioleoylphosphatidylcholine monolayers on mercury electrodes. *Langmuir*, 15:3672–3678, 1999.

M.J. Russo, H. Bayley, and M. Toner. Reversible permeabilization of plasma membranes with an engineered switchable pore. *Nature Biotechnology*, 15:278–282, 1997.

T. Saji, T. Yamada, and S. Aoyagui. Electron-transfer rate constants for redox systems of fe(iii)/fe(ii) complexes with 2,2'-bipyridine and/or cyanide ion as measured by the galvanostatic double pulse method. *Electroanalytical Chemistry and Interfacial Electrochemistry*, 61:147–153, 1975.

J.S. Santos, A. Lundby, C. Zazueta, and M. Montal. Molecular template for a voltage sensor in a novel k$^+$ channel. i. identification and functional characterization of kvlm, a voltage-gated k$^+$ channel from *Listeria monocytogenes. Journal of General Physiology*, 128:283–292, 2006.

M. Sasaki, M. Takagi, and Y. Okamura. A voltage sensor-domain protein is a voltage-gated proton channel. *Science*, 312:589–592, 2006.

R.B.M. Schasfoort and A.J. Tudos. *Handbook of Surface Plasmon Resonance*. The Royal Society of Chemistry, 2008.

S.M. Schiller, R. Naumann, K. Lovejoy, H. Kunz, and W. Knoll. Archaea analogue thiolipids for tethered bilayer lipid membranes on ultrasmooth gold surfaces. *Angew. Chem. Int. Ed.*, 42(2):208–211, 2003.

E.K. Schmitt, M. Nurnabi, R.J. Bushby, and C. Steinem. Electrically insulating pore-suspending membranes on highly ordered porous alumina obtained from vesicle spreading. *Soft Matter*, 4:250–253, 2008.

T.W. Schneider and D.A. Buttry. *Journal of the American Chemical Society*, 115:12391–12397, 1993.

M.H. Schoenfisch and J.E. Pemberton. Air stability of alkanethiol self-assembled monolayers on silver and gold surfaces. *Journal of the American Chemical Society*, 120: 4502–4513, 1998.

H. Schrempf, O. Schmidt, R. Kummerien, S. Hinnah, D. Muller, M. Betzler, T. Steinkamp, and R. Wagner. A prokaryotic potassium ion channel with two predicted transmembrane segments from *Streptomyces lividans*. *The EMBO Journal*, 14:5170–5178, 1995.

P. Schulz, J.J. Garcia-Celma, and K. Fendler. Ssm-based electrophysiology. *Methods*, 46: 97–103, 2008.

P. Schulz, B. Dueck, A. Mourot, L. Hatahet, and K. Fendler. Measuring ion channels on solid supported membranes. *Biophysical Journal*, 97:388–396, 2009.

D.K. Schwartz. Mechanisms and kinetics of self-assembled monolayer formation. *Annual Review of Physical Chemistry*, 52:107–137, 2001.

J. Seelig, R. Lehrmann, and E. Terzi. Domain formation induced by lipid-ion and lipid-peptide interactions. *Molecular Membrane Biology*, 12:51–57, 1995.

H. Sellers, A Ulman, Y. Shnidman, and J.E. Eilers. Structure and binding of alkanethiolates on gold and silver surfaces: implications for self-assembled monolayers. *Journal of the American Chemical Society*, 115:9389–9401, 1993.

F. Sesti, S. Rajan, R. Gonzalaz-Colaso, N. Nikolaeva, and S.A. Goldstein. Hyperpolarization moves s4 sensors inward to open mvp, a methanococcal voltage-gated potassium channel. *Nature Neuroscience*, 6:353–361, 2003.

K. Shimazu, I. Yagi, Y. Sato, and K. Uosaki. *Langmuir*, 8:1385–1387, 1992.

K. Shimazu, Y. Sato, I. Yagi, and K. Uosaki. Packing state and stability of self-assembled monolayers of 11-ferrocenyl-1-undecanethiol on platinum electrodes. *Bulletin of the Chemical Society of Japan*, 67:863–865, 1994.

G.B. Sigal, M. Mrksich, and G.M. Whitesides. Using surface plasmon resonance spectroscopy to measure the association of detergents with self-assembled monolayers of hexadecanethiolate on gold. *Langmuir*, 13:2749–2755, 1997.

T. Simonson and C.L. Brooks III. Charge screening and the dieletric constant of proteins: Insights from molecular dynamics. *Journal of the American Chemical Society*, 118: 8452–8458, 1996.

S.J. Singer and G.L Nicolson. The fluid mosaic model of the structure of cell membranes. *Science*, 175:72031, 1972.

E.K. Sinner and W. Knoll. Functional tethered membranes. *Curr. Opin. Chem. Biol.*, 5: 705–711, 2001.

A.B. Steel, T.M. Herne, and M.J. Tarlov. Electrochemical quantitation of dna immobilized on gold. *Analytical Chemistry*, 70:4670–4677, 1998.

C. Steinem, A. Janshoff, W. Ulrich, M. Sieber, and H. Galla. Impedance analysis of supported lipid bilayer membranes: A scrutiny of different preparation techniques. *Biochim. Biophys. Acta*, 1279:169–180, 1996.

O. Stern. The theory of electrolytic double shift. *Zeitschrift fur Elektrochemie un Angewandte Physikalische Chemie*, 30:508–516, 1924.

J. Stettner and A. Winkler. Characterization of alkanethiol self-assembled monolayers on gold by thermal desorption spectroscopy. *Langmuir*, 26:9659–9665, 2010.

T. Stora, J.H. Lakey, and H. Vogel. Ion-channel gating in transmembrane receptor proteins: Functional activity in tethered lipid membranes. *Angewandte Chemie International Edition*, 38:389–392, 1999.

M. Stratmann. *Advanced Materials*, 2:191, 1990.

H. Strosnider. Whole-cell bacterial biosensors and the detection of bioavailable arsenic. Technical report, U.S. Environmental Protection Agency, 2003.

A. Studer, S. Demarche, D. Langenegger, and L. Tiefenauer. Integration and recording of a reconstituted voltage-gated sodium channel in planar lipid bilayers. *Biosensors and Bioelectronics*, 26:1924–1928, 2011.

W.K. Subczynski, A. Wisniewska, J.-J. Yin, J.S Hyde, and A. Kusumi. Hydrophobic barriers of lipid bilayer membranes formed by reduction of water penetration by alkyl chain unsaturation and cholesterol. *Biochem.*, 33:7670–7681, 1994.

R. Subramanian and V. Lakshminarayanan. A study of kinetics of adsorption of alkanethiols on gold using electrochemical impedance spectroscopy. *Electrochim. Acta*, 45: 4501–4509, 2000.

L. Sun and R.M. Crooks. *Journal of the Electrochemical Society*, 138:L23–25, 1991.

M.M. Sung, K. Sung, C.G. Kim, S.S. Lee, and Y. Kim. Self-assembled monolayers of alkanethiols on oxidized copper surfaces. *Journal of Physical Chemistry B*, 104:2273–2277, 2000.

F. Tadini-Buoninsegni, G. Bartolommei, M.R. Moncelli, R. Guidelli, and G. Inesi. Pre-steady state electrogenic events of ca^{2+}/h^{+} exchange and transport by the ca^{2+}-atpase. *Journal of Biological Chemistry*, 281:37720–37727, 2006.

M. Tanaka and E. Sackmann. Supported membranes as biofunctional interfaces and smart biosensor platforms. *Physica Status Solidi (a)*, 203(14):3452–3462, 2006.

T. Tanaka, S.J. Li, K. Kinoshita, and M. Yamazaki. La^{3+} stabilizes the hexagonal ii (hii) phase in phosphatidylethanolamine membranes. *Biochim. Biophys. Acta*, 1515:189–201, 2001.

Y.T. Tao. Structural comparison of self-assembled monolayers of n-alkanoic acids on the surfaces of silver, copper, and aluminum. *Journal of the American Chemical Society*, 115:4350–4358, 1993.

S. Tauriainen, M. Karp, W. Chang, and M. Virta. *Applied Environmental Microbiology*, 63:4456, 1997.

S. Terrettaz and H. Vogel. Investigating the function of ion channels in tethered lipid membranes by impedance spectroscopy. *MRS Bulletin*, 30:207–210, 2005.

S. Terrettaz, M. Mayer, and H. Vogel. Highly electrically insulating tethered lipid bilayers for probing the function of ion channel proteins. *Langmuir*, 19:5567–5569, 2003.

H.T. Tien and A. Ottova-Leitmannova. *Membrane Biophysics as Viewed from Experimental Bilayer Lipid Membranes (Planar Lipid Bilayers and Spherical Liposomes).* Membrane Science and Technology. Elsevier, Amsterdam, 2000.

S. Tsuneda, T. Ishida, N. Nishida, M. Hara, H. Sasabe, and W. Knoll. Tailoring of a smooth polycrystalline gold surface as a suitable anchoring site for a self-assembled monolayer. *Thin Solid Films*, 339:142–147, 1999.

A. Ulman. Formation and structure of self-assembled monolayers. *Chemical Reviews*, 96: 1533–1554, 1996.

N. Unwin. Refined structure of the nicotinic acetylcholine receptor at 4 å resolution. *Journal of Molecular Biology*, 346:967–989, 2005.

A.E. Vallejo and C.A. Gervasi. Eis studies of valinomycin-mediated k^+ transport through supported lipid bilayers. *J. Electroanal. Chem.*, 603:51–58, 2007.

I.K. Vockenroth, P.P. Atanasova, J.R. Long, A.T.A. Jenkins, W. Knoll, and I. Koper. Functional incorporation of the pore forming segment of achr m2 into tethered bilayer lipid membranes. *Biochim. Biophys. Acta*, 1768:1114–1120, 2007.

I.K. Vockenroth, P.P. Atanasova, A.T.A. Jenkins, and I. Koper. Incorporation of α-hemolysin in different tethered bilayer lipid membrane architectures. *Langmuir*, 24: 496–502, 2008a.

I.K. Vockenroth, D. Fine, A. Dodobalapur, A.T.A. Jenkins, and I. Koper. Tethered bilayer lipid membranes with giga-ohm resistances. *Electrochem. Comm.*, 10:323–328, 2008b.

I.K. Vockenroth, C. Ohm, J.W.F Robertson, D.J. McGillivray, M. Losche, and I. Koper. Stable insulating tethered bilayer lipid membranes. *Biointerphases*, 3(2):FA68–73, 2008c.

T. Voets, K. Talavera, G. Owsianik, and B. Nilius. Sensing with trp channels. *Nat. Chem. Bio.*, 1(2):85–92, 2005.

M. Volmer, M. Stratmann, and H. Viefhaus. *Surface and Interface Analysis*, 16:278, 1990.

P. Wagner, M. Henger, H-J. Guntherodt, and G. Semenza. Formation of in situ modification of monolayers chemisorbed on ultraflat template-stripped gold surfaces. *Langmuir*, 11:3867–3875, 1995.

M.M. Walczak, C. Chung, S.M. Stole, C.A. Widrig, and M.D. Porter. Structure and interfacial properties of spontaneously adsorbed n-alkanethiolate monolayers on evaporated silver surfaces. *Journal of the American Chemical Society*, 113:2370–2378, 1991.

M.M. Walczak, C.A. Alves, B.D. Lamp, and M.D. Porter. Electrochemical and x-ray photoelectron spectroscopic evidence for differences in the binding sites of alkanethiolate monolayers chemisorbed on gold. *Journal of Electroanalytical Chemistry*, 396:103–114, 1995.

B. Walker, J. Kasianowicz, M. Krishnasastry, and H. Bayley. A pore-forming proteins with a metal-actuated switch. *Protein Engineering Design & Selection*, 7:655–662, 1994.

S. Wang, D. Du, and X. Xu. Self-assembly of metalloporphyrin-l-cysteine modified gold electrode. *Journal of Applied Electrochemistry*, 34:495–500, 2004.

J.F. Watts and J. Wolstenholme. *An Introduction to Surface Analysis by XPS and AES*. Wiley, 2003.

S. A. Weiss, S. D. Evans, R. Bushby, P. J. F. Henderson, and L. J. C. Jeuken. Characterisation of ubiquinol oxidase activity in a native-like membrane using voltammetry. In *15th European Bioenergetic Conference*, pages S67–S67, Dublin, IRELAND, 2008. Elsevier Science Bv.

S. A. Weiss, R. J. Bushby, S. D. Evans, P. J. F. Henderson, and L. J. C. Jeuken. Characterization of cytochrome bo(3) activity in a native-like surface-tethered membrane. *Biochem. J.*, 417:555–560, 2009.

D. Weitz, D. Harder, F. Casagrande, D. Fotiadis, P. Obrdlik, B. Kelety, and H. Daniel. Functional and structural characterization of a prokaryotic peptide transporter with features similar to mammalian pept1. *Journal of Biological Chemistry*, 282:28322839, 2007.

C.A. Widrig, C. Chung, and M.D. Porter. The electrochemical desorption of n-alkanethiol monolayers from polycrystalline au and ag electrodes. *Journal of Electroanalytical Chemistry*, 310:335–359, 1991.

L.M. Williams, S. D. Evans, T.M. Flynn, A. Marsh, P.F. Knowles, R. Bushby, and N. Boden. Kinetics of the unrolling of small unilamellar phospholipid vesicles onto self-assembled monolayers. *Langmuir*, 13(4):751–757, 1997.

P.M. Williams, A. Moore, M.M. Stevens, S. Allen, M.C. Davies, C.J. Roberts, and S.J.B. Tendler. On the dynamic behaviour of the forced dissociation of ligand-receptor pairs. *Journal of the Chemical Society - Perkin Transactions*, 2:5–8, 2000.

M. Wittkampf, K. Cammann, M. Amrein, and R. Reichelt. Characterization of microelectrode arrays by means of electrochemical and surface analysis methods. *Sensors and Actuators B*, 40:79–84, 1997.

H-C. Wu, Y. Astier, G. Maglia, E. Mikhailova, and H. Bayley. Protein nanopores with covalently attached molecular adapters. *Journal of the American Chemical Society*, 129: 16142–16148, 2007.

S-Z. Xu, P. Sukumar, and F.et al Zeng. Trpc channel activation by extracellular thioredoxin. *Nature*, 451:69–73, 2008.

S.Z. Xu, F. Zeng, G. Boulay, C. Grimm, C. Harteneck, and D.J. Beech. Block of trpc5 channels by 2-aminoethoxydiphenyl borate: a differential, extracellular and voltage-dependent effect. *British Journal of Pharmacology*, 145:320–328, 2005.

S.Z. Xu, K. Muraki, F. Zeng, J. Li, P. Sukumar, S. Shah, A.M. Dedman, P.K. Flemming, D. McHugh, J. Naylor, A. Cheong, A.N. Bateson, C.M. Munsch, K.E. Porter, and D.J. Beech. A sphingosine-1-phosphate-activated calcium channel controlling vascular smooth muscle cell motility. *Circulation Research*, 98:1381–1389, 2006.

K. Yamauchi, K. Doi, Y. Yoshida, and M. Kinoshita. Archaebacterial lipids: highly proton-impermeable membranes from 1,2-diphytanyl-*sn*-glycero-3-phosphocholine. *Biochimica et Biophysica Acta*, 1146:178–182, 1993.

C. Yang, D. Rairight, and A. Mason. On-chip electrochemical impedance spectroscopy for biosensor arrays. In *IEEE Sensors 2006*, EXCO, Daegu, Korea, 2006.

P.L. Yeagle. *Advances in Cholesterol Research*, pages 114–116. Telford Press, Caldwell, NJ, 1990.

P.L. Yeagle. *Biochemie*, 73:1303–1310, 1991.

T. Yorimitsu and M. Homma. Na^+-driven flagella motor of vibrio. *Biochimica et Biophysica Acta (BBA) - Bioenergetics*, 1505:82–93, 2001.

L. Yue, B. Navarro, D. Ren, A. Ramos, and D. Clapham. The cation selectivity filter of the bacterial sodium channel, nachbac. *J. Gen. Physiol.*, 120:845–853, 2002.

B. Zadek and C.M. Nimigean. Calcium-dependent gating of mthk, a prokaryotic potassium channel. *Journal of General Physiology*, 127:673–685, 2006.

M. Zagnoni, M.E. Sandison, P. Marius, A.G. Lee, and H. Morgan. Controlled delivery of proteins into bilayer lipid membranes on chip. *Lab on a Chip*, 7:1176–1183, 2007.

E. Zakharian and R.N. Reusch. *Streptomyces lividans* potassium channel kcsa is regulated by the potassium electrochemical gradient. *Biochemical and Biophysical Research Communications*, 316:429–436, 2004.

F. Zeng, S-Z. Xu, P.K. Jackson, D. McHugh, B. Kumar, S.J. Fountain, and D.J. Beech. Human trpc5 channel activated by a multiplicity of signals in a single cell. *J Physiol*, 559(3):739–750, 2004.

L. Zhang, C. Booth, and P. Stroeve. Phosphatidylserine/cholesterol bilayers supported on a polycation/alkylthiol layer pair. *J. Colloid Interface Sci.*, 228:82–89, 2000.

X.-M. Zhao, J.L. Wilbur, and G.M. Whitesides. Using two-stage chemical amplification to determine the density of defects in self-assembled monolayers of alkanethiolates on gold. *Langmuir*, 12:3257–3264, 1996.

A. Zhou, A. Wozniak, K. Meyer-Lipp, M. Nietschke, H. Jung, and K. Fendler. Charge translocation during cosubstrate binding in the na$^+$/proline transporter of e. coli. *Journal of Membrane Biology*, 343:931–942, 2004.

J. Zhou, K. Ren, Y. Zheng, J. Su, Y. Zhao, D. Ryan, and H. Wu. Fabrication of a microfluidic ag/agcl reference electrode and its application for portable and disposable electrochemical microchips. *Electrophoresis*, 31:3083–3089, 2010.

D. Zuber, R. Krause, M. Venturi, E. Padan, E. Bamberg, and K. Fendler. Kinetics of charge translocation in the passive downhill uptake mode of the na$^+$/h$^+$ antiporter nhaa of escherichia coli. *Biochimica et Biophysica Acta*, 1709:240–250, 2005.

Appendix A

Philips Research Electrode Designs

A.1 Series 1 electrodes (P1)

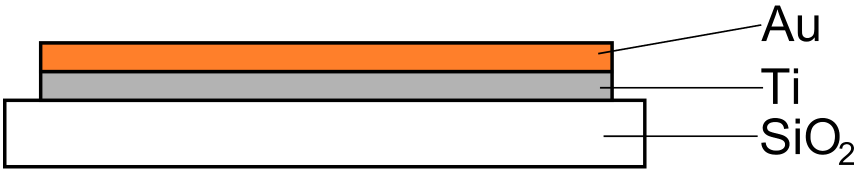

Figure A.1: Schematic of layers in series 1 (P1) electrodes. Glass substrate was 750 μm thick. Ti adhesion layer was 20 nm thick. Au layer was 200 nm thick.

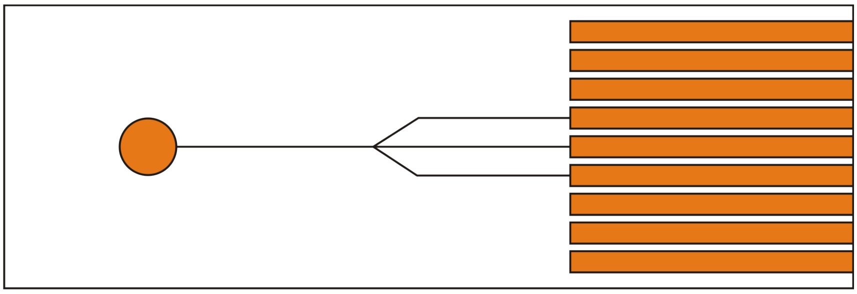

Figure A.2: Schematic layout of P1A electrodes

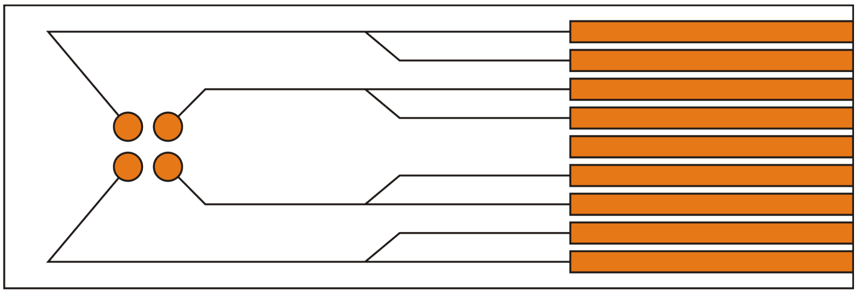

Figure A.3: Schematic layout of P1B electrodes

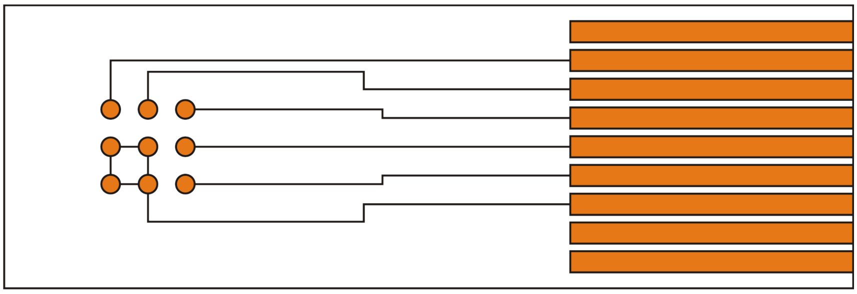

Figure A.4: Schematic layout of P1C electrodes

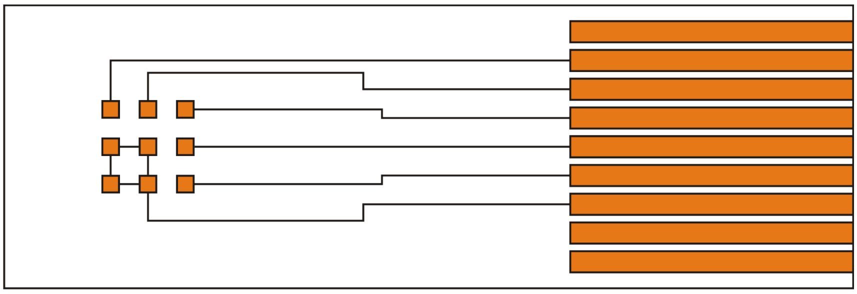

Figure A.5: Schematic layout of P1D electrodes

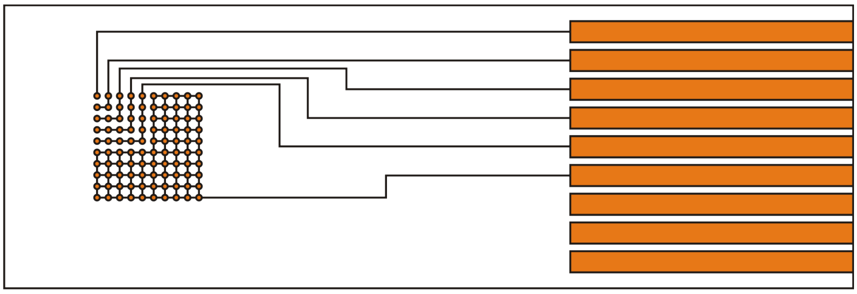

Figure A.6: Schematic layout of P1E electrodes

A.2 Series 2 electrodes (P2)

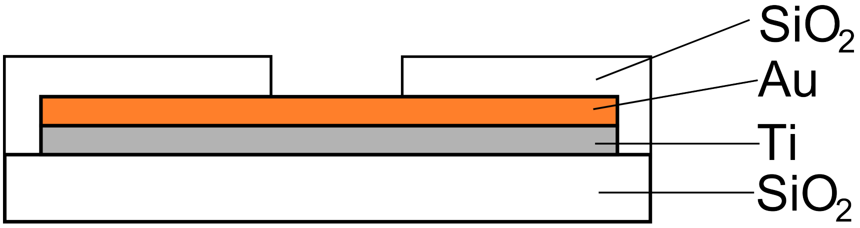

Figure A.7: Schematic of layers in first iteration of series 2 (P2) electrodes. Glass substrate was 750 μm thick. Ti adhesion layer was 20 nm thick. Au layer was 200 nm thick. Insulating SiO_2 layer was 500 nm thick.

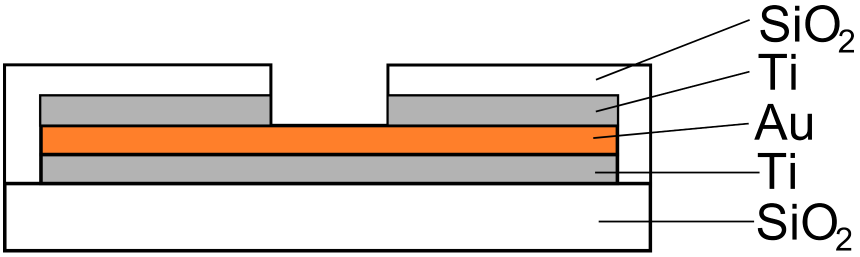

Figure A.8: Schematic of layers in second iteration of series 2 (P2) electrodes. Glass substrate was 750 μm thick. Ti adhesion layer was 20 nm thick. Au layer was 200 nm thick. Ti adhesion layer was 20 nm thick. Insulating SiO_2 layer was 500 nm thick.

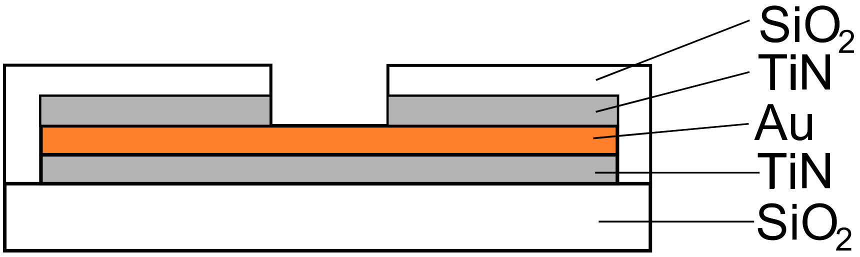

Figure A.9: Schematic of layers in second iteration of series 2 (P2) electrodes. Glass substrate was 750 μm thick. TiN adhesion layer was 20 nm thick. Au layer was 200 nm thick. TiN adhesion layer was 20 nm thick. Insulating SiO_2 layer was 500 nm thick.

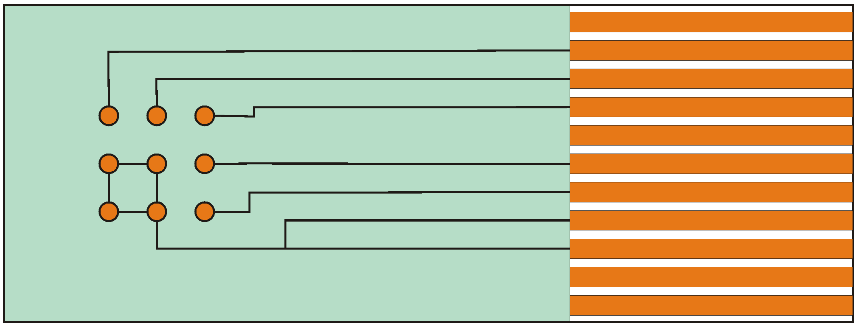

Figure A.10: Schematic layout of P2C electrodes

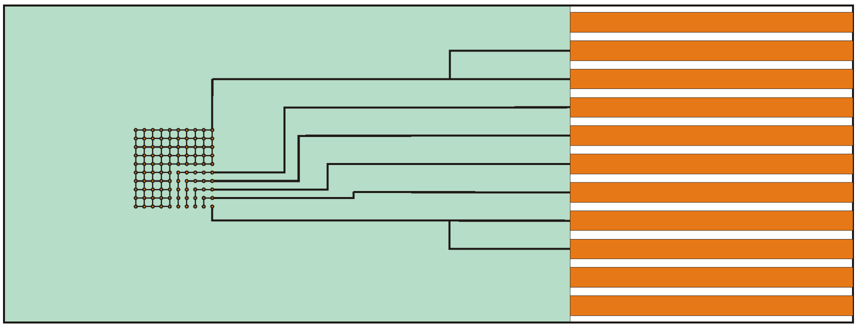

Figure A.11: Schematic layout of P2E electrodes

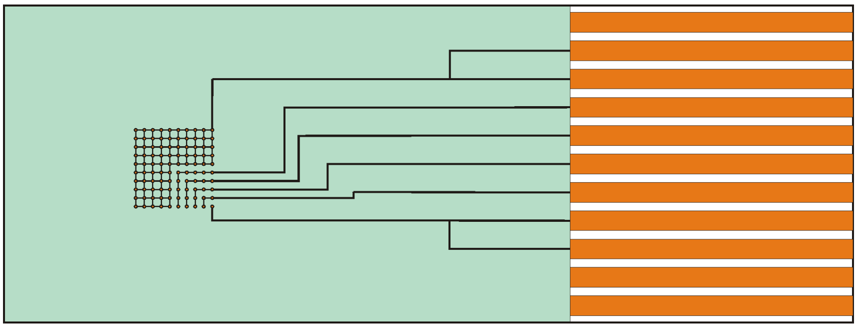

Figure A.12: Schematic layout of P2F electrodes

Appendix B

Effect of HF on Removal of Ti Layer Present on P2 MKII Electrodes

Identification of a TiO_2 layer on the surface of P2 MKII electrodes led to attempts to remove the layer.

Fuming nitric acid (FNA) was used to remove organic material, followed by a Ti etch (7 H_2O : 2 FNA : 1 HF) heated to 48 °C for a several seconds. This mix was significantly more concentrated than that used originally in post-processing of the electrodes (165 H_2O : 5 FNA : 1HF).

B.1 EIS

The ability of ODT SAMs to form on the cleaned electrodes was investigated with EIS to check for any improvement in the surface conditions.

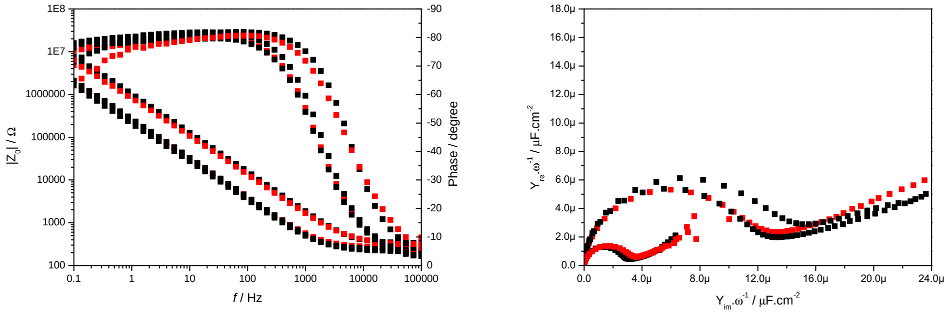

(a) ODT - Bode Plot

(b) ODT - Normalised Admittance Plot

Figure B.1: EIS of ODT SAMs formed on P2 MKII electrodes following Ti etching. Large variability between samples and v high capacitances suggests that SAMs are still unable to form to a sufficient standard. Black = P2MKII C; Red = P2MKII E.

As can be seen from Figure B.1b, the SAM capacitance is still highly variable averaging 7.79 ± 2.11 μF.cm^{-2}. However, whereas in Figure 3.16b the SAM capacitances are all different, in Figure B.1b the SAM capacitances converge into two groups of 2.67 ± 0.08 μF.cm^{-2} or 11.21 ± 0.51 μF.cm^{-2}. While two different electrode designs, C and E, were used in the experiments, their use does not correlate with the division of results as can be seen by the distribution of the black (C-type) and red (E-type) plots in Figure B.1b. There is no significant difference between Figures 3.16a and B.1a. Phase shift remains in the region of -80°and SAM resistances are similar.

While the division in the results is clear, the cause for it is not. Widespread TiO_2 deposition would be expected to give unordered capacitances such as those in Figure 3.16b. If the Ti etch has had a significant effect on the surface chemistry, it could be expected to be more systematic in nature bringing all the capacitances within a single range. Investigating the surface further with XPS and SAES may highlight factors that lead to this effect.

B.2 Electron Spectroscopy

The Ti etch cleaned electrodes were further examined by XPS and scanning Auger electron spectroscopy to check for alterations in the chemical composition of the electrode surface.

Au 4f peaks in Figure B.2b at 87.7 eV and 84.0 eV correspond to the $4f_{5/2}$ and 4f7/2 transitions of Au. The lack of a peak at 85.9 eV suggests that there are no, or very limited, Au oxides present on the surface. Figure B.2c presents a complex O 1s peak that has been deconvoluted, using peak fitting software, and determined to be comprised of 3 peaks at 530.0 eV, 531.4 eV and 532.5 eV. The peak at 530.0 eV is most likely the O 1s transition of TiO_2 and the peak at 532.5 eV corresponds well to the O 1s transition of SiO_2, whilst the peak at 531.4 eV is unidentified. The TiO_2 and SiO_2 peaks were present prior to the Ti etch in Figure 3.20c, however the unidentified peak at 531.4 eV was not. This may be a fitting artifact, or could be attributed to a surface contaminant brought about by the Ti etching process. Figure B.2d has two peaks at 459.1 eV and 465.0 eV, which correspond to the Ti $2p_{3/2}$ and Ti $2p_{1/2}$ transitions respectively. Small hump can be seen around 472.6 eV, however there are no transitions in this region that would make sense to assign it as a peak. Somewhat unexpectedly, a pair of significant peaks were observed at 374.2 eV and 368.2 eV (Figure B.2a). The 374.2 eV peak corresponds to the $3d_{3/2}$ transition of Ag in Ag_2O, while the 368.2 eV peak can be attributed to the $3d_{5/2}$ transition of Ag in either Ag_2O, AgO or metallic Ag. The presence of these peaks, which were not previously observed, are most likely due to a source of contamination during the Ti etch phase.

The ratio of the major peaks can be seen in Table B.1. The high proportion of Ti 2p counts in comparison to Au 4f counts suggests that despite the Ti etch procedure significant levels of Ti contamination remain. The very high proportion of O 1s counts is due to the contributions from TiO_2 and SiO_2. The low proportion of Ag 3d suggests

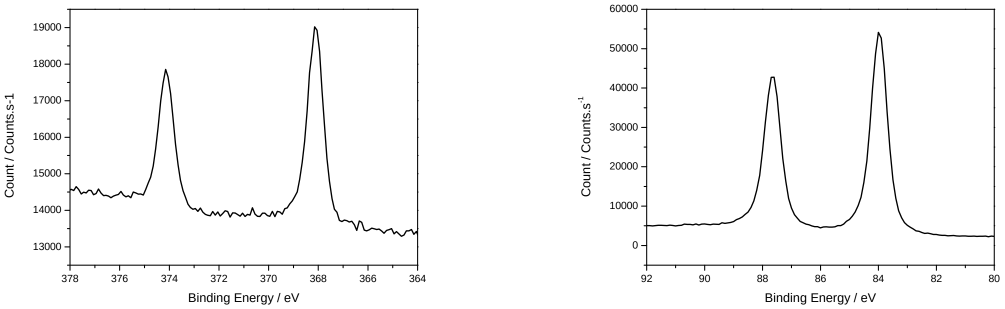

(a) Ag 3d

(b) Au 4f

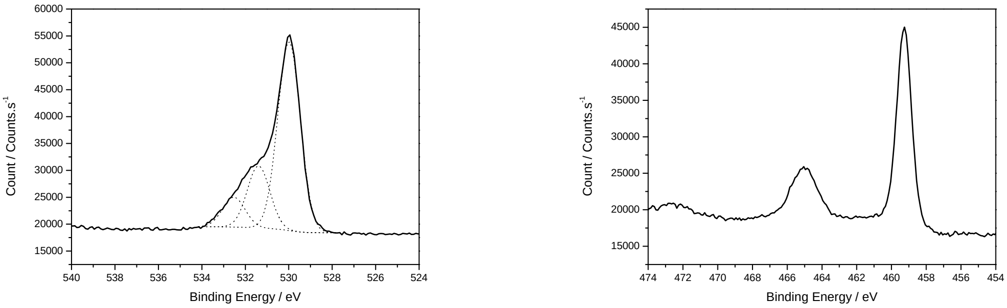

(c) O 1s

(d) Ti 2p

Figure B.2: XPS spectra of electrodes exposed to Ti etch. Data shows significant levels of surface contamination TiO_2.

that it is more likely to be a contaminant rather than a true reflection of the electrode composition.

Sample	Ag 3d	Au 4f	O 1s	Ti 2p
Ti Etch	1.07	11.95	69.44	17.53

Table B.1: XPS ratios following Ti etch. Ratios displayed as % of total counts

Figure B.3 shows a single P2 MKII C electrode after undergoing Ti etching. Figure B.3a is a SEM image of the electrode's surface, where contrast can be observed in a similar manner to that seen in the previously discussed microscopy images. The SAES contrast maps in Figures B.3b and B.3c demonstrate the distribution of O and Ti, respectively. As can be seen in Figure B.3b, the electrode surface has far less O that the surrounding SiO_2 layer. Figure B.3c shows the presence of Ti on the surface of the electrode but not on the surrounding SiO_2. While previous XPS data has indicated that the electrode is covered with a layer of TiO_2, it must be remembered that with electron spectroscopic techniques electron transitions of atoms several nm below the surface can be observed, as explained in Section 2.6. As such the O 1s peaks for a SiO_2 layer hundreds of nm thick and a TiO_2 layer a few nm thick will present a large degree of contrast despite the levels of O on the surface of each material being similar.

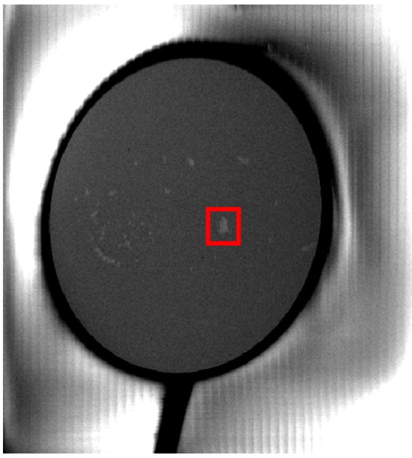

(a) SEM

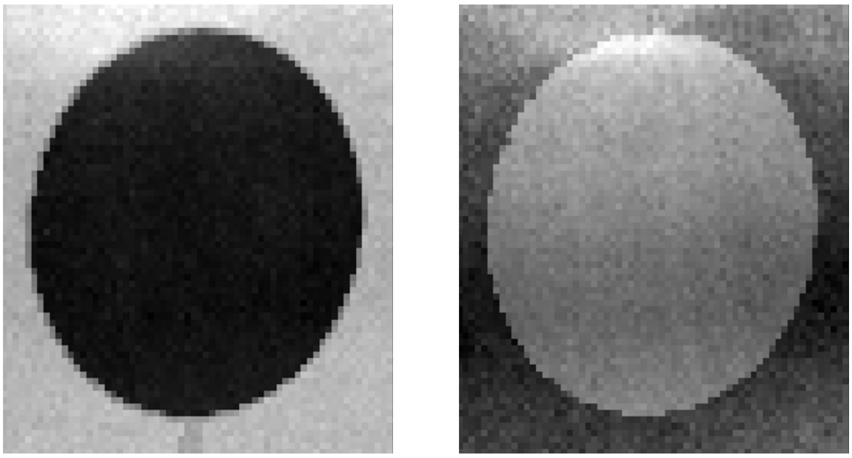

(b) SAES - O KVV

(c) SAES - Ti LVV

Figure B.3: SEM and SAES contrast maps of P2 MKII electrodes following Ti etch protocol. Outlined area = area studied in Figure B.4.

One sample area of contrast outlined in Figure B.3a, was selected for high spacial resolution scanning Auger emission spectroscopy imaging, as shown in Figure B.4a. This SEM image clearly shows defined regions of dark and bright contrast similar to those seen previously in light microscopy images (Figures 3.17-3.19) as well as the SEM images of P2 MKI electrodes in Figure 3.14.

Contrast maps for Ag MVV, Au NVV, O KVV and Ti LVV Auger electrons were generated to inspect the elemental composition of this region (Figures B.4b-B.4e, respectively). Figures B.4b (Ag MVV) and B.4c (Au NVV) show lighter regions of contrast that are confined to the same areas with the bright contrast in the SEM image. The contrast for Au NVV is brighter than for Ag MVV which would agree with the count ratios calculated by XPS that show Ag to have a far smaller signal than Au.

Figures B.4d and B.4e on the otherhand present dark contrast that is localised to the bright region of the SEM image. In this case the level of contrast is far greater for Ti LVV

transitions than O KVV transitions, suggesting that either the O containing material is confined to a thinner layer than the Ti, i.e. the surface; or that the difference between the two regions is less apparent due to O containing material also coinciding with the bright contrast region found in the SEM image, in the form of AgO, Ag_2O or Au_2O_3 as suggested by XPS data in Figure B.2c for example.

These figures indicate therefore that that the bright region observed in Figure B.4a is the bulk Au layer of the electrode, with some Ag contamination. Whether this is confined to the surface or found throughout the sample is questionable. The dark region observed in Figure B.4a is the same TiO_2 layer that was described prior to the Ti etching step. Additionally, oxides are found all over the electrode, although in greater concentrations within the TiO_2 layer.

There are numerous small patches similar in composition to the one examined in Figure B.4 distributed over the electrode surface. However, Figure B.3 shows that the majority of the electrode is covered with the TiO_2 layer. This is a far less favourable surface for SAM formation than the low RMS Au surfaces used previously in this thesis. It is no wonder therefore that highly variable capacitances are found.

A 2010 paper by Martinez, Gregori and Mates in Thin Solid Films provides evidence of the diffusion of Ti into Au when exposed to high temperatures (200 - 400°C). These temperatures are likely to have been achieved during the deposition of the SiO2 layer. Ti diffusion has been reported over distances of up to 260 nm making this a significant process that potentially results in Ti being dispersed throughout the Au layer. The paper further reports that this effect can be negated by replacing the Ti layer with TiN, which is more thermally resistant.

(a) SEM

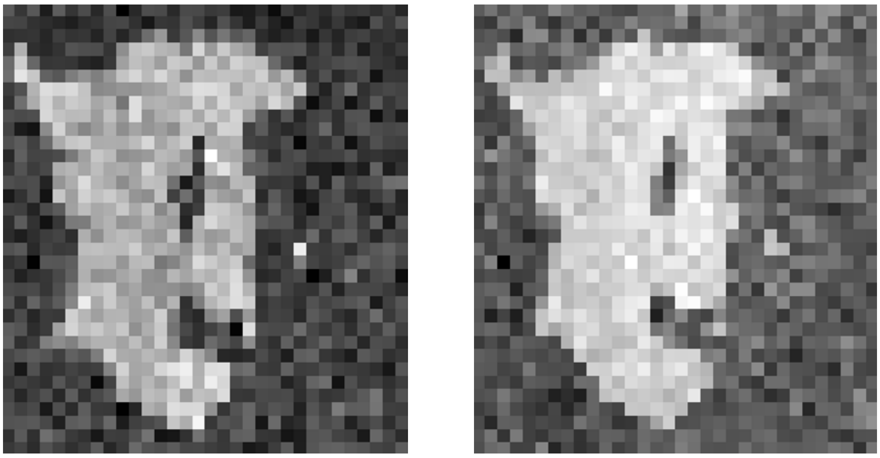

(b) SAES - Ag *MVV*

(c) SAES - Au *NVV*

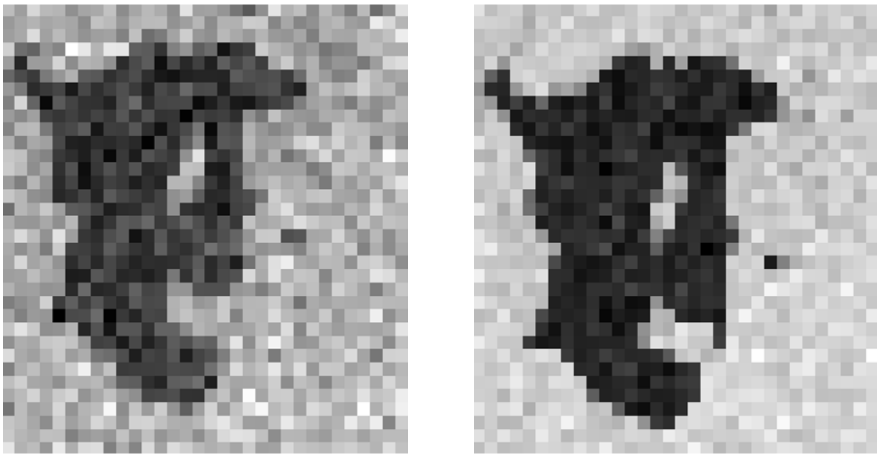

(d) SAES - O *KVV*

(e) SAES - Ti *LVV*

Figure B.4: SEM and SAES contrast maps of P2 mkII electrodes following Ti etch protocol.